TOWARDS ELECTRIC FIELD AND ATOM NUMBER UPGRADES FOR A HIGHER SENSITIVITY SEARCH FOR THE ATOMIC ELECTRIC DIPOLE MOMENT OF RADIUM-225

By

Gordon Arrowsmith-Kron

A DISSERTATION

Submitted to
Michigan State University
in partial fulfillment of the requirements
for the degree of

Physics — Doctor of Philosophy

2025

ABSTRACT

The discovery of a permanent non-zero Electric Dipole Moment (EDM) would be a clean signature of a new source of Charge-Parity (CP) violation in the universe. Radium-225 is an ideal candidate for these searches, due to its nuclear octupole deformation. This gives it a large intrinsic nuclear Schiff moment, and a nearly degenerate parity doublet, which cause an enhancement factor in the search for new sources of CP violation for a given EDM sensitivity. Previous measurements of the EDM of the Radium-225 atom were able to achieve a sensitivity on the order of $10^{-23}\ e \cdot \text{cm}$. The next generation of this experiment aims to achieve sensitivity of $10^{-26}\ e \cdot \text{cm}$, which in the global picture would set new limits on various CP violating sources. Crucial to this sensitivity enhancement is an upgrade to the high voltage used to couple the EDM to an external electric field. By achieving higher voltages with better understanding of electric field reversibility, statistical sensitivity can be increased and systematic uncertainty reduced. In addition, the Isotope Harvesting (IH) program at the Facility for Rare Isotope Beams (FRIB) will once again enable radium-225 to be procured for the experiment. To ensure optimal harvesting efficiency, the study of various techniques to create a beam of atomic radium will be necessary. For this reason, an atomic beam fluorescence apparatus has been built at FRIB.

ACKNOWLEDGMENTS

First and foremost, I would like to thank my advisor Jaideep Singh, who has patiently and helpfully guided me in my journey through graduate school. I would like to thank my thesis comittee, including Kei Minamisono, Tyler Cocker, Heiko Hergert, and Yue Hao for the advice throughout my graduate school career. I would like to thank all the other graduate students I have worked with in Spinlab, including Aiden Boyer, Nicholas Nusgart, Karina Martirosova, Yousuf Alishan, Himanshi, Erin White, Roy Ready, and Ben Loseth. I would also like to thank everyone I worked with at Argonne National Laboratory, such as Kevin Bailey, Matt Dietrich, Thomas O'Connor, Peter Mueller, Donald Booth, Michael Bishof, and Tenzin Rabga. I would like to thank Kim Crosslan, who I could always count on for wonderful help. I would like to thank other friends of mine that I have had here at Michigan State University, such as Kellen McGee, Dan Salazar, and Hank Thurston. Let me also take this time to thank my friends from home in New York City, such as Mark, Ness, Anik, Austin, Max Price, Max Drogin, and Josh. Finally, I would like to thank my incredibly supportive family, including Joan, Charley, Edmund, Billy, Anne, David, Richard, Deborah, Virginia, Steve, Jenny, and Charley Croft.

TABLE OF CONTENTS

Chapter 1. Introduction

This thesis documents ongoing efforts to improve the sensitivity of the radium-225 EDM experiment, to further constrain the upper limit of various sources of Charge-Parity (CP)-violation. Radium-225 has an octupole deformation in its nucleus that gives it a large nuclear Schiff moment, enhancing its sensitivity to sources of CP-violation. This experiment utilizes laser cooling and trapping to perform a spin precession measurement in the presence of a static electric field, which a non-zero atomic EDM will couple to. By reversing the direction of the electric field and looking for a phase shift in the spin precession, an EDM can be searched for. Care must be taken to ensure these electric fields are perfectly reversible, to reduce systematic uncertainties. Also crucial to this experiment is a reliable, steady supply of radium-225, which is a rare isotope with a half-life of only 15 days. Previous sources of radium-225 have shifted priorities away from fundamental symmetries measurements since the initial data runs in 2015. The Isotope Harvesting (IH) program at the Facility for Rare Isotope Beams (FRIB) will, once operational, make up for this shortfall. Questions remain, however, as to the efficiency with which an atomic beam can be created from isotopes harvested from the FRIB beam dump. The upgrades currently underway for the radium EDM experiment include a new optical cycling scheme to laser cool and trap atoms, as well as plans to dress the excited states of the spin precession measurement to allow for a cleaner signal. In addition, higher electric fields with improved reversibility are planned, as well as studying the efficiency with which beams of atomic radium can be created. The High Voltage (HV) upgrade requires the design and construction of a new apparatus at Michigan State University (MSU) to facilitate larger electric field magnitudes. It also requires atomic

theory calculations to quantify the various systematic effects that arise in atoms trapped in an Optical Dipole Trap (ODT). In addition, the beam efficiency studies requires an Atomic Beam Fluorescence (ABF) setup to be built at MSU, and then tested with laser spectroscopy of metallic calcium to measure its sensitivity. This thesis is organized into 7 further chapters. Chapter 2 details the theory of CP violation and EDMs, gives an overview on the reasons for measuring them, and what kinds of measurement media can be used. Chapter 3 talks about the reasons for using radium-225 specifically, and details the radium EDM experiment overall. Chapter 4 reports on efforts to utilize radium-223 as a temporary substitute. Chapter 5 details ongoing efforts to quantify the systematic effects that occur in EDM measurements done on atoms subject to static electric fields that are held in an ODT. Chapter 6 describes the progress on upgrading the HV apparatus at MSU. Chapter 7 details the assembly and testing of the ABF apparatus to be used for efficiency studies. Chapter 8 overall describes the work done by the author, and details future work needed to be done.

Chapter 2. Background & Motivation

2.1 Baryon Asymmetry of Universe

2.1.1 Discovery of the Cosmic Microwave Background

One of the greatest measurements in human history was achieved essentially by accident. A.A. Penzias and R.W. Wilson, two radio astronomers, were trying to reduce the background noise seen from their radio telescope at the Crawford Hill Laboratory in Holmdel, New Jersey. This noise was "isotropic, unpolarized, and free from seasonal variations,"[1] and was significantly higher than what was expected from Ohmic losses and atmospheric absorption. The paper they published was along side another paper [2] that interpreted the results from the noise as coming from Cosmic Microwave Background (CMB) radiation, which predicted a CMB temperature of 3.5 K. This measurement, which remarkably was able to make a measurement relating to the entire universe from a single telescope, became the subject of much research. Interestingly, the CMB was found to be anisotropic - its background temperature changes slightly depending on place in the sky it is measured at. This change in temperature throughout the sky can be mapped, and used to discover things about the universe, such as the relative lack of antimatter compared to matter.

2.1.2 Baryon Asymmetry

The asymmetry between the matter and antimatter seen in the universe can be characterized by the Baryon Asymmetry Parameter. This is given by

$$\eta = \frac{\eta_B - \eta_{\bar{B}}}{\eta_\gamma} \tag{2.1}$$

where η_B is the baryon density, $\eta_{\bar{B}}$ is the antibaryon density, and η_γ is the relic photon density. It can be experimentally determined from two sources.[3] The first is from Big Bang Nucleosynthesis (BBN). After the Big Bang, simple nuclei began to form as the universe cooled. η_B can be derived by measuring the abundances of these nuclei, such as ^{7}Li, or ^{3}He. Observed abundances of deuterium give the most precise determination of η_B. This is because the only significant source of deuterium in the universe that exists is that which is left over from the Big Bang, so no other deuterium has been created in stellar processes. The current deuterium mass fraction from BBN is $B/H|_p = (25.47 \pm 0.29) \times 10^{-6}$ which corresponds to a derived η value of

$$\eta = (6.040 \pm 0.118) \times 10^{-10} \tag{2.2}$$

There is another way of extracting the η parameter coming directly from anisotropy in the CMB. Measurements of the CMB anisotropy yield a baryon density parameter of $\Omega_b h^2 = .02237 \pm .00015$, which corresponds to a η value of [4]:

$$\eta = (6.104 \pm .058) \times 10^{-10} \tag{2.3}$$

which is well in agreement with the observation from BBN. This means that, having measured this parameter with two completely different types of observations, the observed baryon asymmetry parameter is well fixed, though observations in BBN with lithium remain in tension with this value. The question remains of how this asymmetry came to be, and

why there is something rather than nothing. Either the universe started out with an initial asymmetry between matter and antimatter, or matter and antimatter were initially created in equal amounts but the evolution of the universe overall favored matter over antimatter. This explanation of the origin of matter and antimatter is known as Baryogenesis.

2.1.3 Sakharov Conditions

In 1967, Andrei Sakharov proposed three criteria necessary for Baryogenesis [**?**]. The three conditions are the presence of:

1. Baryon number violating interactions
2. C and CP violating interactions
3. Interactions out of thermal equilibrium.

While the Standard Model does satisfy conditions one and three, it does not provide enough CP-violation to sufficiently explain the observed value of η.

2.1.4 Baryon Asymmetry Predicted from CP Violation

The observed CP-violation within the Standard Model can be generally represented by a phase in the Cabibbo-Kobayashi-Maskawa (CKM) matrix. The CKM matrix is a 3x3 matrix which describes the probability of weak interactions between different quark flavors. The 9 elements of the CKM matrix can be described by the sines and cosines of 3 mixing angles θ, and a CP-violating phase δ. Calculations can be done to predict the baryon asymmetry that results from this CP-violating phase of the CKM matrix. One such calculation [5] gives a value of $\eta \approx 10^{-27}$.

This means that there is a 17 order of magnitude difference between the observed η and the one predicted by current sources of CP violation. This implies there may be other sources of CP violation yet to be discovered. A brief overview of various symmetries shall now be given.

2.1.5 List of Discrete Symmetries

Physical parameters can be described by their behavior under discrete transformations. The three main transformations are now described.

2.1.5.1 Parity

A parity transformation (P) is a spatial inversion. It occurs through the interchange of coordinates $[x, y, z] \rightarrow [-x, -y, -z]$, or in spherical coordinates $[r, \theta, \phi] \rightarrow [r, \pi - \theta, \phi + \pi]$. An visual demonstration of this transformation can be seen in Figure 2.1.

Figure 2.1: Diagram of a parity transformation. Left: two charged particles before a parity transformation. Right: the same two particles after a parity transformation. Note the change in sign of the position and velocity components of each particle.

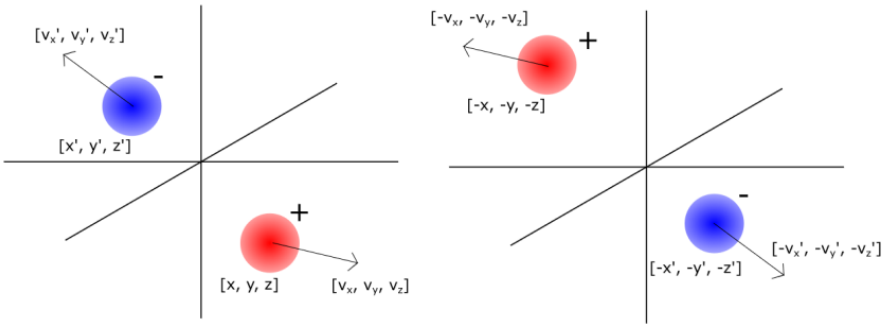

It was believed that the laws of physics remained the same under this transformation.

This was experimentally shown to be false by the Madame Wu experiment, which will be discussed in Section 2.2.1.

2.1.5.2 Charge

A charge conjugation (C) occurs when matter is exchanged for anti-matter. This causes charges to change sign like $Q \rightarrow -Q$, but it also affects other quantities, such as baryon number and lepton number. An example can be seen in Figure 2.2

Figure 2.2: Diagram of a charge conjugation transformation. Left: two charged particles before charge conjugation. Right: the same two particles after charge conjugation. Note the change in sign of the electric charge.

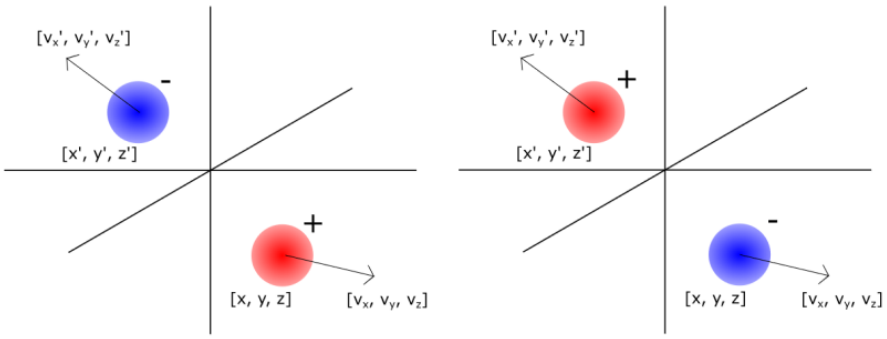

2.1.5.3 Time

A time-reversal transformation (T) occurs when the arrow of time is reversed, causing time variables to change sign: $t \rightarrow -t$. An example can be seen in Figure 2.3.

2.1.5.4 Charge-Parity

A Charge-Parity transformation (CP) is the application of charge conjugation and parity transformation. After P-symmetry was shown to be broken in weak interactions, it was

Figure 2.3: Diagram of a time reversal transformation. Left: two charged particles before time reversal transformation. Right: the same particles after time reversal transformation. Note the sign change in velocity.

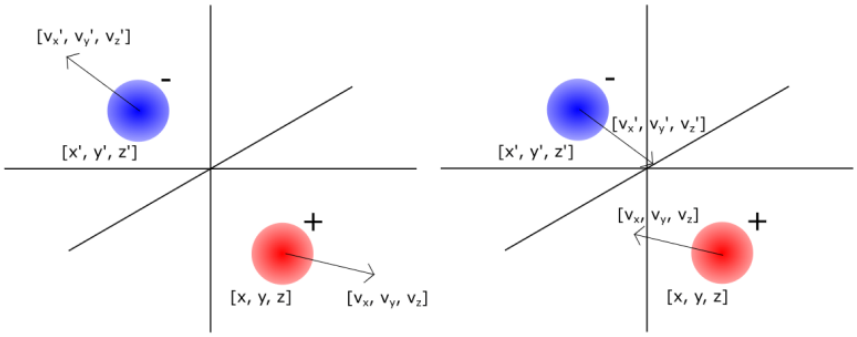

believed that CP-symmetry was always conserved [6]. This was also shown to be false [7].

2.1.5.5 Charge-Parity-Time

A Charge-Parity-Time transformation (CPT) is the application of all three discrete symmetry transformations. It is currently believed that a CPT-transformation is always symmetric, though many experiments are searching for interactions where a CPT-transformation is not symmetric.

2.1.5.6 Lorentz Invariance

In the framework of special relativity, space-time events can be presented as a contravariant 4-vector $a^\mu = [ct, x, y, z]$ or as a covariant 4-vector $b_\mu = g_{\mu\nu}b^\nu = [ct', -x', -y', -z']$, where $g_{\mu\nu}$ is the Minkowski metric tensor. In this system, the value $a^\mu b_\mu = c^2tt' - xx' - yy' - zz'$ is invariant under a transformation of both vectors a^μ and b_μ by the Lorentz transformation

$$\Lambda^{\nu}_{\mu} = \begin{bmatrix} \gamma & -\beta\gamma & 0 & 0 \\ -\beta\gamma & \gamma & 0 & 0 \\ 0 & 0 & 1 & 0 \\ 0 & 0 & 0 & 1 \end{bmatrix} \tag{2.4}$$

where $\gamma = \frac{1}{\sqrt{1-\beta^2}}$ is the Lorentz factor and $\beta = \frac{v}{c}$, in the case where all motion is along the x-direction. This transformation property is known as Lorentz invariance. As a result of this invariance, Lorentz scalars remain the same in all reference frames. A breaking in CPT symmetry would imply a break in Lorentz invariance.

2.2 Violations of Discrete Symmetries

2.2.1 P-violation

In 1956, T.D. Lee and C.N.Yang [8] called into question whether the weak interaction preserves parity, as had been presumed. This question resulted in a famous experiment conducted by C.S. Wu and her collaborators at the National Bureau of Standards [9]. In this experiment, a ^{60}Co beta decay source was polarized, and the beta decay angular distribution measured twice, at two different anti-parallel polarization directions. Gamma radiation was used to monitor the degree of polarization. A clear asymmetry was seen between the two polarizations, demonstrating a non-conservation of P-symmetry. Afterwards, an experiment measuring the polarization of muons decayed from pions was done by measuring the electron distribution from the muon decay[10]. After the publication of these results, Landau [6] proposed that space could remain isotropic even with parity non-conservation, so long as CP-symmetry held. For several years afterwards it was believed that CP-symmetry was

conserved in weak interactions instead of P-symmetry.

2.2.2 CP-violation

An experiment studying the decay of kaons in 1964 [7] revealed a decay path which is only possible through CP-violation. This showed that CP-symmetry is not a conserved quantity in the universe, though it is only violated in the weak interaction as far as is currently known. CPT-symmetry is still assumed to be conserved, as no violation has yet been found. A signature of T-violation is thus a signature of CP-violation as well.

2.3 Electric Dipole Moments as Signatures of New Physics

New sources of CP-violation can be looked for in a variety of ways. One very clean signature of CP-violation is the existence of a non-zero Electric dipole Moment, or EDM.

2.3.1 Definition of EDM

When looking at a distribution of charges from far away, it becomes convenient to write the charge distribution in a multipole expansion. This is done by expanding the potential of the charge distribution in a form like

$$V(\mathbf{r}) = V_{\text{mon}}(\mathbf{r}) + V_{\text{dip}}(\mathbf{r}) + V_{\text{quad}}(\mathbf{r}) + ... \tag{2.5}$$

where the dependence on $r = \|\mathbf{r}\|$ goes like:

$$V(\mathbf{r}) = \frac{1}{r} f_{\text{mon}}(\theta, \phi) + \frac{1}{r^2} f_{\text{dip}}(\theta, \phi) + \frac{1}{r^3} f_{\text{quad}}(\theta, \phi) \tag{2.6}$$

where the functions $f(\theta, \phi)$ are the angular dependencies for each term. The function $V_{\text{mon}}(\mathbf{r})$ is the monopole moment, and is simply

$$V_{\text{mon}}(\mathbf{r}) = \frac{1}{r} \frac{1}{4\pi\epsilon_0} \int_{V'} \rho(r') dV' = \frac{Q_{\text{total}}}{4\pi\epsilon_0 r} \tag{2.7}$$

which is just the potential given by a point charge, whose charge is equal to the total of the charge distribution.

The next term in the expansion is given by

$$V_{\text{dip}}(\mathbf{r}) = \frac{\hat{\mathbf{r}}}{4\pi\epsilon_0 r^2} \cdot \int_{V'} \rho(r') \mathbf{r}' dV' \tag{2.8}$$

The integral in the dipole term of the expansion:

$$\mathbf{d} = \int_{V'} \rho(r') \mathbf{r}' dV' \tag{2.9}$$

is known as the "electric dipole moment", or EDM. The strength of the potential due to the EDM vanishes faster as $\|\mathbf{r}\| \to \infty$ when compared to the monopole moment, but this approached zero slower than the higher-order terms such as the quadrupole or octupole moments. EDMs are useful for fundamental symmetry searches because they are a very clean signature of CP-violation as will be discussed in the next section.

2.3.2 Why EDMs Violate Symmetry

The existence of a non-zero permanent EDM is a signature of CP-violation, as can be seen through the Wigner-Eckart theorem. The energy produced by the interaction between a non-zero electric and magnetic dipole moment and an external electric and magnetic field is

$$H = -\boldsymbol{\mu} \cdot \mathbf{B} - \mathbf{d} \cdot \mathbf{E} \tag{2.10}$$

where $\boldsymbol{\mu}$ is the magnetic dipole moment, $\mathbf{E}$ is the electric field, and $\mathbf{B}$ is the magnetic field. The Wigner-Eckart theorem proves that μ and $\mathbf{d}$ must be parallel to the spin. Thus,

$$H = -\mu \left(\frac{\mathbf{S} \cdot \mathbf{B}}{|\mathbf{S}|} \right) - d \left(\frac{\mathbf{S} \cdot \mathbf{E}}{|\mathbf{S}|} \right) \tag{2.11}$$

Where $\mathbf{S}$ is the spin. The transformation properties of each component in the Hamiltonian are summarized in Table 2.1.

Table 2.1: Discrete symmetry transformations of the spin, electric field, magnetic field, and interaction terms.

Value	P-Transformation	C-Transformation	T-Transformation
$\mathbf{S}$	Even	Even	Odd
$\mathbf{E}$	Odd	Odd	Even
$\mathbf{B}$	Even	Odd	Odd
$\mathbf{S} \cdot \mathbf{B}$	Even	Odd	Even
$\mathbf{S} \cdot \mathbf{E}$	Odd	Odd	Odd

Under a T-transformation of the Hamiltonian, it becomes

$$H = -\mu \left(\frac{\mathbf{S} \cdot \mathbf{B}}{|\mathbf{S}|} \right) + d \left(\frac{\mathbf{S} \cdot \mathbf{E}}{|\mathbf{S}|} \right) \tag{2.12}$$

where the magnetic term remains the same and the electric term changes sign. This means

that, should $d \neq 0$, the Hamiltonian will be different under T-transformation. Through the CPT-symmetry, this implies CP-violation as well.

2.3.3 Definition of Nuclear Schiff Moment

According to the Schiff Theorem [11], when approximating a nucleus as a point particle, and assuming non-relativistic motion, a non-zero nuclear EDM will cause a screening effect in the surrounding electrons that completely shields the nuclear EDM. However, the nucleus also has what is called a Schiff moment, and this will induce an atomic EDM in the surrounding atom. An excellent derivation of this can be given by references [12] and [13] and will be presented below:

Consider an electrostatic potential of the form

$$\phi(\mathbf{R}) = \int \frac{e\rho(\mathbf{r})}{|\mathbf{R}-\mathbf{r}|} d^3r + \frac{1}{Z}(\mathbf{d}\cdot\nabla)\int \frac{\rho(\mathbf{r})}{|\mathbf{R}-\mathbf{r}|} d^3r \tag{2.13}$$

This potential represents the nuclear electrostatic potential with the effects of electron screening included. Here, $e\rho(\mathbf{r})$ is the nuclear charge density, and $d = e\int \rho(\mathbf{r})\mathbf{r}d^3r$ is the nuclear EDM.

The quantity $\frac{1}{|\mathbf{R}-\mathbf{r}|}$ can be expanded like

$$\frac{1}{|\mathbf{R}-\mathbf{r}|} = \sum_l \frac{r_<^l}{r_>^{l+1}} P_l(\cos(\theta)) \tag{2.14}$$

where P_l are the Legendre polynomials, θ is the angle between $\mathbf{r}$ and $\mathbf{R}$, and $r_<$ and $r_>$ correspond to the smaller and larger of the quantities $\mathbf{R}$, $\mathbf{r}$. The first P- and T-violating expansion contributions from each term in the original potential are:

$$\phi^{(1)}(\mathbf{R}) = e\int \frac{\rho(\mathbf{r})r_<}{r_>^2}\cos(\theta) + \frac{1}{Z}(\mathbf{d}\cdot\nabla)\int \frac{\rho(\mathbf{r})}{r_>}d^3r \tag{2.15}$$

which corresponds to the l = 1 expansion of the first term, and the l = 0 expansion of the second term. This can then be further simplified to

$$\phi^{(1)}(\mathbf{R}) = \frac{e}{R^2}\int_0^R \rho(\mathbf{r})r\cos(\theta)d^3r + eR\int_R^\infty \frac{\rho(\mathbf{r})\cos(\theta)}{r^2}d^3r + \frac{\mathbf{d}\cdot\hat{\mathbf{r}}}{ZR^2}\int_0^R \rho(\mathbf{r})d^3r \tag{2.16}$$

and then be written as a series of dot products

$$\phi^{(1)}(\mathbf{R}) = \frac{e\mathbf{R}}{R^3}\cdot\int_0^R \mathbf{r}\rho(\mathbf{r})d^3r + e\mathbf{R}\cdot\int_R^\infty \frac{\mathbf{r}}{r^3}\rho(\mathbf{r})d^3r - \frac{e\langle\mathbf{r}\rangle\cdot R}{ZR^3}\int_0^R \rho(\mathbf{r})d^3r \tag{2.17}$$

Now consider the case where $\mathbf{R}\to\infty$. The first term becomes

$$\frac{e\mathbf{R}}{R^3}\cdot\int_0^\infty \mathbf{r}\rho(\mathbf{r})d^3r = \frac{e\mathbf{R}\cdot\langle\mathbf{r}\rangle}{R^3} \tag{2.18}$$

and the third term becomes

$$\frac{e\langle\mathbf{r}\rangle\cdot R}{ZR^3}\int_0^\infty \rho(\mathbf{r})d^3r = \frac{Ze\langle\mathbf{r}\rangle\cdot\mathbf{R}}{ZR^3} = \frac{e\langle\mathbf{r}\rangle\cdot\mathbf{R}}{R^3} \tag{2.19}$$

This can be used to turn the limits of the integral from $0 \to R$ to $R \to \infty$, as can be seen in the equation below:

$$\frac{e\mathbf{R}}{R^3} \cdot \int_0^R \mathbf{r}\rho(\mathbf{r})d^3r - \frac{e\langle\mathbf{r}\rangle \cdot R}{ZR^3}\int_0^R \rho(\mathbf{r})d^3r = \frac{e\mathbf{R}}{R^3} \cdot \int_0^R \mathbf{r}\rho(\mathbf{r})d^3r - \frac{e\langle\mathbf{r}\rangle \cdot R}{ZR^3}\int_0^R \rho(\mathbf{r})d^3r + 0 \tag{2.20}$$

$$= \frac{e\mathbf{R}}{R^3} \cdot \int_0^R \mathbf{r}\rho(\mathbf{r})d^3r - \frac{e\langle\mathbf{r}\rangle \cdot R}{ZR^3}\int_0^R \rho(\mathbf{r})d^3r + \frac{e\langle\mathbf{r}\rangle \cdot R}{ZR^3}\int_0^\infty \rho(\mathbf{r})d^3r - \frac{e\mathbf{R}}{R^3} \cdot \int_0^\infty \mathbf{r}\rho(\mathbf{r})d^3r \tag{2.21}$$

$$= -\left(\frac{e\mathbf{R}}{R^3} \cdot \int_0^\infty \mathbf{r}\rho(\mathbf{r})d^3r - \frac{e\mathbf{R}}{R^3} \cdot \int_0^R \mathbf{r}\rho(\mathbf{r})d^3r\right) + \left(\frac{e\langle\mathbf{r}\rangle \cdot R}{ZR^3}\int_0^\infty \rho(\mathbf{r})d^3r - \frac{e\langle\mathbf{r}\rangle \cdot R}{ZR^3}\int_0^R \rho(\mathbf{r})d^3r\right) \tag{2.22}$$

$$= -\frac{e\mathbf{R}}{R^3} \cdot \int_R^\infty \mathbf{r}\rho(\mathbf{r})d^3r + \frac{e\langle\mathbf{r}\rangle \cdot R}{ZR^3}\int_R^\infty \rho(\mathbf{r})d^3r \tag{2.23}$$

This can be used to write the potential as:

$$\phi^{(1)}(\mathbf{R}) = e\mathbf{R} \cdot \left[\int_R^\infty \left(\frac{\langle\mathbf{r}\rangle}{ZR^3} - \frac{\mathbf{r}}{R^3} + \frac{\mathbf{r}}{r^3}\right)\rho(\mathbf{r})d^3r\right] \tag{2.24}$$

From here, consider a generic wavefunction of an electron:

$$\psi = \begin{bmatrix} f(R) \\ -i(\sigma \cdot \hat{\mathbf{R}})g(R) \end{bmatrix} \Omega_{jlm} = h(R)\Omega_{jlm} \tag{2.25}$$

where $f(R)$ and $g(R)$ are radially dependent functions, $h(R)$ is the whole vector, and Ω_{jlm} is a spherical spinor. The potential $\phi^{(1)}(\mathbf{R})$ is both odd in parity, and close to the nucleus. The only orbital wavefunctions that have a significant presence near the nucleus are l = 0 and 1. Since this potential is odd in parity, the only relevant matrix element to

resolve is that between l = 0 and l = 1. The matrix element can be written explicitly like:

$$\langle s|-e\phi^{(1)}(\mathbf{R})|p\rangle = e^2\int_0^\infty\int_0^{2\pi}\int_0^\pi \psi_s^\dagger \mathbf{R}\cdot\left[\int_R^\infty\left(\frac{\langle\mathbf{r}\rangle}{ZR^3}-\frac{\mathbf{r}}{R^3}+\frac{\mathbf{r}}{r^3}\right)\rho(\mathbf{r})d^3r\right]\psi_p R^2\cos(\theta_R)d\theta_R d\phi_R dR \tag{2.26}$$

$$= -e^2\int_0^\infty\int_0^{2\pi}\int_0^\pi \psi_s^\dagger \frac{\mathbf{R}}{R}\cdot\left[\int_R^\infty\left(\frac{\langle\mathbf{r}\rangle}{Z}-\mathbf{r}+\frac{R^3\mathbf{r}}{r^3}\right)\rho(\mathbf{r})d^3r\right]\psi_p\cos(\theta_R)d\theta_R d\phi_R dR \tag{2.27}$$

$$= -e^2\int_0^{2\pi}\int_0^\pi \Omega_s^\dagger\hat{\mathbf{R}}\Omega_p\cos(\theta_R)d\theta_R d\phi_R \cdot\int_0^\infty\int_R^\infty h_s^\dagger(R)\left(\frac{\langle\mathbf{r}\rangle}{Z}-\mathbf{r}+\frac{R^3}{r^3}\mathbf{r}\right)\rho(\mathbf{r})h_p(R)d^3rdR \tag{2.28}$$

To simplify notation, define the inner product

$$U_{sp} = h_s^\dagger(R)h_p(R) = f_s(R)f_p(R)+g_s(R)g_p(R) \tag{2.29}$$

and define the matrix element

$$\langle s|\hat{\mathbf{R}}|p\rangle = \int_0^{2\pi}\int_0^\pi \Omega_s^\dagger\hat{\mathbf{R}}\Omega_p\sin(\theta_R)d\theta_R d\phi_R \tag{2.30}$$

Then, these can be used to write Equation 2.28 as

$$\langle s|-e\phi^{(1)}(\mathbf{R})|p\rangle = -e^2\langle s|\hat{\mathbf{R}}|p\rangle\cdot\int_0^\infty\int_R^\infty h_s^\dagger(R)\left(\frac{\langle\mathbf{r}\rangle}{Z}-\mathbf{r}+\frac{R^3}{r^3}\mathbf{r}\right)\rho(\mathbf{r})h_p(R)d^3rdR \tag{2.31}$$

$$= -e^2\langle s|\hat{\mathbf{R}}|p\rangle\cdot\int_0^\infty\int_0^r h_s^\dagger(R)\left(\frac{\langle\mathbf{r}\rangle}{Z}-\mathbf{r}+\frac{R^3}{r^3}\mathbf{r}\right)\rho(\mathbf{r})h_p(R)dRd^3r \tag{2.32}$$

$$= -e^2\langle s|\hat{\mathbf{R}}|p\rangle\cdot\int_0^\infty\left[\left(\frac{\langle\mathbf{r}\rangle}{Z}-\mathbf{r}\right)\int_0^r U_{sp}(R)dR+\frac{\mathbf{r}}{r^3}\int_0^r U_{sp}(R)R^3dR\right]\rho(\mathbf{r})d^3r \tag{2.33}$$

The quantity $U_{sp}(R)$ can be expressed as

$$U_{sp}(R) = \sum_{k=1}^{\infty} b_k R^k \tag{2.34}$$

Substituting this into Equation 2.33 gives

$$\langle s| - e\phi^{(1)}(\mathbf{R})|p\rangle = -e^2\langle s|\hat{\mathbf{R}}|p\rangle \cdot \sum_{k=1}^{\infty} \frac{b_k}{k+1}\left[\frac{\langle \mathbf{r}\rangle}{Z}\langle r^{k+1}\rangle - \frac{3}{k+4}\langle \mathbf{r} r^{k+1}\rangle\right] \tag{2.35}$$

Consider the simplest case where k = 1, then Equation 2.35 becomes

$$\langle s| - e\phi^{(1)}|p\rangle = -\frac{e^2 b_1}{2}\langle s|\hat{\mathbf{R}}|p\rangle \cdot \left[\frac{1}{Z}\langle \mathbf{r}\rangle\langle r^2\rangle - \frac{3}{5}\langle \mathbf{r} r^2\rangle\right] \tag{2.36}$$

This can then be written as

$$\langle s| - e\phi^{(1)}|p\rangle = 4\pi e\mathbf{S} \cdot (\nabla\psi_s^{\dagger}\psi_p)_{R\to 0} \tag{2.37}$$

where the quantity

$$\mathbf{S} = \frac{e}{10}\left[\langle r^2\mathbf{r}\rangle - \frac{5}{3Z}\langle r^2\rangle\langle \mathbf{r}\rangle\right] = S\frac{\mathbf{I}}{I} \tag{2.38}$$

is known as the Schiff moment. Note that this divides the potential into two sections: (1) a contribution from the Schiff moment which depends on the properties of the nucleus, and (2) a contribution from the electronic wavefunctions ψ_s and ψ_p, which are dependent on the properties of the electron distribution. This potential is capable of coupling states of different parity, much like the electric dipole transition coupling necessary for an atomic

EDM to be induced. Thus, an atomic EDM can be written using this potential as:

$$\mathbf{d}_{atom} = -2e\sum_k \frac{\langle i|\mathbf{r}|k\rangle\langle k| - e\phi^{(1)}|i\rangle}{E_i - E_k} = -2e\sum_k \frac{\langle i|\mathbf{r}|k\rangle 4\pi\mathbf{S}\cdot(\nabla\psi_k^\dagger\psi_i)_{R\to 0}}{E_i - E_k} \tag{2.39}$$

where $\nabla\psi_k^\dagger\psi_i$ can be approximated as

$$\nabla\psi_k^\dagger\psi_i \approx Z^2\alpha^2 \tag{2.40}$$

where α is the fine structure constant and Z is the proton count. Equation 2.39 can now be written as

$$\mathbf{d}_{atom} = -2e\sum_k \frac{\langle i|\mathbf{r}|k\rangle 4\pi S Z^2\alpha^2}{E_i - E_k} \tag{2.41}$$

This gives an enhancement factor to EDM searches for heavy nuclei, since the sensitivity scales like Z^2. For octupole deformed nuclei, there is an additional enhancement factor intrinsic to the Schiff moment, which will be discussed later.

2.4 State of the Art in Hadronic CP-Violation Experiments

Precision EDM searches in different types of systems probe different sectors from which new physics might arise. The most precise atomic EDM search constraining new physics in the hadronic sector is the measurement of Hg-199. This experiment gives an upper limit 95% confidence interval of $d_{\mathrm{Hg}} < 7.4 \times 10^{-30}\ e\cdot\mathrm{cm}$ [14].

The experiment consisted of two vapor cells of Hg-199, with a charged plate in between the gas cells, creating an electric field of equal strength in each of the cells, but in opposite directions, as can be seen in Figure 2.4.

Figure 2.4: Diagram of the Hg-199 EDM experimental setup. a): a cross sectional view of the vapor cells. b): a cross sectional view of the apparatus as a whole. Figure taken from [14].

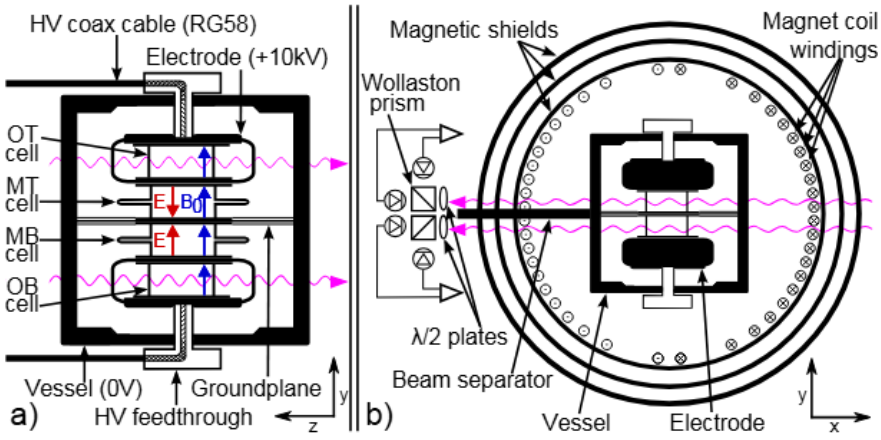

A magnetic field is also applied to the cells to cause the Larmor precession for the phase shift measurement. More detail on the precise workings of an EDM experiment will be given in Section 3.2. Because the vapor cells use the same electrode plate, and the spin precession measurements are done at the same time, there is a great reduction in the uncertainty due to magnetic field instability. This gives the experiment a great deal of precision. However, the Hg-199 atom does not have an octupole deformation, and its leading systematic is due to a magnetic field gradient in the axial direction of its vapor cells, which is seen due to the motion of the mercury atoms. With any shift in position of the cells due to HV, this would create a false EDM signature. The experiment ran with 4 different configurations, with the magnetic field running in either direction, and the electric field both parallel and antiparallel to the magnetic field in order to characterize this systematic effect. This would

be understood to be the dominant systematic effect, which is difficult to reduce. There are improvements that could be implemented to reduce this systematic effect, but they would only result in a factor of two improvement to the current result and would be challenging to achieve at this time.

2.4.1 Connection Between EDMs and New Physics

By performing EDM searches on a wide variety of systems, different sectors of physics where CP-violation can arise are probed. Diamagnetic systems, such as Hg-199, Ra-225, or Xe-129, are good at probing spin dependent electron-nucleus coupling, as well as nucleon-nucleon interactions. Paramagnetic systems, such as Fr or Cs, on the other hand, look for nuclear spin independent electron-nucleus coupling, as well as for the electron EDM. An EDM can be expressed as linear combination of CP-violating factors from various sources [15], as can be seen in equation 2.42

$$d_{atom} = \alpha_{d_e} d_e + \alpha_{C_S} C_s + \alpha_{C_T} C_T + \alpha_{d_n} d_n + \alpha_{d_p} d_p + \alpha_{g_\pi^0} g_\pi^0 + \alpha_{g_\pi^1} g_\pi^1 \tag{2.42}$$

where d_e is the electron EDM, C_S is a CP-violating spin-independent electron-nucleus interaction, C_T is a spin-dependent electron-nucleus interaction, g_π^0 and g_π^1 are pion-nucleon couplings for isospin 0 and 1 respectively, d_p is the proton EDM, and d_n is the neutron EDM. The parameters α_{d_e}, α_{C_S}, α_{C_T}, $\alpha_{g_\pi^0}$, $\alpha_{g_\pi^1}$, α_{d_p}, and α_{d_n} are various coupling constants that can be determined by nuclear, molecular, or atomic structure calculations. The current best limits for CP violating parameters can be found in Table 2.2.

Table 2.2: Current best limits on CP-violating sources. "Global" indicates the contribution from multiple different sources were considered for the constraint. "Single source" indicates that only the best limit was considered, with all contribution coming from a single source of CP violation.

Parameter	Best Sensitivity	Source
d_e	$< 2.1 \times 10^{-29}$ $e \cdot$ cm (global)	[16], [17]
C_S	$< 1.9 \times 10^{-9}$ (global)	[16], [17]
C_T	1.2×10^{-7} (single source)	[14]
g_π^0	2.3×10^{-12} (single source)	[14]
g_π^1	1.2×10^{-12} (single source)	[14]
d_p	2.0×10^{-25} $e \cdot$ cm (single source)	[14]
d_n	$< 1.8 \times 10^{-26}$ $e \cdot$ cm (single source)	[18]

2.5 Current Status of Other EDM searches

At the moment, there are multiple experiments searching for new physics by trying to find new sources of CP-violation. Among these are EDM searches, searching for non-zero signatures in a variety of systems, such as leptons, neutrons, atoms, and molecules.

2.5.1 Neutron EDM searches

There is are multiple ongoing efforts worldwide to search for the EDM of the neutron. At Los Alamos, there is an EDM experiment being performed on ultracold neutrons (UCN) known as the nEDM experiment. The purpose of this experiment is to measure the EDM of the neutron to a target precision of $d_n \leq 2 \times 10^{-27}$ $e \cdot$ cm after 5 years of data collection. The experiment uses a typical EDM measurement cycle: load the neutrons into a trap, let the neutrons precess under an electric field, and then measure the spin direction of the neutrons in their final state, looking for any change in phase under a reversal of the electric field. Tests have been performed measuring the count rate of neutrons under different

neutron holding times, and different applied magnetic fields. They can have an UCN yield of 60,000 neutrons with a 180 s holding time, which should be sufficient to achieve their precision target in the allotted time [19]. Currently, the best nEDM measurement sits at $|d_n| \leq 1.8 \times 10^{-26}\ e \cdot \text{cm}$ performed by the Paul Scherrer Institute (PSI) center for Muon and Neutron Sciences [18]. This experiment utilized the PSI UCN source to provide neutrons to a spin precession chamber, with a spin flipper capable of choosing the direction of spin for the incoming neutrons. The neutrons precess in the chamber for 180 s, with an applied electric field of 11 kV/cm. They are then let out of the chamber, an fall a system of two neutron detectors each equipped with a spin flipper, one of which will be on. The neutron detectors then count the number of spin up and spin down neutrons, and measure the population asymmetry between them. The apparatus is depicted in Figure 2.5. An average of 11,400 neutrons were counted per cycle.

2.5.2 Electron EDM searches

Electron EDMs are searched for in paramagnetic atoms and molecules. The ACME experiment at Harvard used a beam of ThO to measure the EDM of the electron, and set a limit of $d_e < 1.1 \times 10^{-29}\ e \cdot \text{cm}$ in 2018 [17]. This experiment was performed on a moving beam of molecules which were polarized, and allowed to precess over a length of 20 cm, or ~ 1 ms. Then, the orientation of spin was read out by measuring the intensity of scattered light from an excited transition dependent on the spin orientation. The electric field applied was either 80 or 140 V/cm, and the experiment was run for over 350 hours. The leading systematic effect proved to be imperfections in electric field reversibility.

Another experiment was done in 2022 on HfF^+ ions[16]. In this experiment, HfF molecules are created and collimated into a beam, where they ionized and then trapped, allowing an

Figure 2.5: Diagram of the nEDM setup at PSI. Ultracold neutrons travel through a 5 T magnet where they are spin polarized, and then drift up to the spin precession chamber. The UCN then fall down to the neutron detectors with spin flippers which count the number of spin up and spin down neutrons. Figure taken from [18].

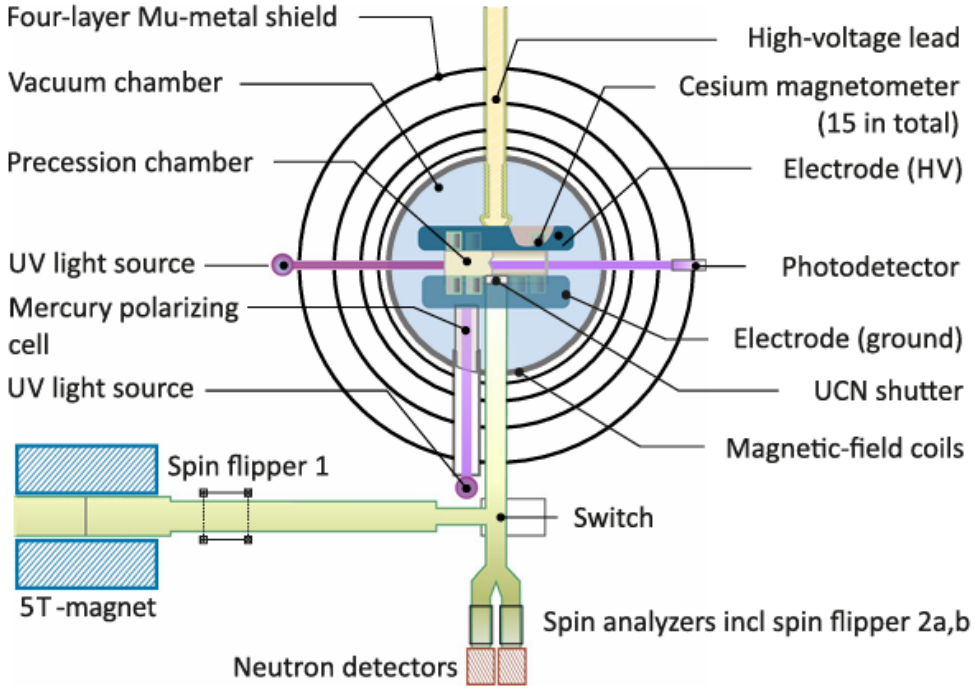

EDM experiment to be performed. The result was a 90% confidence interval upper bound of $d_e < 4.1 \times 10^{-30}\ e \cdot \text{cm}$ which is in agreement with the ThO result.

2.5.3 Yb-171 and Ra-225

At the University of Science and Technology of China, an EDM experiment has been performed on Yb-171, yielding a result with a 95% confidence interval at $d_{Yb_{171}} < 1.5 \times 10^{-26}\ e \cdot \text{cm}$ [20]. This experiment was nearly identical to the radium-225 laser trap experiment (RaEDM) which set a limit of $d_{Ra_{225}} < 1.4 \times 10^{-23}\ e \cdot \text{cm}$ [21].

When considering the enhancement factor in Ra-225 due to its octupole deformation, both of these experiments set roughly the same limit on sensitivity to new physics. The

Yb-171 experiment utilizes a novel Quantum-Non-Demolition (QND) technique [22], that dresses the excited states used for the shadow imaging that is done to perform the final spin measurement. With this technique, they were able to achieve a spin detection efficiency of 50%, far above what the most recent run of the RaEDM experiment was able to achieve [23]. This upgrade is readily applicable for use in the RaEDM experiment, and work is being done to implement it into the next data run. More information on the radium-225 experiment can be found in Chapter 3.

2.5.4 Xe-129

An experiment searching for the EDM of the Xe-129 atom was done, setting a limit of $\|d_A(Xe-129)\| < 8.3 \times 10^{-28}\ e \cdot \text{cm}$ [24]. This experiment utilizes a He-3 co-magnetometer, whose spin precession is measured simultaneously, and used to give a precise measurement of the magnetic field where the Xe-129 atoms are trapped. One long-term goal of the RaEDM and Yb-171 experiments is to implement this co-magnetometer scheme [24].

2.5.5 Tl-205

In 1991, an experiment was performed on the ^{205}TlF molecule to try to measure its nuclear Schiff moment. This experiment used a jet source of the molecules, which passed through an electric field. The experiment yielded a measurement of the molecular EDM of ^{205}TlF at $d_{TlF} = (-1.7 \pm 2.9) \times 10^{-23}\ e \cdot \text{cm}$ [25]. At the Cold molecule Nuclear Time-Reversal EXperiment (CeNTREX) underway at Argonne National Laboratory, efforts are ongoing to measure the nuclear Schiff moment of TlF again [26], first with a beam experiment, and then utilizing laser cooling and trapping. The experiment seeks to measure a CP-violating

energy shift with a sensitivity of ~ 45 nHz.

2.5.6 Nuclear Magnetic Quadrupole Moments

Other CP-violating moments for nuclei exist. In addition to the Electric Dipole Moment, the Magnetic Quadrupole Moment also violates T- and CP-symmetry. It is the magnetic analogue to the electric quadrupole moment, in that the magnetic field of a localized current can be approximated from far away as the sum of magnetic dipole, quadrupole, etc., moments. A proposed experiment [27] plans to measure the nuclear magnetic quadrupole moment in ^{173}Yb in an optical lattice. It hopes to achieve a sensitivity of $\delta M \leq 3.7 \times 10^{-8} \mu_N$fm.

2.5.7 Note About Molecules

Molecules have a large internal electric field, which gives a great enhancement in the effective electric field for a small lab field. This gives them an advantage over single atoms, as can be seen in such experiments as CeNTREX or ACME, which only needed an applied electric field on the order of $E \sim 100$ V/cm, 3 orders of magnitude less than the fields needed for the Ra-225 experiment. In thorium monoxide, for instance, an applied electric field of ~ 10 V/cm provides an effective electric field for the electron EDM of ~ 80 GV/cm [28]. In addition, some molecular structures allow for systematic uncertainty reduction by utilizing internal co-magnetometry. Different types of experiments are being proposed, such as experiments with atomic beams, laser cooled and trapped molecules, and molecules implanted in solids. The main issue with such experiments comes from the fact that slowing and trapping molecules is not very efficient - for example, laser cooling and trapping molecules is very difficult because there are additional vibrational and rotational states in molecules makes the optical cycling

scheme needed for laser cooling very complex.

Chapter 3. The Radium EDM Laser Trap Experiment

The radium-225 EDM (RaEDM) experiment ongoing at Argonne National Laboratory (ANL) and MSU aims to improve the sensitivity to CP-violating factors in the hadronic sector in its next sensitivity upgrade. Even a single order of magnitude improvement of sensitivity would set new CP-violation source limits in the global picture. Radium is an excellent candidate to use because of its large atomic number ($Z = 88$) and its ability to be laser cooled and trapped. In particle, radium-225 is an ideal isotope for this, due to its octupole deformation and non-zero nuclear spin of 1/2.

3.1 Octupole Deformed Nuclei

A nucleus is defined by the number of protons and neutrons it has. For certain nuclei, spontaneous symmetry breaking results in a distortion of the overall shape of the nucleus from being spherically symmetric. Of particular interest are octupole deformed nuclei, which can be described as "pear shaped"[29]. This gives its shape an asymmetry under a parity transformation, giving it both a large nuclear Schiff moment and small parity doublet.

3.1.1 Definition of Octupole Deformation

The general shape of an axially symmetric nucleus, and its deformation from being a perfect sphere, can be expressed in terms of spherical harmonics [30] as can be seen in Figure 3.1

Figure 3.1: Diagram of various nuclear deformations. Taken from [31]. Notice that the $\lambda = 3$ moment is the first term which breaks parity symmetry.

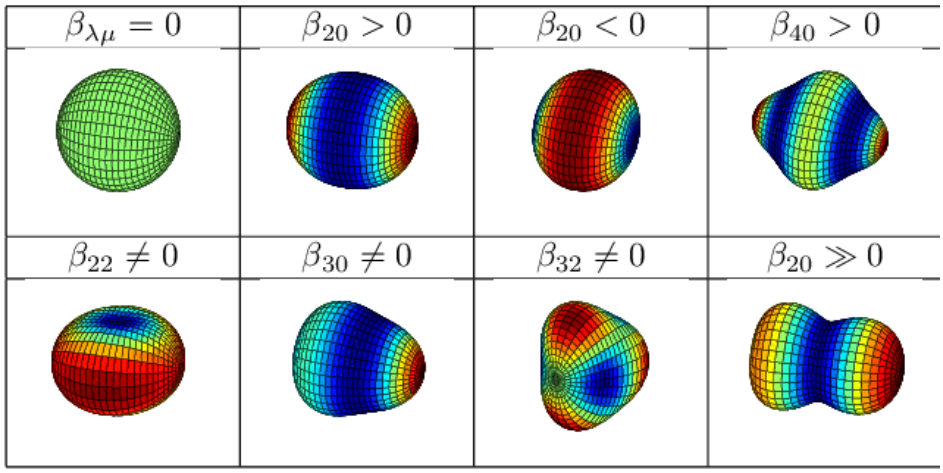

$$R(\theta, \phi) = R_0(1 + \sum_{\lambda=2} \beta_\lambda Y_{\lambda 0}(\theta, \phi)) \tag{3.1}$$

where $Y_{\lambda\mu}$ are the spherical harmonics and β_λ are various coefficients used to describe the nuclear distribution. The first non-zero moments start with $\lambda = 2$, which indicates a quadrupole deformation. Octupole deformations are those associated with $\lambda = 3$. Some common nuclear shapes are depicted in Figure 3.1.

3.1.2 Enhanced Sensitivity to Symmetry Violation

The Schiff moment for a nucleus can be described by

$$S = \langle \Psi_0 | \hat{S}_z | \Psi_0 \rangle = \sum_{i \neq 0} \frac{\langle \Psi_0 | \hat{S}_z | \Psi_i \rangle \langle \Psi_i | \hat{V}_{PT} | \Psi_0 \rangle}{E_0 - E_i} \tag{3.2}$$

where S is the lab frame Schiff moment, $\langle \Psi_0 | \hat{S}_z | \Psi_i \rangle$ is the intrinsic Schiff moment using nuclear wavefunctions, and $\langle \Psi_i | \hat{V}_{PT} | \Psi_0 \rangle$ is a time and parity violating matrix element where

new physics occurs. An octupole deformed nucleus has a parity doublet in its ground state. The term in this sum corresponding to the parity doublet has a small denominator. Furthermore, the octupole deformation results in an enhancement of $\langle \Psi_0 | \hat{S}_z | \Psi_i \rangle$ as well. Thus, a given constraint on S results in tighter constraints on the T-violating parameters in $\hat{V}_{PT}$. The enhancement for radium-225 compared to mercury-199 can be seen in Table 3.1.

Table 3.1: Theoretically calculated coefficients for Schiff moment dependence on nucleon-pion interactions, $S = a_0 g\bar{g}_0 + a_1 g\bar{g}_1$. SIII and SLy4 are models used for calculating the coupling coefficients.

Element	a_0($e \cdot \text{fm}^3$) (SIII)	a_0 ($e \cdot \text{fm}^3$) (SLy4)	a_1($e \cdot \text{fm}^3$) (SIII)	a_1($e \cdot \text{fm}^3$) (SLy4)	Source
Ra-225	-1.0	-3.0	7.0	16.9	[32]
Hg-199	.012	.013	.005	-.006	[33]

3.1.3 Candidate Isotopes

Octupole deformed nuclei have a ladder of nearly degenerate parity doublet nuclear states. As described in the previous section, this level structure makes isotopes like radium-225 very good candidates for EDM experiments, since they have an enhancement in sensitivity to CP-violating physics over atoms like mercury-199. Radium-225's status as a rare isotope with a 15 day half life makes it difficult to measure in an experiment. Another such candidate nucleus is protactinium-229. This isotope may or may not have a parity doublet with an even smaller energy difference - possibly on the order of 10's of eV, as opposed to radium-225's 55 keV parity doublet. This would result in a larger enhancement factor in any EDM measurement performed upon protactinium. It's debated in the literature, however, whether the protactinium-229 parity doublet even exists as its eV scale makes it challenging to verify experimentally [34]. Additionally, its half-life is only a 1.5 days which complicates any

experiments. Efforts are ongoing to experimentally determine whether or not protactinium-229 even has this doublet. Information on various candidate isotopes can be found in Table 3.2.

Table 3.2: Candidate isotopes with the energy splittings of their parity doublet and new physics sensitivity relative to Hg-199. A question mark denotes an estimate of the value.

Nucleus	ΔE(keV)	$\tau_{1/2}$(s)	Sensitivity	Source
Hg-199	1800	stable	1	[14]
Rn-223	10^2?	10^3	10^2	-
Ra-225	55	10^6	10^3	[21]
Pa-229	$(.06 \pm .05)$?	10^5	10^6	-

3.2 EDM Experiments in Laser Traps

Performing experiments on atoms that are trapped using laser beams has advantages over performing experiments in a vapor cell. Radium has a vapor pressure that is too low to be used in a vapor cell, and its 15 day half life poses a significant challenge to preparing a vapor cell. Using a vapor cell is practical with mercury-199, which carries the advantage of being able to measure vastly more atoms in total.

3.2.1 Comparison to Vapor Cells

In a vapor cell, since atoms are moving in the gas phase, they have a significantly higher velocity than those in a laser trap. In addition, the atoms fill out a much larger volume, at $\sim$ 5 cm^3, so there is more sensitivity to spatial variation in the magnetic and electric fields. This spatial variation in the magnetic field is especially important for the mercury-199 experiment [14], as it the largest contribution to the systematic uncertainty.

With a laser trap, the atoms are moving much slower and in a much smaller volume, $\sim 100\ \mu\text{m}^3$. This means that the atoms have less sensitivity to the spatial variation of the magnetic and electric field. However, there are drawbacks - since only successfully laser cooled and trapped atoms can be used, significantly fewer atoms can be measured at one time. Also, the experimental setup at Argonne can only measure a single configuration at a time - with either the electric and magnetic fields oriented parallel or antiparallel to each other. This means that the fields have to be extremely stable with respect to time - the magnetic field has to be the same at all times, and the magnitude of the electric field has to stay the same upon reversal. Some discussion will now be done on the systematic effects of atoms in laser traps.

3.2.2 Systematics in Laser Traps

3.2.2.1 Magnetic Field Gradients

In the mercury-199 experiment, the relatively large volumes taken up by the vapor cells induce sensitivity to any gradient in the magnetic field. Suppose there was a difference in the magnetic field magnitude from one cell to the other: the Larmor precession frequency would be different, creating a false EDM signature. For this reason, two more vapor cells are used, placed above and below the vapor cells used for the EDM measurement. These cells do not have an electric field applied to them. The precession in these cells is also measured, and is used as a co-magnetometer. The true EDM signature used for the mercury-199 experiment is

$$\eta_B \Delta\omega_{EDM} = \eta_B(\Delta\omega_{MT-MB} - k\Delta\omega_{OT-OB}) \tag{3.3}$$

where ω_{MT-MB} is the frequency shift between the cells with an electric field applied, ω_{OT-OB} is the frequency shift between the cells without any electric field applied, one on top and one on bottom, k is a fit parameter assigned to the data from each day, and $\eta_B = \frac{\mathbf{B_0}\cdot\hat{y}}{|\mathbf{B_0}|}$ is a scaling of the magnetic field to account for any temporal variation in the field magnitude. Any measurement in which the $\Delta\omega_{OT-OB}$ is dominant is discarded for the purpose of the experiment, but taken into account for quantifying the systematic error due to axial motion. If, when an electric field is applied, the position of the cells shifts slightly, there is a shift in frequency dependent on the electric field caused by the magnetic field gradient. This gives a false EDM signature. This systematic was quantified at $1.26 \times 10^{-30}\ e \cdot \mathrm{cm}$ [14], which is the dominant systematic effect in the measurement.

By reducing the size of the volume the atoms are measured in, the effect of any B field gradient can be greatly reduced. Whereas the atoms in the mercury-199 experiment take up a volume of $\sim 5\,\mathrm{cm}^3$, the atoms in an optical dipole trap (ODT) take up a volume of $\sim 100\,\mu\mathrm{m}^3$, greatly reducing any effect due to a magnetic field gradient.

3.2.2.2 Comparing Motional Field Effects Between Laser Traps and Vapor Cells

One of the major advantages in using a laser trap is a reduction in the systematic effect associated with motional magnetic fields given by $\mathbf{E} \times \mathbf{v}$. When a charged particle moves through an electric field, the electric field appears in the rest frame of the particle as a magnetic field. This magnetic field then acts upon the particle. This magnetic field has the form:

$$\mathbf{B}_{motion} = \frac{c}{\sqrt{c^2 - v^2}}(\frac{\mathbf{v}}{c^2} \times \mathbf{E}) \approx \frac{\mathbf{v}}{c^2} \times \mathbf{E}$$

The trapped atoms inside have a Doppler cooling limit of 9 µK, which corresponds to a root-mean-squared (RMS) velocity of $v_D = 0.022$ m/s. This creates a magnetic field of $\|\mathbf{B}_{motion}\| = 1.6$ pT. This is an issue, because any change in the magnetic field will create a false EDM signature. Since the atoms are oscillating in the trap, the effect of the magnetic field mostly cancels out - the atoms oscillate in, say, the $\hat{x}$-direction with a time-dependent velocity $v_{\mathrm{x}} = v_{\mathrm{x,max}} \sin(t\omega_{\mathrm{ODT}})$, so the time-averaged effect on the EDM signature across a full period $\tau_{\mathrm{ODT}} = \frac{2\pi}{\omega_{\mathrm{ODT}}}$ is 0. However, the total number of periods the atoms spends in the trap will never be exactly an integer, so there remains a small systematic uncertainty still.

3.3 Experimental Apparatus

The apparatus used for laser cooling and trapping radium atoms, then transporting them to the area where the experiment is performed, is a relatively small but complex experimental setup. It has been compared to "getting a whole lot of plates spinning at the same time, then once they all are, using that window to perform an experiment." This section will provide a rundown and explanation of the various parts of the setup. For further information, see [35], [36], [37]

Figure 3.2: Full apparatus at Argonne National Laboratory. Atoms are emitted from the effusive oven. They are then focused using a transverse cooling element, and slowed using a Zeeman slower into a 3D MOT. After being collected for some time, the atoms are moved into an Optical Dipole Trap to be moved to the experiment chamber, where the EDM measurement is performed.

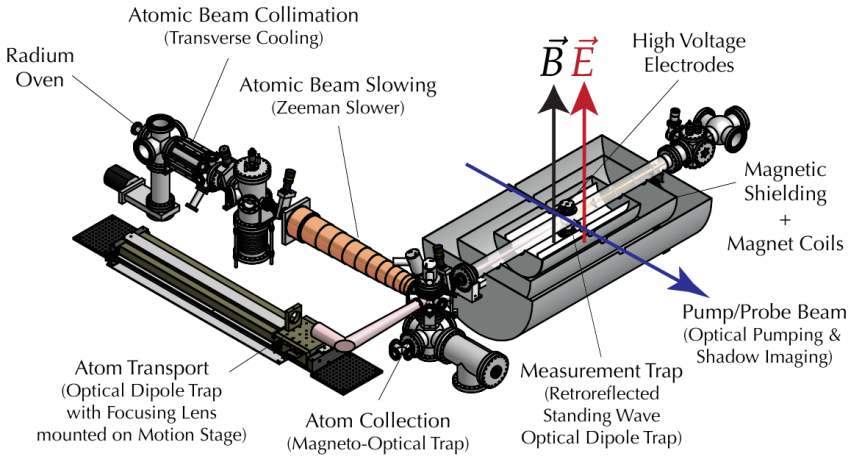

3.3.1 Radium Source/Oven

In order to trap radium, first an atomic beam of neutral radium must be created. The chemistry processes that produce this atomic beam are not well quantified, but are broadly understood [38]. The radium, be it the most abundant radium-226 isotope to calibrate or short-lived radium-225 to measure, arrives to Argonne National Laboratory in the form of radium nitrate. The radium nitrate is deposited onto a piece of aluminum foil along with a small amount of metallic barium and allowed to dry. Once dry, this foil is then placed inside of a titanium crucible and sealed in a transport container. It is then the job of a graduate student to transport the container down the hallway from the radiation preparatory lab to the lab containing the experimental apparatus. Once there, the crucible is installed in a vacuum oven. This oven consists of a resistive filament, woven through pieces of ceramic surrounding the crucible, that heats up the crucible through thermal radiation. A cooling

jacket surrounds the filament, through which chilled water is pumped to keep the rest of the apparatus cool. To prevent the chiller from failing while the oven is on, which would cause pressure to build up in the cooling jacket from water boiling into steam, a temperature sensor and a flow sensor are connected on the same coolant lines. The oven that provides current to the filament has an interlock that trips if the flow stops or the temperature gets too high. Thus, if the coolant stops flowing, power is automatically cut to the filament. After the oven is loaded, to get an initial atomic beam of atoms out, the oven must be "cracked". To crack the oven, the current through the oven filament, and thus the temperature, is steadily increased beyond standard operating conditions. The increase has to be gradual because the oven is exposed to atmosphere during the loading process, causing air to adsorb onto the vacuum chamber surfaces. During the cracking process, this residual air will outgas from the vacuum chamber. While the oven is being warmed up, a fluorescence scan measurement is performed to see if the atoms are beginning to come out of the oven. Once a fluorescence signal is visible from the beam, the cracking is complete, and the oven temperature is quickly turned down, so as not to waste any radium. After this, a beam of neutral radium can be produced at a temperature lower than that used to crack, and trapping can begin.

Table 3.3: Cracking temperatures and sample activities for different isotope oven loads.

Isotope	Typical Cracking Temperature (C)	Typical Activity (Ci)
Ra-226	~ 500	3 μCi
Ra-225	~ 500	10 mCi
Ra-223	~ 500	10 mCi

3.3.2 Transverse Cooling

The transverse cooling is the first component encountered by atoms leaving the oven. This is an element designed to focus the atoms into a more collinear beam by laser cooling them in the two directions perpendicular to the atomic beamline.

Figure 3.3: Diagram of transverse cooling.

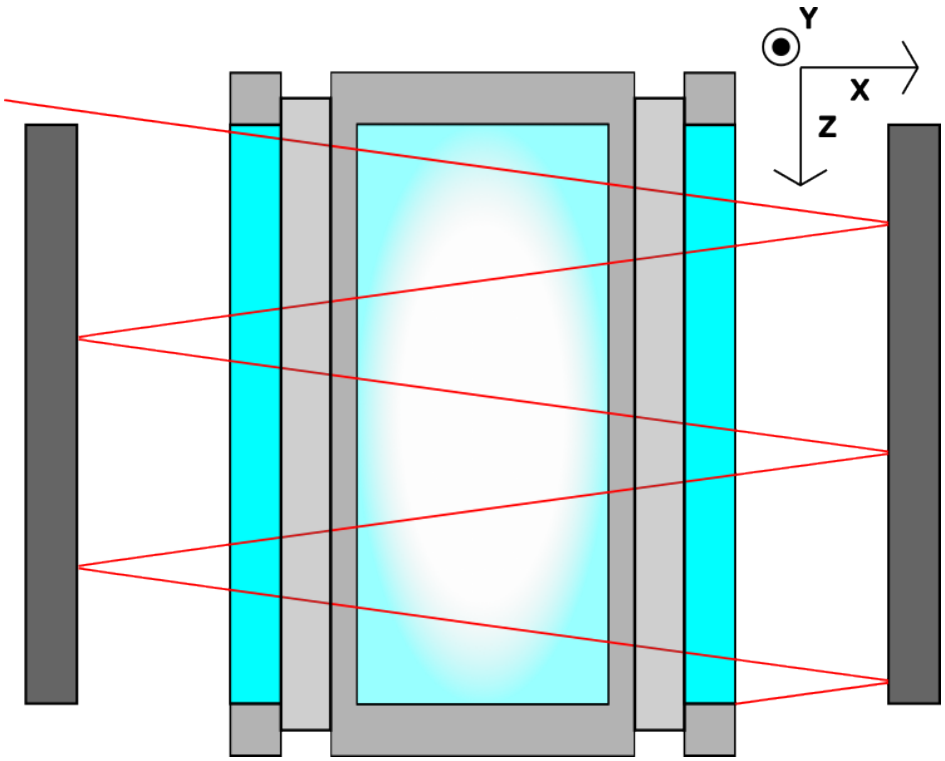

As the atoms emerge from the oven, they do not necessarily emerge perfectly in the $\hat{z}$-direction; they have a small transverse velocity as well:

$$\mathbf{v} = v_z\hat{z} + v_x\hat{x} + v_y\hat{y} \tag{3.4}$$

In order to reduce v_x and v_y, laser cooling is utilized. When an atom is met with a beam of light, it will absorb photons at a rate R_{scatt} dependent on the frequency of the light and

its own atomic transitions, given by [39]:

$$R_{\text{scatt}} = \frac{\Gamma}{2} \frac{\frac{\Omega^2}{2}}{\delta^2 + \frac{\Omega^2}{2} + \frac{\Gamma^2}{4}} \tag{3.5}$$

where Γ is the natural linewidth of the transition, and is equal to $\Gamma = \frac{1}{\tau}$ where τ is the average lifetime of the state. Ω is a quantity known as the Rabi frequency, and $\delta = \omega - \omega_0$ is the detuning of the frequency of the light from the frequency of the transition. The Rabi frequency can be determined by the formula

$$\Omega^2 = \frac{I}{I_{\text{sat}}} \frac{\Gamma^2}{2} \tag{3.6}$$

where I is the laser intensity, and I_{sat} is the saturation intensity given by

$$I_{\text{sat}} = \frac{\pi}{3} \frac{hc}{\lambda^3 \tau} \tag{3.7}$$

For every photon absorbed by the atom, the atom receives a change in momentum equal to

$$p_\gamma = \frac{\hbar \omega}{c} \tag{3.8}$$

When the atom decays from its excited state back to its ground state through spontaneous emission, it emits a photon in a random direction. Thus, over many spontaneous photon emissions, the total change in momentum averages out to zero. Combined with the scattering rate, this means that the total change in momentum per second, or force, on each atom is given by

$$F = p_\gamma R_{\text{scatt}} \tag{3.9}$$

In order to focus the beam, atoms must absorb light which is moving in the direction antiparallel to the atom's motion. This is done by taking advantage of the Doppler shift of the atoms in the atomic beam. When an atom with a non-zero transverse motion encounters a beam of light, the frequency seen by the atom changes by a factor $\Delta\omega = \frac{\omega_{\text{lab}}}{c} v$, where ω_{lab} is the laser frequency in the laboratory frame and v is the velocity of the atom. Thus, by detuning the laser slightly from the normal transition, only atoms traveling in say, the $\hat{x}$-direction will be on resonance with the light traveling in the $-\hat{x}$-direction. This is also true for the $\hat{y}$- and $\hat{z}$-directions.

3.3.3 Zeeman Slower

As the atoms progress down the atomic beamline, they have to be slowed down enough to be able to be trapped. This is done through laser fluorescence, with the laser beam oriented against the direction of motion of the atoms. When an atom meets a beam of light with a frequency on resonance with an atomic transition, it can absorb a photon, and reach an excited state. This absorption imparts momentum to the atom, slowing it down. When the atom decays from its excited state back to its ground state, the atom will emit a photon in an isotropic direction. The average effect of the photons emitted over many decays is therefore zero. Thus, the atom receives a net slowing effect from the laser. There is, however, one problem: as the velocity of the atoms is decreased, there is a Doppler shift in the frequency of the laser that the atoms see, which is a function of the speed of the atoms traveling against the laser. This means, as the atoms slow down, they become off-resonance

with the frequency of the laser. The correct for this problem a tapered magnetic field is applied, and the Zeeman effect shifts the energy levels of the atoms slightly. This keeps the atomic transition on resonance with the laser frequency seen by the atoms, allowing them to continue to be slowed.

The change in the laser frequency seen by the atoms as a function of their velocity in the z-direction is $\Delta\omega = \frac{\omega_{\text{lab}}}{c} v_z$. The desired slowing should give the profile of v_z as

$$v_z(z) = v_0 \sqrt{1 - \frac{z}{L_0}} \tag{3.10}$$

where z is the distance traveled by the atom along the Zeeman slower, v_0 is the maximum initial velocity, and L_0 is the length of the Zeeman slower. Since the primary $^3P_1$ transition has an average lifetime of 420 ns, each "kick" from a photon can be assumed to take up 420 ns. This lifetime limits the maximum speed of an atom that can be slowed in a given distance.

The 714 nm photons used to slow the atoms have a momentum on the order 10^{-27} N $\cdot$ s. A Radium-225 atom traveling at 60 m/s has a momentum of about 10^{-23} N $\cdot$ s. Thus it will require about 25,000 cyclings to come to a stop.

3.3.3.1 Optical Cycling

A level scheme showing the optical transitions used for the RaEDM experiment is shown in Figure 3.4.

Figure 3.4: Radium atomic transitions used for optical cycling. The $^3P_1$ state and $^3D_1$ state are used for the current optical cycling scheme. The $^1P_1$ state is intended to be used in the future.

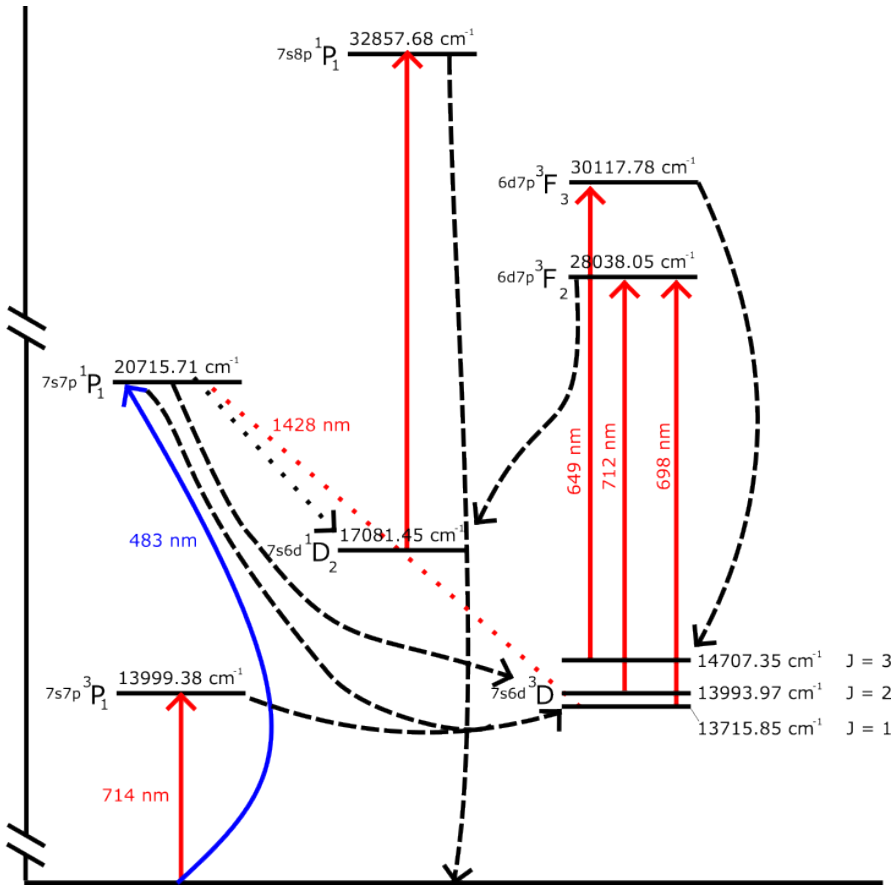

The primary transition is the 714 nm transition, which is induced by a Lighthouse Photonics SPROUT pump continuous wave (CW) laser driving a SirAH Matisse Ti:Sapph laser. The laser is able to output roughly 1.5 W of 714 nm light, which is used in various parts of the experiment, from the transverse cooling to slowing and to the MOT trapping. As discussed in Section 3.3.3, the Zeeman slower is only capable of slowing atoms moving up to 60 m/s, which is less than 1% of the atoms coming out of the oven. Furthermore, due to the .004 % chance of atoms decaying to the relatively long lived $^3D_1$ state and the large number of photons that need to be scattered, the vast majority of atoms will at some point end up

in the $^3D_1$ state, where they no longer are able to be laser cooled. This necessitates the use of a repump laser. The 1428 nm repump laser is normally beat locked to another laser which is locked to a cavity. However, it does not need to be locked to trap atoms, it just needs to be close enough to the right frequency. The purpose of the repump is to transfer atoms out of the dark $^3D_1$ state to the $^1P_1$ state, which most often decays to the $^1S_0$ state, keeping the atoms in the cycle and allowing them to continue to be slowed.

3.3.4 Magneto-Optical Trap

Once the atoms are sufficiently slowed down, they are trapped by a 3-dimensional Magneto-Optical Trap, or MOT. A schematic diagram of how a MOT works is presented in Figure 3.5

Figure 3.5: Concept diagram of MOT. A magnetic field gradient is applied in a certain dimension, which causes a Zeeman splitting among the m_F sublevels as the atoms travel away from the MOT center. This causes the $m_F = +1$ sublevel to be on resonant with the laser light on the right side, and the $m_F = -1$ sublevel to be on resonant on the left side. When +1 circularly polarized light is sent in, only atoms with the $m_F = +1$ sublevel on resonance can absorb the light. This means they can be directed back towards the center of the MOT. The same thing occurs for atoms on the left side. Thus, atoms which drift away from the center receive a kick from the light back towards the center. This can be done in 3-dimensions to create a 3-dimensional trap.

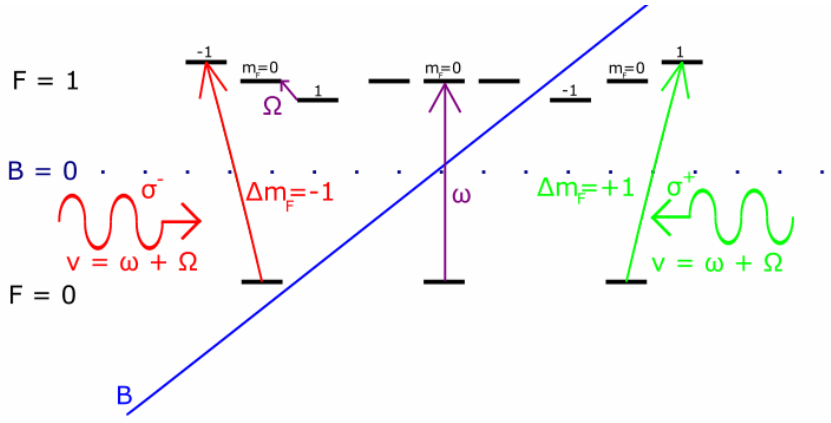

The MOT uses a magnetic field gradient and the Zeeman effect to split the energy levels

of the m_F substates. Two laser beams, each with an opposite circular polarization, are overlapped inside of the MOT. The frequencies of the laser beams are detuned away from the frequency of the primary transition, corresponding to the Zeeman splitting at a certain displacement from the center. To the right of the center of the MOT, the magnetic field causes the $m_F = 1$ state to now be resonant with both lasers. However, because the change in sublevel $\Delta m_F = 1$, only the light being shone from the right can be absorbed by the atom. So, if the atom is on the right side of the MOT, it can only absorb light moving towards the left. This means it only absorbs the momentum of the light moving it to the left, causing it to receive a "kick" back to the center of the trap. The same goes for the left side; the magnetic field gradient causes the $m_F = -1$ sublevel to be on resonance with the laser, but only negative circularly polarized light can be absorbed, so it can only receive a "kick" to the right when it is on the left.

Each of the laser components needs to be slightly detuned depending on where laser light is being directed in the apparatus. This detuning is applied using Acousto-Optic Modulators (AOMs). The entire AOM setup and the typical AOM set frequencies can be found in Figure 3.6 and Table 3.4 respectively.

Table 3.4: Set frequencies required to operate the AOMs for different components in the RaEDM experiment.

AOM	Set frequency (MHz)
Probe	81
Slower	77.7
ULE Offset	79.7

Figure 3.6: Setup of AOMs at Argonne National Laboratory. Various different frequencies for the AOMs are needed. Once the frequency is modulated by the AOM for a given optical element, the laser is directed to a fiber coupling which leads to the optical trap. Elements are in place for the transverse cooling, a non-functioning 2D MOT, the main slowing beam, and the 3D MOT light. The AOMs also allow for ultra fast switching to take place.

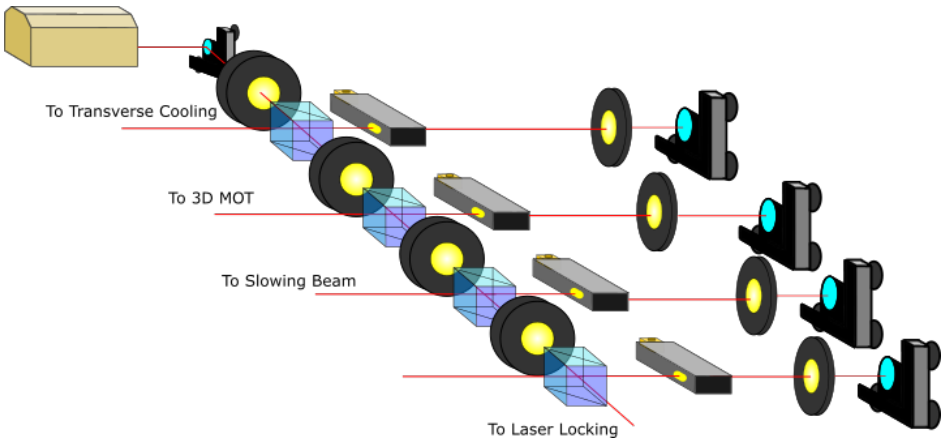

3.3.5 Optical Dipole Trap

Once the atoms are trapped in the MOT, they are transported to a region in between magnetic coils and a pair of electrodes to perform the EDM measurement. This part of the apparatus is called the science chamber. It is magnetically shielded in order to stop ambient magnetic fields from affecting the EDM measurement. The transport of the atoms into the science chamber is performed using an optical dipole trap (ODT) which is referred to as a Bus ODT. A 100 W laser at 1550 nm is focused by a lens on a translation stage that has its focal point focused on the 3D MOT. Once the atoms are moved to the ODT, the translation stage has its lens physically moved to translate the atoms down to the science chamber. Here, the EDM measurement is performed.

3.3.6 Electric Fields

Inside the measurement chamber, a pair of electrodes apply a strong electric field, either parallel or antiparallel to the applied magnetic field. These electrodes have been carefully conditioned to be able to accept very high electric fields without unwanted discharges [40]. In the 2015 data run, the electric field applied to the atoms was ± 67 kV/cm. With new electrodes, and a new HV apparatus, we hope to reach electric field magnitudes of as large as 300 kV/cm.

3.3.7 Magnetic Fields

The magnetic field used for the spin precession measurement is generated by a $\cos\theta$ coil. The magnetic field was specifically chosen to give the Larmor spin precession a specific frequency, which required a field strength of 2.6 μT. This causes the atoms to precess due to the magnetic field with a period of $34.7 \pm .03$ ms [21]. Note that the actual EDM measurement measures a relative phase shift, not an absolute frequency, so the uncertainty in the spin precession frequency does not limit our EDM measurement. The actual method of spin detection will be discussed now.

3.3.8 Spin Detection

After the atoms are translated by the ODT in the $\hat{z}$-direction, they are then held in another 10 W 1550 nm ODT in the $\hat{x}$-direction. This holds the atoms in place for the measurement. In order to perform the measurement, a laser resonant with the $^1P_1$ transition excites the atoms, so that all of them are spin polarized in the $\hat{x}$-direction. Then the laser is turned off and the E field is turned on, so that the atoms precess over 20 seconds, plus an extra phase

Figure 3.7: Conceptual diagram of spin precession measurement. Atoms are trapped in an ODT (indicated by grey color band) and translated between two Niobium electrodes. Spin-precession is induced by the applied electric and magnetic field and then read out via shadow imaging from 483 nm light.

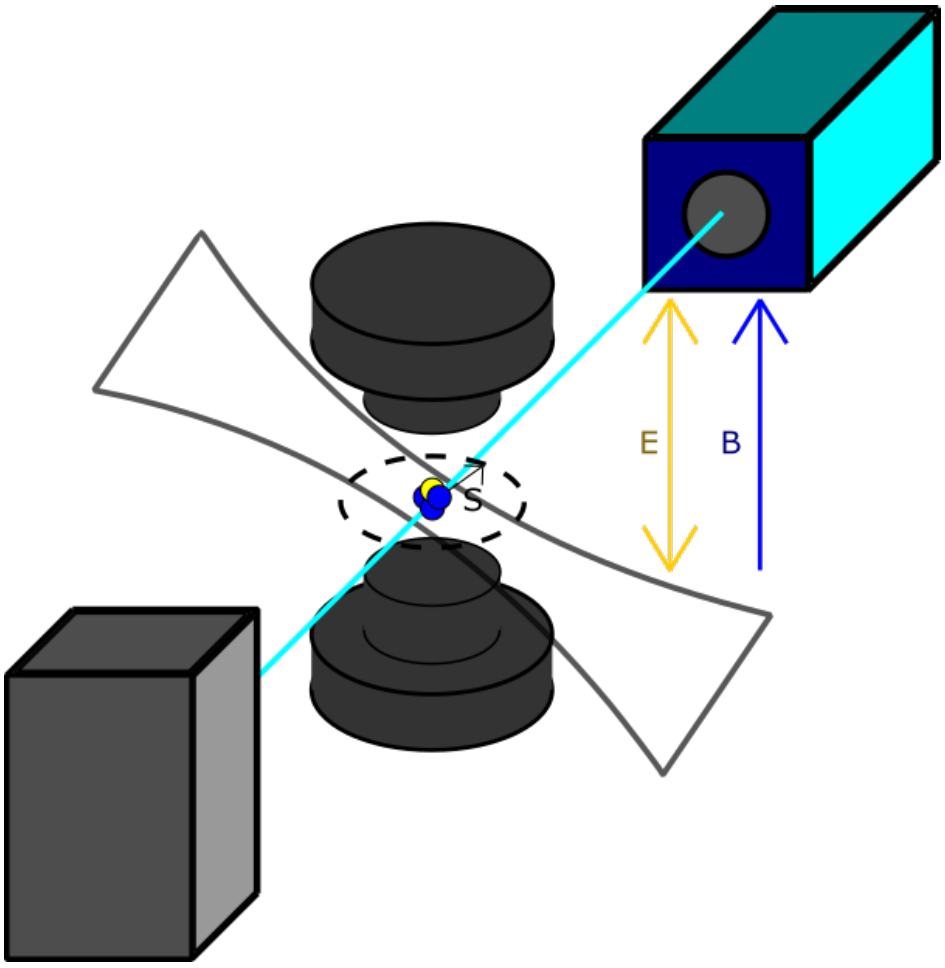

shift of a few ms. Then, a shadow imaging measurement is made as indicated in Figure 3.7. The polarized laser is pulsed again, and depending on the phase of the atoms after precessing around the $\hat{y}$-direction, a percentage of the atoms in the trap absorb light. By looking at the loss of light intensity in the shadow created, the phase of the spin precession versus time can be traced out with many measurements. Every load of atoms has 5 intensity measurements taken by a CCD camera [21]. The imaging is done in a particular timing sequence which is visually depicted in Figure 3.8. The first, third, and fifth images are taken right after the

atoms are polarized and allowed to precess for a time $\Delta T_{1,3,5} = 17.4$ ms, which is half of a single period of the Larmor precession. After each image is taken, the CCD camera reads out all pixels for 300 ms. After the second polarization pulse is applied, the electric field is ramped on with a longer precession time of $\Delta T_{2,4} = 20,000+\delta$ ms where δ is varied from -10 to 40 ms. During the entire cycle, a uniform magnetic field is applied in the measurement chamber.

Figure 3.8: Spin precession measurement cycle. Thicker blue boxes indicate 483 nm polarization pulses. Thinner blue boxes also indicate 483 nm light which is used as a detection pulse. The red box indicates the region with the electric field on. The magnetic field is applied for the entire measurement cycle. Figure taken from [21].

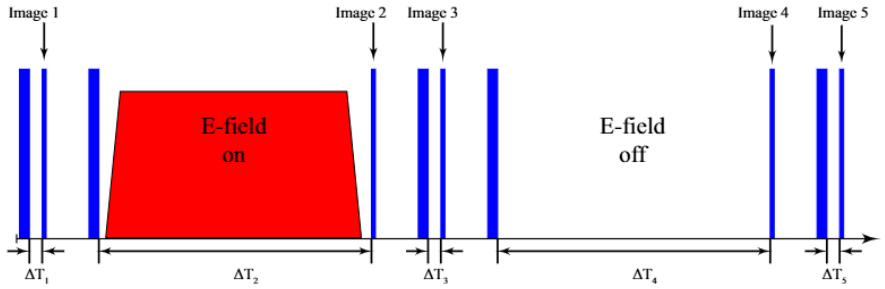

Each image taken during the measurement scheme serves a different purpose. The first image is taken to normalize the specific load for the number of atoms in the trap. The second image is the first spin precession measurement. The third is another normalization measurement for the fourth image, which is the second spin precession measurement where the electric is switch off. The fifth image is a final spin normalization measurement. All of the normalization images are used to account for the number of atoms in the trap at different points in the measurement process. This measurement cycle is repeated many times, at different δ values and with the electric field oriented either parallel or antiparallel to the magnetic field to plot out a sinusoidal curve in the spin phase angle as in Figure 3.9.

Figure 3.9: Nuclear spin precession of ^{225}Ra atoms under three electric field conditions. If a significantly large EDM were observed, a phase shift would be present between the sinusoidal traces for the three electric field conditions.

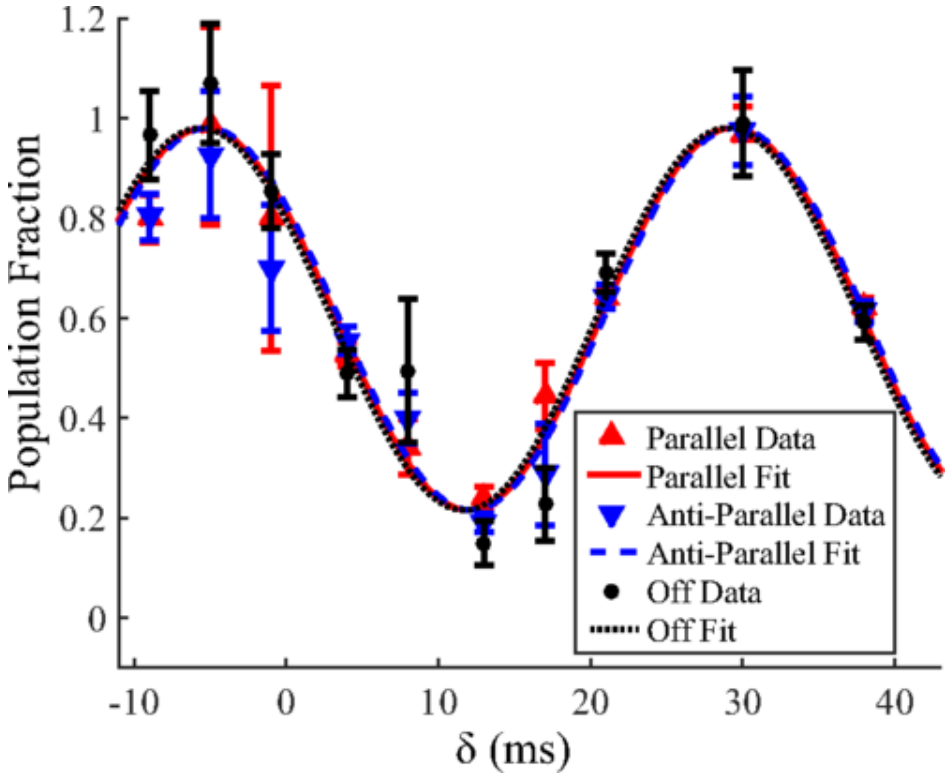

3.4 2015 EDM Run

The RaEDM experiment has had two data runs. The first run took place in 2014, and established a 95% confidence interval of

$$|d(^{225}\mathrm{Ra})| < 5.0 \times 10^{-22} \quad e \cdot \mathrm{cm} \tag{3.11}$$

This was followed the next year by a run that utilized a titanium sublimation pump to allow for longer spin precession time. This run established a 95% confidence interval of

$$|d(^{225}\mathrm{Ra})| < 1.4 \times 10^{-23} \quad e \cdot \mathrm{cm} \tag{3.12}$$

The systematic and statistical uncertainties had to be very well understood to set these limits. We will know discuss both of these uncertainties here.

3.4.1 Statistical Sensitivity

The general formula for the statistical sensitivity is given by the standard quantum limit:

$$\delta d = \frac{\hbar}{E\sqrt{NT\tau\epsilon}} \tag{3.13}$$

where E is the electric field strength, N is the number of atoms trapped per load cycle, T is the total integration time of the experiment, τ is the spin precession time of the atoms, and ϵ is the efficiency of the spin detection of the measurement. At the moment, this experiment is completely limited statistically for the next few orders of magnitude. An overview of the statistical and systematic uncertainties can be found in Table 3.5.

Table 3.5: Statistical and systematic uncertainties for the 2015 RaEDM data run. All of the systematic uncertainties included in this table are at least two orders of magnitude smaller than the statistical contribution, which dominates the uncertainty in the measurement.

Effect	Current Uncertainty($e \cdot$ cm)
Total Statistical Uncertainty	1×10^{-23}
E-Squared Effects	1×10^{-25}
B-Field Correlations	1×10^{-25}
Holding ODT Power Correlations	6×10^{-26}
Stark Interference	6×10^{-26}
E-Field Ramping	9×10^{-28}
Blue Laser Power Correlations	7×10^{-28}
Blue Laser Frequency Correlations	4×10^{-28}
$\mathbf{E} \times \mathbf{v}$ effects	4×10^{-28}
Leakage Current	3×10^{-28}
Geometric Phase	3×10^{-31}
Total Systematic Uncertainty	2×10^{-25}

3.4.2 E-Squared Effects

The primary systematic effect limiting the sensitivity of our experiment is the E-squared effect, which is a systematic shift proportional to the strength of the electric field squared. In addition to spin precession measurements with the electric field applied, measurements are also taken with the electric field switched off. The function that is ultimately fit to the sinusoidal curve drawn out by the spin precession in Figure 3.9 has a contribution from when the electric field is applied or not applied:

$$y_{E=0} = \frac{A}{1+P}[1 - Pcos(\omega \Delta T)] \tag{3.14}$$

for when the electric field is off, and

$$y_{E\neq 0} = \frac{A}{1+P}[1 - Pcos(\omega \Delta T + \theta \pm \frac{\Delta\phi}{2})] \tag{3.15}$$

for when the electric field is on. Here, A is the normalization constant, P is the signal contrast, ω is the spin precession frequency due to magnetic dipole coupling, ΔT is the spin precession time, θ is a phase shift correlated to E-squared effects, and $\Delta\phi$ is the phase shift due to the EDM coupling. The θ term is there specifically to try to fit for non-zero E-squared effects, and since it depends on the fit, it means this systematic is dependent on the statistical uncertainty of the experiment. As the statistical uncertainty is reduced, so should this systematic error. There are also other methods for reducing this systematic effect. Since the E-squared effect is dependent only on the magnitude of the electric field and not its orientation, if the electric field is the same in both the parallel and antiparallel configurations, then this effect will cancel out with regards to the phase shift between these

two measurements. During the 2015 run, the electric fields were verified to be the same strength, to within 0.7%. Efforts are ongoing to improve the precision with which these electrics fields can be measured, which will be discussed later in Chapter 6.

3.4.3 Magnetic Field Correlations

Magnetic field correlations are the other significant systematic effect in the experiment. Since the signal depends on a shift in the Larmor precession frequency dependent on both magnetic and electric fields, it is very important that the drift in the magnetic field over time and between different electric field polarities, or ΔB, is as small as possible. There are three fluxgates installed in the chamber to monitor the signal. A low-pass filter has been installed that should enable the measurement of changes on the order of 6 pT for 1 s of integration time in future measurements.

3.4.4 Holding ODT Power Correlations

Atoms trapped in a holding beam experience an AC Stark shift proportional to the power of the beam trapping them. For the atoms being held in the ODT while precessing, this means that a correlation between electric field direction and ODT power can cause a change in the energy levels that results in a false EDM signature. A detailed calculation of this energy shift for radium-225 is described later in this thesis in chapter 5. This effect is very suppressed, by both the small energy shift calculated, and the fact that the ODT holding beam is greater than 99% linearly polarized. The false EDM signature that arises can be characterized as

$$d_{\text{false}} = \Delta\nu_{m_F=1/2}\frac{h}{2E}\frac{\Delta P}{P_0} \tag{3.16}$$

where $\frac{\Delta P}{P_0}$ is the fractional difference in holding beam power, and $\Delta\nu_{m_F=1/2}$ is the Stark shift caused by the ODT for the $m_F = 1/2$ sublevel. For the 2015 run, there was no observable correlation between $\frac{\Delta P}{P_0}$ and the electric field to a 1σ confidence interval of 8×10^{-5}, resulting in a systematic uncertainty of $6 \times 10^{-26}\ e \cdot \text{cm}$.

3.4.5 Stark Interference

In addition to the Stark shift due to the application of the ODT, there is another shift due to the interaction of ODT and the static electric field applied. This effect is linear in both electric field strength, as well as ODT power. The effect has a form that looks something like

$$\Delta\nu = \nu_1(\hat{b}\cdot\hat{\sigma})(\hat{\epsilon}\cdot\hat{\epsilon_s}) + \nu_2(\hat{b}\cdot\hat{\epsilon_s})(\hat{\epsilon}\cdot\hat{\sigma}) \tag{3.17}$$

where ν_1 and ν_2 are quantities that can be calculated, $\hat{b}$ is the direction of the holding magnetic field, $\hat{\sigma}$ is the spin quantization axis, $\hat{\epsilon}$ is the ODT polarization direction, and $\hat{\epsilon_s}$ is the direction of the static electric field. It was measured that $(\hat{b}\cdot\hat{\sigma})(\hat{\epsilon}\cdot\hat{\epsilon_s}) < .03$ and $(\hat{b}\cdot\hat{\epsilon_s})(\hat{\epsilon}\cdot\hat{\sigma}) < .1$ for our experiment to a 1σ uncertainty. This gives a 1σ uncertainty of $6 \times 10^{-26}\ e \cdot \text{cm}$ for this effect.

3.4.6 Electric Field Ramping

The electric field changes in time while ramping up and down from high voltage, which induces a magnetic field. This effect is carefully controlled so it cancels out between the ramp up and ramp down, using an arbitrary wave-form generator. The magnetic fields that arise from the ramping can be found with Ampere's law. There are two sources associated

with ramping: (1) the current required to charge the electrodes and (2) the change in the electric field. The magnetic field resulting from the ramping current is

$$B_{\text{cur}} = \frac{\mu_0}{4\pi} \int_C \frac{I\mathbf{dI} \times \mathbf{r}'}{|\mathbf{r}'|^3} \tag{3.18}$$

and the magnetic field associated with changing electric field is

$$\int_{\delta\Sigma'} \mathbf{B_{dE/dt}} \cdot \mathbf{dl}' = \mu_0 \epsilon_0 \frac{d}{dt} \int \int_{\Sigma'} \mathbf{E} \cdot \mathbf{dS}' \tag{3.19}$$

A perfectly linear ramp is assumed, and the placement of the atoms is assumed to be near the edge of the electrodes, where the induced magnetic field is strongest. The resulting false EDM signature is

$$\Delta\phi_{\text{false}} = 2\pi t_0 \Delta\nu_{\text{false}} = 2\pi t_0 4\mu |B_{ind}| sin(\theta_{EB})/h \tag{3.20}$$

where t_0 is the duration of the ramp, and B_{ind} is the sum of B_{cur} and $B_{dE/dt}$. This calculation results in a 1σ systematic error of 9×10^{-28} $e \cdot \text{cm}$.

3.4.7 Blue Laser Frequency Correlations

Any correlation between a frequency shift in the blue imaging laser and the electric field orientation can create a false EDM signal. These arise from the fact that a shift in the frequency will change the amplitude A of the precession curve. If this is correlated with the phase shift $\Delta\phi$, it can cause a false shift in $\Delta\phi$. To quantify this effect, part of the 483 nm laser light is put through a reference cavity, and the power output of the cavity constantly measured in real time with a photodiode. Using this, the relative fluctuation in amplitude

was measured to be -75 ± 80 ppm. Then, the fluctuation in output cavity power amplitude can be used to estimate the fluctuation of the photon scattering amplitude by

$$\Delta A_{\mathrm{Ra}} = \frac{3\sqrt{3}}{8} \frac{\Gamma_{\mathrm{cav}}}{\Gamma_{\mathrm{Ra}}} \sqrt{\Delta A_{\mathrm{cav}}} \tag{3.21}$$

where Γ_{cav} is the cavity Full Width Half Maximum (FWHM), Γ_{Ra} is the FWHM of the atomic transition, and $|\Delta A_{\mathrm{cav}}| = 75 \pm 80$ ppm.

Then, the false EDM phase shift is given by

$$\Delta\phi_{\mathrm{false}} = \Delta A_{\mathrm{Ra}} \frac{\rho_{A,\Delta\phi}}{\rho_{A,A}} \tag{3.22}$$

where $\rho_{A,\Delta\phi}$ is the covariance of A and $\Delta\phi$ and $\rho_{A,A}$ is the variance of A. The atoms are detected 390 ms after the electric field is ramped down, with a 1/e time of 160 ms. Thus, the electric field is reduced to 9% of its initial value. This means any effect has an additional 9% suppression factor. This gives a final systematic uncertainty of $4 \times 10^{-28}\ e \cdot \mathrm{cm}$ for this effect.

3.4.8 Blue Laser Power Correlations

The signal used to fit for the EDM effect $\Delta\phi$ is taken via shadow imaging measurement, and is proportional to the power of the laser light used for the atomic scattering. Thus, any correlation between the power of the laser beam and the electric field direction can create a false EDM effect. This uncertainty can be quantified by comparing the backgrounds of adjacent measurements of parallel and antiparallel fields. The comparison yields a 1σ uncertainty in the correlated power functions of 0.2%. Then, using a similar analysis as for the blue laser frequency correlations, a systematic uncertainty of $7 \times 10^{-28}\ e \cdot \mathrm{cm}$ can be

derived.

3.4.9 E × v Effects

As atoms travel with a velocity **v** inside of the ODT, the static electric field applied also appears as a magnetic field, calculated by

$$\mathbf{B_{motion}} = \gamma(\frac{\mathbf{v}}{c^2} \times \mathbf{E}) \tag{3.23}$$

where $\gamma = 1$ for the non-relativistic motion of our atoms. The Doppler cooling limit of our trap is 9 μK, which corresponds to an root-mean-squared velocity of $v_D = 0.022$ m/s. Since the trap can be modeled with a quadratic potential, the atoms oscillate back and forth in each direction with some period τ_{trap}. Over the course of a single period, the effect is canceled out. Assuming the remaining effect of the magnetic field is maximized, the resulting false EDM signature can be quantified by

$$d_{\text{false}} = \frac{\mu|\mathbf{B_{motion}}|}{E}\frac{\tau_{\text{trap}}}{2\tau}sin(\theta_{EB}) \tag{3.24}$$

where τ_{trap} is the period of the harmonic motion of the atoms in the ODT trap, τ is the spin precession time, and θ_{EB} is the angle between the ODT and the applied magnetic field. The oscillation frequency within the trap was calculated to be $\omega_{\text{trap,x}} = 2\pi \times 4.25$ rad/s, with $\tau_{\text{trap}} = 2\pi/\omega_{\text{trap}}$. This gives a 1σ uncertainty of 4×10^{-28} $e \cdot$ cm for this systematic effect.

3.4.10 Discharge and Leakage Current

Electric field correlated currents traveling between the electrodes are especially problematic because they mimic an EDM signature. There are two primary sources of stray current:

(1) leakage current leaking through the Macor holder which holds the electrodes, and (2) current caused by discharges between the electrodes. The most problematic of these comes from the discharges, since it would be possible for a discharge to happen right through the atoms, which would accelerate due to the applied static electric field. This can be modeled with the electrons as an infinite wire, with the false EDM signature then given by

$$d_{\text{false}} = \frac{\mu \mathbf{B_{ind}}}{E} \cdot \hat{B} = \frac{\mu}{E} \frac{\mu_0 I}{2\pi r} \sin\theta_{EB} \tag{3.25}$$

where I is the leakage current, r is the distance of closest approach for the electron beam, and θ_{EB} is the angle between the applied electric and magnetic fields. The value for θ_{EB} was measured to be $\theta_{EB} < 0.1$rad. The leakage current was consistent with 0, and had a 1σ upper limit of 2 pA. This resulted in a 1σ uncertainty for this systematic at $3 \times 10^{-28}\ e \cdot \text{cm}$.

The other leakage path is through the Macor mount which holds the electrodes apart from each other. The resulting systematic from this leakage current was calculated using the leakage current of 2 pA, and was calculated at $9 \times 10^{-29}\ e \cdot \text{cm}$.

3.4.11 Geometric Phase

Any spatial magnetic field gradient combined with a slight difference in the position of the atoms within the trap results in a geometric phase. This experiment uses a thermal cloud, and averages over all types of orbits. The false EDM signal associated with this is taken from [41], and given as

$$d_{\text{false}} = \frac{-F\hbar}{2B_{0z}^2 c^2} |v_{xy}|^2 \frac{\delta B_{0z}}{\delta z} \frac{1}{1 - \frac{\omega_r^2}{\omega_0^2}} \tag{3.26}$$

where $F = 1/2$ is the total spin, $|v_{xy}| = \sqrt{2/3}v_D$ is the RMS speed in the xy-plane, B_{0z} is the magnitude of the applied magnetic field, ω_0 is the Larmor frequency, and ω_r is the trap frequency. The gradient in B_{0z} was taken at .1% per cm, which was the measured upper limit. There are two different trap frequencies for x and y, with $\omega_x = 4$Hz and $\omega_y = 610$Hz. The resulting 1σ value is $7 \times 10^{-30}\ e \cdot \text{cm}$.

3.5 Sensitivity Upgrade Strategy

For the next experimental run of radium-225, a variety of upgrades are being implemented. Once again, the formula for the statistical uncertainty in this measurement looks like

$$\delta d = \frac{\hbar}{E\sqrt{NT\tau\epsilon}} \tag{3.27}$$

where E is the electric field strength, N is the number of atoms trapped per measurement, T is the total integration time of the experiment, τ is the spin precession time, and ϵ is the detection efficiency. In the next experimental run, we intend to increase the spin precession time of τ, as well improve all of the other variables listed.

3.5.1 Improved Trapping Efficiency - Blue Slower

Currently, our experiment is only able to trap atoms moving up to 60 m/s, due to the relatively long lifetime of the $^3P_1$ excited state which is on the order of 10^2ns . This only allows our trap to capture less than 1% of the total atoms out of our oven. We intend to implement a new trapping scheme utilizing the stronger $^1P_1$ transition, which has a much shorter lifetime on the order of 10^1ns called the blue slower. However, using this transition requires the use of a much more complicated repump scheme. With this scheme implemented,

however, atoms moving up to 300 m/s can be trapped, which accounts for 63% of the atoms coming out of the oven as can be seen in Figure 3.10. This corresponds to an increase of roughly 1 order of magnitude in sensitivity. A level scheme which shows the transitions that could be used for optical cycling with the blue slower is shown in Figure 3.11. The repumping scheme requires no less than 5 lasers, as opposed to the two required for the red slower transition.

Figure 3.10: Maxwell-Boltzmann distribution at 500 °C. This distribution is used to derive the percentage of atoms coming out of the oven for a given maximum trapping velocity. Red region represents the fraction of atoms we could trap with the previous scheme used in the 2015 data run. The blue region represents the fraction of atoms we could trap with the proposed blue slower scheme.

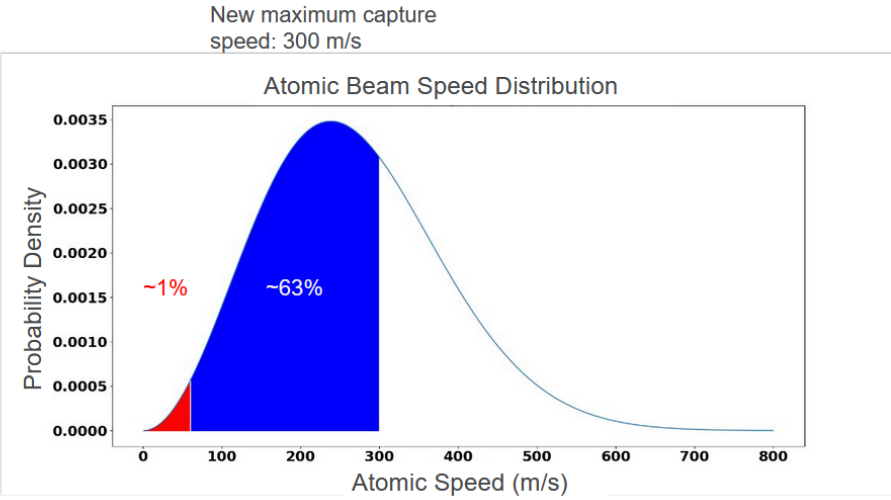

3.5.2 Improved Spin Detection Efficiency - QND

A group at the University of Science and Technology in China has demonstrated improved shadow imaging efficiency using a technique known as Quantum-Non-Demolition (QND) [22]. With our current setup, the radium-225 atoms we measure are only able to scatter 3 photons on average before they decay from the excited state of the transition to a dark

Figure 3.11: Blue Slower optical cycling scheme. The $^1P_1$ transition decays to the ground state faster than the $^3P_1$ transition. However, the $^1P_1$ transition also decays into significantly more dark states than the $^3P_1$ transition. This means more repump lasers are required. The $^3F_2$ state has an uncharacteristically large branching fraction to the $^1D_2$ state, so it is used as a channel to flip the triplet dark states back into singlet states.

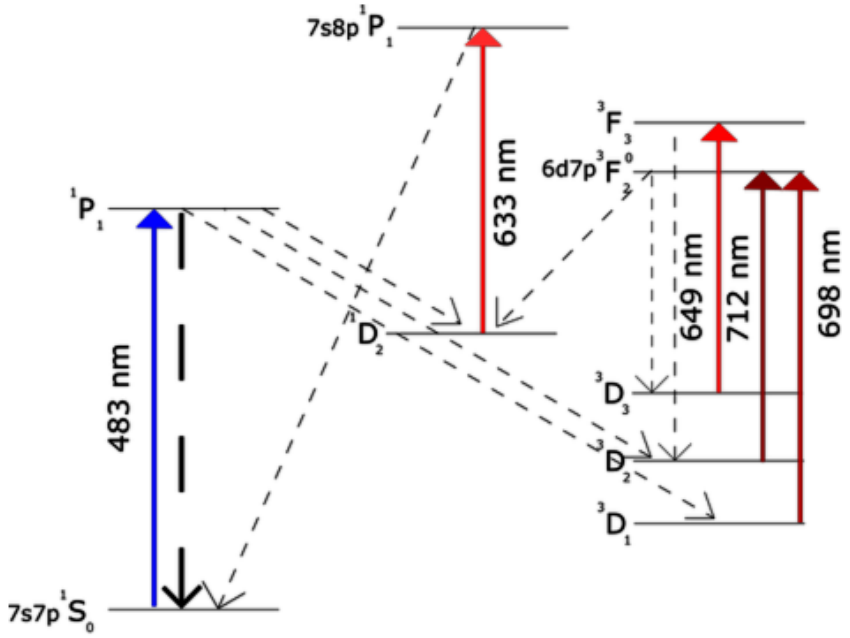

state, where they can no longer be fluoresced. This requires us to take the average of multiple measurements in order to see a clean shadow signal, since relatively few photons are scattered per atom. The QND scheme works by"dressing" the excited states using another laser to make only the desired transition on resonance with our shadow imaging laser. This increases the number of photons scattered per atom from 3 to a few thousand, giving the shadow imaging a much cleaner, clearer signal, and roughly an additional 2 orders of magnitude of sensitivity.

3.5.3 Improved Electric Field - HV

Any increase in the applied electric field will lead to higher sensitivity to an EDM. In the 2015 run, the applied electric field was 65 kV/cm. For the next run, voltages reaching hundreds

of kV/cm are planned. A method has been developed to treat and condition electrodes to be able to create large electric fields, without any discharges that can create leakage currents [40]. Also in progress is the implementation of a new HV switching scheme. Previously, a bipolar ±30 kV power supply was used, with the voltage affixed permanently to one of the electrodes. Now, the plan is to have a unipolar +60 kV power supply. A series of relays swap the high voltage and ground connections between electrodes. This implementation will be discussed more in Chapter 6, and should provide an additional factor of 10 improvement in sensitivity.

3.5.4 New Source of Ra-225 - Isotope Harvesting

The beam dump at the FRIB will allow for the harvesting of rare isotopes created by its unused secondary beam. This beam dump can be used as a source of radium-225 for the RaEDM experiment. An apparatus has been built at MSU to measure the efficiency with which a sample of radium from FRIB could be used to create an atomic beam. These efforts will be discussed further in Chapter 7.

Chapter 4. Radium 223 Trapping Studies

Due to the dearth of radium-225 available for our experiment, radium-223 was explored as a potential substitute. This isotope has a similar enhancement factor to radium-225 in sensitivity for EDM measurements, but adapting to the isotope has proven challenging. The energy levels of certain states of radium-223 have yet to be identified. Work was done to identify these states.

4.1 Comparison to Ra-225

Radium-223 has a similar octupole deformation to the radium-225 nucleus. This makes it a potential substitute, since the experiment is already set up to trap radium. However, there are issues with radium-223 that make it not as ideal as radium-225. Its half-life is only about 11 days, as opposed to the 15 day half-life of Radium-225. More importantly, its nuclear spin is 3/2 as opposed to 1/2 for radium-225. This makes its hyperfine structure much more complicated, and opens radium-223 up to additional systematic effects in the form of the tensor shift. Finally, the precise transition frequencies needed to trap the isotope are not known. Effort was thus made into finding the necessary transition frequencies.

4.2 Energy Level Background

While the electronic structure mostly stays the same between isotopes, there are shifts and hyperfine splittings in the energy levels that are extremely important to identify to be able to laser cool and trap atoms. This can in fact become a benefit, as the laser slowing apparatus

can be specifically tuned to one specific isotope. There are generally three areas where changes in the spectrum emerge: the isotope shift, the hyperfine A coefficient, and the hyperfine B coefficient.

4.3 Known Energy Levels

The current repumping scheme for the radium-EDM experiment relies on 2 different transitions: The 714 nm transition from $^1S_0$ to $^3P_1$, and the 1024 nm transition from $^3D_1$ to $^1P_1$. The values of isotope shifts and A and B coefficients for many isotopes of radium were previously compiled in 2016 Ref. [42]. The isotope shifts and hyperfine coefficients relevant for radium-223 are presented in Table 4.1.

Table 4.1: Isotope shifts and hyperfine coefficients of radium-223 for various states in the optical cycling. A question mark denotes an unmeasured transition.

State	Isotope Shift From Ra-214 (MHz)	A Coefficient (MHz)	B Coefficient (MHz)
$^1S_0$	0	0	0
$^1P_1$	-32453(9)	-344.5(0.9)	421.5 (1.6)
$^3P_1$	-32934(10)	1202.1(0.6)	-470.2 (1.2)
$^3D_1$	?	?	?

Critically, the $^3D_1$ state in the repumping scheme is unknown for radium-223. In fact, the only known parameters for the shift of this state come from the 2015 RaEDM run Ref. [21], described in Table 4.2

Table 4.2: All previously measured isotope shifts relative to Radium-226 and A and B coefficients of the ^{3}D$_1$ state of radium isotopes. Note that there is no B coefficient for Ra-225.

Isotope	Isotope Shift (MHz)	A Coefficient (MHz)	B Coefficient (MHz)
Ra-225	540.2	4687.7	N/A

So, there are three values that need to be predicted for the $^3D_1$ state of radium-223 to have a good idea of how to trap radium-223: the isotope shift, the A coefficient, and the B coefficient.

4.4 Ra-223 Isotope Shift Prediction

There are three physical interactions from which the isotope shift arise: (1) the normal mass shift, (2) the specific mass shift, and (3) the field shift. The normal mass shift is a correction factor resulting from a shift in the center of mass due to the change of mass of the nucleus, and it can be easily accounted for. The specific mass shift is a factor dependent upon the change in electron configuration, and the field shift is another factor dependent on the electron configuration which is also proportional to the nuclear charge radius.

The isotope shift is different for each isotope and atomic transition. The total isotope shift for a given state looks something like

$$\delta\nu_{IS}^{A,A'} = \frac{M - M'}{MM'}(K_{NMS} + K_{SMS}) + F_{FS}\delta\langle r^2\rangle_{MM'} \tag{4.1}$$

where

$$K_{NMS} = m_e\nu_i \tag{4.2}$$

is proportional to the energy of the transition, M and M' are the masses of the isotopes, K_{SMS} is the special mass shift, F_{FS} is the field shift, and $\delta\langle r^2\rangle_{MM'}$ is the change in the mean squared nuclear charge radius.

4.4.1 King Plots

The expression for the isotope shift can be expressed as a frequency difference called the King shift for a specific transition i:

$$\Delta\nu^{i,\text{King}}_{MM'} = K^i_{SMS} + F^i_{FS}\delta\langle r^2\rangle_{MM'}\frac{MM'}{M-M'} = \delta\nu^i_{MM'}\frac{MM'}{M-M'} - K_{NMS} \tag{4.3}$$

where the normal shift mass parameter K_{NMS} is given by Equation 4.2. Thus, the value $\Delta\nu^{i,\text{King}}_{MM'}$ can be calculated. Now, consider the King plots for two different transitions:

$$\Delta\nu^{i,\text{King}}_{MM'} = K^i_{SMS} + F^i_{FS}\delta\langle r^2\rangle_{MM'}\frac{MM'}{M-M'} \tag{4.4}$$

$$\Delta\nu^{j,\text{King}}_{MM'} = K^j_{SMS} + F^j_{FS}\delta\langle r^2\rangle_{MM'}\frac{MM'}{M-M'} \tag{4.5}$$

The change in the mean squared nuclear charge radius is the same for both transitions, and so the equations can be combined into something like

$$\Delta\nu^{j,\text{King}}_{M,M'} = \frac{F_j}{F_i}\Delta\nu^{i,\text{King}}_{M,M'} + K^i_{SMS}\frac{F_j}{F_i} - K^j_{SMS} \tag{4.6}$$

Notice that the parameters $F_{i,j}$ and $K^{i,j}_{SMS}$ are dependent on the transition only, and not the particular isotope. This means that, if the isotope shift for two specific transitions are known for three specific isotopes, then there are at least 2 different $\Delta\nu^{j,\text{King}}_{MM'}$ and $\Delta\nu^{i,\text{King}}_{MM'}$, which allows a linear fit to be created, from which the value of $\frac{F_j}{F_i}$ and $K^i_{SMS}\frac{F_j}{F_i} - K^j_{SMS}$ can be calculated. With this information in hand, if another isotope which has the isotope

shift from only one transition known, then the other missing isotope shift can be calculated. There is one issue: only a single $^3D_1$ isotope shift, the one for radium-225, has ever been measured. This means one further approximation is necessary. For both of the states $^1P_1$ and $^3D_1$ in the 1428 nm repump transition, each has one of its valence electrons in the s-orbital. Generally, in this case, the king plot is dominated by the field shift, since the wavefunction is non-zero at the nucleus. This can be seen in Section 6.3 of Ref. [43], where it is mentioned "The small specific mass shift differences between ionic 4,683 Å and atomic 4,825 Å lines and also between the atomic 4,826 Å and 7,141Å lines are well within the range usually observed for s, p, s^2, and sp configurations."Ref. [43] The data used to come to this conclusion was found in Ref. [44]. Thus, the values of K^j_{SMS} and K^i_{SMS} can be approximated to zero, leaving only

$$\Delta\nu^{j,\text{King}}_{M,M'} = \frac{F_j}{F_i}\Delta\nu^{i,\text{King}}_{M,M'} \tag{4.7}$$

Using the $^1P_1$ and $^3D_1$ states of radium-225, the field shift ratio can be calculated to be

$$\frac{F_{^3D_1}}{F_{^1P_1}} = .2442(.0018) \tag{4.8}$$

resulting in an isotope shift for the $^3D_1$ state of radium-223 to be

$$\Delta\nu^{^3D_1}_{226,223} = 2097(16)\,\text{MHz} \tag{4.9}$$

So, the radium-223 isotope $^3D_1$ state is estimated to be 2102 MHz above the $^3D_1$ state for radium-226. This value can also be calculated with the $^3P_1$ state instead of the $^1P_1$ state, which yields 2099(18) MHz, very much consistent with the previous result.

4.5 Ra-223 $^3D_1$ A Coefficient Prediction

The hyperfine splitting of a given state can be described by the hyperfine A and B coefficients:

$$\Delta E_{\text{hfs}} = \frac{A}{2}C + BC(C+1) \tag{4.10}$$

where C is given by

$$C = F(F+1) - I(I+1) - J(J+1) \tag{4.11}$$

where I is the nuclear spin, J is the total electronic spin, and F is the total spin. The A coefficient of a given isotope, here denoted A_1, can be can be predicted in two different ways. The first is to simply rescale the A coefficient of another isotope, here denoted as A_2 based on the nuclear spins and magnetic moments:

$$\frac{A_1}{A_2} = \frac{\mu_1}{\mu_2}\frac{I_2}{I_1} \tag{4.12}$$

The computed $A_{^3D_1}$ for Ra-223 rescaled from Ra-225 is then:

$$A_{^3D_1} = -574 \pm 15.15 \text{ MHz} \tag{4.13}$$

The values for this calculation come from Ref. [43] and are displayed in Table 4.3

Table 4.3: Coefficient values used to estimate the radium-223 A coefficient via the rescaling method taken from Ref. [43].

A	I	$\frac{\mu_I}{\mu_N}$	Q_s
223	3/2	0.262(5)	1.19(12)
225	1/2	-0.713(13)	-

Another way to estimate the A coefficient of a given isotope is to utilize Breit-Wills theory Ref. [45]. According to this theory, the A coefficient for a state with two valence electrons can be described as a linear combination of two single electron A coefficients.

4.5.1 Breit-Wills Theory

Any perturbation of the Hamiltonian looking like

$$H' = \mathbf{B} \cdot \mathbf{I} \tag{4.14}$$

where $\mathbf{I}$ is the nuclear spin, and $\mathbf{B}$ is any purely electronic matrix vector, will give rise to an energy splitting like

$$\Delta\omega = \frac{A}{2}(F(F+1) - J(J+1) - I(I+1)) \tag{4.15}$$

where A is given by

$$A = \frac{\mathbf{B} \cdot \mathbf{J}}{J(J+1)} \tag{4.16}$$

For a two-electron configuration, the matrix element for decomposing A into single-electron contributions looks like:

$$(j_1, j_2|\mathbf{B} \cdot \mathbf{J}|j_1, j_2) = Q_{12}a_1 + Q_{21}a_2 \tag{4.17}$$

where

$$Q_{ab} = \frac{1}{2}(J(J+1) + j_a(j_a+1) - j_b(j_b+1)) \tag{4.18}$$

The equations for the individual contribution from a single electron is as follows for orbital

angular momentum $l = 0$ Ref. [43]:

$$a_{ns} = \frac{8\pi}{3}\frac{2\mu_0\mu_B}{4\pi}\frac{\mu_I}{I}|\psi(0)|^2_{ns}F_{1/2}(Z_i)(1-\delta)(1-\epsilon) \tag{4.19}$$

and for $l > 0$:

$$a_{nlj} = \frac{2\mu_0\mu_B}{4\pi}\frac{\mu_I}{I}\frac{l(l+1)}{j(J+1)}\langle r^{-3}\rangle_{nl}F_j(Z_i)(1-\delta)(1-\epsilon) \tag{4.20}$$

where $F_j(Z_i)$ is a relativistic correction factor, $(1-\delta)$ is the relativistic Breit-Rosenthal-Schawlow correction, and $(1-\epsilon)$ is the Bohr-Weisskopf correction. The electronic matrix elements can be described as:

$$|\psi(0)|^2_{ns} = \frac{Z_i Z_0^2}{\pi a_0^3 n^{*3}} \tag{4.21}$$

and

$$\langle r^{-3}\rangle_{nl} = \frac{Z_i Z_0^2}{a_0^3 n^{*3} l(l+\frac{1}{2})(l+1)} \tag{4.22}$$

where $n^* = n - \sigma$ is the effective principle quantum number and σ is the quantum defect.

Crucially, the only factor that changes between different isotopes is $\frac{\mu_I}{I}$. This means that the single electron contributions for a given isotope scale like:

$$a_{nlj,N} = a'_{nlj}\frac{\mu_I}{I} \tag{4.23}$$

which means that, if the individual μ_I are known and a_{nlj} is known for any one isotope, the a_{nlj} can be found for another isotope. Ref. [43] provides calculations for various single electron states for Ra-223, the results of which are summarized in Table 4.4

Table 4.4: Single electron a contributions for Radium-223. Values taken from Ref. [43].

State	$a_{7s_{1/2}}$	$a_{7p_{1/2}}$	$a_{7p_{3/2}}$
Value (MHz)	2736	371	20.8

So, with the scaling between Ra-223 and Ra-225, we get $a_{7s_{1/2},225} = -22\,337$ MHz. Consider now the $^3D_1$ state of Radium. This state can be decomposed into the sum of its two electron configurations:

$$2J(J{+}1)A_{^3D_1} = (J(J{+}1){+}j_1(j_1{+}1){-}j_2(j_2{+}1))a_{7s_{1/2}}{+}(J(J{+}1){+}j_2(j_2{+}1){-}j_1(j_1{+}1)a_{6d_{3/2}} \quad (4.24)$$

where the hyperfine A coefficient for the $^3D_1$ state is given by

$$A_{^3D_1} = -\frac{1}{4}a_{7s_{1/2}} + \frac{5}{4}a_{6d_{3/2}} \quad (4.25)$$

For the value of $A_{^3D_1} = 4687.7$ MHz taken from Ref. [46], one can calculate

$$a_{6d_{3/2},225} = -717.24 \text{ MHz} \quad (4.26)$$

and rescaling it to radium-223:

$$a_{6d_{3/2},223} = a_{6d_{3/2},225}\frac{1/2}{3/2}\frac{\mu_{223}}{\mu_{225}} = 87.85 \text{ MHz} \quad (4.27)$$

So, the predicted $A_{^3D_1}$ for Ra-223 is:

$$A_{^3D_1} = -574 \pm 19 \text{ MHz} \quad (4.28)$$

4.6 Ra-223 ^{3}D$_1$ B Coefficient Prediction

Unfortunately, no B coefficient has ever been measured for the $^3D_1$ state of any radium isotope. This prevents it from being able to be scaled. There is only one theoretical calculation of this value, performed in Ref. [47], which gives a theoretical calculation for the B Coefficient of the $^3D_1$ state for radium-223 of $B = 125$ MHz. This value is thus used as a starting point. This gives the final predicted values for the radium-223 $^3D_1$ state shown in Table 4.5

Table 4.5: Estimated values for the ^{3}D$_1$ state of radium-223.

Isotope Shift (MHz)	A Coefficient (MHz)	B Coefficient (MHz)
2097	-574	125

This gives the potential energy transitions for the repump frequency in Table 4.6

Table 4.6: Estimated repump transition frequencies for radium-223 and radium-226.

Isotope	Initial State	Final State	Repump Frequency (cm^{-1})	Frequency Shift (MHz)
Ra-226	$^3D_1$ (F = 1)	$^1P_1$ (F = 1)	6999.835	0
Ra-223	$^3D_1$ (F = 5/2)	$^1P_1$ (F = 5/2)	6999.779	-1676
Ra-223	$^3D_1$ (F = 3/2)	$^1P_1$ (F = 5/2)	6999.736	-2955
Ra-223	$^3D_1$ (F = 5/2)	$^1P_1$ (F = 3/2)	6999.790	-1347
Ra-223	$^3D_1$ (F = 3/2)	$^1P_1$ (F = 3/2)	6999.747	-2626

4.7 Radium-223 Beam Fluorescence

In order to get a rough idea of where the primary transition frequency was for radium-223, a beam fluorescence measurement was done during the initial oven crack. During this period, a very large amount of atomic flux occurs, making it the only time where enough radium-223

is present to perform a beam spectroscopy measurement upon it. On April 16th, 2021, 2 μCi of radium-226 and 10 mCi of radium-223 were loaded into the RaEDM apparatus at Argonne National Laboratory, under standard loading procedure, of quantities shown in Table 4.7

Table 4.7: Initial activity of radium-226 and radium-223 from oven load on 2021-04-16.

Isotope	Activity (initial)	Number of Atoms (initial)
Ra-226	2 μCi	5.4 $\times 10^{15}$ Atoms
Ra-223	10 mCi	5.1 $\times 10^{14}$ Atoms

So, there were approximately 10 times fewer atoms of radium-223 than radium-226 in the oven. The frequency shift in the $^3P_1$ transition between radium-223 and radium-226 is 10484.6 MHz. This, remarkably, is extremely close to 7 times the 1497.8 MHz Free-Spectral-Range (FSR) of the 714 nm laser. Thus, by locking the laser to a mode 7 FSRs away, the ULE EOM frequency required would be nearly identical between radium-226 and radium-223.

4.7.1 Retro-reflected Beam Spectroscopy Principle

A retro-reflected beam spectroscopy measurement was performed during the oven crack. A principle diagram can be seen in Figure 4.1. Despite the best efforts to ensure that a laser beam is perpendicular to an atomic beam, some small angle will always remain. To account for this, so-called retro-reflection is used. This involves reflecting the laser beam back to its source, using a mirror. By ensuring the reflected laser beam is parallel with the incoming laser beam, the true fluorescence frequency can be determined. The incoming laser beam, due to relativistic effects, and assuming a small deviation from perpendicularity, sees the atomic transition frequency ω_1 centered at a value:

$$\omega_1 = \omega_0(1 - \frac{v\sin(\theta)}{c}) \tag{4.29}$$

where ω_0 is the true transition frequency, v is the velocity of the incoming atoms, θ is the deviation from perpendicularity between the laser beam and the center of the atomic beam, and c is the speed of light. The atomic transition frequency seen by the reflected beam is then:

$$\omega_2 = \omega_0(1 + \frac{v\sin(\theta)}{c}) \tag{4.30}$$

The fluorescence spectrum then has two peaks to its shape. By taking the midpoint of these two peaks, the true fluorescence value can be determined:

$$\omega_0 = \frac{\omega_1 + \omega_2}{2} \tag{4.31}$$

4.7.2 Beam Spectroscopy of Radium-223

The average of 3 fluorescence scans was taken, and fit to a sum of two Gaussian functions. This was done for radium-226 and radium-223 data separately. The fit parameters are presented in Table 4.8. The resulting spectrum incorporating the double Gaussian fits and fluorescence scans from the retro-reflected beam spectroscopy are captured in Figures 4.2 and 4.3 for radium-226 and radium-223 respectively. These measurements informed where the $^3P_1$ transition would shift during the operation of our laser systems. Understanding how this transition might shift provides a rough estimate of where the ULE EOM needed to be placed in order to attempt to trap Ra-223 in our 3D MOT.

It should be remembered that the scan for radium-223 was located 7 FSRs away from radium-226, so these were not almost at the same point.

Figure 4.1: Conceptual diagram demonstrating retro-reflected beam fluorescence. Ra-223 and Ra-226 atoms exit the oven with some angular spread. A 714 nm laser is directed perpendicular to the oven nozzle. Radium atoms that exit the oven should fluoresce with this laser light and the fluorescence is captured by a PMT. Atoms that are not traveling perpendicular to the laser see a Doppler shift of the incident 714 nm light. To account for this shift, the 714 nm laser is retro-reflected and used to induce a Doppler shift in the opposite direction. The total fluorescence spectrum will have two peaks, and the midpoint is interpreted as the true resonance frequency of the $^3P_1$ transition.

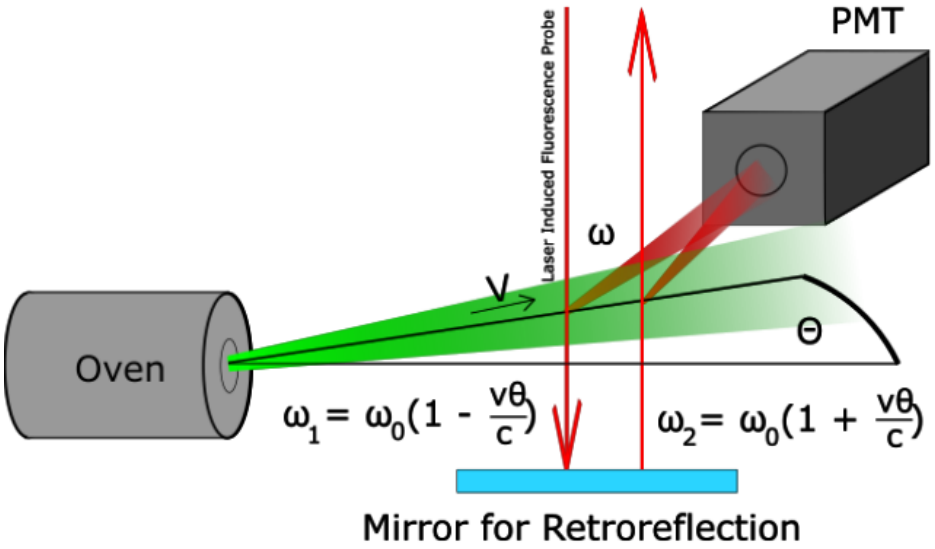

Table 4.8: Double Gaussian fit parameters for Ra-223 and Ra-226.

Isotope	Peak 1 Location (MHz)	Peak 2 Location (MHz)	Center (MHz)
Ra-226	828.12 ± .07	840.94 ± .22	834.53 ± .12
Ra-223	826.27 ± .06	838.08 ± .19	832.18 ± .10

4.8 Ra-223 Trapping Attempts

With the data collected from the beam fluorescence, it was determined that the EOM frequency to attempt to trap radium-223 should be red-detuned by about 2 MHz. After the crack of the oven, nearly a full half-life of radium-223 elapsed before radium-226 was finally able to be trapped. It was found with a ULE EOM Offset of 843.9 MHz.

Figure 4.2: Fluorescence spectrum for radium-226 obtained during oven cracking on 2021-04-16. The blue trace is an average of the 3 different scans performed. The orange trace is the fit to the sum of two Gaussians. The green vertical lines indicate the centers of the two Doppler shifted peaks in the retro-reflected beam measurement. The red vertical line is the midpoint of the Doppler shifted peaks which is interpreted as the resonant frequency for the $^3P_1$ transition. Note that the small angle approximation is used here, where $\theta \approx \sin\theta$.

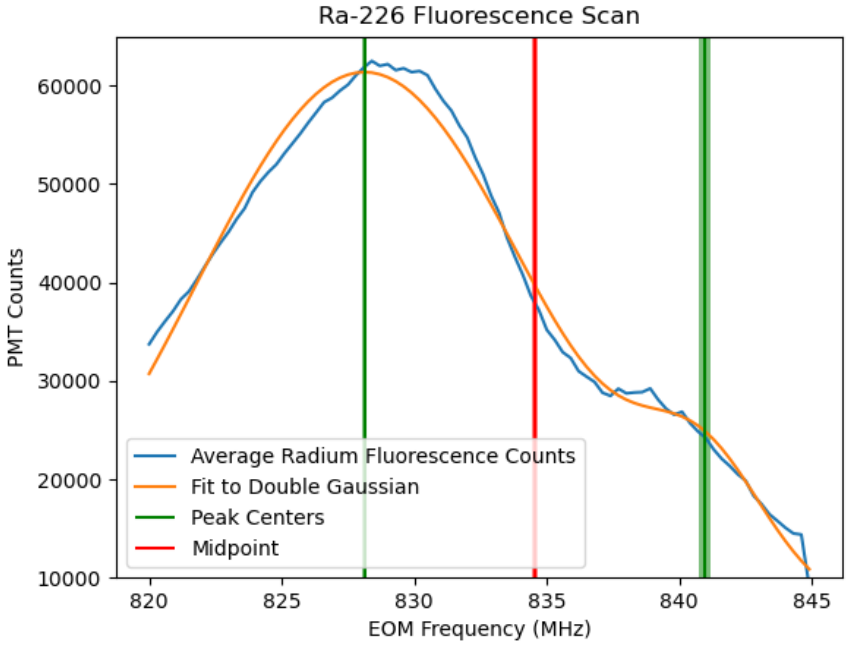

The shift in the EOM frequency from the beam fluorescence center is believed to be due to a misalignment that was found in the retro-reflected beam. The repump frequency used to trap Ra-226 was 6999.835 ± 0.0005 cm^{-1}. The repump laser was not locked during the scanning for radium-226 or radium-223, though it seemed stable enough to be accurate to the 0.001 cm^{-1} level. Data taken on the PMT during these data runs looks something like in Figure 4.5.

The bins with counts below 600 are taken during the MOT loading phase, during which the PMT is blocked from viewing the MOT chamber. The bins with counts above 600 are taken during the MOT probing phase, which is when fluorescence is attempted. For looking

Figure 4.3: Fluorescence spectrum for radium-223 obtained during oven cracking on 2021-04-16. The color assignment of the traces and vertical lines on this plot are identical to those is Figure 4.2.

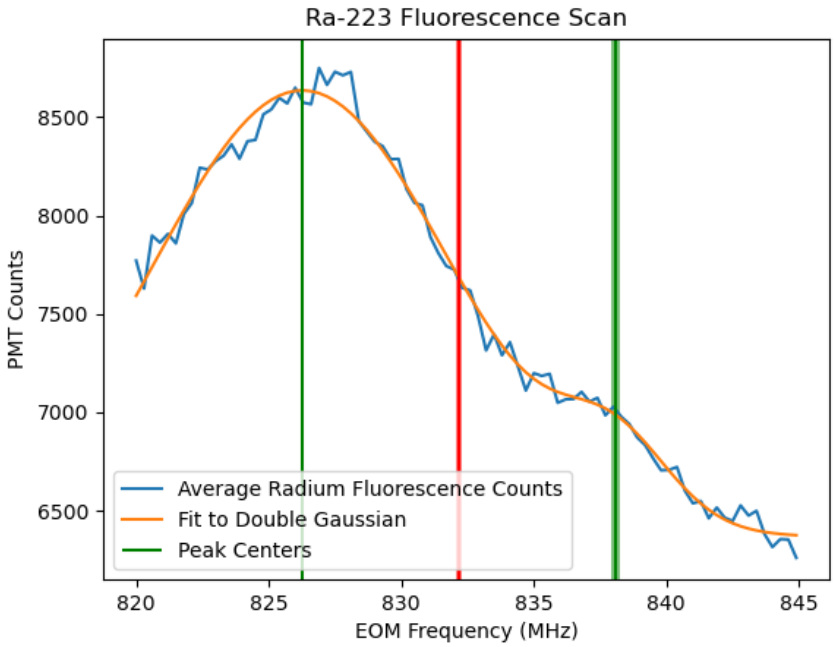

for radium-223 fluorescence, only the probe phase data should be considered. With this in mind, the ULE was set to 841.9 Mhz, and the repump was scanned around. Periodically, the repump was turned off to get a background. For each repump position, the counts for the probe region, defined as anywhere that the counts were greater than 600, were collected and had their mean and standard deviation taken. This was taken as the mean and standard deviation of the measurement. The mean and standard deviations as a function of repump frequency can be seen in Figure 4.6.

The background data, where the repump was off and no trapping should have been seen, looked like Figure 4.7

The conclusion was that, at this ULE frequency and these repump frequencies, Ra-223 trapping was not achieved.

Figure 4.4: Image of the MOT taken with a CCD camera.

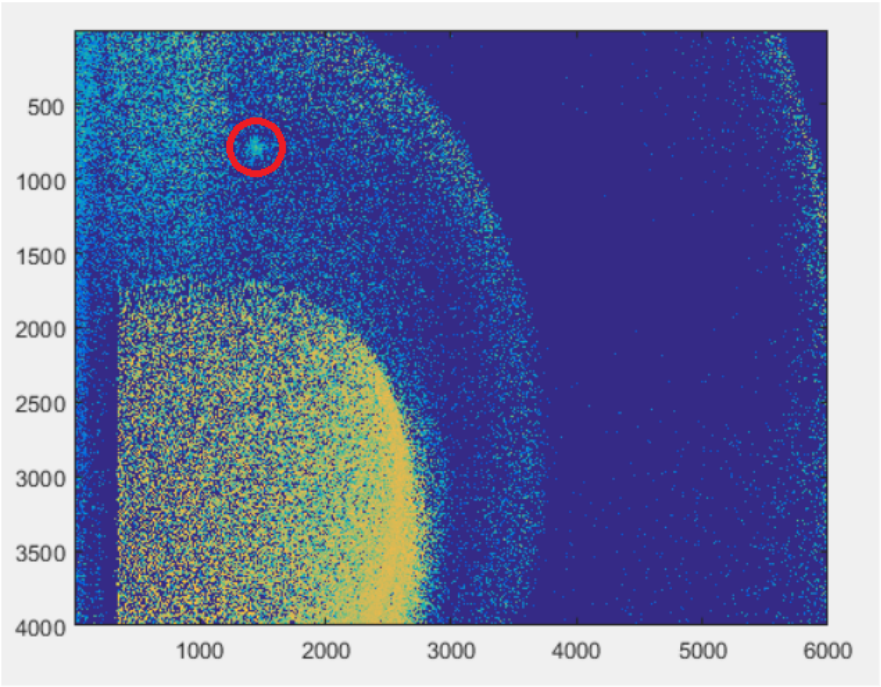

4.9 Future Work

A variety of new techinques could be utilized in the future, to improve the possibility of seeing radium 223:

- Have the MOT already ready to trap radium-226, so precious time radium-223 is not wasted decaying away while looking for it
- have a steady source of radium-223, so that multiple runs can be done.

Figure 4.5: PMT Data taken during MOT cycles. Each cycle consists of one high period, where the gate is open, and a lower period, where the gate is closed.

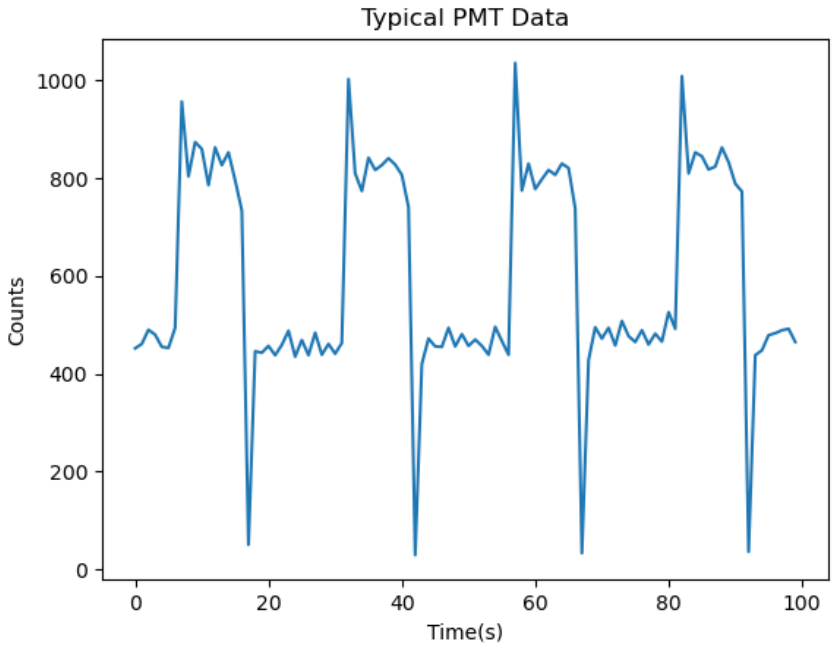

Figure 4.6: Results taken from the radium 223 scan. No signal was seen, since the integrated count rate always remained the same within its uncertainty.

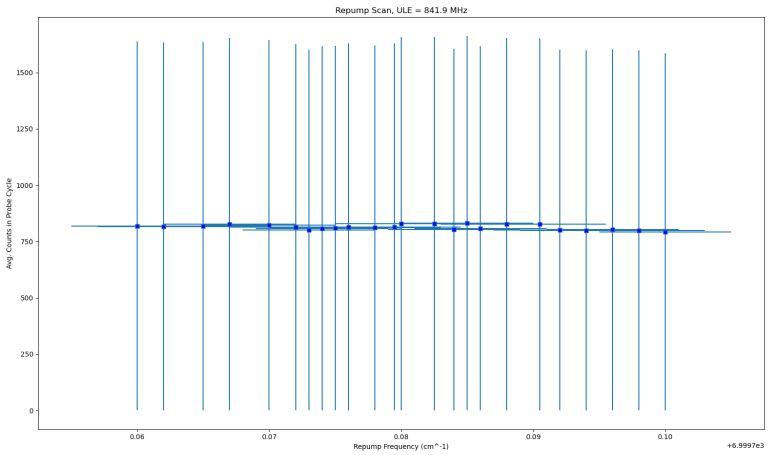

Figure 4.7: Trapping data with repump off. The background with the repump off was the same within error bars to the radium-223 scan, confirming that no signal was seen.

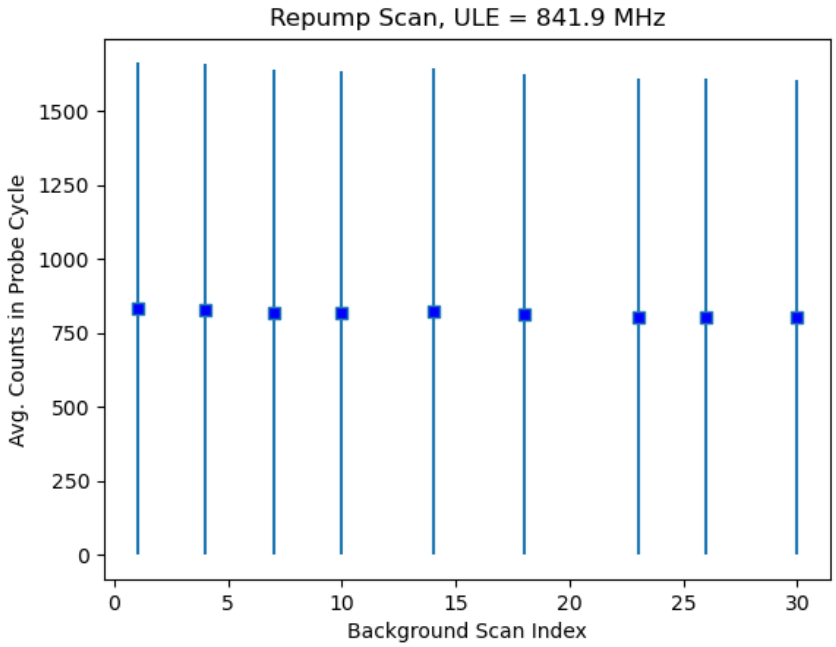

Chapter 5. Calculation of Frequency Shifts Associated with Optical Dipole Trapping

5.1 Systematics Associated with Laser Trapping in EDM measurements

In order to achieve the precision required for the RaEDM experiment, care must be taken to characterize and control for systematic effects. Any effect that might cause a shift in the Larmor precession frequency other than an EDM needs to be carefully studied and characterized to prevent false EDM signatures. The more these systematics can be controlled and suppressed, the better. One of the potential sources of systematic uncertainty comes from the interaction of the atoms being held in an ODT with the static electric field applied. For radium-225, the effect this has can be broken down into two parts: (1) the vector shift, and (2) the Stark shift Ref. [48]. For radium-223, an additional tensor shift is present due to its nuclear spin of 3/2. To characterize their associated systematic uncertainties, atomic calculations are required. An overview of these ongoing calculations will now be given.

5.1.1 Vector Shift

When atoms are trapped in an ODT, there is an added interaction expressed by the Hamiltonian

$$H' = e\mathbf{E} \cdot \sum_i \mathbf{r_i} \tag{5.1}$$

where $\mathbf{E} = \frac{E_0}{2}(\hat{\epsilon}e^{-i\omega t} + \hat{\epsilon}^* e^{i\omega t})$ is the holding field of the ODT. To first order in time-dependent perturbation theory, this results in a vector shift that looks like:

$$\Delta E = \frac{-e^2 E_0^2}{4\hbar}\Sigma_{J',F',m'}\left(\frac{\langle J',I,F',M'|\epsilon\cdot r|J,I,F,M\rangle\langle J,I,F,M|\epsilon^*\cdot r|J',I,F',M'\rangle}{\omega_{J'}-\omega} + \frac{\langle J',I,F',M'|\epsilon^*\cdot r|J,I,F,M\rangle\langle J,I,F,M|\epsilon\cdot r|J',I,F',M'\rangle}{\omega_{J'}+\omega}\right) \tag{5.2}$$

ΔE is an energy shift that has a scalar shift component that is not dependent on the m_F sublevel when the matrix elements are explicitly evaluated. This scalar shift term has no effect on the experiment, because this experiment is sensitive to *changes* in Larmor precession frequency, not the value of the frequency itself. The explicit evaluation of ΔE also gives rise to a vector shift - a term that is linear in the m_F sublevel. The form of this vector shift is:

$$\Delta\nu = \nu_V(|\epsilon_L|^2 - |\epsilon_R|^2)m_F\cos\theta \tag{5.3}$$

where θ is the angle between the ODT propagation and the spin quantization axis, ϵ_L and ϵ_R are the degrees of left and right circular polarization, and ν_V is a term dependent upon power (through the E_0^2 term) and frequency of the ODT - it is here that the vector shift can cause problems. Any power fluctuation correlated with the applied electric field might cause a shift in energy between m_F states that is proportional to the electric field. This would cause a shift in the Larmor precession frequency between applied electric fields that would manifest itself as a false non-zero EDM. Fortunately, there are methods of suppression: For one, the ODT is $> 99\%$ linearly polarized - this introduces a suppression of two orders of magnitude. The ODT is also aligned perpendicular to the spin quantization axis, which is the same axis as the Larmor spin precession, suppressing the effect by another order of

magnitude. Ultimately, the false EDM signal that would be generated can be written as:

$$d_{false} = \Delta\nu_{1/2}\frac{h}{2E}\frac{\Delta P}{P_0} \tag{5.4}$$

where E is the electric field strength, $\nu_{1/2}$ is the vector shift, and $\frac{\Delta P}{P_0}$ is the fractional difference in holding beam powers between different electric field directions. To control for this effect, the ODT power is continuously monitored, and a 1 σ confidence interval upper limit can be placed on $\frac{\Delta P}{P_0}$ to be 8×10^{-5}. Finally, the calculated $\nu_{1/2}$ is found to be 50 Hz Ref. [21]. This all combines to give a 1σ uncertainty of $6 \times 10^{-26} e \cdot cm$ for radium-225.

5.1.2 Tensor Shift

The tensor shift arises from the next order of perturbation theory, and includes a mixing term with the hyperfine structure. This also contributes to the systematic effect related to ODT holding beam power correlation with electric field. The equation associated with this is:

$$\Delta E = \frac{e^2 E_0^2}{4\hbar} \sum_{J',J",F',M'} \frac{\langle J', I, F', M'|\epsilon \cdot \mathbf{r}|J, I, F, M\rangle\langle J, I, F, M|\epsilon^* \cdot \mathbf{r}|J'', I, F', M'\rangle}{(\omega_{J'} - \omega)(\omega_{J"} - \omega)} \times\langle J'', I, F', M'|W|J', I, F', M'\rangle + c.r. \tag{5.5}$$

where $c.r.$ is an additional counter-rotating term. This results in a tensor shift that looks like:

$$\Delta\nu = \nu_T(F)(3\cos^2\phi - 1)m_F^2 \tag{5.6}$$

where ϕ is the angle between the direction of the linearly polarized electric field and the spin quantization axis, and $\nu_T(F)$ is a function of the ODT power and F hyperfine level. This

shift only arises for nuclei with I $\geq$ 1. It thus is non-existent for radium-225. However, it does have an effect in radium-223, albeit with a producing a shift that is predicted to be much smaller than the vector shift. Similarly to the vector shift, the false EDM signal this would give rise to would be

$$2Ed_{\text{false}} = \Delta E_{M_F=3/2,1/2}\frac{\Delta P}{P_0} \tag{5.7}$$

So,

$$d_{\text{false}} = \Delta\nu_{M_F=3/2,1/2}\frac{h}{2E}\frac{\Delta P}{P_0} \tag{5.8}$$

Note that this effect is not minimized when the electric field and spin quantization axis are perpendicular, but rather at a magic angle $\phi = \cos^{-1}\left(\sqrt{\frac{1}{3}}\right)$ as can be seen from Eq. 5.6.

5.1.3 Stark Shift Parity Mixing Effect

The most dangerous effect for this experiment outlined in Ref. [48] is the parity mixing effect. This effect arises from a third-order mixing effect between the static electric field and the electric field of the ODT holding beam. The form for this equation looks like:

$$\begin{aligned}\Delta E = &\frac{e^2\mu_B E_0^2 E_s}{4\hbar^2}\\ &\times \sum_{J',J'',M',M''}[\frac{\langle J',M'|\epsilon\cdot r|J,M\rangle\langle J'',M'',|b^*\cdot(L+2S)|J',M'\rangle\langle J,M|\epsilon_s\cdot r|J'',M''\rangle}{(\omega_{J'}-\omega)(\omega_{J"}-\omega)}\\ &+\frac{\langle J,M'|b\cdot(L+2S)|J,M\rangle\langle J',M'|\epsilon^*\cdot r|JM'\rangle\langle J,M|\epsilon_s\cdot r|J',M'\rangle}{\omega_{J'}(\omega_{J'}-\omega)}] + perm. + c.r.\end{aligned} \tag{5.9}$$

where E_s is the static electric field strength, E_0 is the strength of the ODT electric field, ϵ_s is the static electric field direction, ϵ is the direction of the ODT electric field, b is the direction

of the ODT magnetic field, L is the orbital angular momentum, S is the total spin, ω_J is the transition frequency between atomic states, and ω is the ODT frequency. The *perm.* term contains the the other permutations of these interactions. A picture of those permutations is given here:

Figure 5.1: Diagram of the permutations of the Stark parity mixing effect. b indicates a magnetic dipole transition from the ODT magnetic field, ϵ indicates an electric dipole transition from the ODT electric field, and ϵ_s indicates the Stark interference parity mixing effect from the static electric field. Diagram taken without permission from Ref. [48].

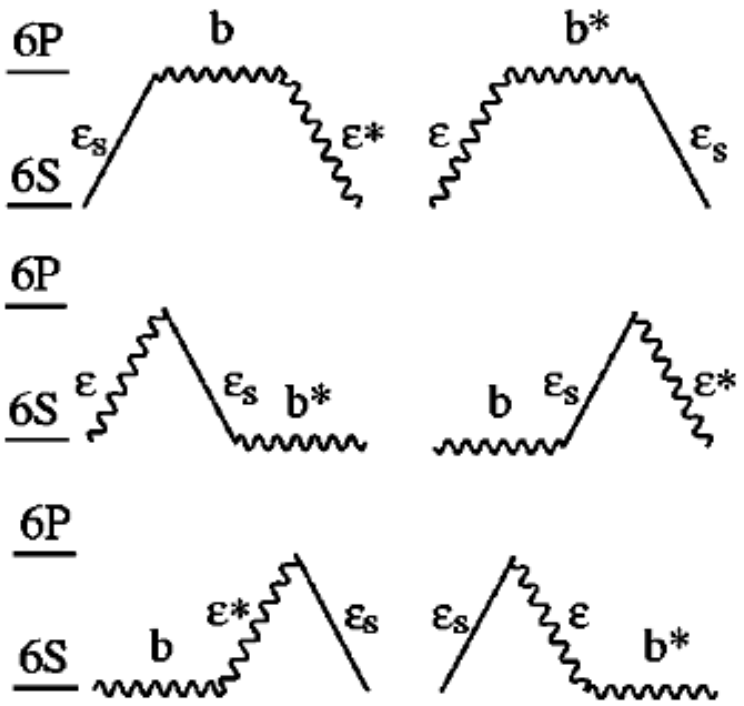

The interactions with ϵ indicate electric dipole transitions induced by the trapping beam, the b interactions indicate magnetic dipole moments induced by the trapping field, and the ϵ_s terms indicate mixing by the static electric field. This happens because static electric field causes states to mix, and some of these have different parities. Normally, since the electric dipole (E1) transition flips parity and the magnetic dipole (M1) transition conserves

it, a state cannot be excited by an E1 transition and then de-excited back to the original state by an M1 transition. However, with the addition of the static electric field, one of the states coupled with E1 can be mixed with a state that can couple to M1. This causes mixing of different parity states, which causes the above process to become allowed. There is also an additional effect that arises from the electric quadrupole (E2) interaction, which has the same parity rule as M1. A good way to consider this is to look at the interactions:

$$H_{E1} = e\mathbf{r} \cdot \mathbf{E} = eyE_0 \cos\omega t \tag{5.10}$$

$$H_{M1} = \frac{e}{2mc}(\mathbf{L} + 2\mathbf{S}) \cdot \mathbf{B} = \frac{e\hbar}{2mc}(L_z + 2S_z)E_0 \cos\omega t \tag{5.11}$$

$$H_{E2} = \frac{e}{6}(3x_i x_j - \delta_{ij} r^2)\frac{\delta E_i}{\delta x_j} = \frac{e\omega}{2c} xyE_0 \sin\omega t \tag{5.12}$$

This causes the multipole amplitudes to be given by:

$$E1 = e\langle \psi_f^0 | E_0 y | \psi_i^0 \rangle \tag{5.13}$$

$$M1 = \frac{e^2 E_s E_0 \hbar}{4mc} \sum_n \frac{\langle \phi_f^0 | y | \phi_n^0 \rangle \langle \phi_n^0 | L_z + 2S_z | \phi_i^0 \rangle}{W_f - W_n} + \frac{\langle \phi_f^0 | L_z + 2S_z | \phi_n^0 \rangle \langle \phi_n^0 | y | \phi_i^0 \rangle}{W_i - W_n} \tag{5.14}$$

$$E2 = \frac{ie^2 \omega E_s E_0}{4c} \sum_n \frac{\langle \phi_f^0 | y | \phi_n^0 \rangle \langle \phi_n^0 | xy | \phi_i^0 \rangle}{W_f - W_n} - \frac{\langle \phi_f^0 | xy | \phi_n^0 \rangle \langle \phi_n^0 | y | \phi_i^0 \rangle}{W_i - W_n} \tag{5.15}$$

Notice how the electric dipole transition couples states ψ_f and ψ_i, which would be a forbidden transition for the magnetic dipole moment. The Stark effect mixing due to the static electric field allows for the transition to still happen.

The Stark frequency shift depends on 4 vectors, with a dependence on those vectors that

looks like:

$$\Delta\nu_V = \nu_1(\hat{b}\cdot\hat{\sigma})(\hat{\epsilon}\cdot\hat{\epsilon_s}) + \nu_2(\hat{b}\cdot\hat{\epsilon_s})(\hat{\epsilon}\cdot\hat{\sigma}) \tag{5.16}$$

where $\hat{\epsilon}$ is the ODT electric field orientation, $\hat{\sigma}$ is the spin polarization axis, $\hat{\epsilon_\mathbf{s}}$ is the static electric field direction, and $\hat{b}$ is the ODT magnetic field orientation. A diagram of this can be seen in **??**

Figure 5.2: Diagram of the relavent vectors for Equation 5.16. Diagram taken without permission from Ref. [48].

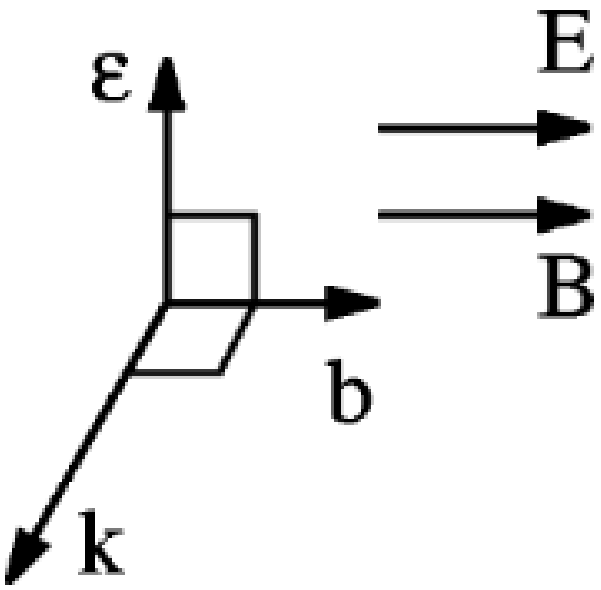

Note that in our experiment, $\hat{\epsilon_s}$ and $\hat{\sigma}$ must point along the same direction in order to be sensitive to the EDM. Thus to suppress this systematic, the best way to thus orient the ODT is so that either $\hat{\epsilon}$ or $\hat{b}$ are perpendicular to $\hat{\sigma}$ (and thus also to ϵ_s, in order to suppress at least one of the dot products in both terms of $\Delta\nu_V$). The single E_s term is scary, since this Stark shift does indeed cause a false EDM signature. When the direction of E_s is flipped, it causes a shift in the energy *depending on the direction.* In addition to the linear effect of E_s, which can cause a false EDM signature, there is also a dependence on the power of

the ODT laser. This effect only arises if there's a correlation between the direction of the electric field and the ODT power. In addition, it allows for the measurement of this false EDM effect. If there's a Larmor frequency shift observed that is dependent on both the electric field strength and the ODT holding beam power, then the values of these ν_1 and ν_2 can be experimentally observed, as was done in an EDM experiment with ytterbium-171 in China Ref. [20]. In this experiment, the angle θ determining the polarization of the ODT was varied, and the resulting false EDM signal was plotted. This is shown in Figure 5.3.

Figure 5.3: False EDM signal created by parity mixing effect in Yb-171. Taken without permssion from Ref. [20]. The ODT polarization angle was varied, and the parity mixing term's sinusoidal dependence on this was observed.

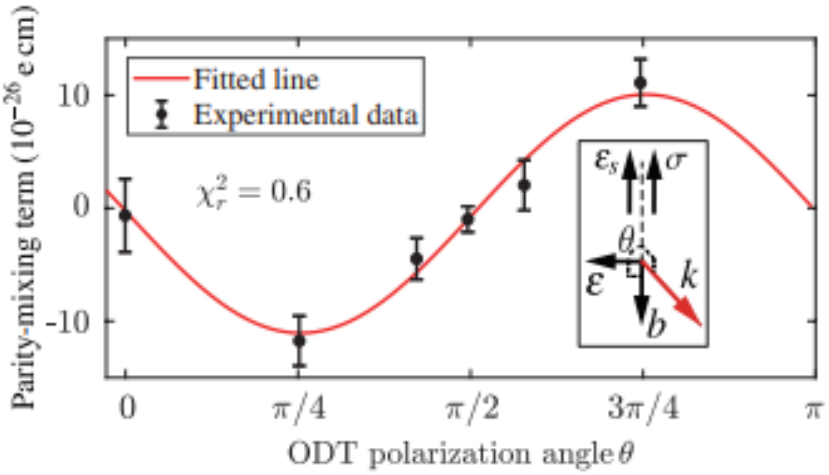

This effect for Radium was calculated out in Ref. [21], and gives a systematic uncertainty of $(\hat{b}\cdot\hat{\sigma})(\hat{\epsilon}\cdot\hat{\epsilon_s}) \leq 0.03$ and $(\hat{b}\cdot\hat{\epsilon_s})(\hat{\epsilon}\cdot\hat{\sigma}) \leq 0.1$ which, combined with the values calculated for ν_1 and ν_2, give a 1 σ systematic uncertainty of 6×10^{-26} $e\cdot$cm. This is the false EDM due to the phase shift in Larmor precession frequency that would be caused by this effect. Ref. [21] contains a brief description of this calculation.

5.2 Reproduction of Published Calculations

Ref. [48] has been used as the basis of calculations of the effects of static electric fields on the energy levels of atoms held in an optical dipole trap. Effort was put into reproducing these calculations, so that they could then be used as the basis for calculating the energy shifts in Ra-225 and Ra-223.

5.2.1 Laser Power Dependency Reproduction

To begin, Ref. [48] calculates the laser power necessary to trap atoms with a trap depth of $100\mu K$ as a function of the laser wavelength. For a Gaussian beam with a beam width of w_0, the radial intensity of the beam as a function of the distance from its center is given by

$$I(r) = I_0 e^{2(\frac{r}{w_0})^2} \tag{5.17}$$

where I_0 is the intensity of the beam at its center, and w_0 is the beam width at its focal point. By performing a polar integral, the total power of the beam can be determined:

$$P_0 = \int_0^{2\pi} \int_0^{\infty} I_0 e^{2(\frac{r}{w_0})^2} r dr d\phi = \frac{\pi}{2} I_0 w_0^2 \tag{5.18}$$

where I_0 can be related to the electric field strength at the center of the trap by:

$$I_0 = \frac{|E_0|^2}{2\eta} \tag{5.19}$$

where η is the impedance of the medium, in this case free space, and E_0 is the electric field strength of the ODT.

Combining Equations 5.18 and 5.19 yields

$$P_0 = \frac{\pi w_0^2 |E_0|^2}{4\eta} \tag{5.20}$$

In order to get rid of the troublesome factor of π in this equation, Gaussian units must be used. In these units, η is scaled like

$$\eta = \frac{4\pi}{c} \tag{5.21}$$

When utilizing the η from Equation 5.21 to derive the total power, we get

$$P_0 = \frac{w_0^2 E_0^2 c}{16} \tag{5.22}$$

which is the formula given, but not derived, in Ref. [48] for the total beam power as a function of the beam width and electric field strength at the center, in Gaussian units.

The formula given in Ref. [48] for the energy depth of the optical dipole trap (ODT) is

$$U = -\frac{e^2 E_0^2}{4m}[\sum_{J'} \frac{f_{J'}}{\omega_{J'}^2 - \omega^2} + \int_{\omega_I}^{\infty} \frac{(df/d\omega')d\omega'}{(\omega' - \omega_{J'})^2 - \omega^2}] \tag{5.23}$$

where m is the electron mass, $f_{J'}$ are the oscillator strengths of the transitions, and ω'_J are the atomic transition frequencies. Ref. [48] specifies only two states for cesium and mercury that are really necessary for a good calculation. For cesium, these states are $6P_{1/2}$ and $6P_{3/2}$. The oscillator strengths for both of these states are provided, and the energy levels can be found on the NIST website [49]. These are presented in Table 5.1.

The formula then effectively becomes

Table 5.1: Oscillator strengths and atomic transition frequencies for the excited states used for vector shift calculation. Oscillator strengths taken from Ref. [48] and transition frequencies taken from Ref. [49].

Element	J'	$\omega_{J'}(cm^{-1})$	$f_{J'}$
Cs	1/2	11178.2686	0.35
Cs	3/2	11732.3079	0.72
Hg	1/2	54068.781	1.2
Hg	3/2	39412.300	0.025

$$U = -\frac{e^2 E_0^2}{4m} \sum_{J'=\{1/2,3/2\}} \frac{f_{J'}}{\omega_{J'}^2 - \omega^2} = k_b(-100\ \mu K) \tag{5.24}$$

note that U is the energy of the trap, so U is negative, meaning the negative has to be taken of the trap depth.

Figure 1 in Ref. [48] is a plot of the required ODT laser power versus frequency. The total beam power is a function of E_0^2, and E_0^2 can be found with a rearranging of the above formula:

$$E_0^2 = -\frac{4mU}{e^2 \sum_{J'}} \frac{f_{J'}}{\omega_{J'}^2 - \omega^2} \tag{5.25}$$

By finding E_0^2 as a function of ω, and then the resulting power as a function of ω, Figure 1 in Ref. [48] can be reproduced for both mercury and cesium, as is seen in Figures 5.4 and 5.5.

The reproduction of these plots is necessary for the calculation of the vector and tensor shifts.

Figure 5.4: Cesium ODT power requirement reproduction. This gives the necessary power to create an ODT trap depth of 100 μK for cesium, for a given ODT frequency. In this case, the value ω_1 is the first atomic transition frequency of cesium.

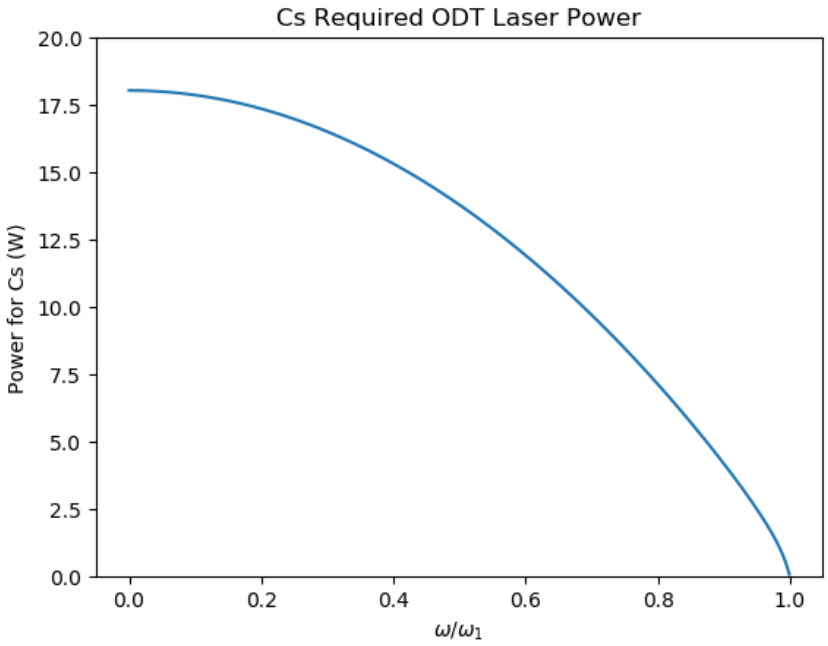

5.3 Vector Shift Reproduction

In order to reproduce the plots in Ref. [48], time dependent perturbation theory is necessary. A derivation is now given.

5.3.1 Derivation of the Energy Shift from Time-Dependent Perturbation Theory

The unperturbed eigenstates are the normal $|J, I, F, M\rangle$ hyperfine states for the unperturbed Hamiltonian, which form an orthonormal basis:

$$\langle J', I, F', M'|J, I, F, M\rangle = \delta_{J'J}\delta_{F'F}\delta_{M'M} \tag{5.26}$$

Figure 5.5: Mercury ODT power requirement reproduction. This gives the necessary power to create an ODT trap depth of 100 μK for mercury, for a given ODT frequency. In this case, the value ω_1 is the first atomic transition frequency of mercury.

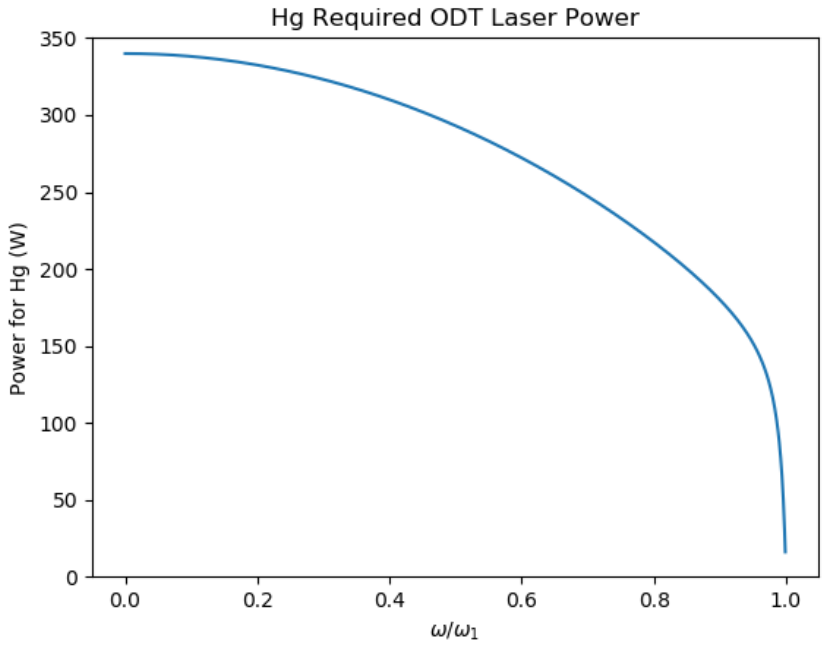

To this system, add an energy perturbation describing the AC Stark shift induced by the ODT light:

$$H'(t) = e\mathbf{E}(t) \cdot \mathbf{r} \tag{5.27}$$

where

$$\mathbf{E}(t) = \frac{E_0}{2}(\hat{\epsilon}e^{-i\omega t} + \hat{\epsilon}^* e^{i\omega t}) \tag{5.28}$$

Then, the full Hamiltonian is:

$$\hat{H} = \hat{H}_0 + \hat{H}'(t) \tag{5.29}$$

where $\hat{H}_0$ is the base Hamiltonian of the atom.

The eigenvectors of $\hat{H}_0$ are a set of orthonormal eigenvectors $|i\rangle$ with eigenvalues

$$\hat{H}_0|i\rangle = E_i|i\rangle \tag{5.30}$$

The time evolution of an atom starting in state $|i\rangle$ can be described by the following total wave function for the entire Hamiltonian:

$$\Psi_i(t) = c_i(t)|i\rangle e^{-\iota E_i \frac{t}{\hbar}} + \sum_{k\neq i} c_k(t)|k\rangle e^{-\iota E_k \frac{t}{\hbar}} \tag{5.31}$$

where at $t = 0$, $c_i(0) = 1$, $c_k(0) = 0$.

Using time-dependent perturbation theory, we start with the time-dependent Schrödinger equation

$$\hat{H}\Psi(t) = \left(\hat{H}_0 + \hat{H}'\right)\Psi(t) = \iota\hbar\frac{\partial\Psi}{\partial t} \tag{5.32}$$

Substituting in the form of $\hat{H}_0$, $\hat{H}'$ which is defined in Equation 5.27, and $\Psi(t)$ which is defined in Equation 5.31, Equation 5.32 becomes

$$\left(\hat{H}_0 + \hat{H}'\right)\Psi(t) = c_i(t)\hat{H}_0|i\rangle e^{-\iota E_i \frac{t}{\hbar}} + \sum_{k\neq i} c_k(t)\hat{H}_0|k\rangle e^{-\iota E_k \frac{t}{\hbar}} + c_i(t)\hat{H}'|i\rangle e^{-\iota E_i \frac{t}{\hbar}} + \sum_{k\neq i} c_k t\hat{H}'|k\rangle e^{-\iota E_k \frac{t}{\hbar}}$$

(5.33)

$$i\hbar\frac{\partial\Psi}{\partial t} = \iota\hbar\left(\dot{c}_i(t)|i\rangle e^{-\iota E_i \frac{t}{\hbar}} + \sum_{k\neq i}\dot{c}_k(t)|k\rangle e^{\iota E_k \frac{t}{\hbar}} + c_i(t)\frac{-\iota}{\hbar}E_i|i\rangle e^{-\iota E_i \frac{t}{\hbar}} + \sum_{k\neq i} c_k(t)\frac{-\iota}{\hbar}E_k|k\rangle e^{-\iota E_k \frac{t}{\hbar}}\right) \tag{5.34}$$

Subtracting the $\hat{H}_0$ terms in Equation 5.3.1 by the corresponding terms in Equation 5.34

gives

$$c_i(t)\hat{H'}|i\rangle e^{-\iota E_i \frac{t}{\hbar}} + \sum_{k\neq i} c_k t\hat{H'}|k\rangle e^{-\iota E_k \frac{t}{\hbar}} = \iota\hbar\dot{c}_i(t)|i\rangle e^{-\iota E_i \frac{t}{\hbar}} + \iota\hbar \sum_{k\neq i} \dot{c}_k(t)|k\rangle e^{-\iota E_k \frac{t}{\hbar}} \quad (5.35)$$

Substituting in the first order $c_i(0) = 1$, $c_k(0) = 0$:

$$\hat{H'}|i\rangle e^{-\iota E_i \frac{t}{\hbar}} = \iota\hbar\dot{c}_i(t)|i\rangle e^{-\iota E_i \frac{t}{\hbar}} + \iota\hbar \sum_{k\neq i} \dot{c}_k(t)|k\rangle e^{-\iota E_k \frac{t}{\hbar}} \quad (5.36)$$

Collapsing Equation 5.36 to the $\langle i|$ wavefunction,

$$\langle i|\hat{H'}|i\rangle e^{-\iota E_i \frac{t}{\hbar}} = \iota\hbar\dot{c}_i(t)e^{-\iota E_i \frac{t}{\hbar}} \quad (5.37)$$

Isolating the $\dot{c}_i(t)$ term in Equation 5.37,

$$\dot{c}_i(t) = \frac{\langle i|\hat{H'}|i\rangle}{\iota\hbar} \quad (5.38)$$

for $j \neq i$,

$$\langle j|\hat{H'}|i\rangle e^{-\iota E_i \frac{t}{\hbar}} = \iota\hbar\dot{c}_j e^{-\iota E_j \frac{t}{\hbar}} \quad (5.39)$$

therefore,

$$\dot{c}_j(t) = \frac{1}{\iota\hbar}\langle j|\hat{H'}|i\rangle e^{\iota(E_j - E_i)\frac{t}{\hbar}} \quad (5.40)$$

Now, Equation 5.38 can be integrated to determine $c_i(t)$. For $\hat{H'} = e\overrightarrow{E} \cdot \overrightarrow{r}$,

$$\langle i|\hat{H'}|i\rangle = 0 \quad (5.41)$$

which means that the time-derivative of $c_i(t')$ is zero,

$$\frac{dc_i(t')}{dt'} = 0 \tag{5.42}$$

$$dc_i(t') = 0 \times dt' \tag{5.43}$$

$$\int_{c_i(0)}^{c_i(t)} dc_i(t) = \int_0^t 0 dt' \tag{5.44}$$

$$c_i(t) - c_i(0) = 0 \tag{5.45}$$

which means that $c_i(t)$ is constant and is defined by the initial condition $c_i(0)$,

$$c_i(t) = c_i(0) = 1 \tag{5.46}$$

to first order. For $k \neq i$,

$$\frac{dc_k(t')}{dt'} = \frac{1}{\iota\hbar}\langle k|\hat{H}'|i\rangle e^{\iota(E_k - E_i)\frac{t'}{\hbar}} \tag{5.47}$$

$$\int_{c_k(0)}^{c_k(t)} dc_k(t') = \frac{1}{\iota\hbar}\int_0^t \langle k|\hat{H}'(t')|i\rangle e^{\iota(E_k - E_i)\frac{t'}{\hbar}} dt' \tag{5.48}$$

since $c_k(0) = 0$, integration yields

$$c_k(t) = \frac{1}{\iota\hbar}\int_0^t \langle k|\hat{H}'(t')|i\rangle e^{\iota(E_k - E_i)\frac{t'}{\hbar}} dt' \tag{5.49}$$

The $c_k(t)$ values can be substituted into Equation 5.35 to give

$$\begin{aligned}&\hat{H}'|i\rangle e^{-\iota E_i \frac{t}{\hbar}} + \sum_{k\neq i} \frac{1}{\iota\hbar} \int_0^t \langle k|\hat{H}'(t')|i\rangle e^{\iota(E_k - E_i)\frac{t'}{\hbar}} dt' \hat{H}'|k\rangle e^{-\iota E_k \frac{t}{\hbar}} \\ &= \iota\hbar \dot{c}_i(t)|i\rangle e^{-\iota E_i \frac{t}{\hbar}} + \iota\hbar \sum_{k\neq i} \dot{c}_k(t)|k\rangle e^{-\iota E_k \frac{t}{\hbar}}\end{aligned} \tag{5.50}$$

Equation 5.50 can be projected onto $\langle i|$ such that

$$\iota\hbar \dot{c}_i(t) e^{-\iota E_i \frac{t}{\hbar}} = \langle i|\hat{H}'|i\rangle e^{-\iota E_i \frac{t}{\hbar}} + \sum_{k\neq i} \frac{1}{\iota\hbar} \int_0^t \langle k|\hat{H}'(t')|i\rangle e^{\iota(E_k - E_i)\frac{t'}{\hbar}} dt' \langle i|\hat{H}'|k\rangle e^{-\iota E_k \frac{t}{\hbar}} \tag{5.51}$$

which allows for $\dot{c}_i(t)$ to be isolated,

$$\dot{c}_i(t) = \frac{\langle i|\hat{H}'|i\rangle}{\iota\hbar} + \sum_{k\neq i} \frac{-1}{\hbar^2} \int_0^t \langle k|\hat{H}'(t')|i\rangle e^{\iota(E_k - E_i)\frac{t'}{\hbar}} dt' \langle i|\hat{H}'|k\rangle e^{\iota(E_i - E_k)\frac{t}{\hbar}} \tag{5.52}$$

For $H'(t) = e\overrightarrow{E} \cdot \overrightarrow{r}$, $\langle i|H'|i\rangle = 0$ so the first term in Equation 5.52 vanishes, leaving

$$\frac{dc_i(t')}{dt'} = \sum_{k\neq i} \frac{-1}{\hbar^2} \int_0^{t'} \langle k|\hat{H}'(t")|i\rangle e^{\iota(E_k - E_i)\frac{t"}{\hbar}} dt" \langle i|\hat{H}'|k\rangle e^{\iota(E_i - E_k)\frac{t'}{\hbar}} \tag{5.53}$$

the left side can be integrated, using the initial condition $c_i(0) = 1$, allowing $c_i(t)$ to be isolated

$$\int_{c_i(0)}^{c_i(t)} dc_i = \sum_{k\neq i} \frac{-1}{\hbar^2} \int_0^t \int_0^{t'} \langle k|\hat{H}'(t")|i\rangle e^{\iota(E_k - E_i)\frac{t"}{\hbar}} dt" \langle i|\hat{H}'(t')|k\rangle e^{\iota(E_i - E_k)\frac{t'}{\hbar}} dt' \tag{5.54}$$

$$c_i(t) - 1 = \frac{-1}{\hbar^2} \sum_{k\neq i} \int_0^t \int_0^{t'} \langle k|\hat{H}'(t")|i\rangle e^{\iota(E_k - E_i)\frac{t"}{\hbar}} dt" \langle i|\hat{H}'(t')|k\rangle e^{\iota(E_i - E_k)\frac{t'}{\hbar}} dt' \tag{5.55}$$

$$c_i(t) = 1 - \frac{1}{\hbar^2} \sum_{k\neq i} \int_0^t \int_0^{t'} \langle k|\hat{H}'(t")|i\rangle e^{\iota(E_k - E_i)\frac{t"}{\hbar}} dt" \langle i|\hat{H}'(t')|k\rangle e^{\iota(E_i - E_k)\frac{t'}{\hbar}} dt' \tag{5.56}$$

Now, take a look at the actual form of $\hat{H}'(t)$:

$$\int_0^{t'} \langle k|\hat{H}'(t'')|i\rangle e^{\iota(E_k-E_i)\frac{t''}{\hbar}}dt'' = \frac{eE_0}{2}\int_0^{t'}\left(\langle k|\hat{\epsilon}e^{-\iota\omega t"}\cdot\overrightarrow{r}|i\rangle + \langle k|\hat{\epsilon}^* e^{\iota\omega t"}\cdot\overrightarrow{r}|i\rangle\right)e^{\iota(E_k-E_i)\frac{t"}{\hbar}}dt'' \tag{5.57}$$

$$= \frac{eE_0}{2}\left(\int_0^{t'}\langle k|\hat{\epsilon}\cdot\overrightarrow{r}|i\rangle e^{\iota(E_k-E_i-\omega\hbar)\frac{t''}{\hbar}}dt'' + \int_0^{t'}\langle k|\hat{\epsilon}^*\cdot\overrightarrow{r}|i\rangle e^{\iota(E_k+\omega\hbar-E_i)\frac{t''}{\hbar}}dt''\right) \tag{5.58}$$

$$= \frac{eE_0}{2}\left(\langle k|\hat{\epsilon}\cdot\overrightarrow{r}|i\rangle\frac{e^{\iota(E_k-E_i-\omega\hbar)\frac{t'}{\hbar}}-1}{\frac{\iota}{\hbar}(E_k-E_i-\omega\hbar)} + \langle k|\hat{\epsilon}^*\cdot\overrightarrow{r}|i\rangle\frac{e^{\iota(E_k-E_i+\omega\hbar)\frac{t'}{\hbar}}-1}{\frac{\iota}{\hbar}(E_k-E_i+\omega\hbar)}\right) \tag{5.59}$$

Therefore,

$$\begin{aligned} c_i(t)-1 =& \frac{-1}{\hbar^2}\sum_{k\neq i}\int_0^t \frac{eE_0}{2}\left(\langle k|\hat{\epsilon}\cdot\overrightarrow{r}|i\rangle\frac{e^{\iota(E_k-E_i-\omega\hbar)\frac{t'}{\hbar}}-1}{\frac{\iota}{\hbar}(E_k-E_i-\omega\hbar)} + \right. \\ & \left.\langle k|\hat{\epsilon}^*\cdot\overrightarrow{r}|i\rangle\frac{e^{\iota(E_k-E_i+\omega\hbar)\frac{t'}{\hbar}}-1}{\frac{\iota}{\hbar}(E_k-E_i+\omega\hbar)}\right) \\ & \times\frac{eE_0}{2}\left(\langle i|\hat{\epsilon}\cdot\overrightarrow{r}|k\rangle e^{\iota(E_i-E_k-\omega\hbar)\frac{t'}{\hbar}} + \right. \\ & \left.\langle i|\hat{\epsilon}^*\cdot\overrightarrow{r}|k\rangle e^{\iota(E_i+\omega\hbar-E_k)\frac{t'}{\hbar}}\right)dt' \end{aligned} \tag{5.60}$$

$$
\begin{aligned}
c_i(t) = 1 - \frac{e^2 E_0^2}{4\hbar^2} \int_0^t \Bigg(& \langle k|\hat{\epsilon}\cdot\overrightarrow{r}|i\rangle\langle i|\hat{\epsilon}\cdot\overrightarrow{r}|k\rangle \frac{e^{-2\iota\omega t'} - e^{\iota(E_i - E_k - \omega\hbar)\frac{t'}{\hbar}}}{\frac{\iota}{\hbar}(E_k - E_i - \omega\hbar)} \\
& + \langle k|\hat{\epsilon}\cdot\overrightarrow{r}|i\rangle\langle i|\hat{\epsilon}^*\cdot\overrightarrow{r}|k\rangle \frac{1 - e^{\iota(E_i + \omega\hbar - E_k)\frac{t'}{\hbar}}}{\frac{\iota}{\hbar}(E_k - E_i - \omega\hbar)} \\
& + \langle k|\hat{\epsilon}^*\cdot\overrightarrow{r}|i\rangle\langle i|\hat{\epsilon}\cdot\overrightarrow{r}|k\rangle \frac{1 - e^{\iota(E_i - \omega\hbar - E_k)\frac{t'}{\hbar}}}{\frac{\iota}{\hbar}(E_k - E_i + \omega\hbar)} \\
& + \langle k|\hat{\epsilon}^*\cdot\overrightarrow{r}|i\rangle\langle i|\hat{\epsilon}^*\cdot\overrightarrow{r}|k\rangle \frac{e^{2\iota\omega t'} - e^{\iota(E_i + \omega\hbar - E_k)\frac{t'}{\hbar}}}{\frac{\iota}{\hbar}(E_k - E_i + \omega\hbar)} \Bigg) dt'
\end{aligned}
\tag{5.61}
$$

Now consider what exactly is ΔE:

$$
\Delta E = \langle \Psi_i|\hat{H} - \hat{H}_0|\Psi\rangle = \langle i|\hat{H}|\Psi_i\rangle - \langle i|\hat{H}_0|\Psi\rangle \tag{5.62}
$$

$$
\begin{aligned}
\hat{H}|\Psi\rangle = \iota\hbar\frac{\partial\Psi}{\partial t} = {} & \iota\hbar\dot{c}_i(t)|i\rangle e^{-\iota E_i\frac{t}{\hbar}} + c_i(t)E_i|i\rangle e^{-\iota E_i\frac{t}{\hbar}} \\
& + \sum_{k\neq i} \iota\hbar\dot{c}_k(t)|k\rangle e^{-\iota E_k\frac{t}{\hbar}} + c_k(t)E_k|k\rangle e^{-\iota E_k\frac{t}{\hbar}}
\end{aligned}
\tag{5.63}
$$

since

$$
\hat{H}_0|\Psi\rangle = c_i(t)E_i|i\rangle e^{-\iota E_i\frac{t}{\hbar}} + c_k(t)E_k|k\rangle e^{-\iota E_k\frac{t}{\hbar}} \tag{5.64}
$$

this means

$$
(\hat{H} - \hat{H}_0)|\Psi\rangle = \iota\hbar(\dot{c}_i(t)|i\rangle e^{-\iota E_i\frac{t}{\hbar}} + \sum_{k\neq i}\dot{c}_k(t)|k\rangle e^{-\iota E_k\frac{t}{\hbar}}) \tag{5.65}
$$

thus,

$$
\langle \Psi_i|\hat{H} - \hat{H}_0|\Psi\rangle = e^{\iota E_i\frac{t}{\hbar}}\langle i|\iota\hbar\dot{c}_i(t)|i\rangle e^{-\iota E_i\frac{t}{\hbar}} = \iota\hbar\dot{c}_i(t) \tag{5.66}
$$

using the 2nd fundamental theorem of calculus,

$$\begin{aligned}\Delta E = \iota\hbar\frac{-1}{\hbar^2}\sum_{k\neq i}\frac{e^2E_0^2}{4}\Bigg(&\langle k|\hat{\epsilon}\cdot\overrightarrow{r}|i\rangle\langle i|\hat{\epsilon}\cdot\overrightarrow{r}|k\rangle\frac{e^{-2\iota\omega t}-e^{\iota(E_i-E_k-\omega\hbar)\frac{t}{\hbar}}}{\frac{\iota}{\hbar}(E_k-E_i-\omega\hbar)}\\&+\langle k|\hat{\epsilon}\cdot\overrightarrow{r}|i\rangle\langle i|\hat{\epsilon}^*\cdot\overrightarrow{r}|k\rangle\frac{1-e^{\iota(E_i+\omega\hbar-E_k)\frac{t}{\hbar}}}{\frac{\iota}{\hbar}(E_k-E_i-\omega\hbar)}\\&+\langle k|\hat{\epsilon}^*\cdot\overrightarrow{r}|i\rangle\langle i|\hat{\epsilon}\cdot\overrightarrow{r}|k\rangle\frac{1-e^{\iota(E_i-\omega\hbar-E_k)\frac{t}{\hbar}}}{\frac{\iota}{\hbar}(E_k-E_i+\omega\hbar)}\\&+\langle k|\hat{\epsilon}^*\cdot\overrightarrow{r}|i\rangle\langle i|\hat{\epsilon}^*\cdot\overrightarrow{r}|k\rangle\frac{e^{2\iota\omega t}-e^{\iota(E_i+\omega\hbar-E_k)\frac{t}{\hbar}}}{\frac{\iota}{\hbar}(E_k-E_i+\omega\hbar)}\Bigg)\end{aligned} \tag{5.67}$$

Anything of the form $e^{\iota\omega t}$ time averages out to zero. So,

$$\Delta E = \iota\hbar\frac{-1}{\hbar^2}\sum_{k\neq i}\frac{e^2E_0^2}{4}\frac{\hbar}{\iota}\left(\frac{\langle k|\hat{\epsilon}\cdot\overrightarrow{r}|i\rangle\langle i|\hat{\epsilon}^*\cdot\overrightarrow{r}|k\rangle}{E_k-E_i-\omega\hbar}+\frac{\langle k|\hat{\epsilon}^*\cdot\overrightarrow{r}|i\rangle\langle i|\hat{\epsilon}\cdot\overrightarrow{r}|k\rangle}{E_k-E_i+\omega\hbar}\right) \tag{5.68}$$

Thus,

$$\Delta E = -\frac{e^2E_0^2}{4\hbar}\sum_{k\neq i}\left(\frac{\langle k|\hat{\epsilon}\cdot\overrightarrow{r}|i\rangle\langle i|\hat{\epsilon}^*\cdot\overrightarrow{r}|k\rangle}{\omega_{ki}-\omega}+\frac{\langle k|\hat{\epsilon}^*\cdot\overrightarrow{r}|i\rangle\langle i|\hat{\epsilon}\cdot\overrightarrow{r}|k\rangle}{\omega_{ki}+\omega}\right) \tag{5.69}$$

where $\omega_{ki}=\frac{E_k-E_i}{\hbar}$. Note that this is the same as equation 11 given in Ref. [48] for the energy shift.

5.3.2 Calculation of Vector Shift for Cs-133

In order actually get numeric values for the energy shift, the expression

$$\begin{aligned}\Delta E = \frac{-e^2E_0^2}{4\hbar}\sum_{J',F',m'}\Bigg[&\frac{\langle J',I,F',M'|\epsilon\cdot r|J,I,F,M\rangle\langle J,I,F,M|\epsilon^*\cdot r|J',I,F',M'\rangle}{\omega_{J'}-\omega}\\&+\frac{\langle J',I,F',M'|\epsilon^*\cdot r|J,I,F,M\rangle\langle J,I,F,M|\epsilon\cdot r|J',I,F',M'\rangle}{\omega_{J'}+\omega}\Bigg]\end{aligned} \tag{5.70}$$

needs to be put in a form that makes sense to a computer.

This can be done using the formalism of spherical tensors, giving

$$\begin{aligned}\langle J', I, F', M'|\epsilon \cdot r|J, I, F, M\rangle &= \sum_{\rho}(-1)^{\rho+F'-M'+J'+I+F+1} \\ &\times \epsilon_{\rho}\langle J'||r||J\rangle\sqrt{(2F+1)(2F'+1)}\begin{pmatrix} F' & 1 & F \\ -M' & -\rho & M\end{pmatrix}\begin{Bmatrix} J' & F' & I \\ F & J & 1\end{Bmatrix}\end{aligned} \tag{5.71}$$

So,

$$\begin{aligned}&\langle J', I, F', M'|\epsilon \cdot r|J, I, F, M\rangle\langle J, I, F, M|\epsilon^* \cdot r|J', I, F', M'\rangle \\ &= (2F+1)(2F'+1)\langle J'||r||J\rangle\langle J||r||J'\rangle\begin{Bmatrix} J' & F' & I \\ F & J & 1\end{Bmatrix}\begin{Bmatrix} J & F & I \\ F' & J' & 1\end{Bmatrix} \\ &\times \Sigma_{\rho,\rho'}(-1)^{\rho+\rho'+2F'+2F-M'-M+J'+J+2I+2}\epsilon_{\rho}\epsilon^*_{\rho'} \\ &\times \begin{pmatrix} F' & 1 & F \\ -M' & -\rho & M\end{pmatrix}\begin{pmatrix} F & 1 & F' \\ -M & -\rho' & M'\end{pmatrix}\end{aligned} \tag{5.72}$$

Note: Both $\begin{pmatrix} F' & 1 & F \\ -M' & -\rho & M\end{pmatrix}$ and $\begin{pmatrix} F & 1 & F' \\ -M & -\rho' & M'\end{pmatrix}$ have to be nonzero to contribute to the sum. By the rules of Wigner 3J symbols,

$$-M' - \rho + M = 0 \tag{5.73}$$

and

$$-M - \rho' + M' = 0 \tag{5.74}$$

Therefore,

$$\rho = M - M' = -\rho' \tag{5.75}$$

Furthermore, by the triangle inequality rules, $\rho = 0, \pm 1$. Therefore, $M' = M - 1, M, M + 1$ if the term is to be nonzero.

Now, consider the epsilons:

$$\hat{\epsilon} = \epsilon_L \frac{-\hat{x} - \iota\hat{y}}{\sqrt{2}} + \epsilon_R \frac{\hat{x} - \iota\hat{y}}{\sqrt{2}} \tag{5.76}$$

Thus,

$$\hat{\epsilon} = \epsilon_L \hat{e}_{+1} + \epsilon_R \hat{e}_{-1} \tag{5.77}$$

and,

$$\hat{\epsilon}^* = -\epsilon_R \hat{e}_{+1} - \epsilon_L \hat{e}_{-1} \tag{5.78}$$

So, Therefore, the term is also zero for $\rho = 0$. Thus, the two M' needed to be summed over

Table 5.2: Values of circular polarizations.

$\epsilon_{+1} = \epsilon_L$	$\epsilon^*_{+1} = -\epsilon_R$
$\epsilon_0 = 0$	$\epsilon^*_0 = 0$
$\epsilon_{-1} = \epsilon_R$	$\epsilon^*_{-1} = -\epsilon_L$

are $M + 1, M - 1$

Consider now

$$
\begin{aligned}
&\Sigma_{J',F',M'}\langle J',I,F',M'|\epsilon\cdot r|J,I,F,M\rangle\langle J,I,F,M|\epsilon^*\cdot r|J',I,F',M'\rangle \\
&=\Sigma_{J',F'}(2F+1)(2F'+1)\langle J'||r||J\rangle\langle J||r||J'\rangle \begin{Bmatrix} J' & F' & I \\ F & J & 1 \end{Bmatrix}\begin{Bmatrix} J & F & I \\ F' & J' & 1 \end{Bmatrix} \\
&\times\Sigma_{M'=M\pm1}(-1)^{2F'+2F-M'-M+J'+J+2I+2}\epsilon_{M-M'}\epsilon^*_{M'-M} \\
&\times\begin{pmatrix} F' & 1 & F \\ -M' & M'-M & M \end{pmatrix}\begin{pmatrix} F & 1 & F' \\ -M & M-M' & M' \end{pmatrix}
\end{aligned}
\tag{5.79}
$$

Note: by the rules of wigner 3J symbols,

$$
\begin{aligned}
&\begin{pmatrix} F & 1 & F' \\ -M & M-M' & M' \end{pmatrix} \\
&=(-1)^{F+F'+1}\begin{pmatrix} F' & 1 & F \\ M' & M-M' & -M \end{pmatrix}=(-1)^{2(F+F')}\begin{pmatrix} F' & 1 & F \\ -M' & M'-M & M \end{pmatrix}
\end{aligned}
\tag{5.80}
$$

Therefore,

$$
\begin{aligned}
&\Sigma_{J',F',M'}\langle J',I,F',M'|\epsilon\cdot r|J,I,F,M\rangle\langle J,I,F,M|\epsilon^*\cdot r|J',I,F',M'\rangle \\
&=\Sigma_{J',F'}(2F+1)(2F'+1)\langle J'||r||J\rangle\langle J||r||J'\rangle \begin{Bmatrix} J' & F' & I \\ F & J & 1 \end{Bmatrix}\begin{Bmatrix} J & F & I \\ F' & J' & 1 \end{Bmatrix} \\
&\times\Sigma_{M'=M\pm1}(-1)^{4F'+4F-M'-M+J'+J+2I+2}\epsilon_{M-M'}\epsilon^*_{M'-M}\begin{pmatrix} F' & 1 & F \\ -M' & M'-M & M \end{pmatrix}^2
\end{aligned}
\tag{5.81}
$$

Furthermore,

$$\langle J||r||J'\rangle = (-1)^{J-J'}\langle J'||r||J\rangle^* \tag{5.82}$$

and, by the rules of Wigner 6-j symbols,

$$\begin{Bmatrix} J' & F' & I \\ F & J & 1 \end{Bmatrix} = \begin{Bmatrix} F & J & I \\ J' & F' & 1 \end{Bmatrix} = \begin{Bmatrix} J & F & I \\ F' & J' & 1 \end{Bmatrix} \tag{5.83}$$

So,

$$\begin{aligned} &\Sigma_{J',F',M'}\langle J', I, F', M'|\epsilon\cdot r|J, I, F, M\rangle\langle J, I, F, M|\epsilon^*\cdot r|J', I, F', M'\rangle \\ &= \Sigma_{J',F'}(2F+1)(2F'+1)(-1)^{J-J'}|\langle J'||r||J\rangle|^2 \begin{Bmatrix} J' & F' & I \\ F & J & 1 \end{Bmatrix}^2 \\ &\times \Sigma_{M'=M\pm1}(-1)^{4F'+4F-M'-M+J'+J+2I+2}\epsilon_{M-M'}\epsilon^*_{M'-M} \begin{pmatrix} F' & 1 & F \\ -M' & M'-M & M \end{pmatrix}^2 \end{aligned} \tag{5.84}$$

Now,

$$|\langle J'||r||J\rangle|^2 = \frac{3\hbar(2J+1)}{2m\omega_{JJ'}} f_{JJ'} \tag{5.85}$$

where $f_{JJ'}$ is the oscillator strength

Therefore,

$$\sum_{J',F',M'} \langle J', I, F', M'|\epsilon \cdot r|J, I, F, M\rangle\langle J, I, F, M|\epsilon^* \cdot r|J', I, F', M'\rangle$$

$$= \sum_{J',F'} (2F+1)(2F'+1)(-1)^{J-J'} \frac{3\hbar(2J+1)f_{JJ'}}{2m\omega_{JJ'}} \begin{Bmatrix} J' & F' & I \\ F & J & 1 \end{Bmatrix}^2 \times \tag{5.86}$$

$$\sum_{M'=M\pm1} (-1)^{4F'+4F-M'-M+J'+J+2I+2} \epsilon_{M-M'} \epsilon^*_{M'-M} \begin{pmatrix} F' & 1 & F \\ -M' & M'-M & M \end{pmatrix}^2$$

Likewise,

$$\sum_{J',F',M'} \langle J', I, F', M'|\epsilon^* \cdot r|J, I, F, M\rangle\langle J, I, F, M|\epsilon \cdot r|J', I, F', M'\rangle$$

$$= \sum_{J',F'} (2F+1)(2F'+1)(-1)^{J-J'} \frac{3\hbar(2J+1)f_{JJ'}}{2m\omega_{JJ'}} \begin{Bmatrix} J' & F' & I \\ F & J & 1 \end{Bmatrix}^2 \times \tag{5.87}$$

$$\sum_{M'=M\pm1} (-1)^{4F'+4F-M'-M+J'+J+2I+2} \epsilon^*_{M-M'} \epsilon_{M'-M} \begin{pmatrix} F' & 1 & F \\ -M' & M'-M & M \end{pmatrix}^2$$

Figure 5.6: ODT energy level shift due to both the scalar and vector shift reproduced using Equation 5.88.

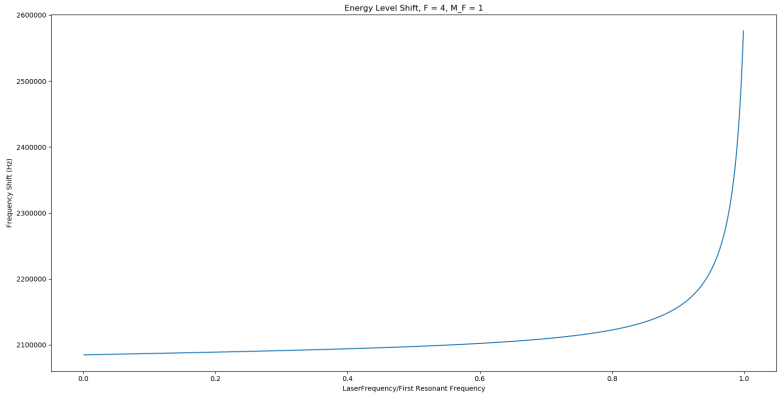

Therefore,

$$\Delta E = \frac{-e^2 E_0^2}{4\hbar} \sum_{J',F'} [(2F+1)(2F'+1)(-1)^{J-J'} \frac{3\hbar(2J+1)f_{JJ'}}{2m\omega_{JJ'}(\omega_{JJ'}-\omega)} \begin{Bmatrix} J' & F' & I \\ F & J & 1 \end{Bmatrix}^2 \times$$
$$\sum_{M'=M\pm1} (-1)^{4F'+4F-M'-M+J'+J+2I+2} \epsilon_{M-M'} \epsilon^*_{M'-M} \begin{pmatrix} F' & 1 & F \\ -M' & M'-M & M \end{pmatrix}^2 +$$
$$(2F+1)(2F'+1)(-1)^{J-J'} \frac{3\hbar(2J+1)f_{JJ'}}{2m\omega_{JJ'}(\omega_{JJ'}+\omega)} \begin{Bmatrix} J' & F' & I \\ F & J & 1 \end{Bmatrix}^2 \times$$
$$\sum_{M'=M\pm1} (-1)^{4F'+4F-M'-M+J'+J+2I+2} \epsilon^*_{M-M'} \epsilon_{M'-M} \begin{pmatrix} F' & 1 & F \\ -M' & M'-M & M \end{pmatrix}^2] \tag{5.88}$$

Using Equation 5.88, the shift in energy levels can be found as shown in Figure 5.6

This shift includes an M_f independent scalar shift, as well as a linearly M_f dependent

Figure 5.7: ODT energy level vector shift for Cs-133.

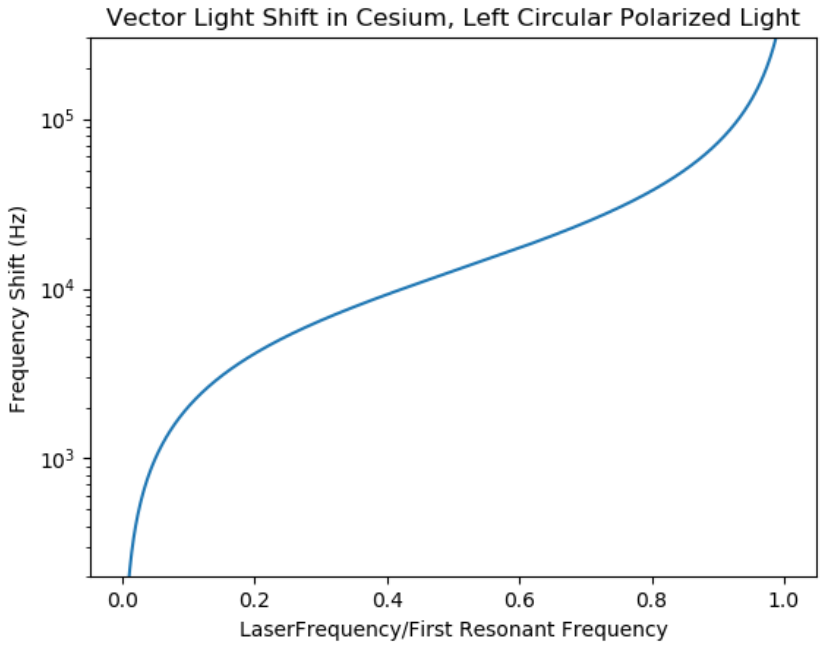

vector shift. Using this calculation, a reproduction of figure 4 in Ref. [48] was successfully made, and can be seen in Figure 5.7.

the ΔE is the shift in energy for a single ground state - that is to say, it has a specific F and m_F dependence. There is both a scalar shift, and a vector shift that results from this calculation - the scalar shift is the same for all the the m_F sublevels, while the vector shift goes linearly with m_F. The dependence on this is given in the Ref. [48] by equation 14:

$$\Delta\nu_{F=I\pm1/2} = \pm\nu_V(\omega)(|\epsilon_L|^2 - |\epsilon_R|^2)m_F cos\theta \tag{5.89}$$

the $cos\theta$ term is dependent upon θ, which is the angle between the ODT trap propagation and the spin quantization axis. It is assumed to be 0 for the purposes of calculating the frequency dependence $\nu_V(\omega)$. By having the trap and spin quantization perpendicular,

as is done in the RaEDM experiment, the total vector shift can be minimized. The m_F dependence is linear. The dependence on F flips the sign of the change in energy, so the energy gets positive with negative m_F values, and vice versa. It has no bearing on the magnitude of the vector shift. The polarization dependence is given in the term $|\epsilon_L|^2 - |\epsilon_R|^2$. This means that the shift is maximized when the polarization is completely circularly polarized, and that flipping the direction of circular polarization flips the sign of the vector shift as well. In addition, it also suggests that the vector shift should be minimized when the ODT is linearly polarized: when both $|\epsilon_L|^2$ and $|\epsilon_R|^2$ are equal to $\frac{\sqrt{2}}{2}$. Finally, there is the dependnce on ω, which is the actual quantity plotted. In order to get this, the scalar shift has to be subtracted out. The easiest way to do this is to subtract out the term wtih $m_F = 0$:

$$\Delta\nu_{F=I\pm1/2,m_F} = \Delta E(F, m_F) - \Delta E(F, 0) \tag{5.90}$$

The accuracy of this calculation can be tested by testing the dependence of the vector shift on each of these variables.

Consider the m_F dependence. Here is a plot of the vector shift of the m_F sublevels for F = 4:

The vector shift here is linear with m_F - at each ω, each m_F level is separated by the same amount. Further more, the m_F levels go in order, from -4 to +4.

Now, consider F = 3 :

The plot is the same, with one notable exception: instead of going from -3 to +3, it goes from +3 to -3. This is expected, as the change in F is supposed to change the sign of the vector shift.

Finally, consider the polarization dependence. Fix $\frac{\omega}{\omega_1} = .501$, and vary $\epsilon_L = \sqrt{1 - |\epsilon_R|^2}$

Figure 5.8: Vector shift dependence on M_F sublevel for F = 4.

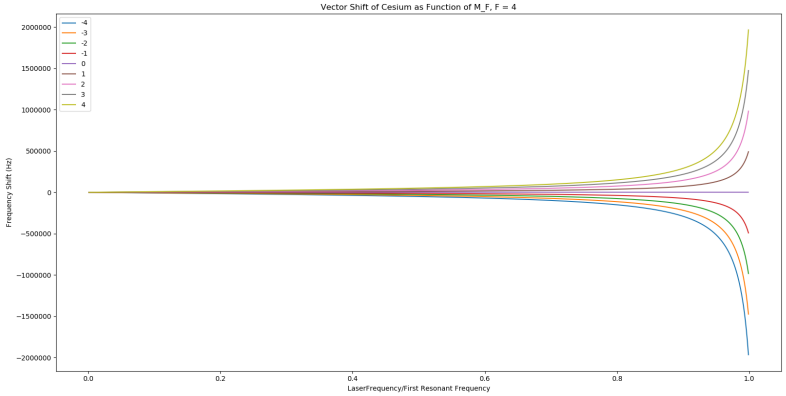

Figure 5.9: Vector shift dependence on M_F sublevel for F = 3.

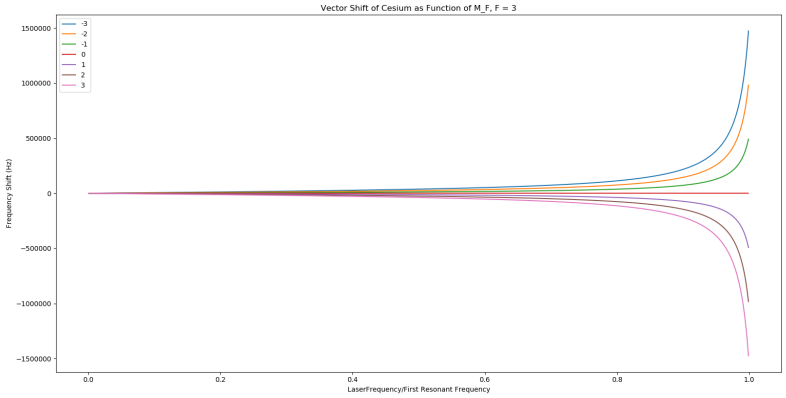

Figure 5.10: Vector shift dependence on ϵ_L.

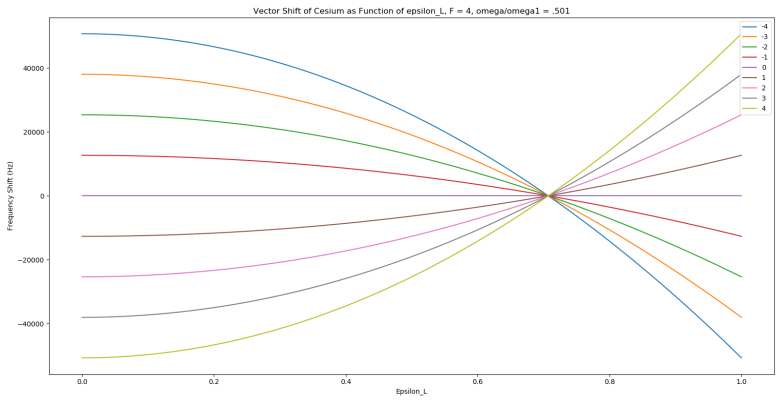

from 0 to 1:

Once again, the correct behavior is observed. The shift is minimized at $\frac{\sqrt{2}}{2}$.

Another test that can be done is to compare to a known value given by Ref. [48]. This paper calculates the vector shift at $\lambda = 10\mu m$ to be $\Delta\nu = m \times 170\mu Hz$. Note that this is after a 7 order of magnitude deduction that it makes, with 3 orders of magnitude from minimizing circular polarization, and 3 orders of magnitude by making θ as close to $\frac{\pi}{2}$ as possible. The code used to reproduce these plots returns a value of 1806 Hz, which after a 7 order of magnitude reduction, gives $\approx 181\mu Hz$. So, there is a slight discrepancy here, though it is only 6% higher. Considering that this paper was published in 1999, questions arise if there were issues with the precision of the computers available at the time.

It's important to make clear the dependence on the hyperfine structure: the hyperfine structure is included in the angular momentum coupling. However, it is not included in any correction to the energy level $\omega_{J'J}$ as a function of F. The same energy value is used for all the F' levels for the excited state. Considering the hyperfine structure contribution is much smaller than the overall energy level, this is an acceptable approximation to make. It will

Figure 5.11: ODT energy level vector shift for Hg-199.

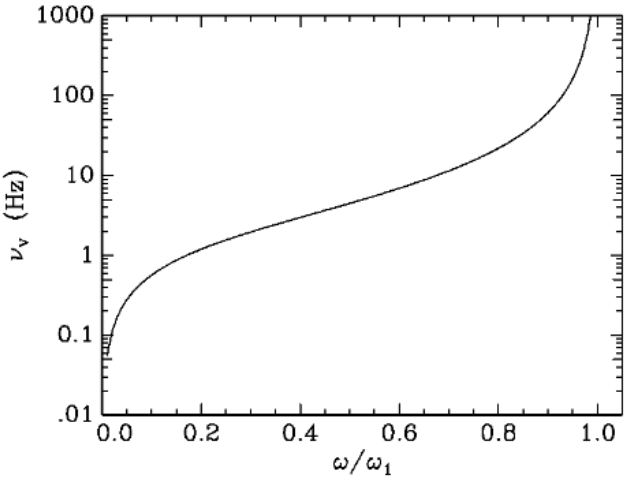

not be, however, for the mercury vector shift, since making this approximation results in the vector shift being identically zero. It is necessary to include the splitting of the hyperfine levels in the terms $\omega_{J'J}$.

5.3.3 Ongoing Efforts to Caculate the Vector Shift for Hg-199

In Ref. [48], the vector shift for Hg-199 is also calculated, and its plot can be seen in Figure 5.11.

With the vector shift for Cs-133 successfully reproduced, the next step is to modify the calculation to account for two valence electrons, instead of one. Thankfully, Ref. [48] also contains a vector shift calculation for Hg-199, which has two valence electrons. Once this calculation can also be reproduced, it should be a simple matter to modify the code to work with Radium-225. As such, attempts to reproduce Figure 5.11 are ongoing. Simply swapping the values of the energy levels from Cs-133 to Hg-199 creates a plot that is non-monotonic, as can be seen in Figure 5.12.

Figure 5.12: First attempt to reproduce Hg-199 vector shift.

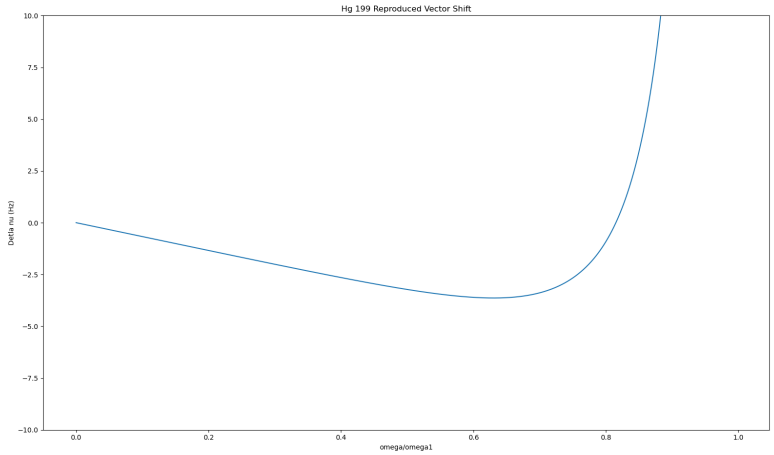

This plot is clearly in discrepancy with Ref. [48], since it crosses zero. This recent calculation seems to line up with other code previously used by the Radium team, which is available. This code seems to also have found a crossing at zero, which lines up very closely with the more recent code. Its plot can be seen in Figure 5.13.

Figure 5.13: Previous RaEDM calculation of Hg-199 vector shift.

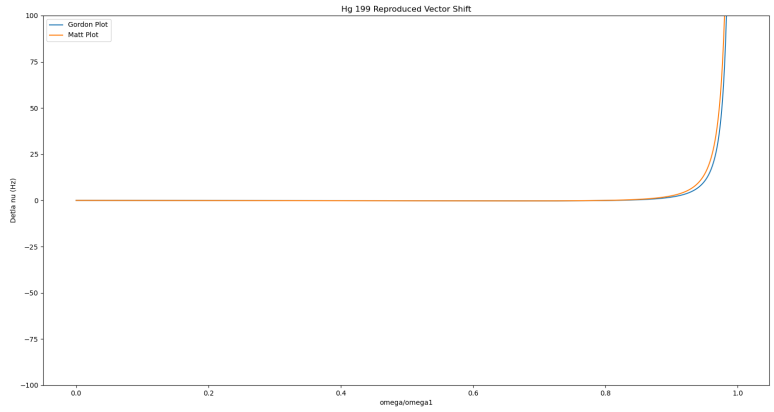

There were concerns about whether or not significant alterations had to be made to the form of the formula, due to the fact that there are two valence electrons instead of 1 - For

instance, the energy perturbation that results in the vector shift for cesium is of the form

$$H' = e\mathbf{E} \cdot \mathbf{r} \tag{5.91}$$

where r is the position of the valence electron. Was this form also good for two valence electrons, or would $\mathbf{r}$ have to be replaced with $\mathbf{r_1}$? What would that do to the $|\langle J'||r||J\rangle|^2$ term? Would each J have to be written as the sum of a j_1 and j_2?

It was concluded that this was not necessary, due to equation 9.188 in Sobelman. This equation reads

$$-\frac{2m}{3\hbar}\sum_{\gamma',J'}\omega(\gamma J;\gamma',J')\sum_{M'}|\langle\gamma JM|\sum_{j}\mathbf{r_j}|\gamma' J'M'\rangle|^2 = Z \tag{5.92}$$

where $\sum_j \mathbf{r_j}$ is the sum over all electrons in the system. The book then compares this with equation 9.48, which gives the definition for the oscillator strength:

$$-f(\gamma J;\gamma' J') = \frac{2m}{3\hbar e^2}\frac{\omega_{\gamma J,\gamma' J'}}{2J+1}\sum_{MM'}|\langle\gamma JM|\mathbf{D}|\gamma' J'M'\rangle|^2 \tag{5.93}$$

From this equation, it was unclear whether this definition only applies for hydrogen-like atoms. Thankfully, after equation 9.188, it writes:

$$-\frac{2m}{3\hbar}\frac{1}{(2J+1)}\sum_{\gamma',J'}\omega(\gamma J;\gamma' J')\sum_{MM'}|\langle\gamma JM|\sum_{i}\mathbf{r_i}|\gamma' J'M'\rangle|^2 = \sum_{\gamma' J'}f(\gamma J;\gamma' J') \tag{5.94}$$

This seems to suggest that, individually, even for a multi-electron atom, each oscillator

strength $f(\gamma J;\gamma' J')$ is given by

$$f(\gamma J;\gamma' J') = -\frac{2m}{3\hbar}\frac{1}{(2J+1)}\omega(\gamma J;\gamma' J')\sum_{MM'}|\langle\gamma JM|\sum_i \mathbf{r_i}|\gamma' J' M'\rangle|^2 \tag{5.95}$$

In other words, the oscillator strength isn't somehow broken up into the contributions from individual electrons, but instead encompasses the information from all electrons as a whole. This means that the formula

$$|\langle J'||r||J\rangle|^2 = \frac{3\hbar(2J+1)}{2m\omega_{JJ'}}f_{JJ'} \tag{5.96}$$

is used in the same way for Hg as for Cs.

5.3.4 Future Work

Further work is needed on these calculations, in a variety of ways.

1. The mercury-199 calculation needs to be fixed, to make sure that it aligns with previous results. Once fixed, it should be straightforward to plug in values for radium-225.

2. Work needs to be done characterizing the stark shift, which is paritcularly dangerous for false EDM effects.

Chapter 6. Electric Field Upgrades

A key part of the radium-EDM experiment is the static electric field used to cause a frequency shift due to a non-zero EDM. The electric field has to be as strong as possible, while also having as little leakage current as possible, with discharges being rare. It must also have a very uniform electric field that can be reversed. Looking at the sensitivity equation

$$\delta d = \frac{\hbar}{2E\sqrt{NT\tau\epsilon}} \tag{6.1}$$

it can be seen that the most effective way to decrease uncertainty in d is to increase the electric field, since there is a 1-to-1 correlation in orders of magnitude. Unfortunately, increasing the electric field is more difficult than might seem. In addition to more frequent electrode discharges, all the equipment used in the High Voltage (HV) switching system must be rated to the required voltage. Efforts are underway to increase the electric field for the next radium-225 data run, through electrode conditioning and an upgraded HV switching system. This switching system will also improve reversibility of the electric field.

6.1 Setup from Previous Radium-225 Runs

The RaEDM experiment requires a stable magnetic field for Larmor spin precession. This can be disturbed by magnetic field caused by leakage currents. The leakage can come from two sources: Extremely small currents that travel through the ceramic mounting for the electrodes, and from discharges between the electrodes created by microscopic defects and irregularities on the electrode surface. This was measured at the experimental setup at

Argonne National Laboratory (ANL) using a Macor support structure, and button-shaped copper electrodes of dimensions shown in Figure 6.1.

Figure 6.1: Dimensions for copper electrodes used in 2016 EDM measurement. All units in mm.

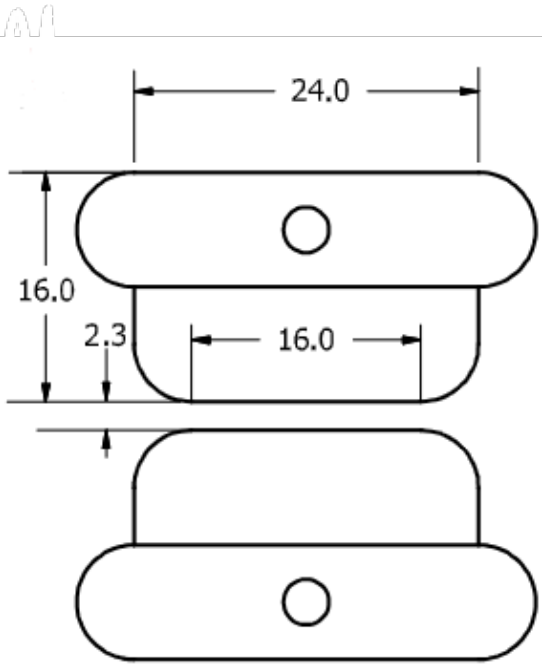

Correct field alignment and direction is absolutely critical to this experiment. "To avoid systematic effects at [the 10^{-26} $e \cdot \text{cm}$] level, we must align our fields to within 0.002 radians of their design orientations" [21]. Many of the systematic effects that are present in this experiment can be suppressed by precise field alignment. This can be seen, for instance, in the stark interference effect detailed in Chapter 5. This systematic effect is proportional to $\hat{b} \cdot \hat{\sigma}$ and $\hat{b} \cdot \hat{\epsilon}_s$, where $\hat{b}$ is the direction of the ODT magnetic field, $\hat{\sigma}$ is the direction of spin quantization, and $\hat{\epsilon}_s$ is the direction of the static electric field. If the spin quantization axis and static electric field are perfectly parallel, and $\hat{b}$ perfectly perpendicular to both, then this systematic has no effect. However, in the real world, the orientations of these angles can only be guaranteed to within certain tolerances. To characterize the orientations of these fields,

an NIST-traceable digital level with 350 μrad absolute accuracy was used. In addition, the ceramic Macor holder holding the electrodes also serves as an extreme electrical insulator. For the duration of the data run, a Picoammeter was used to monitor the leakage current flowing across the electrodes and Macor holder. This leakage current was characterized to a 1σ accuracy as being less than 2 pA. The smaller this leakage current is, the smaller the resulting systematic effect is. Care also needs to be taken to minimize the frequency of discharges between the electrodes, as electrons moving from one electrode to the other generates a current. This sudden current generates an electric field correlated magnetic field, which greatly disturbs the experiment.

6.2 Electrode Conditioning for Higher Electric Field Generation

The next RaEDM run is attempting an improvement in sensitivity of 3 orders of magnitude. In previous data runs, the electric field was provided by a pair of copper electrodes, held 2.3 $\pm$ .1 mm apart. The bottom electrode was permanently grounded, and the top connected to a bipolar power supply. A $\pm$ 15.5 kV voltage was applied to the top electrode, generating a $\pm$ 67 kV/cm electric field. The whole apparatus was in vacuum. For future data runs, fields on the order of hundreds of kV/cm are desired. Realizing this improvement in electric field requires solving difficult problems. During the spin precession measurement, it is vital that leakage current be kept to a minimum, and that sudden discharges between the electrodes be avoided. If a discharge occurs during a spin precession measurement, the data taken during that measurement cannot be used. Furthermore, as the electric field is increased, these discharges become more frequent. If upcoming RaEDM data runs are to use higher

electric fields, something must be done to reduce the frequency of these discharges. The solution is electrode conditioning.

6.2.1 Electrode Processing Techniques

The discharges seen between the electrodes are caused by microscopic imperfections on the electrode surface. To reduce these defects, a wide variety of cleaning, polishing, and conditioning techniques were performed. Other materials, such as titanium and niobium, were tried. Magnetic Johnson noise and hardness are the important consideration to take into account when selecting the material to use, as well as previous documentation of their electric field stability. Surface processing techniques included buffered chemical polishing, silicon carbide machine polishing, ultrasonic rinses, and high pressure rinses. From there, they were installed in a HV conditioning apparatus under clean room conditions. A summary of the various techniques utilized is given in Table 6.1.

Table 6.1: Surface processing of various HV electrodes. Guide: OF = Oxygen Free. G2 = Grade-2. Simichrome Polish by Hand. DPP = Diamond Paste Polish by Hand. LPR = Low Pressure Rinse. HPR = High Pressure Rinse. HF = Hydrofluoric Chemical Polish. EP = Electropolish. BCP = Buffered Chemical Polish. SiC = Silicon Carbide Machine Polish. CSS = Colloidal Silica Suspension Machine Polish. VB = 420 - 450 C Vacuum Outgas Bake. WB=150-160 C Water Bake. USR = Ultrasonic Rinse after Detergent Bath.

Material	Pair	Surface Processing
OF Copper	Cu_{12}	Simichrome → EP → USR → WB
LG Niobium	Nb_{14}	SiC → BCP → DPP → CSS → USR → VB → LPR → HPR
LG Niobium	Nb_{23}	SiC → BCP → USR → VB v HPR → Resurface BCP → HPR
G2 Titanium	Ti_{24}	SiC → HF → USR → VB → HPR
G2 Titanium	Ti_{13}	SiC → HF → EP → USR → VB → HPR
LG Niobium	Nb_{56}	SiC → BCP → USR → HPR → WB
LG Niobium	Nb_{78}	SiC → BCP → USR → HPR

Of these, pair Cu_{12} was used in the first RaEDM data runs. The Nb_{56} pair is currently installed in the apparatus at ANL. The conditioning process will now be described.

6.2.2 Electrode Conditioning Procedure

Electrode conditioning was done by holding the electrodes at high voltage for long periods of time, with the belief that over hours of time the rate of discharges would decrease. The apparatus used to do this can be seen in Figure 6.2, taken from [40]

Figure 6.2: MSU HV test apparatus. 1) 9699334 Agilent Turbo-V vibration damper 2) Pfeiffer HiPace 80 turbomolecular pump with foreline Edwards nXDS10i A736-01-983 dry scroll rough pump and two valves 3) Matheson 6190 Series 0.01 micron membrane filter and purge port 4) Ceramtec 30 kV 16729-03-CF HV feedthroughs 5) 0.312 in. 2 electrodes in PEEK holder (resistivity 1016 M cm) 6) 20 AWG Kapton-insulated, gold-plated copper wire 7 MKS 392502-2-YG-T all-range conductron/ion gauge 8) Shielded protection circuit: Littelfuse SA5.0A transient voltage suppressor, EPCOS EX-75X gas discharge tube, Ohmite 90J100E 100 resistor in series with Keithley 6482 2-channel picoammeter 9) Ohmite MOX94021006FVE 100 M resistors in series with Applied Kilovolts HP030RIP020 HV.

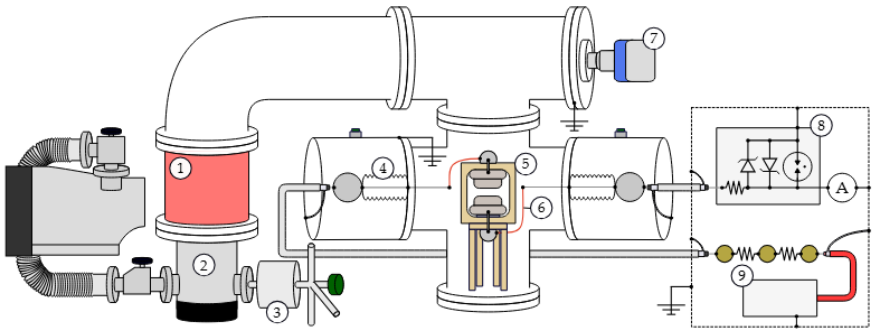

The electrode stand at MSU utilizes the material PEEK, and not Macor. Similar to the design at ANL, the top electrode is permanently affixed to a high voltage power supply, and the bottom is permanently held at ground. The circuit utilizes a picoammeter to measure the current in real time. A measurement of the current consists of taking the average and standard deviation of 8192 samples taken at 16 kHz for Nb_{56} and Nb_{78}, and 30 kHz for Ti_{13} and Nb_{23}. This current reading was used to characterize the leakage current, as well as detect any discharges. The conditioning was done in 4 minute cycles. The voltage was

ramped up to the positive polarity, where it was held for 60 seconds. Afterwards, the high voltage was reduced back to zero, where it was kept for another 60 seconds, and a signal sent to the HV power supply to reverse the polarity. Then, 60 seconds of high voltage in the reversed direction was applied, and then another 60 seconds with HV off. This was done to simulate the cycle of measurements during the RaEDM measurement. By doing this for many hours, with the voltage being steadily ramped up, the electrodes could be conditioned with discharges kept to a minimum. Utilizing this technique, the Nb_{56} pair was conditioned to be able to accept fields of 20 kV/mm with no discharges. It was then installed in the apparatus at ANL, where it was revalidated to accept this field strength. A display of the results of this conditioning can be seen in Figure 6.3, also taken from [40]

Figure 6.3: Conditioning results for Nb_{56} electrodes.

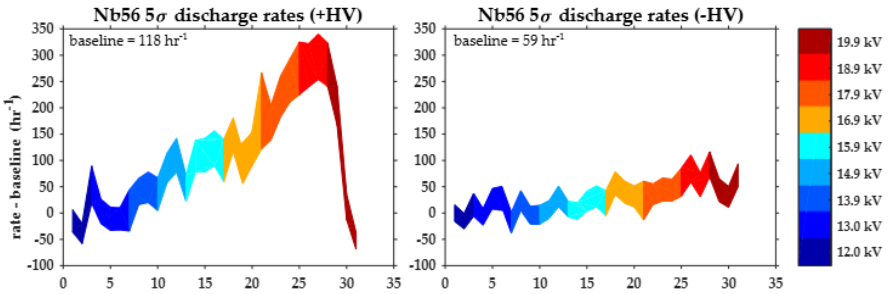

During the conditioning, it was noted that discharge rates markedly increased for negative polarity instead of positive polarity. This suggests a fundamental difference in the circuitry within the Applied Kilovolts bipolar power supply between the positive and negative polarities. This suggests other potential discrepancies between the two electric field directions, such as in electric field strength. Any discrepancy would cause an increase in the E^2 systematic effect. To resolve this, efforts are underway to utilize a unipolar power supply with a system of relays to swap the polarity between electrodes. An improved HV divider

will also allow for more precise measurements of the electric field generated.

6.3 Upgrades Needed to Achieve Higher Voltage

To increase electric field strength and decrease systematic uncertainties, new components and parts are necessary. They will now be discussed.

6.3.1 HV Power Supply

Two different power supplies were utilized to perform electrode conditioning for the RaEDM experiment. The apparatus at ANL currently uses a Spellman HV CZE 2000 power supply. The electrodes conditioned at Michigan State Unversity (MSU) utilize an Applied Kilovolts HP030RIP020 power supply. The next round of conditioning will utilize a Heinzinger PNChp60000-1 power supply, to allow for higher applied voltages and improved stability.

Table 6.2: Important specifications for the various power supplies utilized throughout the radium EDM experiment.

Specification	Spellman HV	Applied Kilovolts	Heinzinger
Model Number	CZE 2000	HP030RIP020	PNChp60000-1
Maximum Voltage	30 kV	30 kV	60 kV
Polarity	$\pm$	$\pm$	+
Maximum Current	.3 mA	.25 mA	1 mA
Maximum Voltage Drift over 8 Hours	0.02%	0.05%	.0001%
Maximum Voltage Drift at 30 kV over 8 Hours	6 V	15 V	30 mV
Maximum Voltage Ripple	.1% V_{p-p}	.001% V_{p-p}	.001% $V_{p-p} \pm 50$mV
Maximum Voltage Ripple at 30 kV	30 V	300 mV	350 mV

6.3.2 High Voltage Feedthroughs

This increase in power requires many components to be replaced with compenents rated to the increased voltage. Two of these components are the HV feedthroughs which lead the

high voltage into the electrode test stand. The 30 kV Ceramtec feedthroughs previously installed were upgraded to 50 kV versions. Specifications can be found in Table 6.3

Table 6.3: Important specifications for various models of feedthroughs available for installation on the HV conditioning test stand.

Model	Max. Voltage	Max. current	Diameter of Inuslator	Fitting
16729-03-CF	30 kV	3 A	1.5”	2.75” CF Flange
21184-01-CF	50 kV	10 A	1”	2.75” CF Flange

The fact that these new feedthroughs are rated only to 50 kV and not 60 kV means some kind of hardware limiting the output of the HV power supply to only 50 kV will be required.

6.3.3 High Voltage Cables

Another component crucial to the setup are the cables leading from the cage to the electrode stand. These are M1 Mammoflex cables manufactured by Claymount. They are coaxially shielded cables with a single conductor inside, able to handle 60 kV of voltage. In the future, Varex Imaging L4-type cables may be used. Their specifications can be found in Table 6.4

Table 6.4: HV cable specifications.

Model	Max. Voltage	Max. Current	Internal Resistance	Internal Capacitance
M1-type Mammoflex	60 kV	3 A	$\geq 10^{12}\Omega \cdot m$	171 pF/m
L4-Type Cable	75 kV	9 A	$\geq 5 \times 10^{12}\Omega \cdot m$	865 pF/m (bare conductor)

The HV components and circuitry necessary for switching the voltage from electrode to electrode is kept in a grounded metallic box, known as the HV cage.

6.3.4 HV Cage Design

In order to safely perform the high voltage work necessary for electrode conditioning, a grounded cage must surround any hot components. This cage must have adequate spacing

to prevent discharge from hot components to grounded components.

6.3.4.1 Old Cage Design

The previous high voltage cage was created with a maximum voltage of ±30 kV specified. The breakdown of voltage in air was taken as about 75 kV/in. When considering humidity, it became possible for the breakdown voltage to be reduced by a factor of 2, to 37.5 kV/in. This implies that for 30 kV, a minimum of .8 inches of distance should be between any hot components and ground. With an additional factor of 5 for safety, the old cage was designed with a minimum distance of 4 inches between any hot components and ground. The internal components can be seen in Figure 6.4.

Figure 6.4: Overview of inside of the previous HV cage. 15) 1 3/8 brass ball connector on glazed grade L5 ceramic, 5 cylindrical standoffs 16) Ohmite MOX94021006FVE 10 W, 45 kV-rated 100 MΩ resistors 17) Spinlab transient protection circuit in light- tight EM shield. Littelfuse SA5.0A transient voltage suppressor (TVS) diode, EPCOS EX-75X gas discharge tube (GDT), Ohmite 90J100E 1.08 kV, 11 W-rated 100 Ω resistor 19) Applied Kilovolts HP030RIP020 bipolar power supply 20) Keithley 6482 2-channel picoammeter 21) NIST-traceable high voltage divider, Ross model VD30-8.3-BD-LD-A 880.8:1 120 MΩ.

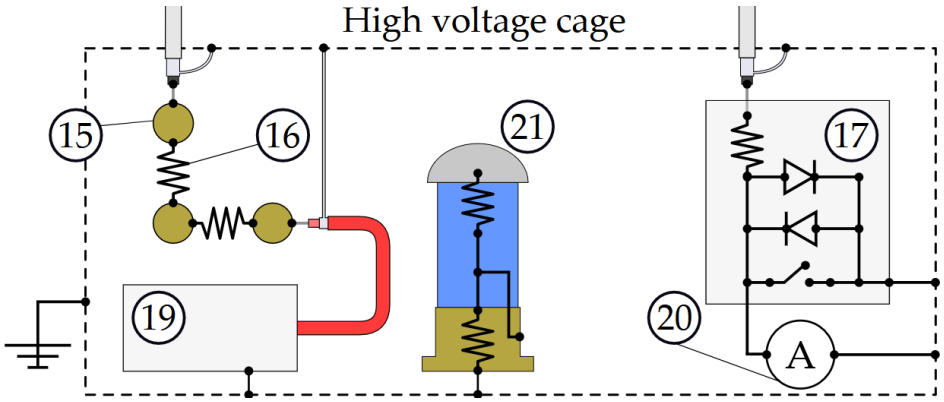

This layout was able to be used for leakage testing the new mechanical relays at 30 kV. To utilize the full 60 kV of the new high voltage system, however, a new cage is required.

6.3.4.2 New Cage Design

The new HV system requires not only large relays, but two large HV dividers as well. These all need to be housed with a larger distance from hot components to ground, due to the factor of 2 increase in voltage. Current FRIB guidelines require 1 inch of separation for every 10 kV. This would necessitate 6 inches of separation between all hot components and ground. Designs of the new cage have already been considered, with concepts like the one seen in Figure 6.5.

Figure 6.5: Non-finalized diagram of the new HV cage concept.

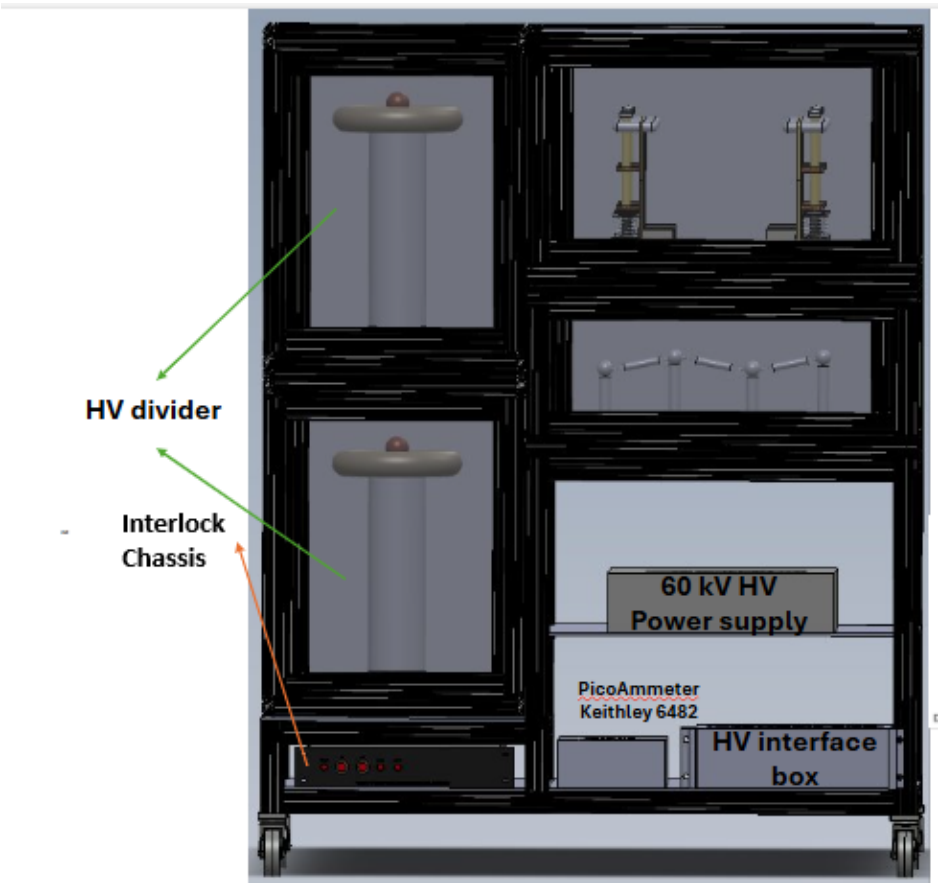

In addition, another size of protection may be needed for the HV stand itself to protect the feedthroughs going into the vacuum chamber. Sufficient radiological shielding will also

be needed so that x-rays produced by discharge will not increase radiation doses above acceptable levels. A previous calcuation done for 30 kV is shown in Figure 6.6

Figure 6.6: Maximum X-ray power spectrum from 1 mA electron current at 30 kV, after passing through 5 mm of Pyrex 7740.

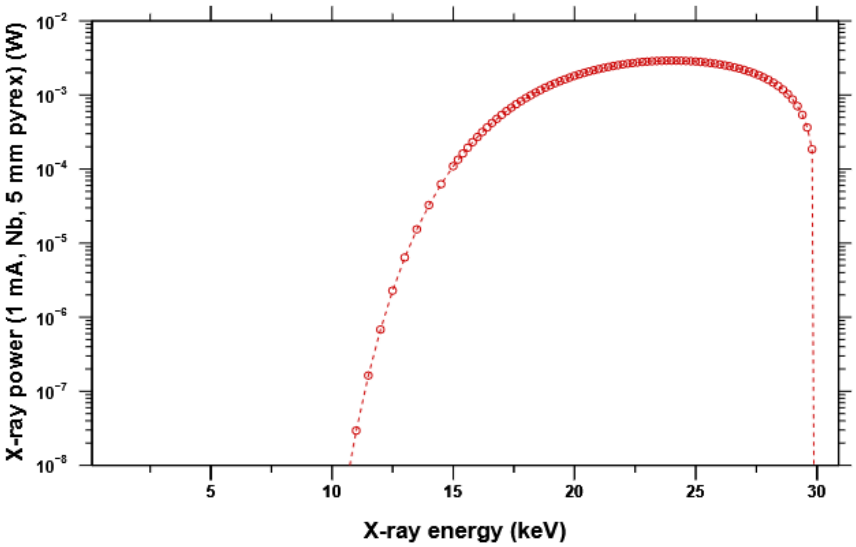

Efforts are underway to reproduce this plot, to then be able to modify its calculation to 60 kV of voltage. This new HV cage will also require an interlock system to prevent unwanted contact between personnel and hot components.

6.4 Upgrades to Improve E-Field Reversibility

Previously, the RaEDM experiment, for both the main apparatus at Argonne and the electrode conditioning stand at MSU, used the apparatus shown in Figure 6.7

With a unipolar power supply, a new apparatus like the one shown in Figure 6.8 is required.

This switching system, utilizing high voltage, needs careful consideration. Not only does

Figure 6.7: Diagram of the legacy HV RaEDM apparatus.

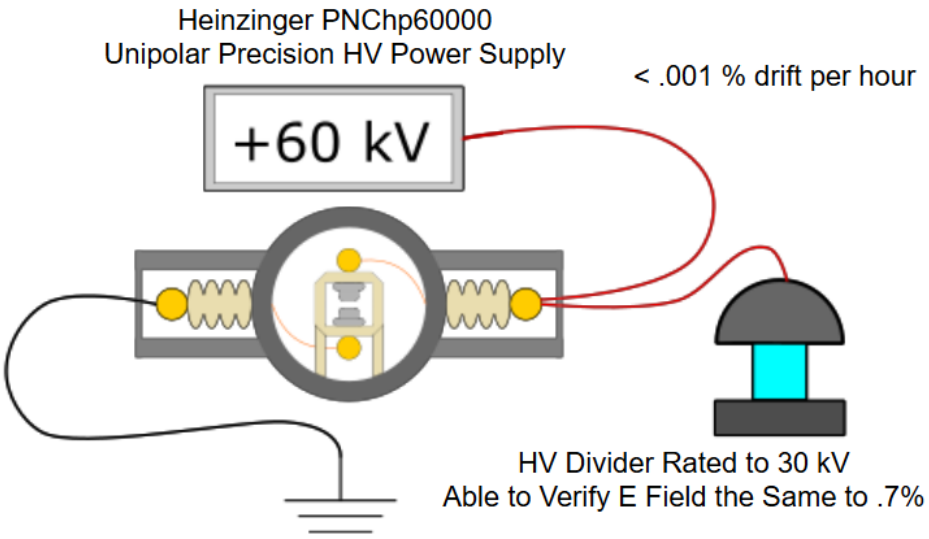

leakage current have to be minimized, and all components rated to the new high voltage, but safety is paramount. For this reason, new components are needed, and safety systems and interlocks put in place.

6.4.1 Relay Circuit

A precise circuitry diagram of the old HV conditioning setup can be seen in Figure 6.9

For the new setup, a new circuit must be made, and can be seen in Figure 6.10

The relays for this upgrade were important to get right, and will now be discussed.

6.4.2 Mechanical Relays

The new setup will utilize four Single-Pole Single-Throw (SPST) mechanical relays for the high voltage switching. The specifications for these relays is shown in Table 6.5

These relays have a pair of mechanical switches on the side, that are depressed when the relay is closed. There are three contacts on each switch, that make the switch able to be

Figure 6.8: Diagram of the planned HV RaEDM apparatus.

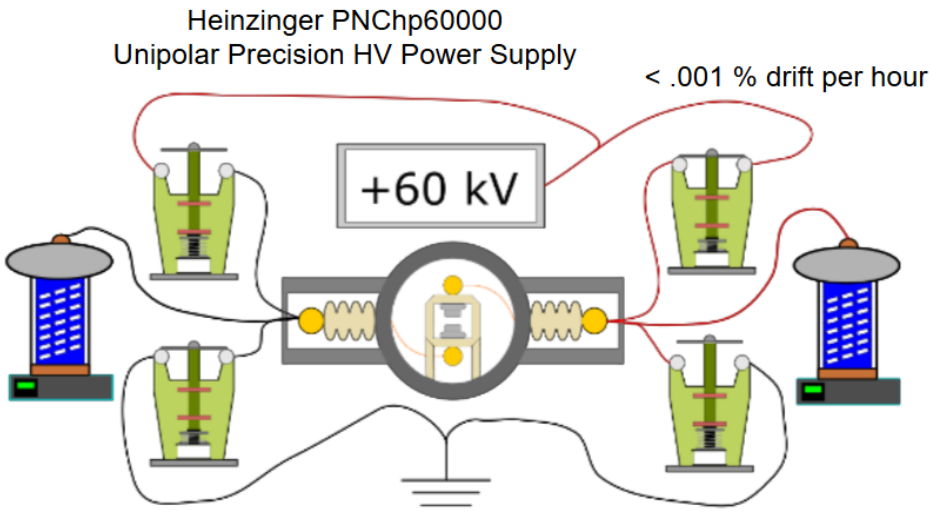

Table 6.5: Specifications for the SPST relays used for HV switching.

Manufacturer	Ross Engineering
Part Number	E60-NO-80
Contact Rating	60 KV
Insulation to Groud	80 kV
Maximum Dimensions	$6 \times 4 \times 14.25$ (in)
Rated Resistance (Open)	
Actuation Power	115 V, 60 Hz Coil
Maximum Switching Time	140 ms

used in either a normal closed or normal open capacity. Since these are mechanical, they are very useful for diagnosing whether a switch is open or closed, as they aren't susceptible to any bugs in the software. They can be utilized to design a completely hardware-based logic interlock system, as will be discussed later. These two switches with three contacts each give a total of six contacts. In addition, there are two more to actuate the relay, by applying standard American 125 V 60 Hz wall power to its coil. This gives a total of eight contacts, two of which are at high voltage. The nature of the high voltage means that an insulating

Figure 6.9: Diagram of the legacy circuit.

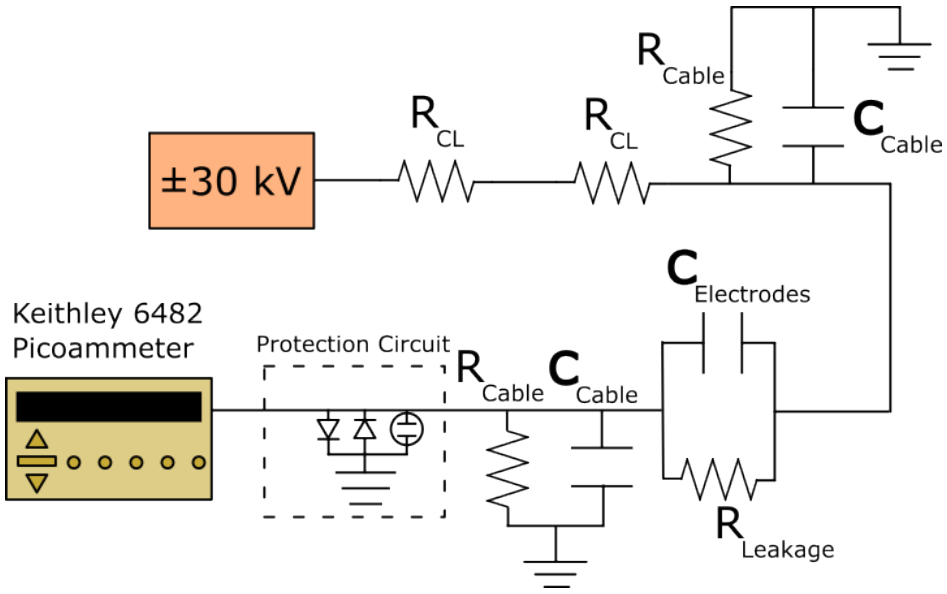

shield is needed, to prevent unwanted contact. This is done by utilizing a 3D-printed shield, which can be fastened onto the base of the relay utilizing 3D-printed brackets. An overview of attaching the shields to the relays will be given in the appendix. The various contacts are attached to feedthroughs that allow for the electrical components to be accessed from the outside. The feedthroughs allow for 120 VAC power to be provided with a standard power cord. Actuating the relay amounts to turning this 120 VAC power on and off. This can be accomplished utilizing a Powertail. The Powertail is a power module that has an outlet that turns on and off from a 5 V input signal.

6.4.3 Solid State Relay

In addition to the mechanical relays, a Behlke HTS-500-10 HV solid state relay will also be used directly after the power supply. This is to allow the HV to quickly disconnect, at a rate faster than the mechanical relays can. The specifications of the relay are shown in Table 6.6

Interfacing with this relay requires additional circuitry to control. Such a circuit should

Figure 6.10: Planned circuitry for the HV upgrade.

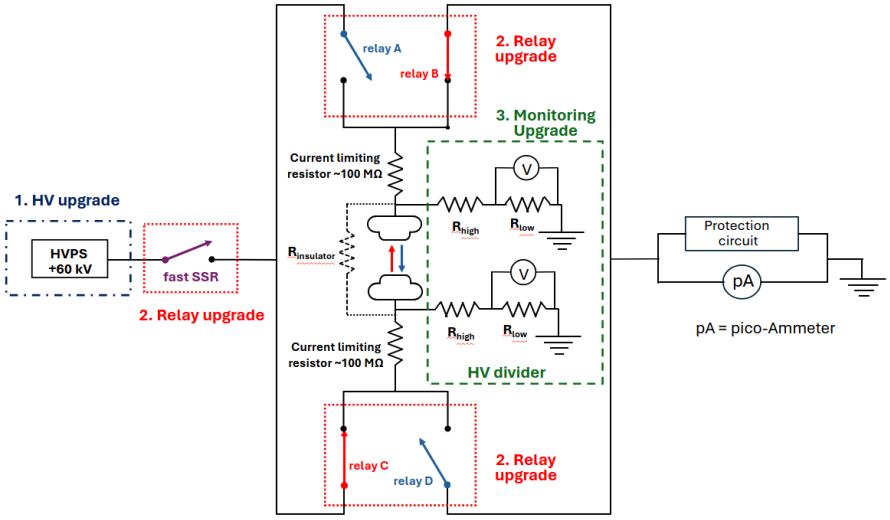

Table 6.6: Specifications for the HV solid state relay.

Specification	Value
Model	Behlke HTS-500-10
Maximum Voltage	50 kV
Minimum Turn-On Time	200 ns
Minimum Turn-Off Time	210 ns
Interface	4-pin pinout

look something like in Figure 6.11

With all these mechanical relays, hardware interlocks will be necessary to make sure high voltage never goes straight to ground.

6.4.4 Interlock Design

An essential component of the HV safety cage is the presence of interlocks that interrupt the power to the high voltage power supply. This means that, if anyone should attempt to access the inner workings of the cage, the power will be immediately interrupted and shut off. The circuitry to do this is contained in the interlock Chassis.

Figure 6.11: Circuit diagram for interfacing with the solid state relay.

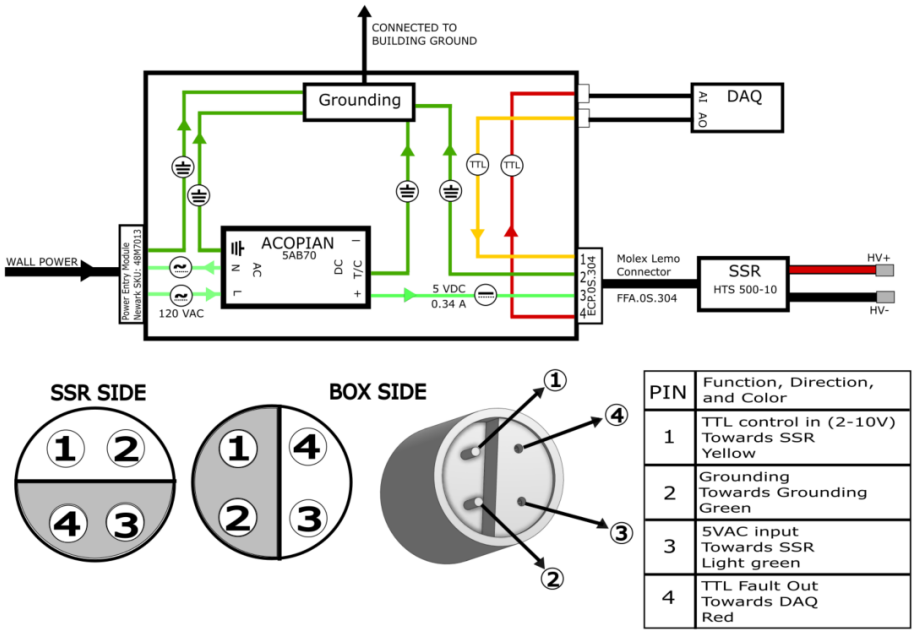

A similar system, with interlocked soup cans and doors, will have to exist in the new HV cage. In addition, another interlock system will be needed so that at no point does the high voltage get connected directly to ground. In a system such as this:

it's important that hardware based logic be implemented to prevent shorts to ground. A logic system needs to be built something like in Figures 6.15 and 6.16.

The mechanical switches on either side of the relays can prove very useful for this, since they provide a way, free of any software, of telling whether or not a relay is open or closed. Consider a setup like in Figure 6.17

With this setup, there are normally open relays interrupting the logic that flows from the control to the powertails that turn the power on and off to the mechanical relays. Should relay 1 close, then the voltage closing the control relay for relay 2 is interrupted, and it opens. Even if a signal is sent to close relay 2, it will not be received by its powertail. The

Figure 6.12: Interlock chassis circuitry diagram Pt. 1.

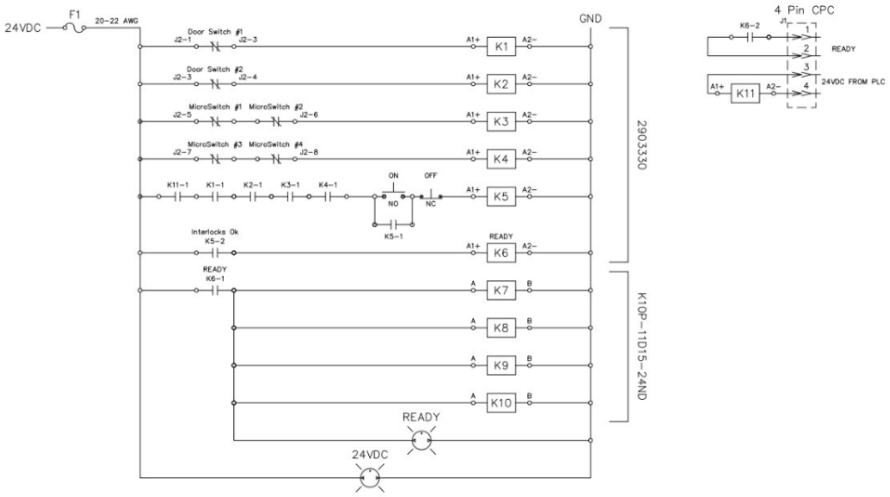

same is true for relay 2 interrupting relay 1. Notice that, should something fail with the 5V power supply that powers the interface, the relays inside will both result to their normal open positions, and neither relays 1 or 2 will be able to be closed. The implementation of a system like this was the reason for the choice of 4 SPST relays, instead of 2 SPDT relays. With these relays in place, a more precise measurement of the voltage across the electrodes was desired. For this reason, new HV dividers were needed.

6.5 Upgrades to Electric Field Monitoring

In the most recent limit measured for the EDM of Radium-225, the E field across the electrodes could only be verified to be the same for both orientations to within .7%. To change this, a more precise way to measure the voltage applied to the electrodes is needed. In addition, due to the new relay setup, two of these HV dividers would be needed instead of one. the choice of design to use was settled upon a design traceable to the Physikalish-Technische Bundesanstalt (PTB) from Germany. Three of these HV dividers were previously

Figure 6.13: Interlock chassis circuitry diagram Pt. 2.

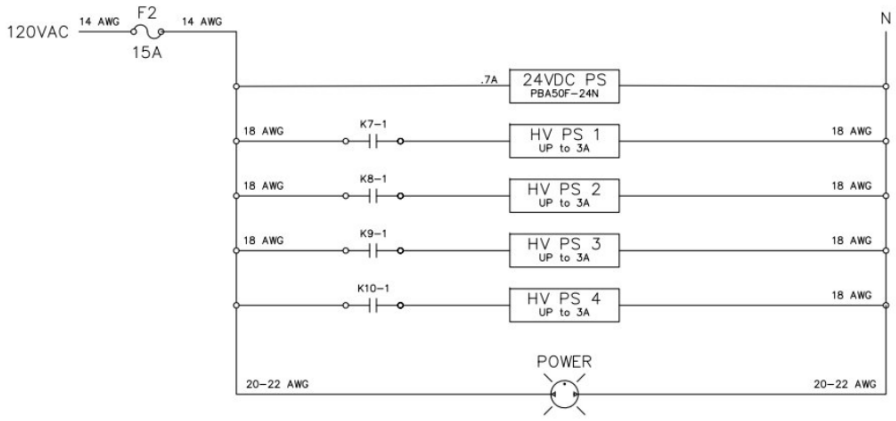

Figure 6.14: Basic relay setup.

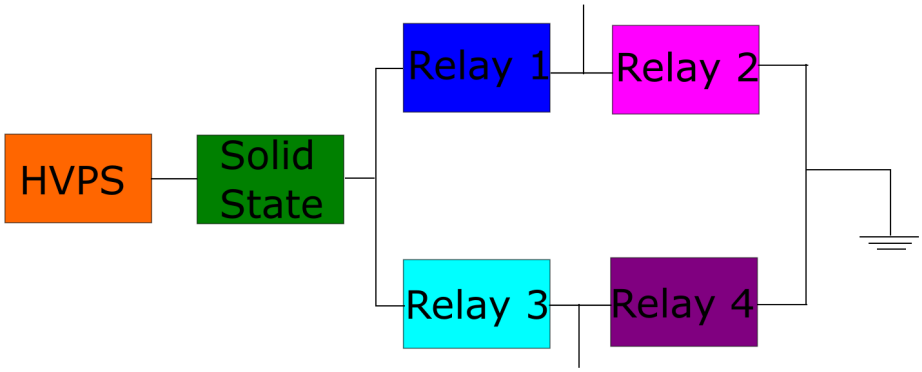

made, one by PTB, and two in the lab of Kei Minamisono at FRIB. One of the FRIB HV Dividers was given to us, for our use. The other would have to be custom made. Great progress has been made with its assembly, though issues with the temperature controlling circuitry still exist. The assembly is discussed in detail in the appendix.

6.5.1 HV Divider Operation

The HV divider consists of a corona ball and disk at its top where high voltage can be applied, a temperature-controlled cylinder with HV resistors wound around in series a spiral pattern

Figure 6.15: Relay logic Pt. 1.

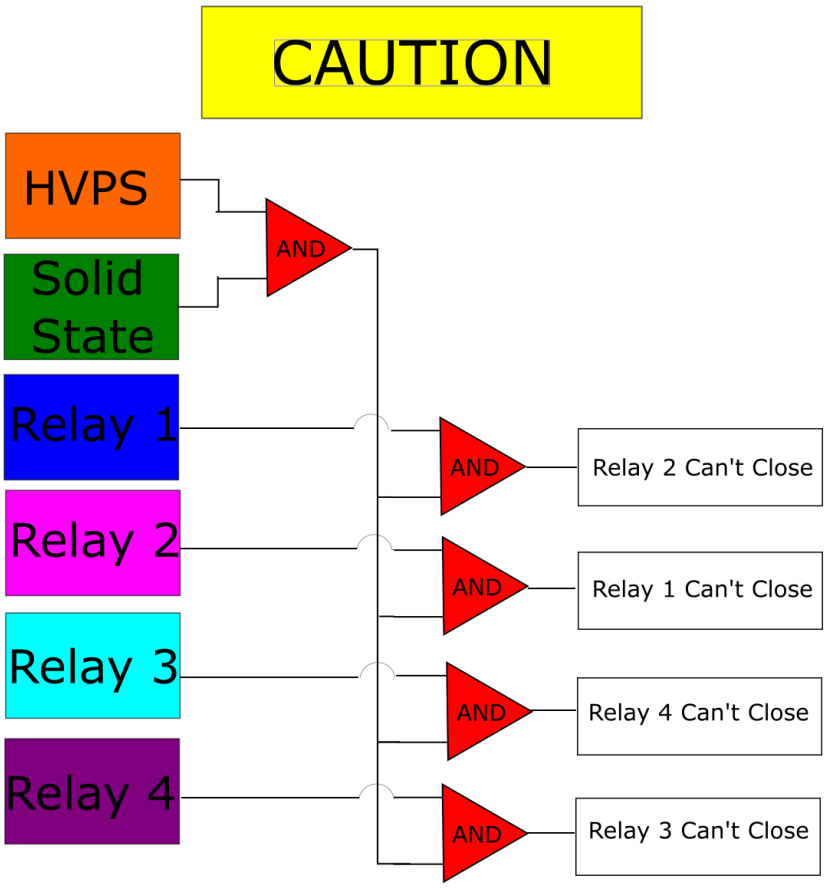

below it, and a metal box at the bottom containing the relevant circuitry for operating the temperature control. This Circuitry can be seen in Figure 6.18

The HV dividers winding down the center pillar lower the voltage to an acceptable level, with extremely precise HV resistors. These resistors are rated to each handle 1 kV across them, and are 10 MΩ each. They come in sets of 5, meant to be used each in series. The resistors used for these HV dividers in particular are marked "MDN1475", indicating that the resistors are individually selected based on their individual temperature coefficients, so that the five resistors in series have, in aggregate, as low of a temperature coefficient as possible. As such, it's extremely important that sets of 5 stay together, and that these are

Figure 6.16: Relay logic Pt. 2.

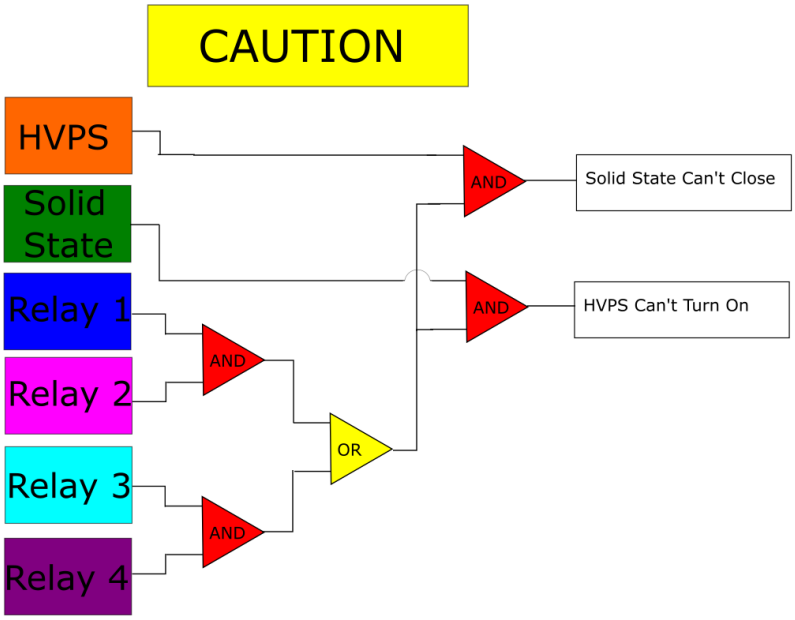

marked. Twelve sets of 5 resistors are used, so that for 60 kV applied at the top, each individual resistor only receives a 1 kV voltage drop across it. The total resistance is thus 600 MΩ. In series with this coil of resistors is a very precise 700 Ω resistor. It is across this resistor that the voltage is measured. For a maximum voltage applied of 60 kV, there will only be a 70 mV voltage across the 700 Ω resistor - this can then be safely measured by a voltmeter. In the metal box below the main cylinder lies the temperature control system. This utilizes a temperature feedback console that continuously measures the temperature with a temperature probe inside the cylinder, and sends current to a transistor whenever it needs to warm up. When working properly, this will create a stable temperature in the HV divider, which improves the stability of the resistors.

Figure 6.17: Diagram of hardware logic to interrupt relays.

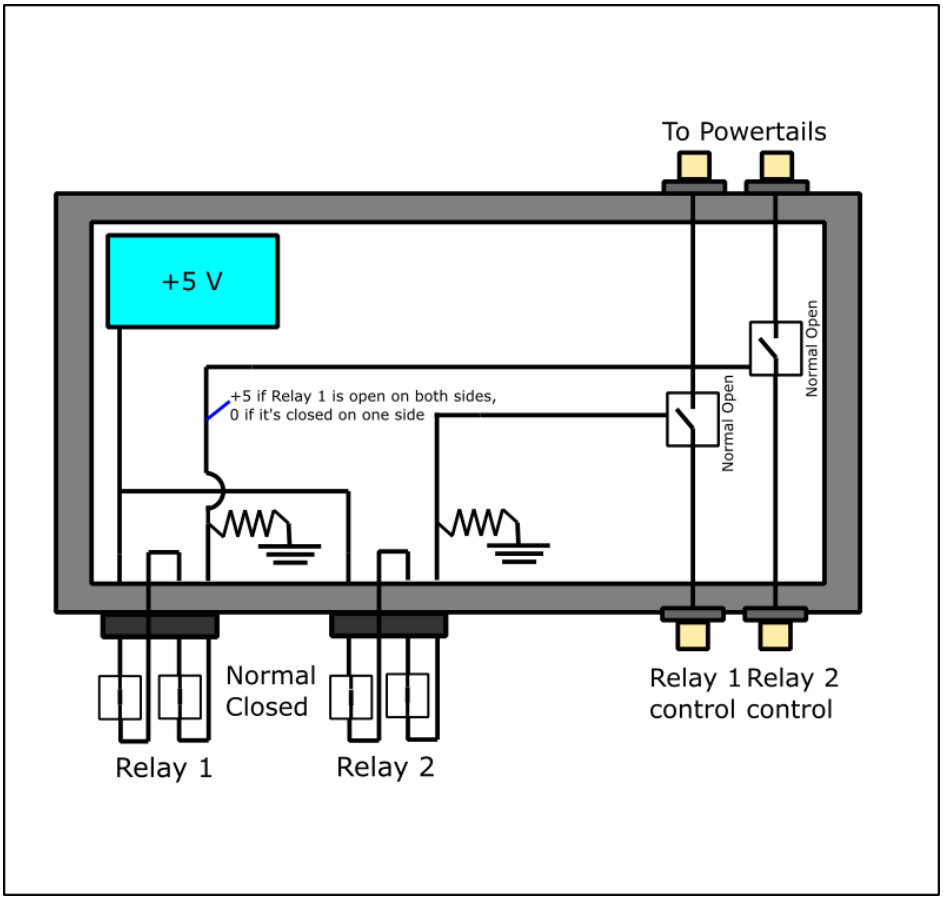

6.5.2 HV Divider Specifications

The HV divider provided to us, HVD-3, was tested versus the HV divider made by PTB. To perform this test, both dividers were attached to the same 30 kV power supply, and two voltmeters were used to measure the data simultaneously. The purpose was to see how closely the two measured the same voltage. Data taken looked like Figure 6.19, using another test with HVD-1 as an example.

Three runs were done of this experiment, performed by Professor Kei Minamisono, and the results for the B-HVD3 divider can be seen in Table 6.7

For each run, the standard deviation of the difference between the two, $\sigma_{PTB-BHVD}$, was

Figure 6.18: Diagram of the circuitry for the HV divider temperature controller.

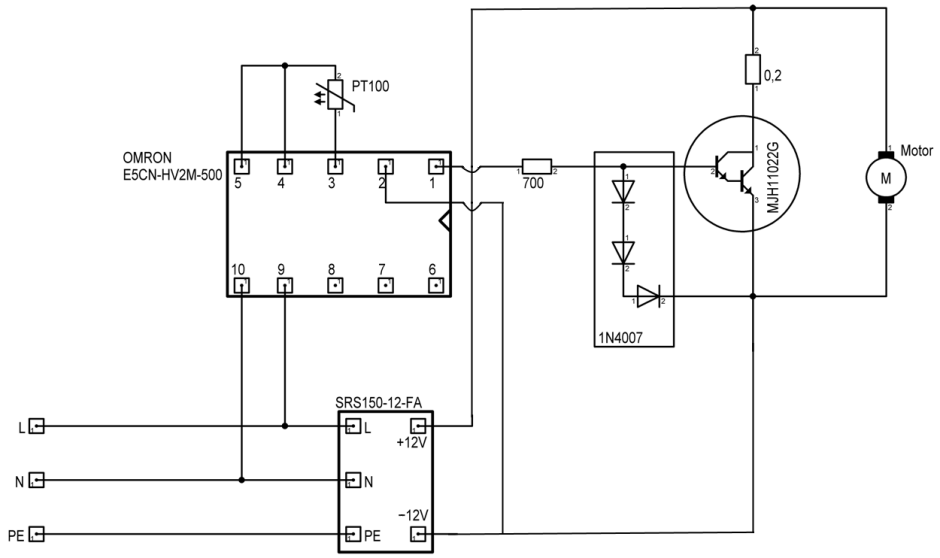

Figure 6.19: Difference in relative voltage to average voltage between two different HV dividers.

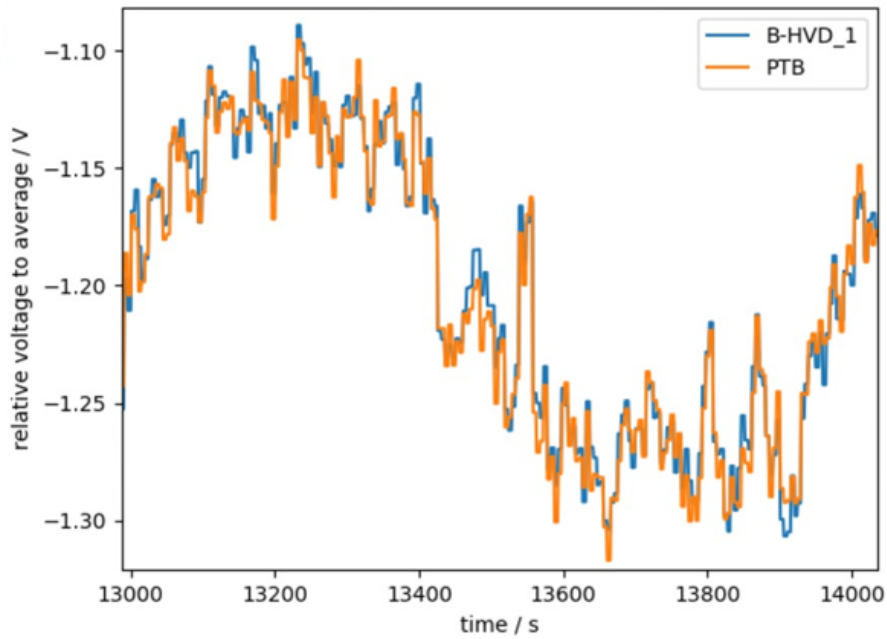

Table 6.7: Experimental runs for B-HVD3.

Run	Voltage (kV)	Voltmeter 1	Voltmeter 2	PTB/ B-HVD3	$\sigma_{PTB-BHVD}$
1	30 kV	B-HVD3	PTB	1.000052	.27 ppm
2	30 kV	PTB	B-HVD3	1.000026	.23 ppm
3	10 kV	PT	B-HVD3	1.000025	.10 ppm

Figure 6.20: Legacy protection circuit for the HV setup.

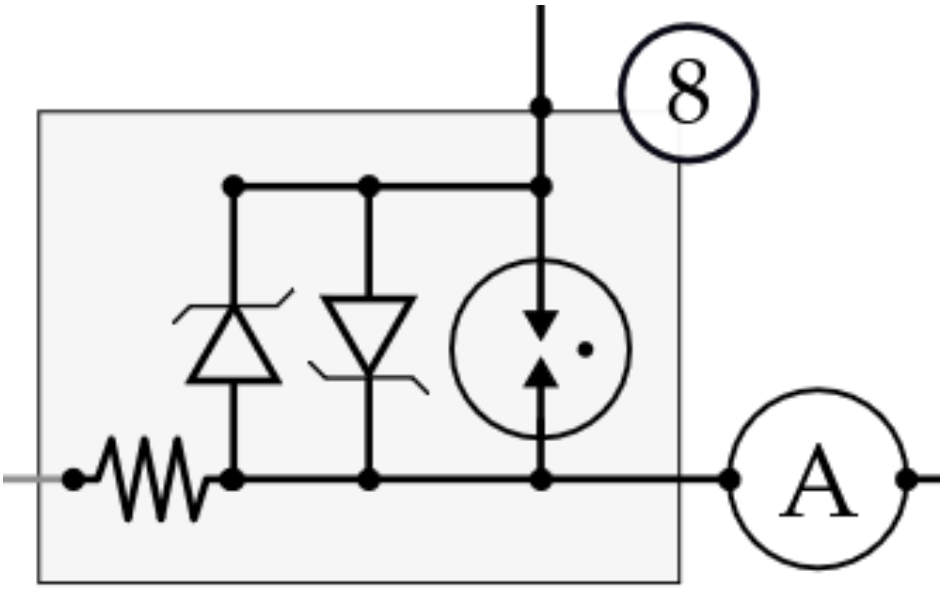

less than a single part per million. With two of these HV dividers, part-per-million sensitivity to E field reversibility can be achieved. Another crucial component to this experiment is the monitoring of leakage current. This utilizes a Picoammeter, with a protection circuit to protect it from intermittent discharges. This protection circuit took time to get right, and will now be discussed.

6.5.3 Protection Circuit Development

The original protection circuit that was present in the old circuit diagram looked like 6.20

The diodes used were 5.0A TVS diodes, in parallel in opposite directions, and an EC75X

Gas Discharge Tube. The resistor used was 1 $k\Omega$. The picoammeter, of model type Keithley 6482, was attached parallel to all three. Some relevant specifications are given in Table 6.8

Table 6.8: Specifications of Keithley 6482 picoammeter.

Specification	Value
Model	Keithley 6482
Maximum Current Range	$\pm$20 mA
Minimum Current Range	$\pm$2 nA
Resolution at Minimum Current Range	1 fA
Current Input	Triaxial Cable
Reading Output	Analog or Digital
Maximum Input Impedance	20 $k\Omega$ @ 2 nA setting

To test the protection circuit, a Keithley 6221 current source was used. Some specifications are in Table 6.9

Table 6.9: Specifications of the Keithley 6221 current source.

Specification	Value
Model	Keithley 6221
Maximum Current Range	100 mA
Minimum Current Range	2 nA
Voltage Compliance Range	.1V to 105V (Typically set to 47 V)
Current Output	Triaxial Cable
Remote Control Protocol	SCPI

The current source has a "Voltage Compliance," which is the maximum voltage the current source is willing to output to reach the desired current output. Typically, this was set to 47 V, lower than the 50 V lab threshold where additional safety measures need to be taken. Care had to be taken that any observed cutoff current was the result of the protection circuit working as intended, and not caused by the voltage hitting the compliance limit. Testing the circuit was done by attaching the current source to the protection circuit, and sweeping the output current.

Figure 6.21: Diagram of the legacy protection test circuit.

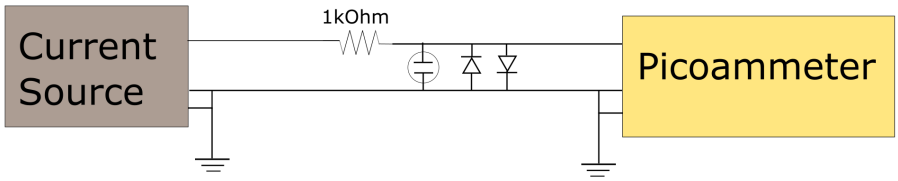

In this diagram, for the triaxial connections, the top wire is the inner conductor, the middle wire is the outer conductor, and the lower wire is the braided shield around the triax. A test was done to vary the input current from -200 nA to 200 nA twice, once with the current source directly attached to the picoammeter, and once with the legacy protection circuit installed. At each current source setting, the picoammeter was allowed to run for a few seconds, so that a histogram could be made of the data, shown in Figure 6.22

Figure 6.22: Histogram of picoammeter readings for the protection circuit test.

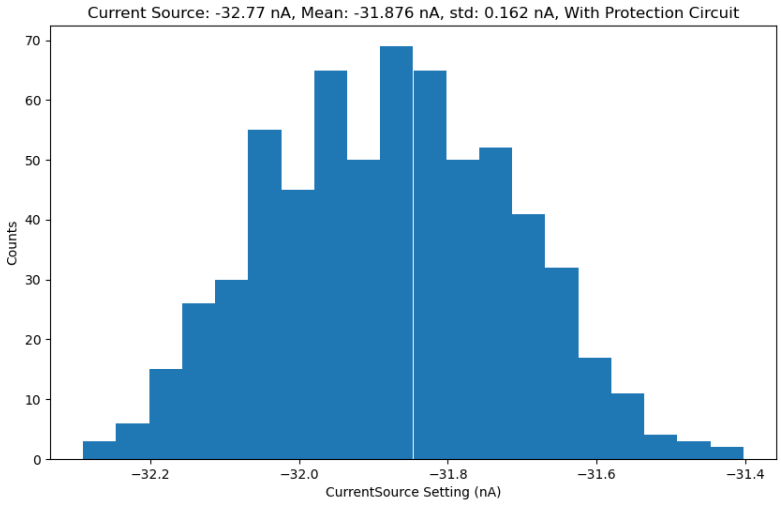

By taking the mean and standard deviation of this data, a central value and error could be retrieved. From there, the readings could be plotted relative to the current source setting.

Figure 6.23: Legacy protection circuit current readings compared to baseline.

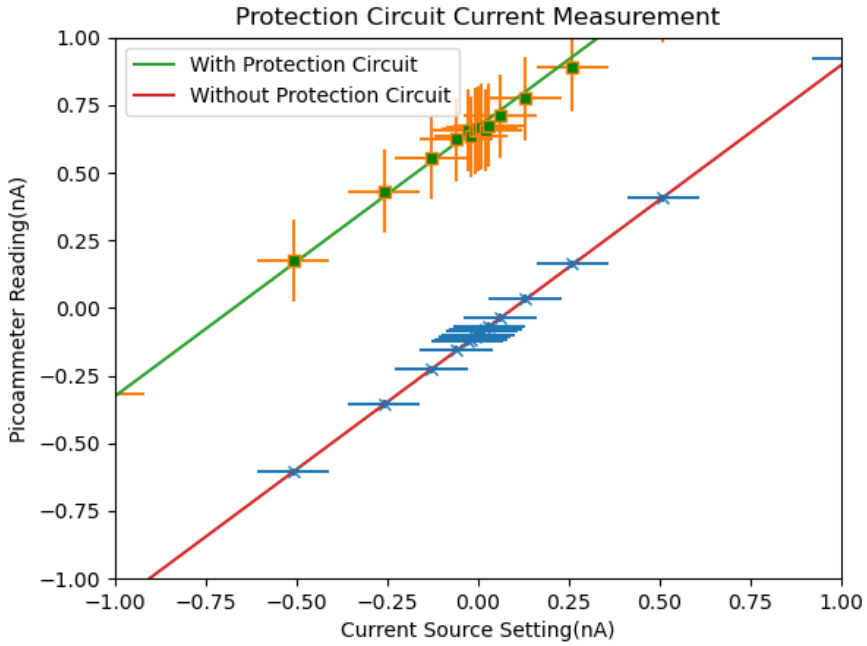

Note the horizontal errorbars in Figure 6.23, which account for the error specification in the current supply. The coefficients for the linear fit are shown in Table 6.10

Table 6.10: Values of the linear fit to the legacy protection circuit and baseline data.

Test	Slope	Offset (nA)
No Protection Circuit	.99562 ± .00002	-.098 ± .001
With Protection Circuit	.9955 ± .0001	.670 ± .006

The issue seen was a lack of a cutoff above 200 nA, as well as a slight offset in the current reading, equivalent to 670 pA. This suggested that the protection circuit needed some modifications. A different system was built, shown in Figure 6.24

This setup made sure to isolate the loop of current from the surroundings. In order to collect and record the data, the analog output voltage was used. This utilized a triaxial output. The outer shield was grounded to the box, and connected to the ground as well,

Figure 6.24: Diagram of the intermediate setup.

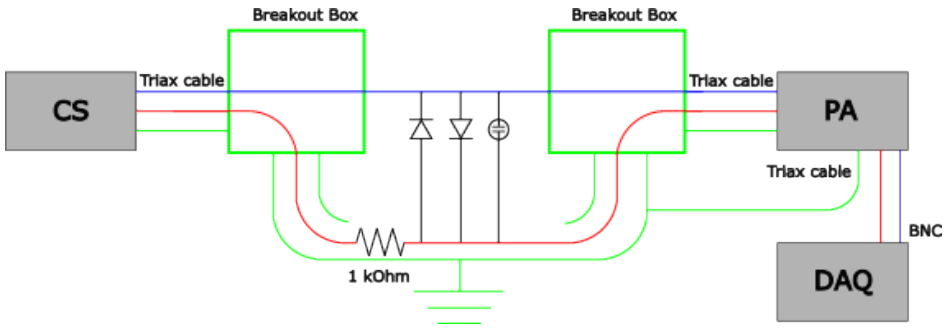

while the inner and outer conductors were attached to an NI DAQ card to collect data. While taking data, there was a discrepancy noted between what was being read on the computer, and what was being displayed on the display of the picoammeter. A test was done where at each step of the current source, data would be taken by the computer, and an approximate value would be taken for the reading displayed. The data taken by the computer at each step had a histogram made, with the mean and standard deviation. The value for the displayed reading was taken to have an uncertainty of .1 nA. A residual plot was then made, of the difference between the displayed reading and the computer-measured reading. The uncertainty was propagated from both measurements to the residual, shown in Figure 6.25

This gives a linear relationship of the residuals, with a slope of -.00502 $\pm$ .00005. Clearly, some kind of cross talk was going on. The solution to this was to instead use a GPIB digital connection to read from the picoammeter. As development continued, it was desired to be able to change the current cutoff. The solution to this was to include a resistor in series with the picoammeter, so that at a specified current, the voltage would cause current to flow through the diodes. This used the circuit shown in Figure 6.26

Four different resistor values were used, and each had two current scans performed. The

Figure 6.25: Residual between the picoammeter display and analog reading.

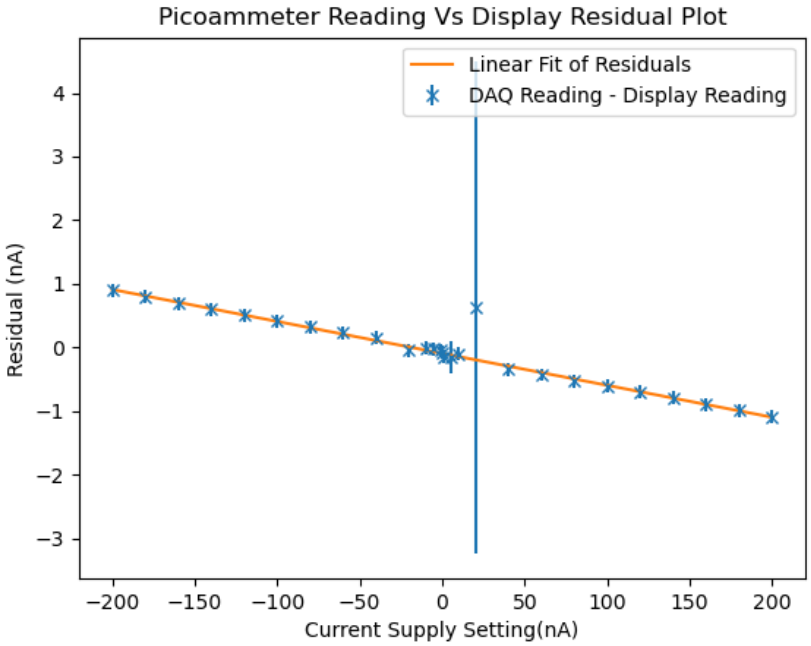

first scan would scan from -200 to 200 nA. the second scan scanned from -2 to 2 mA. It should be noted when these scans were performed, the current was still recorded through the voltage analog output. As such, the uncertainty was taken to be .5% of the measured current, in accordance with the study done on the residual between the picoammeter display and the analog output reading.

for the -200 to 200 nA scans, the graphs looked linear, and a fit was taken of the slope of applied current to measured current.

Cutoff behavior was observed for the -2 to 2 mA scans however. The maximum current measured was taken as the cutoff voltage

Below is a table of the these values:

These slopes being less than one were an issue, since what was measured on the picoammeter did not match the current actually sent to the circuit. A measurement of 1 pA with a

Figure 6.26: Diagram of the protection circuit utilizing resistors to determine the cutoff current.

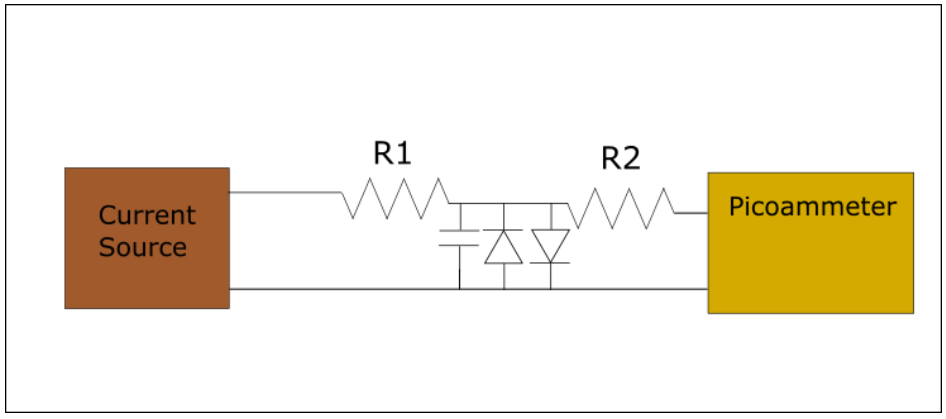

Table 6.11: Table of the cutoff and linear slope values for various resistors.

Resistance	Slope (Linear Region)	Maximum Measured Cutoff Current
300 MΩ	.000371 ± .000002	1.76 nA
100 MΩ	.001111 ± .000004	9.23 nA
300 kΩ	.273 ± .001	1764 nA
100 kΩ	.530 ± .002	5279 nA

100 MΩ resistor installed would actually correspond to 1 nA of current. However, it was still desired that the cutoff current be kept low. The solution to this was to replace the diodes with ones with different specifications. The 5.0A TVS diodes were replaced with 1N3595 diodes.

Table 6.12: Specifications for various diodes used in the protection circuit.

Specification	5.0A TVS Diode	1N3595 Diode
Manufacturer	Littelfuse	Fairchild/Onsemi
Direction	Unidirectional	Unidirectional
Breakdown Voltage	6.4 - 7.0 V @ 10 mA	150 V @ 100 μA
Forward Voltage	No Information	.52 - .68 V @ 1.0 mA

A similar test was then run for the setup with the 5.0A TVS diodes, except this time the 1N3595 diodes were used, and the R1 resistor was replaced with a 100 MΩ resistor. As

Figure 6.27: Data showing a linear region for the 100 kΩ resistor.

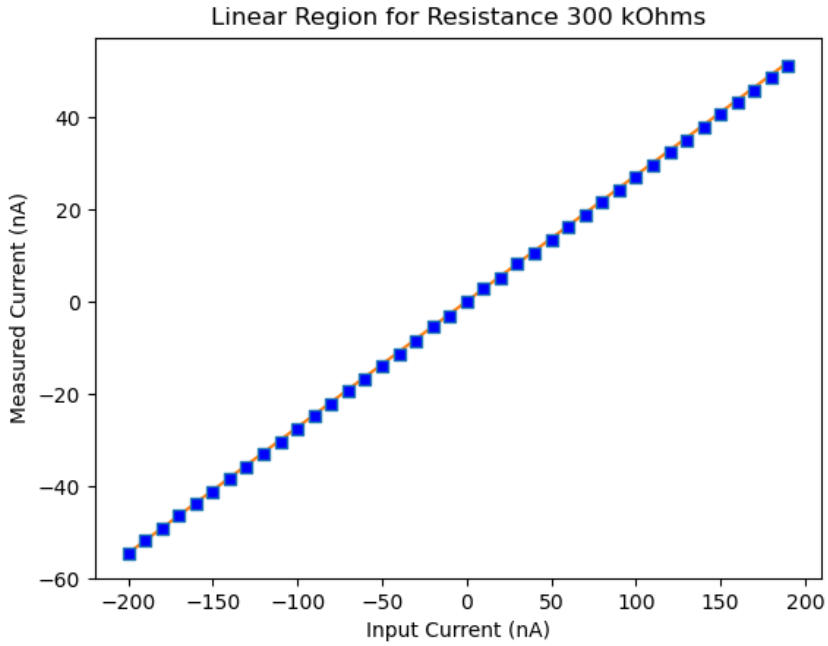

this resistor was in series with the rest of the circuit, it was not believed that it would have any effect other than to increase the voltage necessarily put out by the current source, which was not relevant. The test was run for R2 values of 100 MΩ and 200 MΩ. The slopes were determined by a range from -.2 to .2 nA, and the cutoff from a range from -8 to 8 nA. The results are below.

Table 6.13: Results for the protection circuit using 1N3595 Diodes with varying values for R2.

Resistor	Slope	Cutoff Current
100 MΩ	.945 ± .001	2.28 nA
200 MΩ	.889 ± .007	1.17 nA

With these new diodes, the cutoff currents are again in the nA range, but with a slope much closer to 1. It may be desired to use smaller resistors, which will get a slope even closer to 1, but with a slightly higher cutoff current.

Figure 6.28: Data showing the cutoff region for the 100 kΩ Resistor.

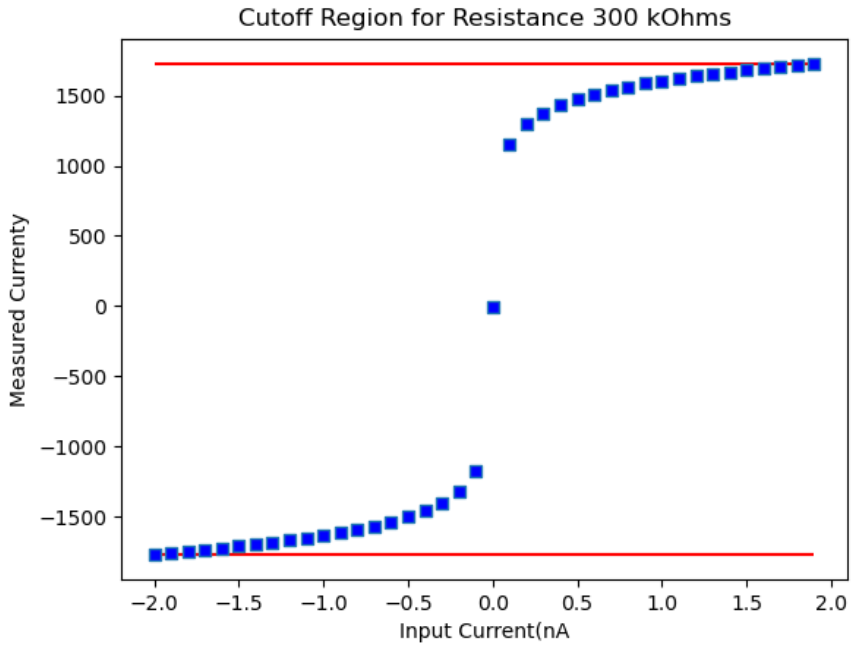

Chapter 7. Atomic Beam Fluorescence Studies

7.1 Increased Demand of Radium

Radium-225 has been established as being an ideal candidate for fundamental symmetries research. However, its scientific potential reaches into medical research as well. This makes procuring it for fundamental physics research difficult, since medical research takes clear priority for the distribution of available radium-225. With the FRIB coming online, and the water beam dump nearing operation, a new source of radium-225 should be available. The amount of radium-225 created, while unfortunately not enough to contribute to medical research, should still be sufficient for fundamental symmetries research.

7.1.1 Ac-225 Targeted Alpha Therapy

Radium-225 decays through β^- emission, resulting in actinium-225. The decay chain of actinium-225 contains 3 α decays and 1 more β^- decay before reaching stable bismuth-209. This decay chain can be seen in Figure 7.1.

This makes actinium-225 an ideal candidate for Targeted Alpha Therapy (TAT). TAT uses alpha emitters for killing cancer cells, which has advantages over other kinds of radiation. The "short range of alpha radiation in human tissue correspond[s] to only a few cell diameters,", which "allows the selective killing of targeted cancer cells while sparing surrounding healthy tissue." Furthermore, "the high energy of alpha radiation of several MeV and its associated high linear energy transfer leads to highly effective cell killing."[51].

Promising results of TAT using actinium-225 have shown success in treating "difficult"

Figure 7.1: Decay chain of Th-229. Figure taken without permission from [50].

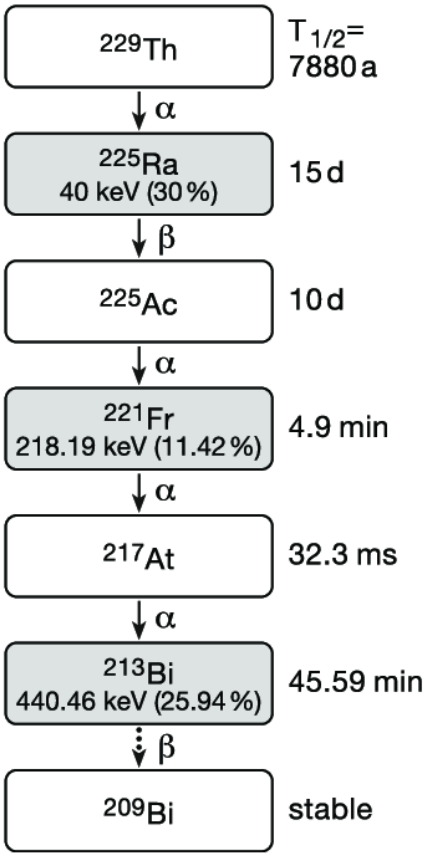

[51] cancers, and some images of treatment can be seen in Figure 7.2. This, fantastically, has caused a great deal of interest in actinium-225 as a medical isotope. As a result, radium-225 for fundamental symmetries measurements is no longer available from previous sources. For this reason other sources from which to procure radium-225 must be investigated.

7.1.2 Tests of Fundamental Symmetries

The radium-225 isotope is the backbone the backbone of this experiment, due to its octupole deformed nuclear structure. This gives it a large nuclear Schiff moment, as well as a nearly degenerate parity doublet. Both of these properties together give it an enhancement in the sensitivity to new physics in any EDM measurement performed upon it. However, radium-

Figure 7.2: PET/CT scans of progression of actinium-225 cancer treatment. Image taken without permission from [51].

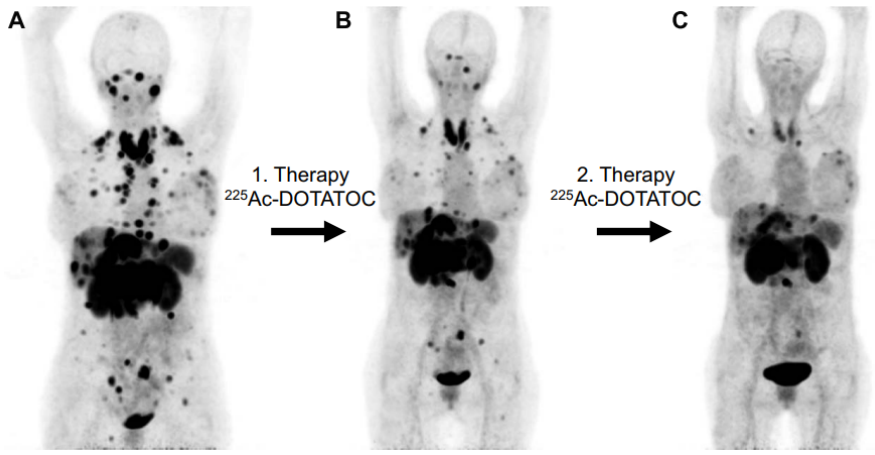

225 also has a 14-day half life, making it a rare isotope. This makes sources of radium-225 few and far between.

7.2 Sources of Radium

The procurement of radium-225 has proven to be a particularly challenging problem to overcome in our experiment. We have looked to a variety of sources for the atoms for our measurement:

7.2.1 Sources of Radium-225 for Previous Data Runs

In the two previous data runs of the RaEDM experiment, the radium-225 used was sourced from the National Isotope Development Center at Oak Ridge National Laboratory (ORNL). The first data run used two separate samples, one 3 mCi, and one 6 mCi. The second data run was done with a single 9 mCi sample of radium-225[21]. The origin of this radium at Oak Ridge National Laboratory is from a source of thorium-229, which has a half life of

7,917 years. This relatively long-lived nucleus then slowly decays into radium-225, which it is then harvested from. It is this source that now supplies ongoing medical research. Other sources are thus needed.

7.2.2 Radium-223 as a Surrogate

For a time, radium-223 was explored as a potential substitute. This could still be procured from ORNL for fundamental physics experimentation. It has a similar octupole deformation to radium-225, which gives it a similar enhancement factor for EDM measurements. However, there are reasons why it is less than ideal. Its half life is only 11 days, instead of 14, and it has a nuclear spin I = 3/2 instead of 1/2. This not only makes adds more hyperfine F levels to its excited states, but it also introduces hyperfine B coefficients into the theory of the hyperfine splitting. This made trapping it a challenge, as some of these spectroscopic properties for the necessary Ra-223 levels have never been measured. As described in Chapter 4, an effort was made to find these values, but the supply of radium-223 was also interrupted at ORNL, and this came to a halt.

7.2.3 Using a Thorium-229 Generator as a Source of Radium

A recent effort to laser cool and trap radium-225 ions at UC Santa Barbara [52] was able to use radium-225 for its experiment, through using an oven containing thorium-229. 8 μCi of Th-229 was loaded into a titanium crucible, and heated to 350-400 C. This resulted in a long-term oven of radium-225, as the thorium continuously decays into radium. However, the resulting number of radium-225 ions trapped was 12 on average[52], which while sufficient for measuring the energy levels and states of the radium-225 ion, is rather low for the number of

atoms we need for an EDM experiment. This could be improved by increasing the amount of thorium-229 put into the oven, but there are limits to how much we can put in due to the resulting increase in radioactivity. Any source of thorium-229 we put in will be at least slightly contaminated with other isotopes of thorium, many of which have significantly smaller half-lives.

Table 7.1: Table of the decay properties of Thorium isotopes.

Isotope	Half-Life	Decay Mode	Dps in 1 ng of Material
Th-229	7916 years	α	7.25 Bq
Th-228	1.9 years	α	30.4 kBq

As can be seen, a sample of thorium-229 with even a 1% thorium-228 contaminant will have over 97.6% of its total activity come from the thorium-228. With activity being a key safety concern, this greatly reduces the amount of thorium-229 that can be put in an oven given an upper limit of activity.

7.2.4 Isotope Harvesting at FRIB

The FRIB at Michigan State University is capable of accelerating nuclei to energies of over 200 MeV/u, for the purpose of the creation of rare isotopes. These are created by accelerating a primary beam of ionized atoms to these energies, and hitting them against a stationary target. After the target, an apparatus is in place to perform measurements on the secondary beam that results. A large part of the primary beam does not react with the target and continues on. These unreacted particles left over are not part of the secondary beam and will be deposited in a water beam dump. Impacting the beam dump will cause nuclei in the unreacted primary to fragment. Harvesting the rare isotopes produced in the beam dump been proposed as a potential source of rare isotopes, and the concept of harvesting isotopes

from it has been proven [53]. It has been mostly completed, and is awaiting operation. Once in operation, with the right beams such as uranium and thorium, radium-225 will be available once more.

7.2.5 Forming Atomic Beams from Harvested Isotopes

Radium-225 will be harvested from the FRIB beam dump dissolved in water, alongside other products of the secondary beam. From there, radiochemistry can be done to isolate the radium, and deliver it in the form of radium nitrate - the form that it arrived in from Oak Ridge National Laboratory. To form an atomic beam from the radium, the same process would be used as for previous RaEDM measurements [21]. The radium nitrate is dried upon a square of aluminum foil, alongside two 25 mg pieces of metallic barium. The aluminum foil is then crumpled up, and placed inside a titanium crucible, where it is inserted into the apparatus and heated to 500 °C. Eventually, radium will begin to flow out of the crucible, at which point it is "cracked." Then, smaller flow rates of radium can be created by turning down the temperature of the oven. The exact process by which this reaction occurs is not well understood. Notably, the temperature at which a "crack" occurs varies between oven loads.

Table 7.2: Oven crack temperatures of various oven loads.

Date	Load	Crack Temperature
02/28/2020	1 μCi ^{226}Ra	528 °C
07/23/2020	First ^{223}Ra load	525 °C
03/11/2021	2 μ Ci ^{226}Ra	524 °C
04/16/2021	2 μ Ci ^{226}Ra and 10 mCi ^{223}Ra	-

The radium-225 EDM experiment is currently statistics and not systematics limited. This means that the more efficiently a beam of radium can be created, the higher the resulting

statistical sensitivity will be. It is entirely possible that a more efficient chemistry process than what is currently used exists.

For this purpose, an Atomic Beam Fluorescence (ABF) setup has been built at Michigan State University, to study different chemical processes using non-radioactive chemical surrogates. Experimentation can be done where a known amount of calcium is dissolved in water and prepared by FRIB radiochemistry personnel in the form of calcium nitrate. Calcium was chosen due to its non-radioactive nature, as well as its similar electronic structure to radium. Furthermore, Harvesting calcium from FRIB has already been demonstrated with high efficiency [54]. The dissolved calcium can then be loaded into the oven with aluminum foil and barium, using the same procedure as for radium. This hopefully will produce a beam of atomic calcium when heated. By measuring the atomic flux of the emitted calcium beam, and knowing the amount of calcium initially put in, the efficiency with which an atomic beam is created can be characterized. In addition, with non-radioactive sources, different chemical procedures can be tested. Calcium can arrive in other forms, such as calcium chloride, and the metallic barium can be replaced with other elements as well. In this way, the efficiency can be measured for different chemical loading procedures, and any improvement in efficiency can be identified to be tried for radium.

Test studies have been done with metallic calcium, and a signal has successfully been seen. The goal at this stage, before testing other processes, is to refine the setup to be able to resolve an atomic flux at the 10^8 atoms per second level. A variety of studies were performed to characterize the lowest atomic flux currently visible, and a summary is now given.

7.3 Characterizing the Lowest Resolvable Atomic Flux with Metallic Calcium Fluorescence Studies

The signature of seeing fluorescence of calcium was a peak in the plot of fluorescence count rate versus laser frequency, which was uncorrelated to power fluctuation. This required scanning the laser frequency, and being able to measure in real time the count rate within a given interval around the laser frequency, and the laser power. Scans were done on different days, under varying conditions. Within a given day, the only change made was to the laser power. From day to day, the overall apparatus of the optical setup could change. For each scan, the fluorescence signal was characterized by the area under the peak. This involved fitting to the overall trend. Signal sizes at varying powers within a given day could then be compared to each other, and a fit done of the fluorescence signal as a function of laser power. A more detailed description of the ABF apparatus is given in Section 7.3.1

7.3.1 Experimental Setup

The ABF experimental apparatus, depicted in Figure 7.3, consists of an effusive oven, attached to a 6-way cross viewing chamber. The oven creates the atomic beam, which flows into the 6-way cross in the z direction. The 6-way cross has two viewports in the x direction, and a single viewport in the y direction. This allows for laser light to be shown in the x direction, perpendicular to the atomic beam, and the fluorescence this causes to be collected on an SPD in the Y direction. The laser light is created by an MSquared laser system. Data is taken in real time using a Labview program. The particulars for this setup are now discussed.

Figure 7.3: Conceptual diagram of the MSU atomic beam fluorescence apparatus. Atoms are emitted from the effusive oven, where the drift into the 6-way cross to interact with laser light created by an MSquared laser system. Fluorescence is collected on an SPD and counted with an SR400 counter.

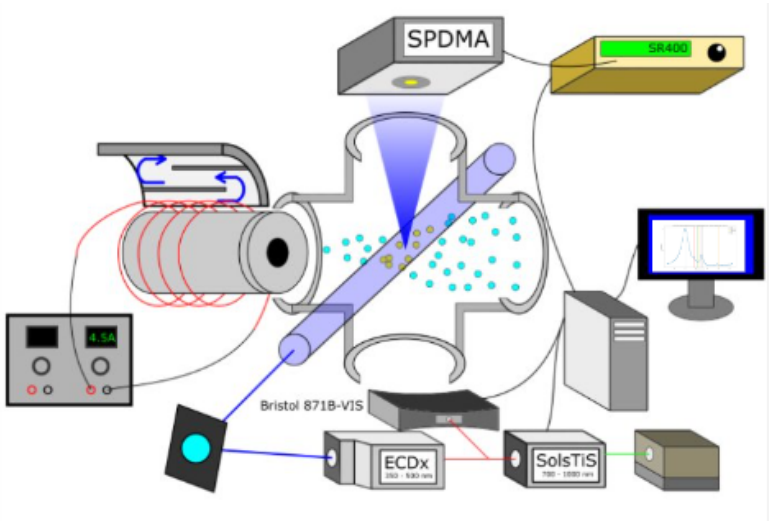

7.3.1.1 Effusive Oven

The effusive oven currently installed is the second oven manufactured by Spinlab at MSU. The first was shipped to the Massachusets Institute of Technology, for use with their study of Radium Fluoride. The one currently in use was custom fabricated, based on designs and lessons learned from making the first one. It was fabricated in the machine shop at the Biophysical Sciences building at MSU. A detailed description of its assembly will be in the appendix, but a brief overview is provided here. The overall shell of the oven is a 4.5"-flange 6-way cube. One of the flanges contains a 3" long reducing nipple which reduces from 4.5" to 2.75". The crucible and nozzle is inserted in this nipple. This crucible and nozzle assembly is displayed in Figure 7.4

Another flange perpendicular to this provides a cooling jacket, designed to be placed right at the center of the cube. The water lines are cooled using a Thermotek chiller set to

Figure 7.4: Diagram of the Titanium crucible for oven loading.

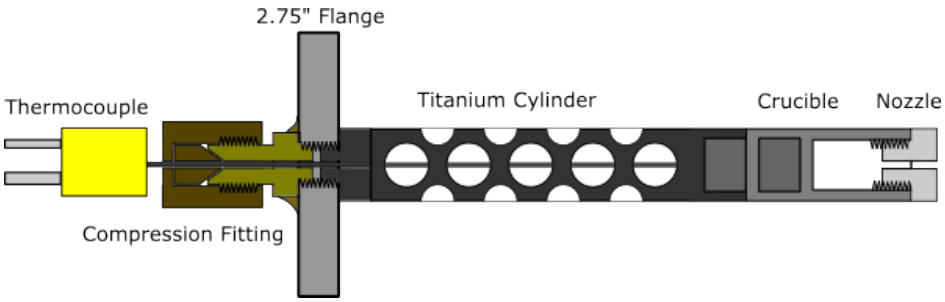

Figure 7.5: Diagram of the atomic beam effusive oven.

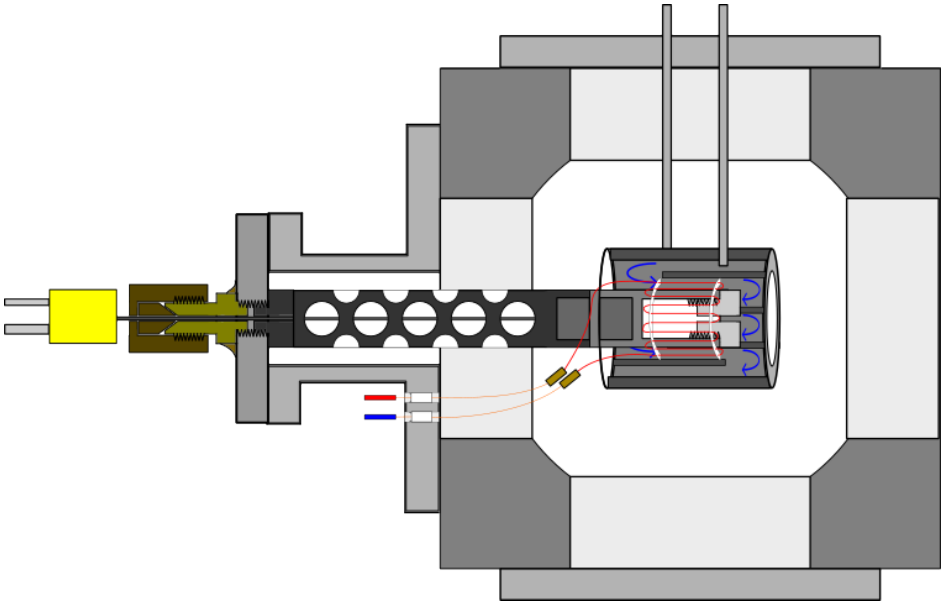

20 °C. A vacuum pump assembly and ion gauge are also attached, so as to pump down to vacuum. Within the vacuum chamber is sat a Tantalum wire that serves as a filament. This is woven through the holes of two ceramic discs, so that filament surrounds the crucible, but no part of of the filament comes into contact with the outer oven. The filament is connected to feedthroughs welded into the reducing nipple, which lead to a power supply from which current can be run.

The temperature of the crucible is monitored in real time with a K-type thermocouple. The relationship between oven current and equilibrium oven temperature was studied, and

can be seen in Figure 7.6

Figure 7.6: Plot of the effusive oven temperature versus power supply current.

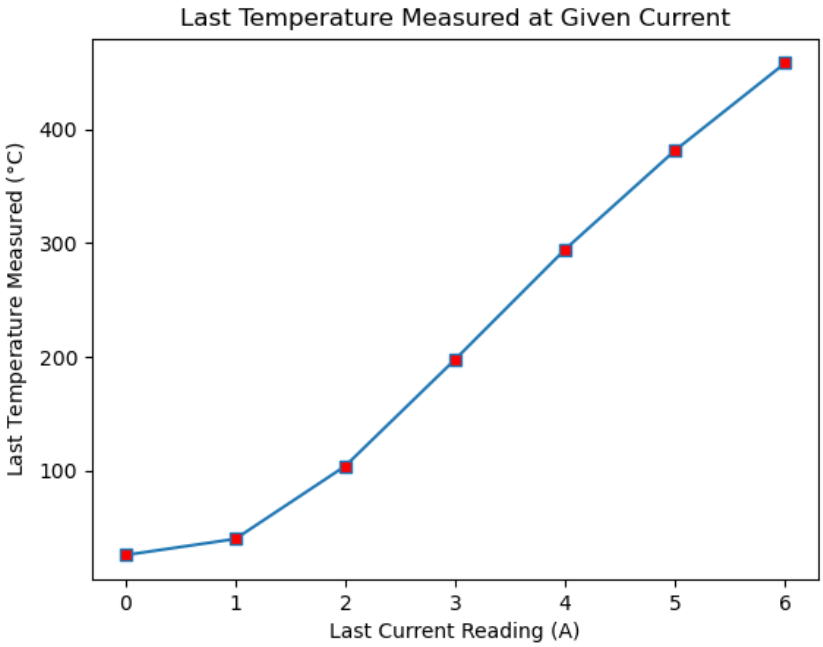

The points on this plot are summarized in Table **??**.

Table 7.3: Table of the temperatures created by different current settings for the filament power supply.

Current (A)	Temperatures (°C)
0.0	26.0
1.0	40.2
2.0	104.2
3.0	198.0
4.0	294.7
5.0	381.5
6.0	458.2

7.3.1.2 Fluorescence Interaction inside the 6-way Cross

Attached to the oven via a 4.5" - 2.75" reducing flange is a 6-way cross. This is the chamber where the fluorescence takes place.

Figure 7.7: Full diagram of the atomic beam fluorescence setup. Atoms emitted from the effusive oven are excited by laser light, and have excitation collected by an single photon detector.

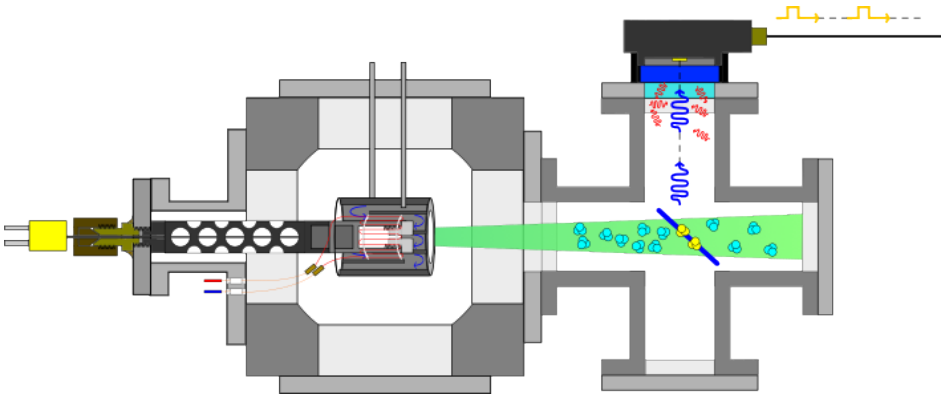

Directly across from the 6-way cross is a blank flange. On either side, perpendicular to the atomic beam, are two anti-reflection coated viewports. These allow for laser light to be directed in and out, and overlap with the atomic beam. On the top of the 6-way cross, perpendicular to both the atomic beam and laser beam, is the 422 nm filter and Thorlabs SPDMA single photon detector that is used use to count the fluorescence count rate. The SPDMA detects individual photons hitting it, and outputs a proportional number of TTL signals that requires counting. The 422 nm filter is used to filter out background light that is off-resonance from the transition that is actually trying to be fluoresced.

7.3.1.3 Laser System

The laser beam sent into the 6-way cross is created from a laser system consisting of a 532 nm Lighthouse Photonics SPROUT pump laser, an MSquared SOLSTiS titanium-sapphire

laser capable of outputting 700 - 1000 nm light, and an MSquared ECDX doubling cavity, capable of outputting 350 - 500 nm of light. To fluoresce calcium, both the SOLSTiS and ECDX had to be utilized to produce light at a wavelength of $\sim 422\,\text{nm}$. The laser was locked using a Bristol 871-VIS wavemeter, which was coupled using a FG050UGA 50 μm multi-mode fiber. A table of various isotope peaks is given as Table 7.4.

Table 7.4: Table of the transition wavelengths of the most abundant calcium isotopes.

Isotope	Abundance	I	Transition	Vacuum Wavelength (nm)	Ti:Sapph Output (nm)
Ca-40	.96941	0	$^1S_0 \rightarrow^1 P_1(F = 0 \rightarrow 1)$	422.7917	845.5834
Ca-44	.02086	0	$^1S_0 \rightarrow^1 P_1$	422.7912	845.5825
Ca-42	.00647	0	$^1S_0 \rightarrow^1 P_1$	422.7915	845.5830
Ca-48	.00187	0	$^1S_0 \rightarrow^1 P_1$	422.7908	845.5816
Ca-43	.00135	7/2	$^1S_0 \rightarrow^1 P_1(F = 7/2 \rightarrow 5/2)$	422.7913	845.5826
Ca-43	.00135	7/2	$^1S_0 \rightarrow^1 P_1(F = 7/2 \rightarrow 7/2)$	422.7913	845.5827
Ca-43	.00135	7/2	$^1S_0 \rightarrow^1 P_1(F = 7/2 \rightarrow 9/2)$	422.7914	845.5828

Table 7.5: Table of the detuning of the relevant calcium transitions relative to the most abundant isotope.

Isotope	Transition	Detuning from Ca-40 (GHz)	Reference
Ca-40	$^1S_0 \rightarrow^1 P_1(F = 0 \rightarrow 1)$	0	[55]
Ca-44	$^1S_0 \rightarrow^1 P_1$	.7738	[55]
Ca-42	$^1S_0 \rightarrow^1 P_1$	.3931	[55]
Ca-48	$^1S_0 \rightarrow^1 P_1$	1.513	[55]
Ca-43	$^1S_0 \rightarrow^1 P_1(F = 7/2 \rightarrow 5/2)$	.6788	[55], [56]
Ca-43	$^1S_0 \rightarrow^1 P_1(F = 7/2 \rightarrow 7/2)$	.6287	[55], [56]
Ca-43	$^1S_0 \rightarrow^1 P_1(F = 7/2 \rightarrow 9/2)$	.5554	[55], [56]

The isotope shifts and A and B coefficients for the Ca-43 isotope are given in Table 7.6.

Table 7.6: Table of the hyperfine coefficients of Ca-43.

Ca-43	Value	Reference
A Coefficient	-15.54 MHz	[56]
B Coefficient	-3.48 MHz	[56]

Figure 7.8: Diagram of the laser setup directly in front of the BLUREI laser. This remained unchanged.

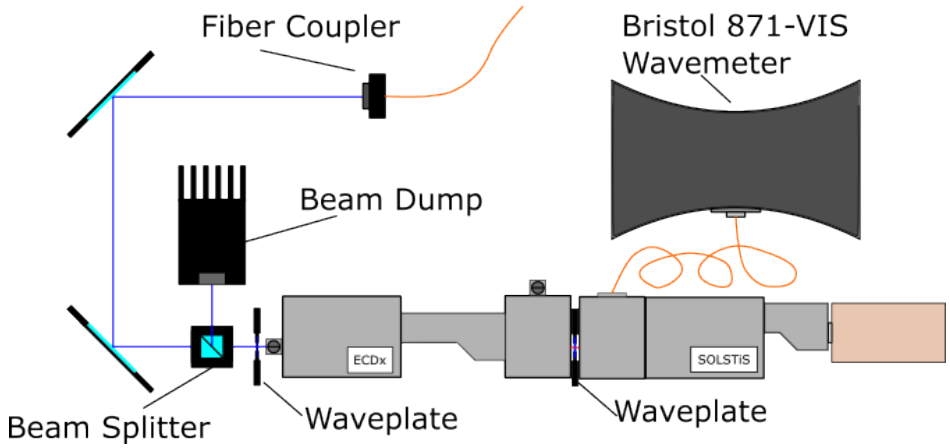

7.3.1.4 Optical Setup

In order to properly fluoresce calcium, simply creating the beam was not enough - it had to be guided to the interaction region of the atomic beam. The optical setup to do this went through several iterations, labeled setups 1-5. The optical system consisted of two separate parts. The first was directly in front of the laser, designed to couple the output beam into the fiber. It was also used to adjust the power sent into the fluorescence chamber, with any excess power being sent to a beam dump. A diagram can be seen in Figure 7.8

The optical setup directly in front of BLUREI remained unchanged during each study. The optics after the fiber, which were directly on the ABF stand, went through various changes. This optical setup served multiple purposes: it had to depolarized the beam by sending it through a depolarizer, ideally with as large a beam as possible. Then, it shrank

the size of the beam with a series of telescoping lenses, before sending a collimated beam through the 6-way cross. Finally, the beam exited from the 6-way cross and had to be focused onto a powermeter, so a measurement of the power could be made.

5 different setups in total were used over the course of the scan studies. A description of each setup can be found in Table 7.7.

Table 7.7: Table of various setups of different scans.

Setup	Description
Setup 1	Same as Setup 2, but elastic alignment tools were left in place for the scan, likely increasing the background significantly
Setup 2	See 7.9. Uses two telescopes, one with 100/-50 mm telescoping pair, and one with 250/150 mm telescoping pair
Setup 3	On 06/26/2024, black acktar tape was installed for background reduction purposes. This involved removing the ABF apparatus from its stand with the optical components, and putting it back, altering the optical components. After doing background scans with this setup, it was noticed that the laser was not aligned well through the center.
Setup 4	After the background scan was done on 07/03/2024, it was noticed that the laser was no longer aligned through the center, due to moving the apparatus. It was realigned through the center, giving setup 4.
Setup 5	To reduce the size of the beam going through the 6-way cross, the second 250/150 mm telescoping lenses were replaced with a single 500 mm lens. See 7.10 for a diagram.

Figures for the two main overall setups are given in Figures 7.9 and 7.10.

Throughout these studies, the size of the beam was clearly a major source of error, as its shape was difficult to control. The fiber used to move the light onto the ABF stand was a 40 m long multimode fiber, meaning that different modes could be coupled into it. This caused wide variations in the beam profile. A study was done with simulation code to determine the effect that the beam width has on the laser profile, and the conclusion was that it was minimal. More detail on this simulation will be given later.

The lasers are controlled by software native to them on the computer. In order to control the lasers, lock them to the wavemeter, and simultaneously record the wavelength and count TTL signals, software had to be created.

7.3.1.5 Atomic Fluorescence Spectrum Meausrement Software

The measurement software for the atomic beam fluorescence setup was custom made, and uses LabVIEW version 2022. The software made not only takes data, but also locks the laser to the wavemeter. In order to figure out how to do this, a program had to first be made that strictly served the purpose of locking the laser. This program, LockingFluorescenceCombinedV7, is described in detail in the appendix, but a brief inteview is given here. The interface of the program is shown in Figure 7.11.

Figure 7.9: Diagram of the laser apparatus used for setup 2.

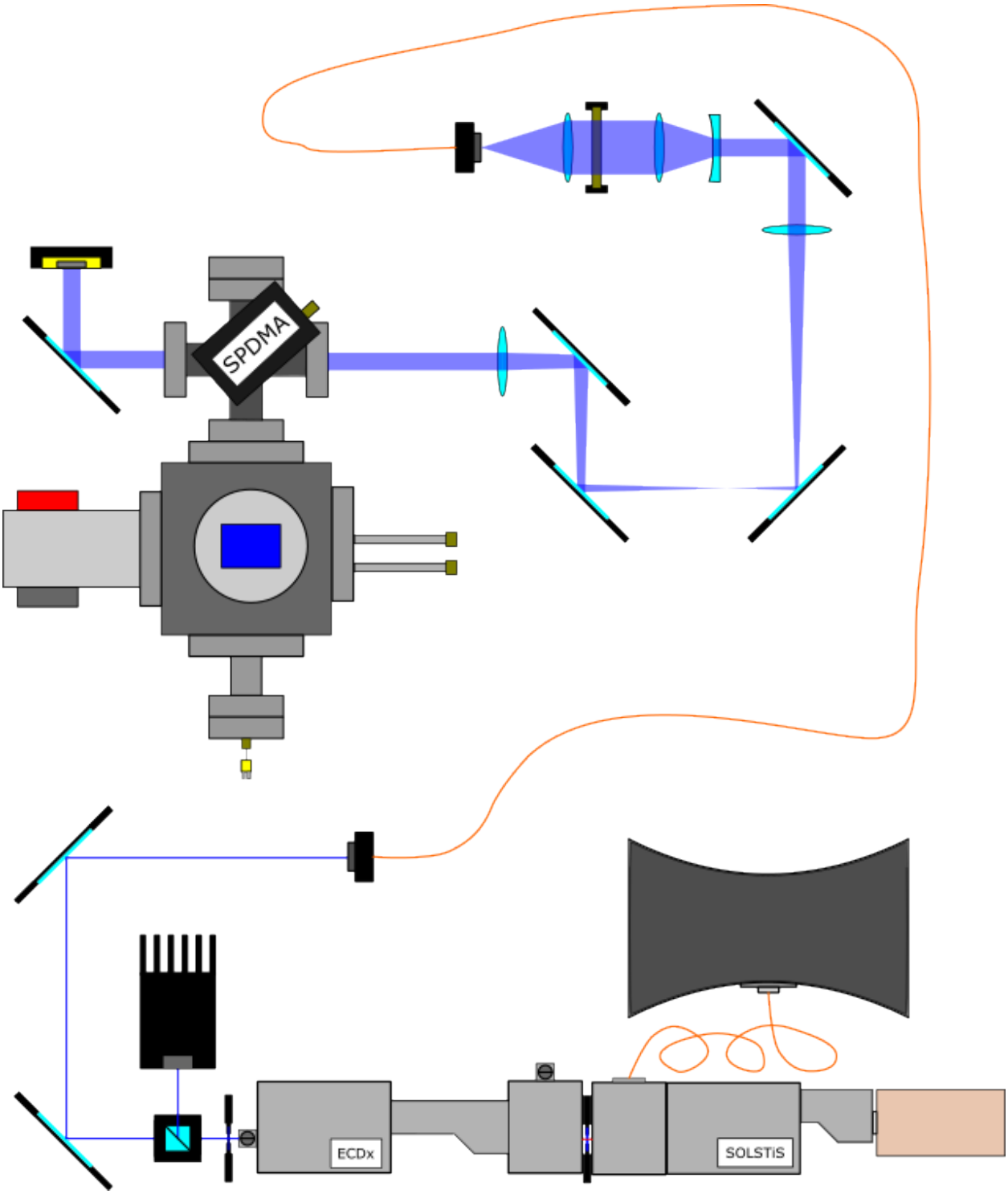

Figure 7.10: Diagram of the laser apparatus used for setup 5.

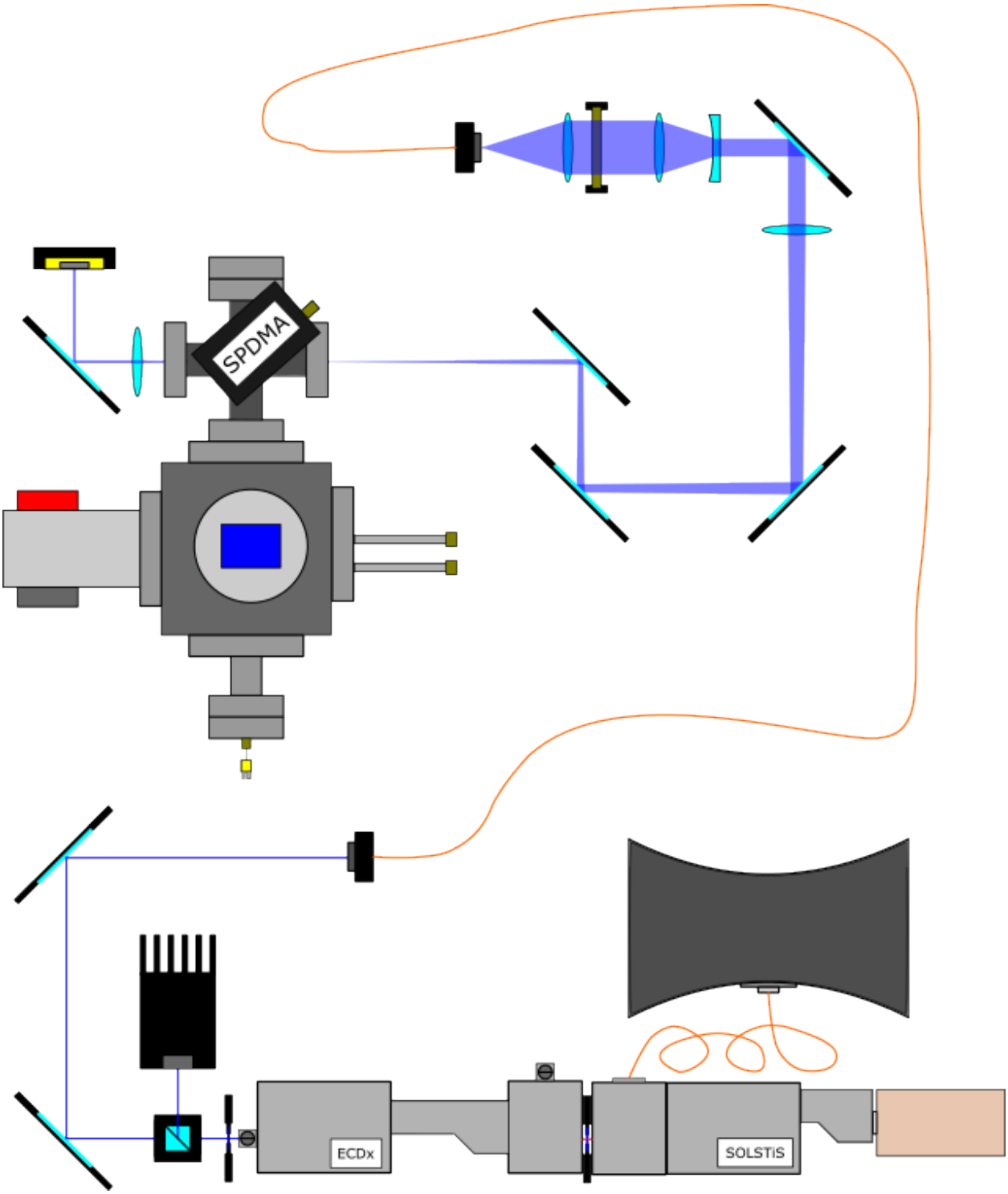

Figure 7.11: Image of the front panel of the fluorescence measurement software.

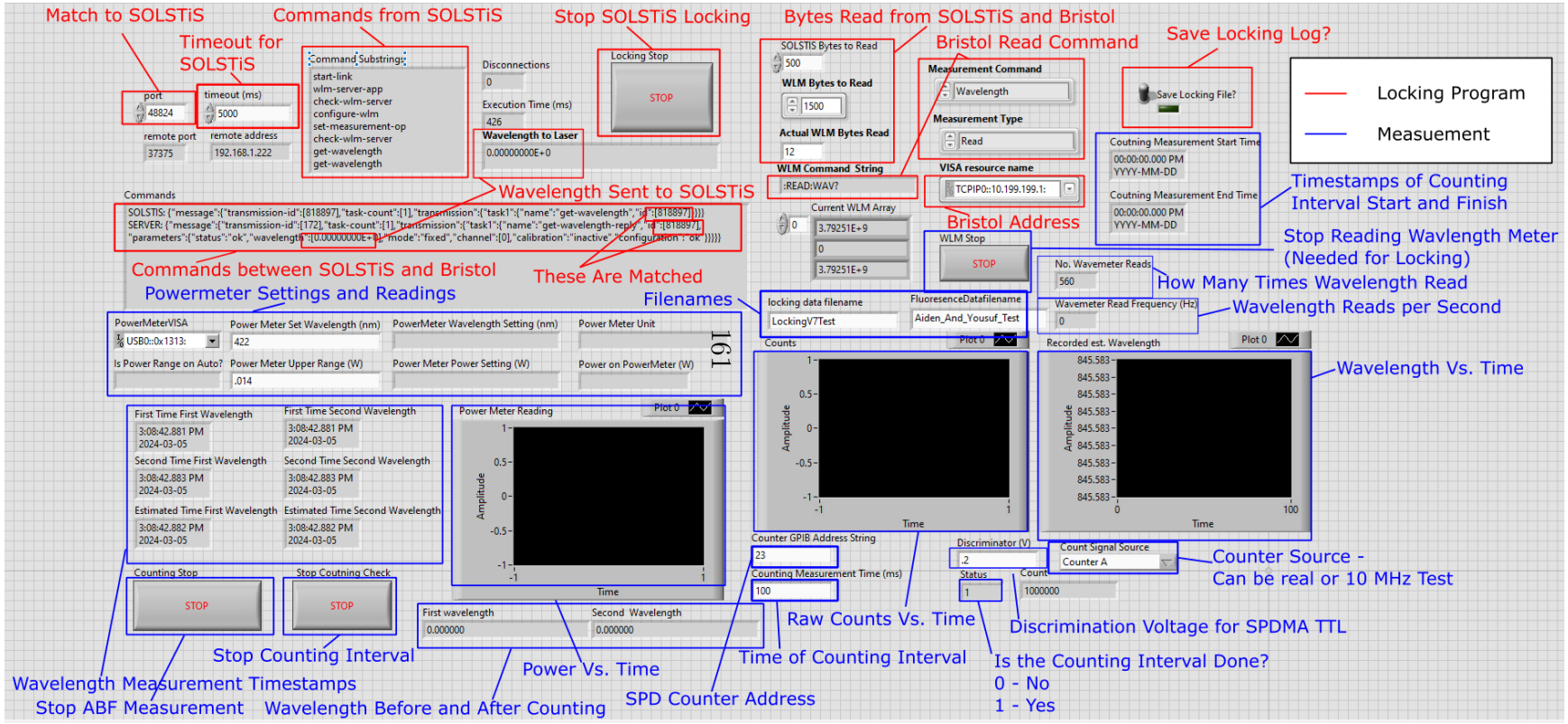

The program essentially runs by constantly reading from the wavemeter, and updating a corresponding local variable. Every time the value is needed, either because it's been asked by the laser locking or it needs to be logged, this local variable is referenced, which holds the most recent measurement. Logged into the data at each step are the results of the counting interval, two wavelength measurements, four timestamps, and a laser power reading.

The timestamps are provided by the computer, the wavelengths from the wavemeter, the power from a PM1000 Thorlabs power meter, and the counting interval from an SRS400 Counter. The counter takes inputs from the SPDMA, and counts them using a 10 MHz internal clock. This clock can also be used to test the counter. The length of the counting interval can be set in milliseconds. It is reset every time upon program start, and the resetting process takes roughly 5 seconds to occur. Once the reset is done, the counter is automatically fed the necessary commands to configure the settings needed, and the counting measurements start. Typically, 100 ms counting intervals are used. Each data point is separated in time by roughly 110 ms, so it seems that all the other data taking operations take around 10 ms. This means that the program is actually measuring the counts 10% of the time. This seems to be fine, but does limit how short the counting interval should be. A counting interval of 10 ms, for example, would be non-ideal, since only 50% of the time would the measurement actually be counting.

7.3.1.6 Typical Experimental Values

With so many instruments, it can be hard to keep track of what each needs to be set to. A summary table is given below:

Table 7.8: Summary of the parameters for the SPDMA.

SPDMA		
Dark Count Rate	Photon Detection Efficiency @ 422 nm	Sensor Diameter
$\approx$ 100 Hz	89.4% (Rough Estimate)	500 μm
Max. Count Rate	TTL Output Height (Low)	TTL Output Height (High)
20 MHz	0 V	3.5 V

Table 7.9: Summary of the settings and parameters for the SR400 counter.

SR400		
Input (set)	Timing Clock (set)	Counting Mode (set)
Counter A	10 MHz Internal Clock	A, B separate
Discriminator Voltage	Counting Interval Length (Typical)	Reset time
.2 V	100 ms	$\approx$ 5s

Table 7.10: Summary of the settings and parameters for the coolant chillers.

Chillers	
ABF Cooling Jacket Chiller Temp (Typical)	SOLSTiS Chiller (Typical)
20 C	20 C

Table 7.11: Summary of the settings for the laser.

SOLSTiS		
Scan Start	Scan End	Scan Rate
845.581 nm	845.585	5 MHz/s
ECD Lock?	Laser Scan Doubled Light Max Power through Fiber	Sprout Power (set)
ON	20 mW	18 W

Table 7.12: Summary of the settings for the current source for the oven.

Current Source	
Current and Voltage Range	Source Setting
8A, 20V	Current Source

7.4 Data Summary

Five fluorescence studies were done, each for a particular day. Each fluorescence study involved performing a fluorescence scan under varying powers. The integrated fluorescence signal as a function of laser power is linear in the low power regime. By getting a value for this slope, it can be compared to simulated values to get a measurement of the atomic flux. Other studies were done to reduce the background signal of our measurement. A summary table is given below:

Table 7.13: Summary of the spectroscopic studies perfromed on Calcium.

Purpose	date	T	Power Range (# of scans)	Background Suppression	Laser Beam Profile	Background Power Slope (First Method)	Scan Rate
-	-	°C	mW (-)	-	-	kHz / mW	MHz/s
Background	05/10/2024	Room Temp	1 → 8 (5)	422 nm Filter	Setup 2	465.4 ± 2.7	2
Background	07/03/2024	Room Temp	1 → 12 (5)	422 nm Filter, Black Aktar Tape	Setup 3	93.28 ± .85	5
Purpose	date	T	Power Range (# of scans)	Background Suppression	Laser Beam Profile	Low Power Curve Area Slope	Scan Rate
-	-	°C	mW (-)	-	-	GHz · kHz / mW	MHz/s
Ca High Flux	05/02/2024	457	.5 → 4 (5)	422 nm filter	Setup 1	785.3 ± 64.6	2
Ca High Flux	05/10/2024	380	.5 → 8 (3)	422 nm filter	Setup 2	96.08 ± 2.94	2
Ca High Flux	07/03/2024	457	3 → 12 (4)	422 nm filter, Black Aktar Tape	Setup 4	3503 ± 365	5
Ca Low Flux	07/08/2024	338	1 → 7 (5)	422 nm filter, Black Aktar Tape	Setup 4	1.894 ± .103	5
Ca Low Flux	07/22/2024	338	3 → 16 (8)	422 nm filter, Black Aktar Tape	Setup 5	1.672 ± .171	5

More detail will now be given, starting with how the integrated signal was characterized.

7.5 Fluorescence Signal Analysis

For each scan, the fluorescence count rate, power reading, and laser wavelength are all taken in real time, through the software previously discussed. Each raw data file contains data taken both before the scan, and after. This excess data must be cut out for a proper count rate versus wavelength plot to be made. This requires the actual scan data to be defined.

7.5.1 Defining the Scan Interval

When the raw data file is plotted line by line, the count rate and power look something like this:

Figure 7.12: Raw Scan Data File. Red indicates the laser power reading, and is on the left. Blue indicates the count rate, and is on the right.

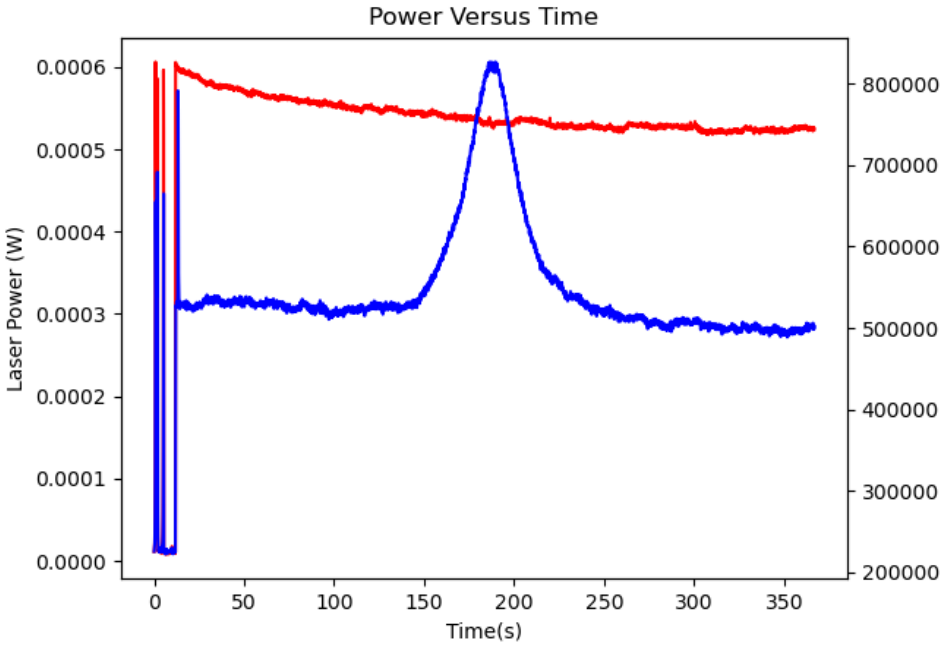

The best way to define the scan is to look at the wavelength versus data point index, and use it to custom define the beginning and end of the scan. Since the fluorescence occurs in the middle of the scan, it's not a big deal to exclude the very tail ends of the scan. This ensures all of the data being analyzed is relevant. The wavelength plot looks something like this:

Figure 7.13: Scan Wavelength Versus Time. The linearly increasing region is the area of interest for the scan.

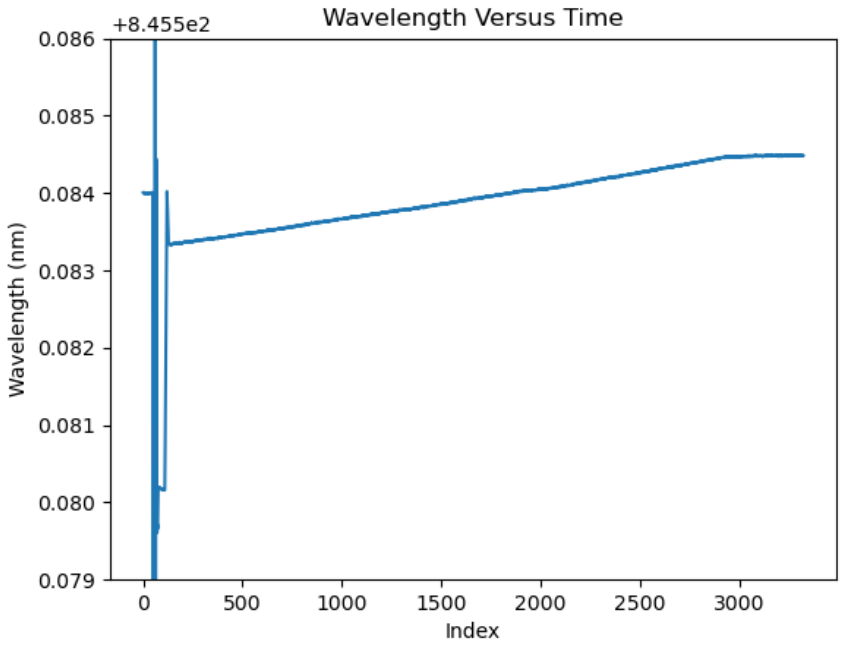

The scan interval is then very clear: It's the section which sees a gradual increase in the wavelength. By selecting two of the indices, one at the very beginning of the scan, and one at the very end, only the relevant data is used. Since the down time in between each scan can change, this has to be done separately for each measurement. If the software was updated to allow for the scan to be controlled from the LABVIEW data acquisition program, it might become possible to only take the scan data. For now though, the LABVIEW program has

no idea when the scan starts and ends, so this is necessary.

7.5.2 Characterizing the Background Decay

As the scan progresses, the power of the laser decays at what looks like exponential rate. This is an artifact that needs to be taken into account, since the background counts of the signal are modeled to be linear with the laser power:

$$f_{Background}(P) = M \cdot P + C \tag{7.1}$$

where C is the background counts with the laser off, P is the laser power, $f_{Background}$ is the background count rate, and M is the slope in kHz/mW.

The laser power is modeled to have an exponential dependence on frequency, of the form:

$$P(\omega) = P_0 + Ae^{B\omega} \tag{7.2}$$

The laser power fluctuation varies from scan to scan. It can be relatively small:

In this case, only increasing roughly 10 μW. There are cases where it is quite significant, however:

In this case, the power rises from 2.1 mW to 2.8 mW - an increase of 700 μW, 33% of the power level. This causes a variation in the count rate due to the power level, as can be seen below:

Clearly, the relation between the power and background level is very correlated. Consider now the effect this drift has on the counts. If the P dependence on ω is substituted in:

$$f_{Background}(\omega) = M \cdot P_0 + M \cdot Ae^{B\omega} + C \tag{7.3}$$

Figure 7.14: Plot of a small laser power fluctuation during a scan. Empirically, it appears to be exponential.

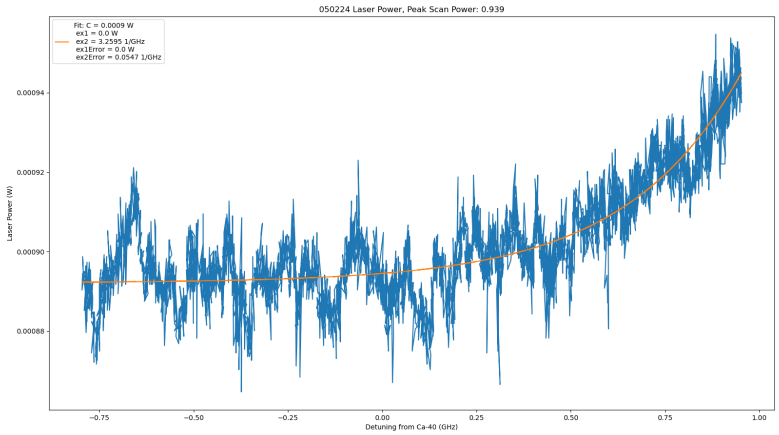

many of these variables can be aborbed into a single parameter. Thus,

$$f_{Background}(\omega) = C' + M'e^{B\omega} \tag{7.4}$$

It should be noted that the parameter B remains the same between the power dependence, and the count rate dependence. Thus, by fitting to the power dependence, the exponential decay for the background counts can be derived. The actual count rate as a function of detuning frequency can be seen below:

7.5.3 Signal Scan Analysis

The shape of the peak caused by the fluorescence closely matches a Lorentzian profile. The equation fit to the total count rate line shape has the form:

$$f(\omega) = C + De^{B\omega} + \frac{A}{\pi}\frac{\frac{\Gamma}{2}}{(\omega - b)^2 + (\frac{\Gamma}{2})^2} \tag{7.5}$$

Figure 7.15: Plot of a large laser power fluctuation during a scan. Once again, this appears to be somewhat exponential.

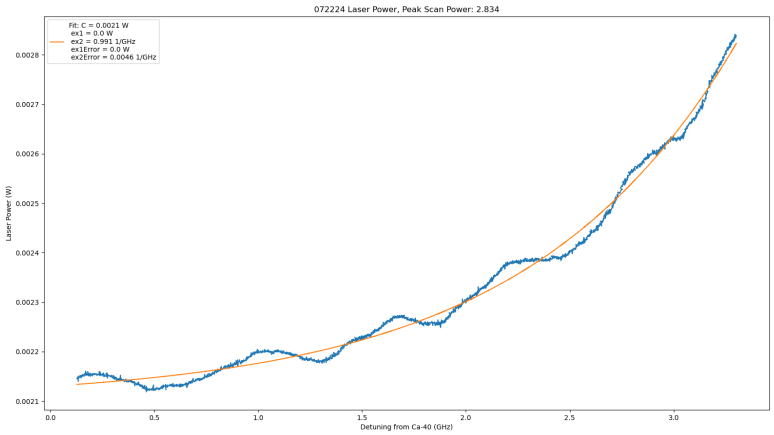

where the value of B is taken from the value derived from the power decay. Using this formula, the background counts for the scan can be considered as

$$f_{Background}(\omega) = C + De^{B\omega} \tag{7.6}$$

and the signal curve as

$$f_{Signal}(\omega) = \frac{A}{\pi}\frac{\frac{\Gamma}{2}}{(\omega - b)^2 + (\frac{\Gamma}{2})^2} \tag{7.7}$$

The parameter of interest from scan to scan for the signal curve is the integrated count rate under the signal. Conveniently, the Lorentzian function is such that

$$I_{Signal} = \int_{-\infty}^{\infty} f_{Signal}(\omega)d\omega = \frac{A}{\pi}\int_{-\infty}^{\infty}\frac{\frac{\Gamma}{2}}{(\omega - b)^2 + (\frac{\Gamma}{2})^2}d\omega = \frac{A}{\pi}\pi = A \tag{7.8}$$

So, by fitting to the Lorentzian, the area can be easily derived as the value taken by A.

Figure 7.16: Plot of the raw scan data, with a large power fluctuation occuring during a scan.

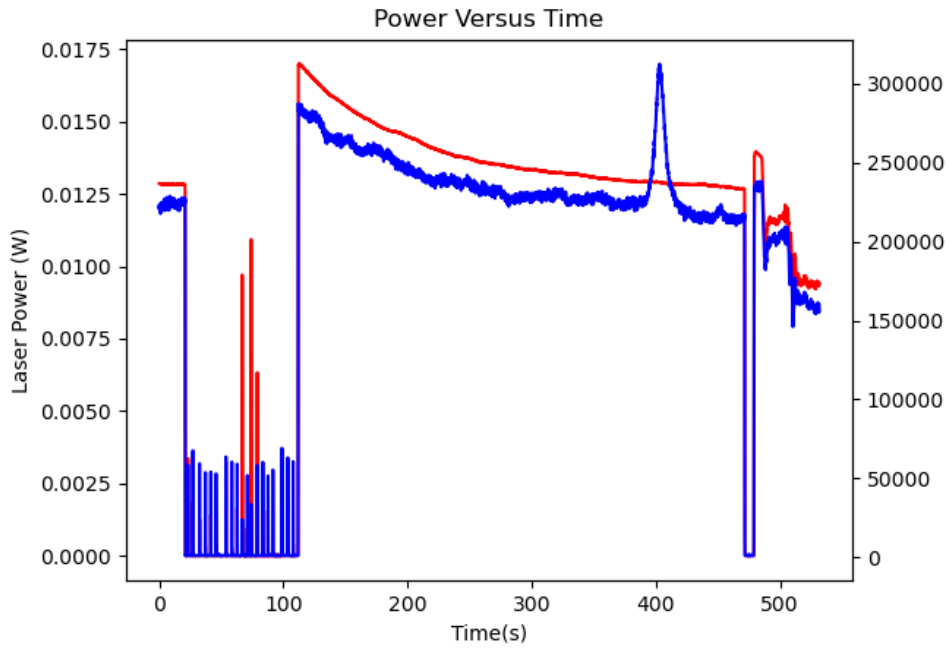

7.5.4 Uncertainty Quantification

To perform the fits, the uncertainty for each count rate and power data point had to be known. For the count rate, this was attempted in two different ways: either with Poisson statistics, where for the count rate taken by

$$f = \frac{N}{\Delta T} \tag{7.9}$$

The uncertainty was found by

$$\sigma_F = \frac{\sqrt{N}}{\Delta T} \tag{7.10}$$

The other method was to take the standard deviation of the first 50 data points in a

Figure 7.17: Plot of an exponential and lorentzian fit to the scan data.

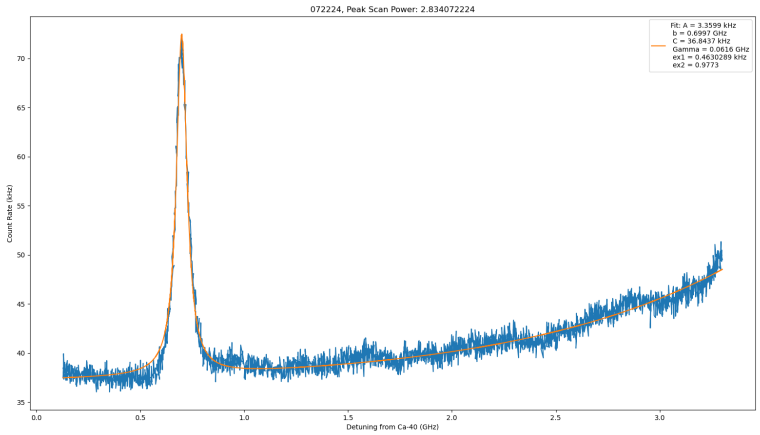

count file, where the count rate was assumed to be flat. The defined background counts are displayed as a histogram in Figure 7.18.

By taking the standard deviation of these points, a reasonable expression for the variation in the counts due to statistics can be derived. This analysis performed on the 07/22/2024 data looked like:

In addition to the uncertainties for the individual count rate points, the error in the power readings had to be accounted for. Not only did each individual power data point have uncertainty, which was necessary to know for the fit to exponential data for the count rate exponential decay parameter, but there also had to be some kind of quantization to account for the variation in overall power during the scan. For fitting the power to the exponential, the uncertainty in the data was characterized by taking the overall standard deviation of the laser power data set. As for characterizing the power for each scan, there were two ways to do this: one was to simply to take the mean and standard deviation of the laser power as the power level, and the associated uncertainty, as shown in the previous plot. The other way was to find the power at the frequency where the the peak height was found to be, use that

Figure 7.18: Histogram of the counts associated with the background.

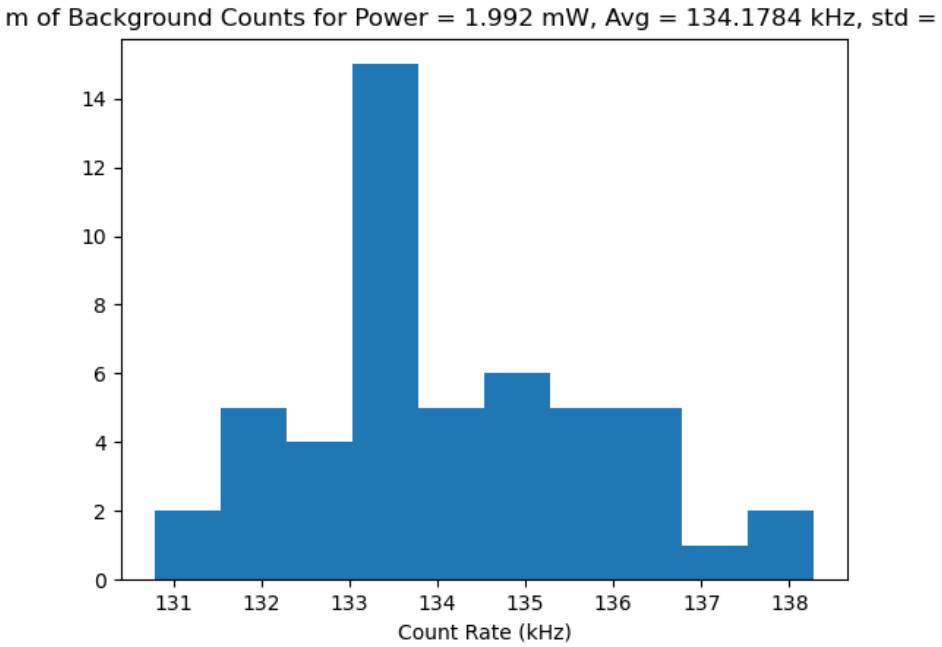

Figure 7.19: Fit to the area under the curves versus average laser power.

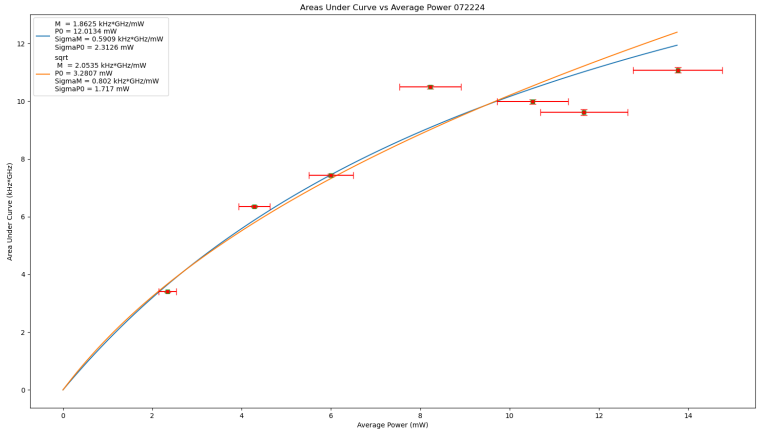

as the power for the curve, and take the standard deviation of the 50 data points around it to use as an uncertainty. The resulting plots looked like this:

Figure 7.20: Fit to the area versus the peak laser power.

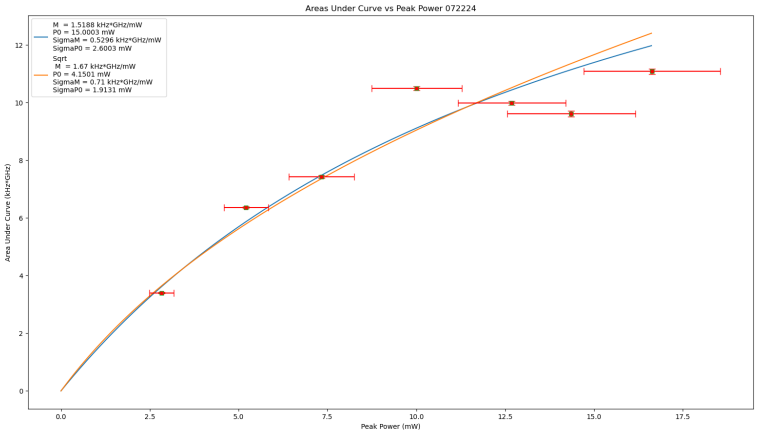

With two methods of determining the uncertainty of the count rates, and two methods of defining the power of the scan, this resulted in 4 different plots to analyze, the fourth of which for 07/22/2024 is shown here:

Figure 7.21: Poissonian fit to the area versus the peak laser power.

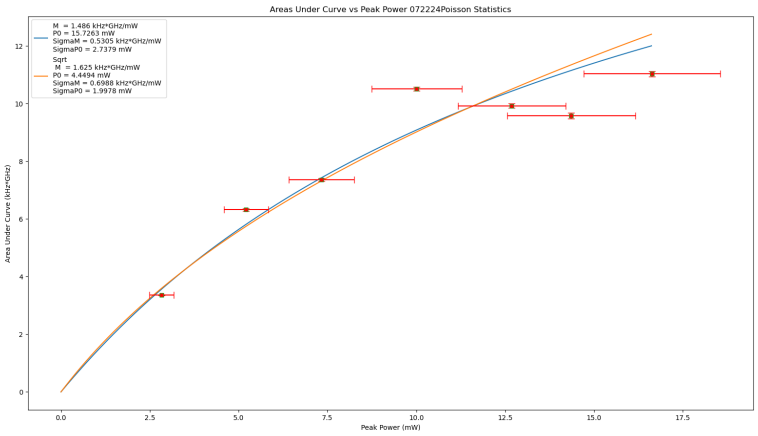

7.5.5 Results of Background Study

For each scan, the background could be parameterized from this analysis. Ideally, the background counts should be linear with the power of the laser. The background counts can be parameterized by using the constant background offset C, with the uncertainty being that of the total background, found by the formula:

$$\sigma_{Background} = \sqrt{\sigma_C^2 + \sigma_D^2 e^{2B\omega_p} + \sigma_B^2 D^2 \omega_p^2 e^{2B\omega_p}} \tag{7.11}$$

where B, C, and D are the parameters from the equation from $f_{Background}(\omega)$ and ω_p is the frequency of the laser at the peak height. The background parameters C with this error were plotted as a function of peak power, and linear fits taken. They looked like:

Figure 7.22: The background counts plotted versus the laser power at the height of the signal on 07/22/2024.

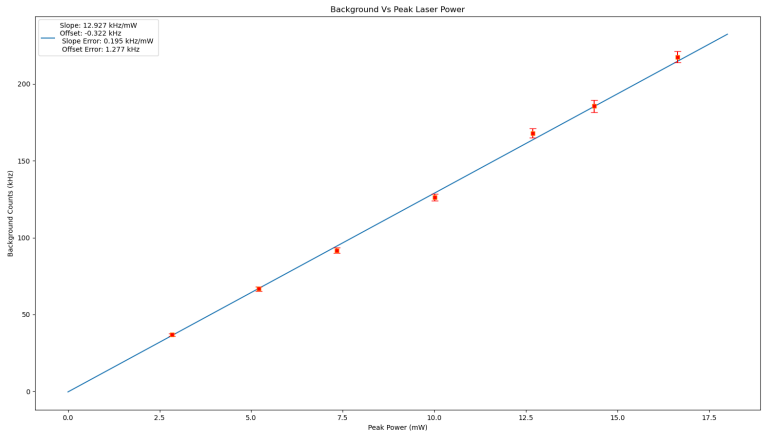

Seven studies of the background were taken, two of them dedicated signal scans with the oven off. The background and uncertainty of the background scans was parameterized by simply taking the mean and standard deviation of the data taken. A plot was made of the

linear slopes of these 7 studies:

Table 7.14: Table of the background slopes for each study.

Date	Oven Temp	Background Slope	Setup	Blackout Tape Installed
-	C	kHz/mW	-	y/n
05/02/2024	457	1170 ± 40	setup 1	n
05/10/2024	Room Temp	465.4 ± 2.7	setup 2	n
05/10/2024	380	449.4 ± 24.8	setup 2	n
07/03/2024	Room Temp	93.28 ± .85	setup 3	y
07/03/2024	457	29.6 ± 3.9	setup 4	y
07/08/2024	338	49.07 ± .25	setup 4	y
07/22/2024	338	12.93 ± .20	setup 5	y

To compare these studies, it's important to remember that the oven temperature should have no effect on the background. The study done on 05/02/2024 was done with an obstruction that likely caused a large amount of extra light to scatter throughout the 6-way cross. This gives an explanation as to why it was so much higher than all the other slopes. The two studies done on 05/10/2024 are very well in agreement with each other. Once the blackout tape was installed, the background counts went down significantly. The first scan done on 07/03/2024 was done with setup 3, and was misaligned through the 6-way cross. This could have caused internal reflections that increased the background, since the laser wasn't straight going through. It was realigned for setup 4, and the background slope went down significantly. There was a slight increase between 07/03/2024 and 07/08/2024 - This is harder to explain, though it could simply be that the optics shifted around somewhat. Finally, for setup 5 on 07/22/2024, the laser was more tightly focused going through the 6-way cross, and it resulted in the lowest background slope that was seen. It can be concluded that the blackout tape had a significant effect, reducing the background slope by an order of magnitude. It also is clear that alignment of the laser through the 6-way cross has a definite effect as well. It should also be noted that, on 05/10/2024, the background slope

was reproducable when everything was kept the same.

7.5.6 Dependence of Area on Scan Rate

For these studies, the scan rate parameter used was either 2 or 5 MHz/s. Since the analysis technique finds the area under the count rate curve with respect to wavelength, and not time, the scan rate should not have any observable effect. However, on a scan from 07/03/2024, 3 scans were taken at 5 MHz/s, but another scan taken at 2 MHz/s gave a point that seemed very much like on outlier for the data. When added to the data taken at 5 MHz/s, the following plot can be made:

Figure 7.23: Data from 07/03/2024 with 2 MHz/s scan rate area plotted.

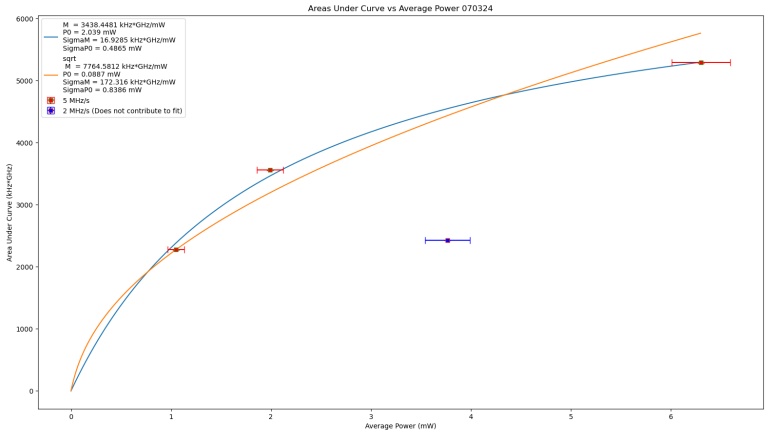

The area of the curve done at 2 MHz/s, shown in blue, seems like a significant outlier. The other evidence for there being some dependence on scan rate can be seen in the difference in low power slopes from the studies on 05/02/2024 and 07/03/2024:

The main difference was an obstruction present in setup 1 that was not present in setup 4, which should have an effect on the background but not the signal. The other was the scan

Table 7.15: Table of low power slopes that suggest a dependence of the slope on the scan rate.

Date	Temperature	Laser Beam Profile	Scan Rate	Low Power Slope
-	C	-	MHz/s	GHz · kHz / mW
05/02/2024	457	setup 1	2	785.3 ± 64.6
07/03/2024	457	setup 4	5	3503 ± 365

rate. Further study should be made to see if this scan rate does or does not play a part in the signal size.

7.5.7 Area Vs. Power Analysis

The dependence of area under the curve, for low power, is essentially linear. As the power increases, the area get saturated, and the curve flattens. In order to perform this analysis, the signal areas versus powers were fitted to two different functions. The first was:

$$A(P) = M\frac{P}{1+\frac{P}{P_0}} \tag{7.12}$$

and the second:

$$A(P) = M\frac{P}{\sqrt{1+\frac{P}{P_0}}} \tag{7.13}$$

The fitting made sure to account for the uncertainties in both X and Y. The scipy.ODR package was used for the fitting, which is essentially a python wrapper for a FORTRAN code known as ODRPACK. The general idea behind the code can be found in [57]

7.5.8 Results

Overall, the fit to the $M\frac{P}{1+\frac{P}{P_0}}$ function worked much better. For each study performed, a table such as below was made:

Table 7.16: Fitting results for 07/22/2024 data.

07/22/2024	m, Fit to $\frac{mP}{1+\frac{P}{P0}}$	m, Fit to $\frac{mP}{\sqrt{1+\frac{P}{P0}}}$
-	GHz · kHz / mW	GHz · kHz / mW
Averaged Power, Flat Statistics	1.863 ± .591	2.054 ± .802
Peak Power, Flat Statistics	1.519 ± .530	1.670 ± .710
Averaged Power, Poisson Statistics	1.822 ± .592	1.998 ± .789
Peak Power, Poisson Statistics	1.486 ± .531	1.625 ± .699

The tables for all 5 studies are in the appendix. The parameter M was the parameter which determined the low-power slope. This was important to characterize, so that it could be compared to simulation. The m_0 and P_0 parameters are the initital guesses for the ODR fit. To get an idea of the systematic uncertainty for the M parameter, the standard deviation of the 4 different analysis measurements was taken. The resulting systematic uncertainty is reported in the summary table. This value of M, combined with simulated values of M dependent on atomic flux, would allow us to derive a reasonable estimate for our total atomic flux.

7.6 Simulation

Getting a value for atomic flux from fluorescence signal is not simple. This is because the relationship is extremely geometrically dependent. At a basic level, the relationship between atomic flux and low power slope looks something like:

$$M = G \cdot \Phi \tag{7.14}$$

where G is a linear geometric factor. Simulation is required to determine this geometric factor.

7.6.1 Single Atom Fluorescence Rate

The necessity of a computer for this simulation is due to the complicated nature of the region of fluorescence. At each point in space, there is a spatially-dependent atomic flux, atomic velocity, laser intensity, and solid angle for photon detection

The fluorescence works by exciting the calcium atoms from the ground state to the excited state. To calculate the single-atom fluorescence rate, one has to account for spontaneous emission, absorption, and stimulated emission. A simple two-level system is used.

Spontaneous emission occurs when an atom in the excited state decays back to the ground state, without the aid of lasers. Consider a group of atoms with a ground population fraction a(t) and an excited state population fraction b(t). The rate of change due to this can be described by:

$$\frac{da}{dt} = \frac{db}{dt} = Ab(t) \tag{7.15}$$

where A is the Einstein A coefficient for the state.

Absorption occurs when an atom absorbs a photon, say from a laser, and reaches an excited state. The rate of absorption depends on the laser power. It can be described by the function:

$$R(\mathbf{r}, \nu_\gamma) = \int_0^\infty \phi(\nu, \nu_\gamma, FWHM, \mathbf{r})\sigma(\nu)d\nu \tag{7.16}$$

where $\phi(\nu, \mathbf{r})$ is the number of photons per unit area, per time, per frequency, and

$$\sigma(\nu) = (\frac{h\nu}{c})B_a L(\nu) \tag{7.17}$$

is the absorption cross section. This is dependent on the Einstein absorption B-coefficient

$$B_a = \frac{c^3}{8\pi h\nu^3}\frac{g_b}{g_a}A = \frac{g_b}{g_a}B_b \tag{7.18}$$

where g_b and g_a are the number of degenerate levels states a and b, equivalent to 2J+1. The function $L(\nu)$ is described by:

$$L(\nu) = \frac{1}{2\pi}\frac{\frac{A}{2\pi}}{(\nu - \nu_a)^2 + \frac{A^2}{16\pi^2}} \tag{7.19}$$

where ν_a is the frequency of the atomic transition.

As for $\phi(\nu, \mathbf{r})$, the function can be split into an expression:

$$\phi(\nu, \nu_\gamma, FWHM, \mathbf{r}) = \frac{P_\gamma}{h\nu}\mathbf{S}(\mathbf{r}) \times \mathbf{G}(\nu, \nu_\gamma, FWHM) \tag{7.20}$$

where $\mathbf{S}(\mathbf{r})$ is the normalized fraction of photons per unit area, and $\mathbf{G}(\nu, \nu_\gamma, FWHM)$ is the normalized fraction of photons per unit frequency.

A gaussian beam is assumed, and the distribution of frequencies within the laser is assumed to have a gaussian distribution. Thus,

$$\mathbf{S}(\mathbf{r}) = \frac{I(\mathbf{r})}{P_\gamma} = \frac{2}{\pi w^2(z)} e^{-\frac{2\rho^2}{w^2(z)}} \tag{7.21}$$

where P_γ is the laser power, $w(z)$ is the beam radius at position z along the laser beam, ρ is the radial distance from $\mathbf{r}$ to the laser beam, and $I(\mathbf{r})$ is the laser beam intensity at position $\mathbf{r}$.

As for the frequency distribution,

$$\mathbf{G}(\nu, \nu_\gamma, FWHM) = \frac{2\sqrt{ln(2)/\pi}}{FWHM} e^{-rln(2)\frac{(\nu-\nu_\gamma)^2}{FWHM^2}} \tag{7.22}$$

where ν_γ is the set laser frequency, and FWHM is the Full-Width Half-Max of the laser frequency distribution.

In the region where the power is low - as in, where the linear nature of the low power slope dominates - the single atom fluorescence rate is roughly equivalent to the excitation rate.

7.6.2 Doppler Broadening

In addition to the geometric factor caused by the shape of the beam profile, there is an additional geometric factor caused by the angular distribution of atoms coming out of the nozzle.

Atoms moving with a transverse velocity component to the laser will see the laser frequency ν either red shifted or blue shifted by

$$\nu_a = \nu(1 - cos(\alpha)\frac{v}{c}) \tag{7.23}$$

where v is the velocity coming out of the nozzle, and α is the angle of the atom coming out of the oven with respect to an atom coming out straight. It can be characterized by

$$cos(\alpha) = \frac{\mathbf{r} \cdot \hat{\mathbf{x}}}{||\mathbf{r}||} \tag{7.24}$$

Thus, the position of the atom matters not only for the laser intensity at a given position, but also for the direction of travel for an atom at a given position. Furthermore, the magnitude of the velocity also matters - an atom moving with a higher velocity will see a greater frequency shift at a given position. The velocity distribution of the atoms coming out of the oven is assumed to follow a maxwell-boltzmann distribution:

$$g(v) = \sqrt{\frac{2}{\pi}}(\frac{m}{k_b T})^{3/2} v^2 e^{-(\frac{v}{v_p})^2} \tag{7.25}$$

where

$$v_p = \sqrt{\frac{2k_b T}{m}} \tag{7.26}$$

This has to be characterized in the single-atom fluorescence rate by a new modification to the integral:

$$R(\nu_\gamma, \nu_a, \mathbf{r}) = \int_0^\infty \int_0^\infty \phi(\nu, \nu_\gamma, FWHM, \mathbf{r}) \sigma_D(\nu, \nu_a, \mathbf{r}) g(v) d\nu dv \tag{7.27}$$

7.6.3 Atomic Flux Dependence on Position

The last positional dependence that has to be integrated over is the atomic flux, with has an angular distribution out of the nozzle. The nozzle can be characterized by:

$$\gamma = \frac{2a}{L} \tag{7.28}$$

where a is the nozzle radius, and L is the nozzle length. The angular dependence out of the nozzle is also affected by collisions between the atoms in the nozzle. The Knudsen number, K_{nL}, is used to characterize the density of atoms[58]

$$K_{nL} = \frac{\lambda}{l} \tag{7.29}$$

where λ is the mean free path of atoms in the channel, and l is a typical distance traveled by the atoms between bounces off the nozzle. The value of this parameter determine if the flow is in the "molecular flow" regime, or if atomic collisions become significant. The nozzle used for our ABF studies was 83 mm in length, and 2mm in diameter. This resulted in a ratio of

$$\gamma = .0241 \tag{7.30}$$

For $\gamma << 1$, as is the case here, the Knudsen number can be expressed by:

$$K_{nL} = \frac{\lambda}{2a} \tag{7.31}$$

where a is the radius of the nozzle. The mean free path of the atoms - the average distance between each atom - can be described by:

$$\lambda = \frac{\sigma}{n} \tag{7.32}$$

where σ is the cross section of interaction, and n is the number density of the atoms inside the nozzle. The cross section σ is crudely modeled using the hard sphere approximation, where the atoms are imagined as simply hard spheres of a given radius. The cross section for such an interaction is

$$\pi r_{VDW} \tag{7.33}$$

where r_{VDW} is the Van Der Walls radius of the atom. As for the number density, it can be found with the ideal gas law:

$$PV = n_m RT \tag{7.34}$$

where P is the pressure, V is the volume, n_m is the number of moles, R is the ideal gas constant, and T is the temperature. The number density can thus be found:

$$n = \frac{N}{V} = \frac{n_m A_v}{V} = \frac{PA_v}{RT} \tag{7.35}$$

where A_v is Avagadro's number. The number density n is thus dependent on the pressure and temperature. The pressure itself is dependent upon the temperature and the substance being used. The vapor pressure of the substance is used as the value for P, for which the empirical formula is like:

$$P(T) = 10^{5.006+A+\frac{B}{T}+Clog_{10}(T)+\frac{D}{T^3}}\,[\text{Pa}] \tag{7.36}$$

with the coefficients A, B, C, and D dependent on the substance. This makes the Knudsen number K_n dependent upon 5 parameters for each substance, a table of some of which are

below:

Table 7.17: Vapor pressure parameters for various elements.

Element	A	B	C	D	r_{VDW}	Sources
-	-	K	-	K^3	pm	-
Ca	10.127	-9517	-1.403	0	231	[59], [60]
Ba	4.007	-8163	0	0	268	[59], [60]
Yb	9.111	-8111	-1.0849	0	175 (empirical)	[59], [61]

A plot can then be made of the Knudsen number as a function of temperature for different elements:

Figure 7.24: Knudsen number as function of temperature.

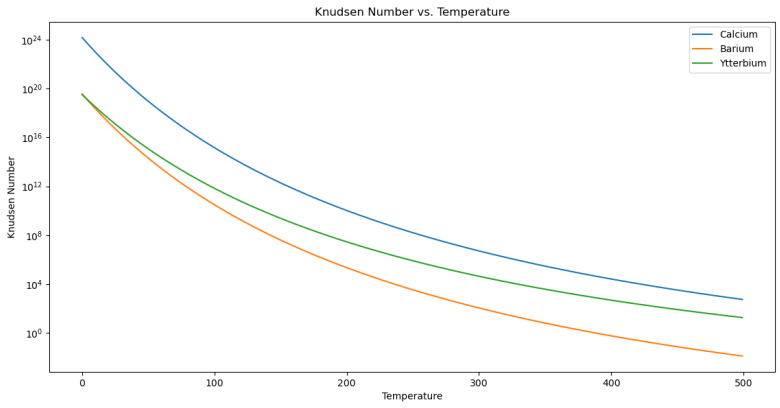

The molecular flow regime can be roughly considered when $K_{nL} > 10$. As can be seen, the curve for Calcium is well above 10 for temperatures between 0 and 500 C. This means collisions between the atoms can be assumed negligible. The atomic flux as a function of time can be described by the formula:

$$\Phi_a(\mathbf{r}) = \frac{dN_a}{dt}\frac{j(\theta)}{r^2} \tag{7.37}$$

where $j(\theta)$ is the angular distribution, r^2 the magnitude squared from the nozzle output,

and

$$\frac{dN_a}{dt} = \frac{n_0 v_a a^2}{4} \tag{7.38}$$

where n_0 is the number density, the same one used to determine the Knudsen number, v_a is the velocity along the z direction, and a is the nozzle radius. The only thing left undefined for the atomic flux is the angular distribution $j(\theta)$.

In the molecular flow regime, the angular distribution equation can be described by the following parameters:

$$p = \frac{\tan\theta}{\gamma} \tag{7.39}$$

$$R(p) = \cos^{-1}(p) - p\sqrt{1-p^2} \tag{7.40}$$

$$\zeta_0 = \frac{1}{2} - \frac{1}{3\gamma^2}\frac{1 - 2\gamma^3 + (2\gamma^2 - 1)\sqrt{1+\gamma^2}}{\sqrt{1+\gamma^2} - \gamma^2 \sinh^{-1}(1/\gamma)} \tag{7.41}$$

$$\zeta_1 = 1 - \zeta_0 \tag{7.42}$$

where γ is the nozzle parameter, ζ_0 is the channel exit collision parameter and ζ_1 is the channel entrance collision parameter. With these equations, the angular distribution can be described by:

$$j_{p\leq 1}(\theta) = \zeta_0 cos\theta + \frac{2}{\pi}\cos\theta((1-\zeta_0)R(p) + \frac{2}{3}(\zeta_1 - \zeta_0)\frac{\cos^2\theta}{\sin\theta}) \tag{7.43}$$

and

$$j_{p\geq 1}(\theta) = \zeta_0 \cos\theta + \frac{4\gamma}{3\pi}(\zeta_1 - \zeta_0)\frac{\cos^2\theta}{\sin\theta} \tag{7.44}$$

Armed with these equations, the value of $\Phi_a(\mathbf{r})$ as a function of position can be modeled for Calcium.

7.6.4 Total Flux from Single Atom Fluorescence Rate

By integrating over the relevant positions in a volume, the geometric factor between the fluorescence counts and the fluorescence spectrum can be derived. The incident power on a photodetector for a given laser frequency can be expressed as:

$$P_d^q(\nu_\gamma) = \int\int h\nu_\gamma \frac{\Phi_a(\mathbf{r})}{v_a} F^q(\nu_\gamma, \mathbf{r}) dV_a \frac{dA_d}{4\pi|\mathbf{d}-\mathbf{r}|^2} \tag{7.45}$$

where q is an index representing the light polarization, $F(\nu_\gamma, \mathbf{r})$ is the single atom fluorescence rate, $\mathbf{d}$ is the position of the center of the photodetector surface, v_a is the velocity component of the atoms in the z direction, and $\Phi_a(\mathbf{r})$ is the atomic flux. The integral is over V_a, the volume of the interaction region, and dA_d, the area of the photodetector. This integral can be better made sense of by looking at it piece by piece:

$$h\nu_\gamma$$

is the energy of the photons being fluoresced

$$\frac{\Phi_a(\mathbf{r})}{v_a}$$

is the volumetric density of the atoms at a position

$$F(\nu_\gamma, \mathbf{r})$$

is the number of photons scattered per atom at a given position, and

$$\int \frac{dA_d}{4\pi|\mathbf{d}-\mathbf{r}|^2}$$

is the fraction of the fluoresced photons that actually hit the detector from a given position.

by multiplying these together, what is derived is:

$$\frac{\text{Energy}}{\text{Photon}} \times \frac{\text{Atoms}}{\text{Volume}} \times \frac{\text{Photons}}{\text{Atom}} \times \frac{\text{DetectorArea}}{\text{SphereSurfaceArea}} = \frac{\text{Energy}}{\text{Volume}}$$

Then, once integrated over the volume, the expression is derived for the total energy fluoresced onto a detector for a given frequency.

To simplify the integral, the assumption is made that the distance from each position in the interaction region to the detector follows the simple formula:

$$\int \frac{dA_d}{4\pi|\mathbf{d}-\mathbf{r}|^2} = \frac{A_d}{4\pi|\mathbf{d}-\mathbf{r}|^2} \tag{7.46}$$

The assumption is also made that the laser light is unpolarized. Once this integral is complete, it outputs data that can be converted back into number of photons, by dividing by the energy of each individual photon, $E_\gamma = h\nu$. By integrating over this, a simulated integrated count rate over a scan can be derived. The last step is to account for the efficiency of the detector, and the fraction of photons that make it through the filter. The specifications

for the Thorlabs SPDMA and Edmund Optics 422 nm filter are used. We use a value of 25% detection efficiency for the SPDMA, which is halfway between the maximum and minimum efficiencies of the detector at 422 nm, depending on the gain setting.

In the future, careful calibration will be needed to determine more precisely the efficiency of the SPDMA. As for the 422 nm filter, the efficiency chosen was chosen to be 89.4%. With these values, it is easy to convert from the photons incident on the photodetector to the actual counts measured:

$$\text{CountsMeasured} = (.894)(.25)\text{IncidentPhotons} \tag{7.47}$$

7.6.5 Simulation Results

These simulations were done under a wide variety of conditions. Specifically, the temperature was varied, to see if it had any effect on the count rate per milliwatt. In addition, the diameter of the beam was varied. The count was integrated under different conditions of temperature and beam size, and the following plot was made of the results:

The simulated data is reported here:

Table 7.18: Table of the simulated integrated area for various settings.

Simulated Oven Temperature	Simulated Beam Diameter	Simulated Integrated Area
C	mm	$\frac{kHz \times GHz}{mW \times 10^{14}\text{AtomsperSecond}}$
338	3	5413.4
338	6	4937.9
380	3	5237.0
380	6	4777.0
457	1.3	4884.3
457	3	4942.8
457	6	4510.7

Figure 7.25: Results of the simulation.

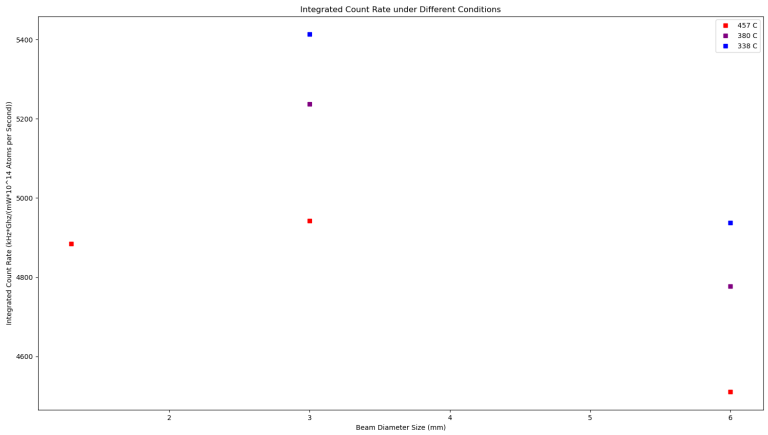

7.7 Analysis of Atomic Flux

With the measured data taken, and the simulated relation between low power slope and total atomic flux in hand, a value could be derived for the atomic flux as a function of temperature. In order to gauge the reliability of this value, it had to be compared to a simple model for the atomic flux coming out of the oven.

7.7.1 Simple Model for Predicting Atomic Flux out of Oven for Metallic Calcium

A simple model of total atomic flux versus temperature could be made using the formula (7.38). This requires the number density, area of the nozzle, and integral over the speed of the atoms. It can be written:

$$\frac{dN_a}{dt}(T) = \frac{a^2}{4}\frac{PA_v}{RT}\int_0^\infty g(v,T)v dv \tag{7.48}$$

where a is the nozzle radius, P is the vapor pressure calculated previously, A_v is Avagadros number, R is the ideal gas constant, T is the temperature in Kelvin, and

$$g(v,T) = \sqrt{\frac{2}{\pi}}(\frac{m}{k_b T})^{3/2} v^2 e^{-(\frac{v}{vp})^2} \tag{7.49}$$

is the Maxwell-Boltzmann distribution. Armed with this model, a value for the atomic flux can be predicted from a given oven temperature T. The atomic flux as a function of the temperature looks like:

Figure 7.26: Simple model of the atomic flux derived from the oven temperature.

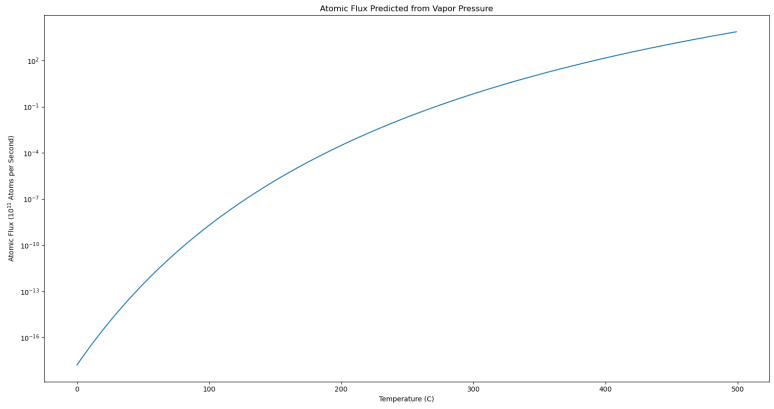

It can now be compared to the data that was taken.

7.7.2 Atomic Flux Calculated from Measurement and Simulation

Once again, the low power slope measured from fluorescence scans can be compared to the atomic flux by the equation:

$$M = G \times \Phi$$

where G is a geometric factor determined by simulation. To compare the fluorescence study to the simple model, all the low power slopes from the study were considered. There were 2 measurements for 338 C, 1 measurement for 380 C, and 2 measurements for 457 C. This resulted in 5 measurements. After this, there were different scaling factors, dependent upon the temperature and beam size. There were 3 scaling factors for 457 C, 2 scaling factors for 380 C, and 2 scaling factors for 338 C.Each measurement had every scaling factor applied to it. This corresponded to 4 atomic flux data points for 338 C, 2 for 380 C, and 6 for 457 C. The uncertainty in the low power slope was also converted to atomic flux, using the same scaling factor. The resulting data points can be seen in the following table:

Table 7.19: Data of the measured atomic flux.

Temperature	Atomic Flux	Uncertainty
C	10^{11} Atoms per Second	10^{11} Atoms per Second
338	.350	.019
338	.384	.021
338	.309	.032
338	.339	.035
380	18.346	.561
380	20.113	.615
457	160.780	13.226
457	158.878	13.070
457	174.097	14.322
457	717.196	74.729
457	708.708	73.845
457	776.598	80.919

This was plotted versus the vapor pressure model curve:

This plot used the statistical uncertainties scaled in the same way as the atomic flux. In order to collapse all the data points into a single measurement, the average of the data at each temperature was taken, as well as the standard deviation. The average was used as a single data point for the temperature, and the standard deviation as the systematic

Figure 7.27: Comparison of the predicted versus measured atomic flux.

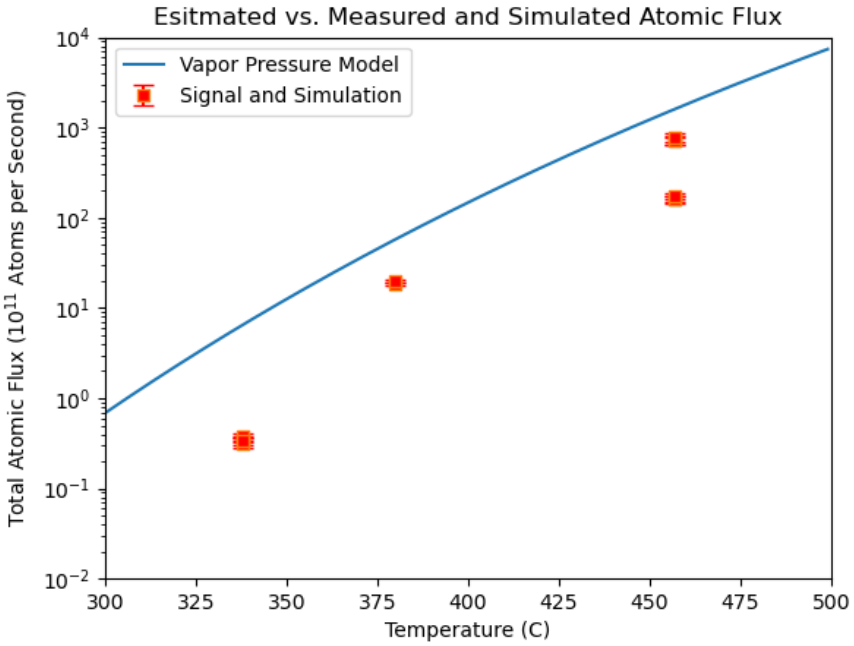

uncertainty. The following plot was made, with the averaged data point, as well as the maximum uncertainty from either the systematic uncertainty or any of the individual statistical uncertainties:

The residuals are given below:

Pressure Prediction]Comparison of Atomic Flux Measurements with Vapor

Pressure Prediction

A table of the data points, the maximum uncertainty, and the number of sigma away from the predicted total atomic flux are below:

Table 7.20: Final measurement data points.

Temperature	Predicted Atomic Flux	Measured Atomic Flux	# of σ Away from Predicted Atomic Flux
C	10^{11} Atoms per Second	10^{11} Atoms per Second	-
338	6.542	.345 $\pm$ .035	-178.9
380	57.826	19.230 $\pm$ 20.113	-1.92
457	1609.300	449.376 $\pm$ 776.598	-1.45

Figure 7.28: Comparison of the predicted versus measured atomic flux with maximum uncertainty.

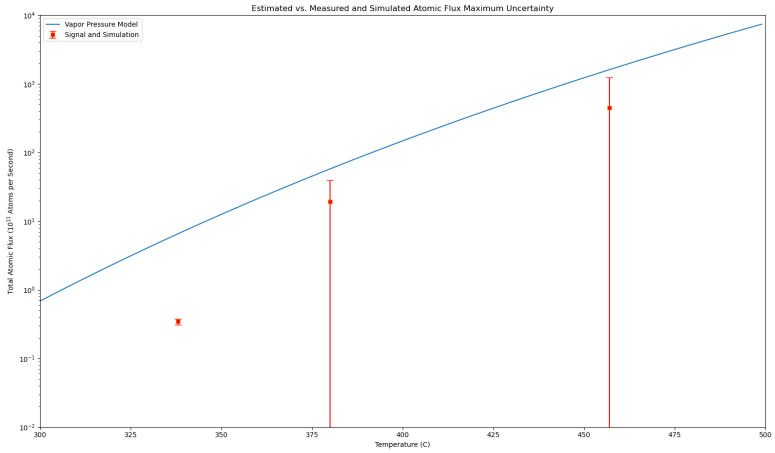

All of the data points fell below the prediction made with the vapor pressure. This suggests that the simple vapor pressure model overestimated the number of atoms coming out of the oven. This is a good sign, since ideally the sensitivity in our oven should be maximized, to better characterize the atomic flux of various chemical processes. The biggest uncertainty came from the 457 °C measurements. This was due to the fact that of the two studies done at this temperature, two quite different values for the low power slope were measured. There were significant changes between these two measurements, however. Not only was black acktar tape installed between these measurements, but the laser had to be realigned between the two studies, meaning that the laser alignment was not exactly in the same place. Finally, the scans were done at two different scan rates. While theory indicates that this should not have changed the area, there is evidence to suggest that this does have a slight effect. Ultimately, the 457 °C and 380 °C studies were within two sigma of the vapor pressure curve, making this not particularly significant for determining whether the vapor pressure curve is a good approximation. The 338 °C C data point, however, is

Figure 7.29: Residuals of the comparison of the predicted versus measured atomic flux with maximum uncertainty.

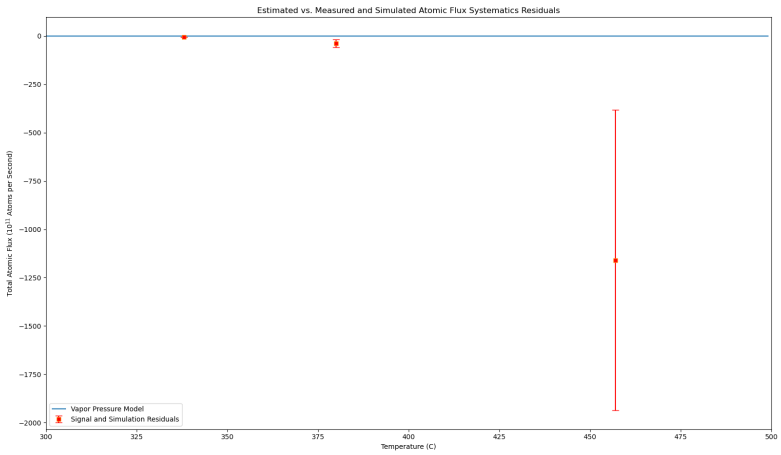

extremely significant. It is over 100σ away from the predicted value - very much an outlier. In addition, this point is the result of two separate studies - the only difference between the two being the swap between setups 4 and 5. To account for uncertainty in the beam size, two different scaling factors were applied to each of the low power slopes derived from the studies. These scaling factors were different, in that the simulated beam size was chosen to be different. The variation due to the differences in scaling factors and measured low power slopes was characterized by taking the systematic uncertainty of the resulting atomic fluxes, and the uncertainty seen is the maximum uncertainty, either systematic or statistical, associated with any of the data points. The fact that this uncertainty is still so small, and the difference in prediction and measurement so large, suggests there is something going on here. Perhaps, as the atomic flux gets lower, the vapor pressure approximation begins to break down. Whatever the case, it seems that the lowest atomic flux that was measured was $\approx 3 \times 10^{10}$ atoms per second, at a temperature where it was predicted to have $\approx 6 \times 10^{11}$ atoms per second. This is encouraging, since the sensitivity goal of the apparatus is to

measure atomic flux on the order of 10^8 atoms per second. It now needs to be seen whether this atomic flux is possible at the moment.

7.7.3 Characterizing Atomic Flux Sensitivity

Getting an idea of the smallest atomic flux measurable by the apparatus requires comparing the fluorescence count rate uncertainty - in essence, the noise from the background - with the signal area. To do this, the gamma parameter from the Lorentzian was taken. The signal area associated with background noise was considered as a Lorentzian, of the same Γ width parameter, with a maximum height equal to the fluorescence count rate uncertainty σ. The equation to get the area from these two parameters is:

$$\frac{\pi}{2}\Gamma\sigma = A \tag{7.50}$$

A table of the relevant data from the scans is below:

Table 7.21: Table of the area associated with uncertainty in the count rate for scans at 338 C.

Date of Scan	Count Rate Uncertainty	Lorentzian Fit Gamma	Uncertainty Area	Average Power	Average Power Uncertainty
07/08/2024	2.63	0.066	0.273	4.84	.056
07/08/2024	2.06	0.073	0.236	3.88	.022
07/08/2024	1.37	0.054	0.116	1.98	.016
07/08/2024	0.93	0.067	0.098	1.07	.020
07/08/2024	2.79	0.078	0.342	7.04	.052
07/22/2024	1.77	0.077	0.214	13.76	1.00
07/22/2024	1.70	0.072	0.192	11.66	.98
07/22/2024	2.11	0.077	0.255	10.52	.80
07/22/2024	1.39	0.085	0.186	8.22	.69
07/22/2024	1.02	0.071	0.114	6.00	.50
07/22/2024	0.97	0.073	0.111	4.82	.35
07/22/2024	0.76	0.063	0.075	2.34	.19

From there, since the background noise should increase linearly with the power, a linear fit can be done to a plot of the average powers with their uncertainties, versus the associated signal area. For the scans on 07/08/2024 and 07/22/2024, the plots looks like:

Figure 7.30: Plot of the linear fit to the background areas from 07/08/2024.

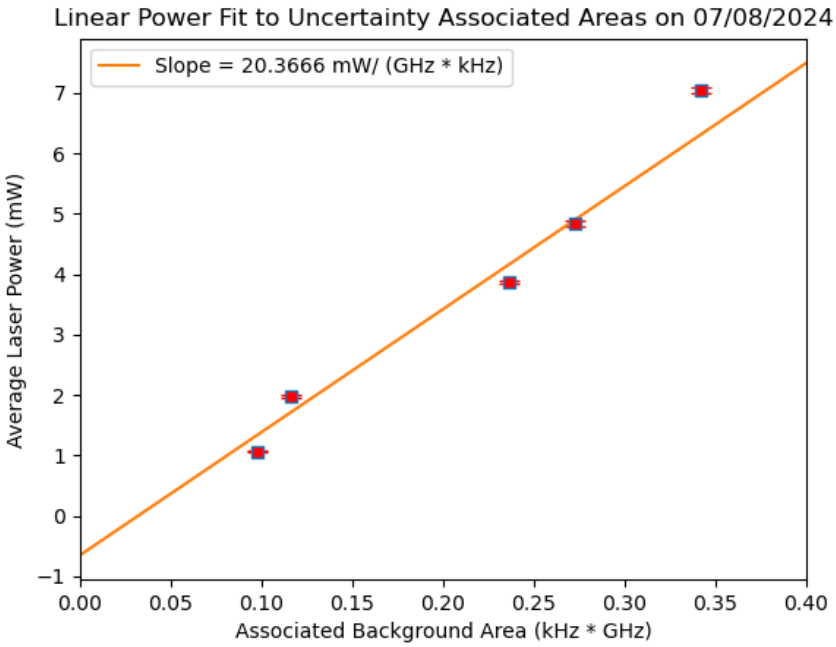

Figure 7.31: Plot of the linear fit to background areas from 07/22/2024.

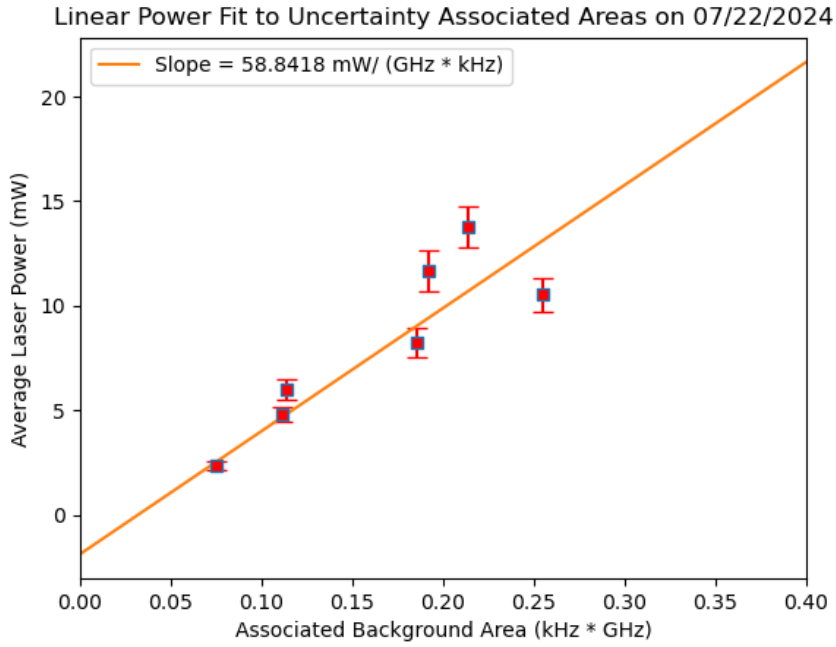

Note the swapping of the X and Y axes, this is to take advantage of the uncertainties associated with the power into the fit. By taking the reciprocal of the slope, the actual slope of $\frac{GHz \times kHz}{mW}$ can be found.

Table 7.22: Table of the slopes associated with the background uncertainties.

Date	Raw Slope	Slope Reciprocal
-	$\frac{mW}{GHz \times kHz}$	$\frac{GHz \times kHz}{mW}$
07/08/2024	20.37	.049
07/22/2024	58.84	.017

from there, each of the two slope reciprocals can be multiplied by one of the geometric factors, to determine the atomic flux associated with a background measurement:

Table 7.23: Atomic flux slope associated with background uncertainties.

Background Power Slope	Geometric Factor	Atomic Flux
$\frac{GHz \times kHz}{mW}$	$\frac{kHz \times GHz}{mW \times 10^{11}\ \text{Atoms} \cdot \text{s}^{-1}}$	$10^{11}\ \text{Atoms} \cdot \text{s}^{-1}$
.049	5.4134	.00905
.049	4.9379	.00992
.017	5.4134	.00314
.017	4.9379	.00344

Taking the maximum value of these, it appears that the signal associated with the background noise is 9.92×10^8 atoms per second - multiplying by a factor of 5, so that the area of the signal is clearly visible versus the background, the minimum signal currently observable is something like:

$$\Phi_{min} \approx 5 \times 10^9\ \text{Atoms} \cdot \text{s}^{-1} \tag{7.51}$$

In order to reach the goal of 10^8 atom per second sensitivity, a further order of magnitude in background reduction is needed. Methods with which this might be realized are now discussed.

7.8 Future Improvements

To reach the desired atomic flux of 10^8 atoms per second, another order of magnitude of sensitivity improvement is needed. This can be achieved mainly through background reduction. The maximum signal sensitivity analysis used, of the two studies at 338 C, the one with the maximum noise associated. It can be seen from the background study that by simply using a more focused beam, the background was reduced by a factor of 4. By utilizing a single-mode fiber, the beam intensity profile could be better controlled, and kept constant. This would aid in the reproducibility of studies, and likely allow for even smaller beam profiles to be used. It can be seen from the analysis of the previous section that the tighter beam resulted in an improvement of sensitivity by a factor of 3. It is also true that laser stability issues were observed towards the end of these studies. Repairing the laser, specifically the Lighthouse Photonics Sprout pump laser, might reduce the exponential drift in power seen during the scans, which was especially profound in the scans on 07/22/2024. Finally, if further sensitivity is needed, the installation of a lens on the inside of the 6-way cross would increase the fluorescence signal seen, though it would make the simulation more complicated to run. A summary of improvements to be made in now given:

1. Utilize a single mode fiber for coupling the laser to the ABF stand

2. Improve laser stability with a better pump laser

3. Install a lens inside the 6-way cross to help focus more fluorescence onto the detector.

Chapter 8. Conclusion

8.1 Overview

Permanent EDM searches serve as a clean way to probe unknown sources of CP violation in the universe. EDM searches on diamagnetic atoms in particular are sensitive to CP violation in the hadronic sector. Radium-225 is particularly sensitive to new physics in this sector, due to the octopole deformation in its nucleus. This atom is a radioactive rare isotope, and procuring it has been difficult. For this reason, substituting it with Radium-223 was attempted, and efforts are ongoing to test the efficiency of various ways of making an atomic beam harvested from the FRIB. Once in an atomic beam, the Radium atoms are laser cooled and trapped, and transported to in between a pair of electrodes for a spin precession measurement. This measurement forms the basis of the EDM measurement, and its sensitivity is directly proportional to the electric field applied. The statistical sensitivity of the experiment also heavily relies on the electric field being perfectly reversible in polarity. For this reason, efforts are also ongoing to increase electric field strength, while also making it more reversible.

I started my graduate career in research working at MSU on conditioning electrodes to accept higher electric fields with low discharge rates. I then moved to Argonne National Laboratory, where I became acquainted with laser cooling and trapping Radium-226. It was here that I became very comfortable working with lasers, including their maintenance and repair. At the time, Radium-223 was proposed as an interim substitute for Radium-225. For this to work, previously unknown energy levels for this isotope would have to be measured.

I managed to fluoresce the primary trapping transition while in a beam, though efforts were unsucessful at fully trapping Radium-223 in the oven load, and the supply of Radium-223 was cut shortly thereafter.

With the skills I'd developed at ANL in hand, I moved back to MSU to setup the apparatus for efficiency measurements of isotopes harvested from MSU's radioactive beam dump. This involved having a custom effusive oven fabricated in a machine shop, and then assembling an apparatus for beam fluorescence. I also had to get the lasers in the lab working again, after they were in a state of disrepair following the COVID lockdowns. This was done with the expertise I gained at ANL, as well as with new skills I had to acquire, such as writing custom software to allow two incompatible laser elements to talk to each other. I also had to write the software necessary for the experiment to run, develop procedures for loading the oven, and debug the system when it was going wrong.

Using this apparatus, I was able to fluoresce a beam of metallic Calcium. I then performed spectroscopic studies to determine that the lowest atomic flux able to be measured with the system is 5×10^9 atoms per second. This information will aid in future studies of isotope beam production, in order to ensure radium flows out of our oven as efficiently as possible.

In addition, I assisted with designing and testing the components necessary for a new HV swiching system. This system aims to use a unipolar 60 kV power supply to not only achieve higher voltages, but also improve field reversiblity through a system of mechanical relays. I selected the power supply to use, as well as the mechanical relays and solid state relay to use. I also did preliminary designs for the HV cage, planned out how to use hardware logic for safety, and assembled an HV divider that will enable measurement of the applied voltages to verify the same voltage to 1 part per million, rather than 7000 parts per million.

In order to get a better idea as to the effect of these upgrades, I performed calculations

to determine the size of systematic errors in the experiment. I was able to successfully reproduce a known calculation for the vector shift due to holding ODT power for Cesium-133, and began work to adapt this code to Mercury-199 as well. Once this code is working, adapting it to Radium should be quite easy, due to the similar electronic structure.

These upgrades will assist with the plan to improve the sensitivity of the RaEDM experiment from 1.4E-23 e cm to a measurement on the order of 1E-26 e cm. Previous data runs utilized an applied E field of $\pm$6.7kV/mm. Electrodes conditioned at MSU were able to reach field strengths of 20 kV/mm with minimal discharges. With the new HV apparatus being assembled at MSU, continued electrode conditioning should hopefully allow for electrodes to be conditioned to up to 50 kV/mm. Such an improvement in E field strength would on its own result in an order of magnitude sensitivity improvement in this EDM search. In addition, the 3 order of magnitude improvement in the sensitivity should reduce the systematic uncertainty in turn. The ABF apparatus built at MSU will open up the ability to test various forms of Radium for use in our experiment, and optimize the efficiency with which we are able to use Radium harvested from the FRIB beam dump. Being able to finally use Radium-225 again will allow the experiment to actually continue. Furthermore, additional upgrades ongoing at ANL, such as the Blue Slower Upgrade and Quantum Non-Demoltion, will further increase sensitivity. Many of the necessary transitions for the upgraded optical cycling scheme have been fluoresced, and once in place, this upgrade should improve the amount of atoms measured 60 fold. With the Quantum Non-Demolition, thousands of times more atoms should be able to be scattered during the shadow imaging measurement, improving the clarity of the image. These elements together will all contribute to a new sensitivity of 1E-26 e cm.

To summarize my contributions to this project:

1. Assembled and built a fluorescence rate counting apparatus, and managed to determine its highest flux rate measureable at 5×10^9 atoms per second

2. Assisted with the designing of a new HV switching system, as well as mostly assembling an HV divider to enable more precise voltage measurements

3. Performed calculations to allow for the characterization of important systematic effects for the RaEDM experiment.

Further work will be need to improve on my work. This includes:

1. Fixing the mercury-199 vector shift calculation

2. Characterizing the stark shift systematic effect

3. Utilizing a single mode fiber for coupling the laser to the ABF stand

4. Improving laser stability with a better pump laser

5. Installing a lens inside the 6-way cross to help focus more fluorescence onto the detector.

6. Assembling a new HV switching system, to allow for electrode conditioning

7. Conditioning electrodes to up to 500 kV/mm

BIBLIOGRAPHY

[1] A. A. Penzias and R. W. Wilson, "A Measurement of Excess Antenna Temperature at 4080 Mc/s.," , vol. 142, pp. 419–421, July 1965.

[2] R. H. Dicke, P. J. E. Peebles, P. G. Roll, and D. T. Wilkinson, "Cosmic Black-Body Radiation.," , vol. 142, pp. 414–419, July 1965.

[3] R. H. Cyburt, B. D. Fields, K. A. Olive, and T.-H. Yeh, "Big bang nucleosynthesis: Present status," *Reviews of Modern Physics*, vol. 88, Feb. 2016.

[4] N. Aghanim, Y. Akrami, M. Ashdown, J. Aumont, C. Baccigalupi, M. Ballardini, A. J. Banday, R. B. Barreiro, N. Bartolo, S. Basak, R. Battye, K. Benabed, J.-P. Bernard, M. Bersanelli, P. Bielewicz, J. J. Bock, J. R. Bond, J. Borrill, F. R. Bouchet, F. Boulanger, M. Bucher, C. Burigana, R. C. Butler, E. Calabrese, J.-F. Cardoso, J. Carron, A. Challinor, H. C. Chiang, J. Chluba, L. P. L. Colombo, C. Combet, D. Contreras, B. P. Crill, F. Cuttaia, P. de Bernardis, G. de Zotti, J. Delabrouille, J.-M. Delouis, E. Di Valentino, J. M. Diego, O. Dor, M. Douspis, A. Ducout, X. Dupac, S. Dusini, G. Efstathiou, F. Elsner, T. A. Enlin, H. K. Eriksen, Y. Fantaye, M. Farhang, J. Fergusson, R. Fernandez-Cobos, F. Finelli, F. Forastieri, M. Frailis, A. A. Fraisse, E. Franceschi, A. Frolov, S. Galeotta, S. Galli, K. Ganga, R. T. Gnova-Santos, M. Gerbino, T. Ghosh, J. Gonzlez-Nuevo, K. M. Grski, S. Gratton, A. Gruppuso, J. E. Gudmundsson, J. Hamann, W. Handley, F. K. Hansen, D. Herranz, S. R. Hildebrandt, E. Hivon, Z. Huang, A. H. Jaffe, W. C. Jones, A. Karakci, E. Keihnen, R. Keskitalo, K. Kiiveri, J. Kim, T. S. Kisner, L. Knox, N. Krachmalnicoff, M. Kunz, H. Kurki-Suonio, G. Lagache, J.-M. Lamarre, A. Lasenby, M. Lattanzi, C. R. Lawrence, M. Le Jeune, P. Lemos, J. Lesgourgues, F. Levrier, A. Lewis, M. Liguori, P. B. Lilje, M. Lilley, V. Lindholm, M. Lpez-Caniego, P. M. Lubin, Y.-Z. Ma, J. F. Macas-Prez, G. Maggio, D. Maino, N. Mandolesi, A. Mangilli, A. Marcos-Caballero, M. Maris, P. G. Martin, M. Martinelli, E. Martnez-Gonzlez, S. Matarrese, N. Mauri, J. D. McEwen, P. R. Meinhold, A. Melchiorri, A. Mennella, M. Migliaccio, M. Millea, S. Mitra, M.-A. Miville-Deschnes, D. Molinari, L. Montier, G. Morgante, A. Moss, P. Natoli, H. U. Nrgaard-Nielsen, L. Pagano, D. Paoletti, B. Partridge, G. Patanchon, H. V. Peiris, F. Perrotta, V. Pettorino, F. Piacentini, L. Polastri, G. Polenta, J.-L. Puget, J. P. Rachen, M. Reinecke, M. Remazeilles, A. Renzi, G. Rocha, C. Rosset, G. Roudier, J. A. Rubio-Martn, B. Ruiz-Granados, L. Salvati, M. Sandri, M. Savelainen, D. Scott, E. P. S. Shellard, C. Sirignano, G. Sirri, L. D. Spencer, R. Sunyaev, A.-S. Suur-Uski, J. A. Tauber, D. Tavagnacco, M. Tenti, L. Toffolatti, M. Tomasi, T. Trombetti, L. Valenziano, J. Valiviita, B. Van Tent, L. Vibert, P. Vielva, F. Villa, N. Vittorio, B. D. Wandelt, I. K. Wehus, M. White, S. D. M. White, A. Zacchei, and A. Zonca, "Planck2018 results: Vi. cosmological parameters," *Astronomy amp; Astrophysics*, vol. 641, p. A6, Sept. 2020.

[5] R. Jora, "Baryon asymmetry in the standard model revisited," 2018.

[6] L. Landau, "On the conservation laws for weak interactions," *Nuclear Physics*, vol. 3, no. 1, pp. 127–131, 1957.

[7] J. H. Christenson, J. W. Cronin, V. L. Fitch, and R. Turlay, "Evidence for the 2π decay of the k_2^0 meson," *Phys. Rev. Lett.*, vol. 13, pp. 138–140, Jul 1964.

[8] T. D. Lee and C. N. Yang, "Question of parity conservation in weak interactions," *Phys. Rev.*, vol. 104, pp. 254–258, Oct 1956.

[9] C. S. Wu, E. Ambler, R. W. Hayward, D. D. Hoppes, and R. P. Hudson, "Experimental test of parity conservation in beta decay," *Phys. Rev.*, vol. 105, pp. 1413–1415, Feb 1957.

[10] R. L. Garwin, L. M. Lederman, and M. Weinrich, "Observations of the Failure of Conservation of Parity and Charge Conjugation in Meson Decays: the Magnetic Moment of the Free Muon," *Physical Review*, vol. 105, no. 4, pp. 1415–1417, 1957.

[11] L. I. Schiff, "Measurability of nuclear electric dipole moments," *Phys. Rev.*, vol. 132, pp. 2194–2200, Dec 1963.

[12] V. V. Flambaum and J. S. M. Ginges, "The nuclear Schiff moment and time invariance violation in atoms," *arXiv*, 2001.

[13] V. Spevak, N. Auerbach, and V. V. Flambaum, "Enhanced T-odd, P-odd electromagnetic moments in reflection asymmetric nuclei," *Physical Review C*, vol. 56, no. 3, pp. 1357–1369, 1997.

[14] B. Graner, Y. Chen, E. G. Lindahl, and B. R. Heckel, "Reduced limit on the permanent electric dipole moment of ^{199}Hg," *Phys. Rev. Lett.*, vol. 116, p. 161601, Apr 2016.

[15] T. Chupp and M. Ramsey-Musolf, "Electric Dipole Moments: A Global Analysis," *arXiv*, 2014.

[16] T. S. Roussy, L. Caldwell, T. Wright, W. B. Cairncross, Y. Shagam, K. B. Ng, N. Schlossberger, S. Y. Park, A. Wang, J. Ye, and E. A. Cornell, "An improved bound on the electrons electric dipole moment," *Science*, vol. 381, no. 6653, pp. 46–50, 2023.

[17] V. Andreev, D. G. Ang, D. DeMille, J. M. Doyle, G. Gabrielse, J. Haefner, N. R. Hutzler, Z. Lasner, C. Meisenhelder, B. R. OLeary, C. D. Panda, A. D. West, E. P. West, and X. Wu, "Improved limit on the electric dipole moment of the electron," *Nature*, vol. 562, no. 7727, pp. 355–360, 2018.

[18] C. Abel, S. Afach, N. J. Ayres, C. A. Baker, G. Ban, G. Bison, K. Bodek, V. Bondar, M. Burghoff, E. Chanel, Z. Chowdhuri, P.-J. Chiu, B. Clement, C. B. Crawford, M. Daum, S. Emmenegger, L. Ferraris-Bouchez, M. Fertl, P. Flaux, B. Franke,

A. Fratangelo, P. Geltenbort, K. Green, W. C. Griffith, M. van der Grinten, Z. D. Grujić, P. G. Harris, L. Hayen, W. Heil, R. Henneck, V. Hélaine, N. Hild, Z. Hodge, M. Horras, P. Iaydjiev, S. N. Ivanov, M. Kasprzak, Y. Kermaidic, K. Kirch, A. Knecht, P. Knowles, H.-C. Koch, P. A. Koss, S. Komposch, A. Kozela, A. Kraft, J. Krempel, M. Kuźniak, B. Lauss, T. Lefort, Y. Lemière, A. Leredde, P. Mohanmurthy, A. Mtchedlishvili, M. Musgrave, O. Naviliat-Cuncic, D. Pais, F. M. Piegsa, E. Pierre, G. Pignol, C. Plonka-Spehr, P. N. Prashanth, G. Quéméner, M. Rawlik, D. Rebreyend, I. Rienäcker, D. Ries, S. Roccia, G. Rogel, D. Rozpedzik, A. Schnabel, P. Schmidt-Wellenburg, N. Severijns, D. Shiers, R. Tavakoli Dinani, J. A. Thorne, R. Virot, J. Voigt, A. Weis, E. Wursten, G. Wyszynski, J. Zejma, J. Zenner, and G. Zsigmond, "Measurement of the permanent electric dipole moment of the neutron," *Phys. Rev. Lett.*, vol. 124, p. 081803, Feb 2020.

[19] D.-T. Wong, M. Hassan, J. Burdine, T. Chupp, S. Clayton, C. Cude-Woods, S. Currie, T. Ito, C.-Y. Liu, M. Makela, C. Morris, C. OShaughnessy, A. Reid, N. Sachdeva, and F. Uhrich, "Characterization of the new ultracold neutron beamline at the lanl ucn facility," *Nuclear Instruments and Methods in Physics Research Section A: Accelerators, Spectrometers, Detectors and Associated Equipment*, vol. 1050, p. 168105, May 2023.

[20] T. A. Zheng, Y. A. Yang, S.-Z. Wang, J. T. Singh, Z.-X. Xiong, T. Xia, and Z.-T. Lu, "Measurement of the electric dipole moment of ^{171}Yb atoms in an optical dipole trap," *Phys. Rev. Lett.*, vol. 129, p. 083001, Aug 2022.

[21] M. Bishof, R. H. Parker, K. G. Bailey, J. P. Greene, R. J. Holt, M. R. Kalita, W. Korsch, N. D. Lemke, Z.-T. Lu, P. Mueller, T. P. O'Connor, J. T. Singh, and M. R. Dietrich, "Improved limit on the ^{225}Ra electric dipole moment," *Phys. Rev. C*, vol. 94, p. 025501, Aug 2016.

[22] Y. A. Yang, T. A. Zheng, S.-Z. Wang, W.-K. Hu, C.-L. Zou, T. Xia, and Z.-T. Lu, "Quantum nondemolition measurement of the spin precession of laser-trapped ^{171}Yb atoms," *Phys. Rev. Appl.*, vol. 19, p. 054015, May 2023.

[23] T. Zheng, Y. Yang, S.-Z. Wang, J. Singh, Z.-X. Xiong, T. Xia, and Z.-T. Lu, "Measurement of the electric dipole moment of ^{171}yb atoms in an optical dipole trap," *Physical Review Letters*, vol. 129, Aug. 2022.

[24] F. Allmendinger, I. Engin, W. Heil, S. Karpuk, H.-J. Krause, B. Niederländer, A. Offenhäusser, M. Repetto, U. Schmidt, and S. Zimmer, "Measurement of the permanent electric dipole moment of the ^{129}Xe atom," *Phys. Rev. A*, vol. 100, p. 022505, Aug 2019.

[25] D. Cho, K. Sangster, and E. A. Hinds, "Search for time-reversal-symmetry violation in thallium fluoride using a jet source," *Phys. Rev. A*, vol. 44, pp. 2783–2799, Sep 1991.

[26] O. Grasdijk, O. Timgren, J. Kastelic, T. Wright, S. Lamoreaux, D. DeMille, K. Wenz, M. Aitken, T. Zelevinsky, T. Winick, and D. Kawall, "Centrex: a new search for time-

reversal symmetry violation in the 205tl nucleus," *Quantum Science and Technology*, vol. 6, p. 044007, sep 2021.

[27] A. Sunaga, Y. Takahashi, A. Vutha, and Y. Takahashi, "Measuring the nuclear magnetic quadrupole moment of optically trapped ytterbium atoms in the metastable state," *New Journal of Physics*, vol. 26, p. 023023, feb 2024.

[28] D. DeMille, N. R. Hutzler, A. M. Rey, and T. Zelevinsky, "Quantum sensing and metrology for fundamental physics with molecules," *Nature Physics*, vol. 20, pp. 741–749, May 2024.

[29] P. A. Butler, "Pear-shaped atomic nuclei," *Proceedings of the Royal Society A: Mathematical, Physical and Engineering Sciences*, vol. 476, no. 2239, p. 20200202, 2020.

[30] N. Auerbach, V. V. Flambaum, and V. Spevak, "Collective t- and p-odd electromagnetic moments in nuclei with octupole deformations," *Phys. Rev. Lett.*, vol. 76, pp. 4316–4319, Jun 1996.

[31] B.-N. Lu, J. Zhao, Z. En-Guang, and S.-G. Zhou, "Potential energy surfaces of actinide and transfermium nuclei from multi-dimensional constraint covariant density functional theories," *EPJ Web of Conferences*, vol. 38, 03 2013.

[32] J. Dobaczewski and J. Engel, "Nuclear Time-Reversal Violation and the Schiff Moment of Ra225," *Physical Review Letters*, vol. 94, no. 23, p. 232502, 2005.

[33] S. Ban, J. Dobaczewski, J. Engel, and A. Shukla, "Fully self-consistent calculations of nuclear Schiff moments," *Physical Review C*, vol. 82, no. 1, p. 015501, 2010.

[34] I. Ahmad, R. R. Chasman, J. P. Greene, F. G. Kondev, and S. Zhu, "Electron capture decay of 58-min $^{229}_{92}$U and levels in $^{229}_{91}$Pa," *Physical Reviews C.*, vol. 92, p. 024313, 2015.

[35] T. Rabga, *Upgrades for an Improved Measurement of the Permanent Electric Dipole Moment of Radium*. PhD thesis, Michigan State University, 2020. Copyright - Database copyright ProQuest LLC; ProQuest does not claim copyright in the individual underlying works; Last updated - 2023-06-21.

[36] M. Kalita, M. Bishof, K. Bailey, M. Dietrich, J. Greene, R. Holt, W. Korsch, Z.-T. Lu, N. Lemke, P. Mueller, T. O'Connor, R. Parker, and J. Singh, "Search for a permanent electric dipole moment (edm) of ^{225}ra atom," in *CLEO: QELS - Fundamental Science, CLEO_QELS 2015*, 05 2015.

[37] R. H. Parker, M. R. Dietrich, M. R. Kalita, N. D. Lemke, K. G. Bailey, M. Bishof, J. P. Greene, R. J. Holt, W. Korsch, Z.-T. Lu, P. Mueller, T. P. O'Connor, and J. T. Singh, "First measurement of the atomic electric dipole moment of ^{225}Ra," *Phys. Rev. Lett.*, vol. 114, p. 233002, Jun 2015.

[38] N. D. Scielzo, J. R. Guest, E. C. Schulte, I. Ahmad, K. Bailey, D. L. Bowers, R. J. Holt, Z.-T. Lu, T. P. O'Connor, and D. H. Potterveld, "Measurement of the lifetimes of the lowest $^3p_1$ state of neutral ba and ra," *Phys. Rev. A*, vol. 73, p. 010501, Jan 2006.

[39] J. D. Jackson, *Classical electrodynamics*. New York, NY: Wiley, 3rd ed. ed., 1999.

[40] R. A. Ready, G. Arrowsmith-Kron, K. G. Bailey, D. Battaglia, M. Bishof, D. Coulter, M. R. Dietrich, R. Fang, B. Hanley, J. Huneau, S. Kennedy, P. Lalain, B. Loseth, K. McGee, P. Mueller, T. P. OConnor, J. OKronley, A. Powers, T. Rabga, A. Sanchez, E. Schalk, D. Waldo, J. Wescott, and J. T. Singh, "Surface processing and discharge-conditioning of high voltage electrodes for the ra edm experiment," *Nuclear Instruments and Methods in Physics Research Section A: Accelerators, Spectrometers, Detectors and Associated Equipment*, vol. 1014, p. 165738, 2021.

[41] J. M. Pendlebury, W. Heil, Y. Sobolev, P. G. Harris, J. D. Richardson, R. J. Baskin, D. D. Doyle, P. Geltenbort, K. Green, M. G. D. van der Grinten, P. S. Iaydjiev, S. N. Ivanov, D. J. R. May, and K. F. Smith, "Geometric-phase-induced false electric dipole moment signals for particles in traps," *Phys. Rev. A*, vol. 70, p. 032102, Sep 2004.

[42] U. Dammalapati, K. Jungmann, and L. Willmann, "Compilation of Spectroscopic Data of Radium (Ra I and Ra II)," *Journal of Physical and Chemical Reference Data*, vol. 45, p. 013101, 02 2016.

[43] K. Wendt, S. A. Ahmad, W. Klempt, R. Neugart, E. W. Otten, and H. H. Stroke, "On the hyperfine structure and isotope shift of radium," *Zeitschrift fr Physik D Atoms, Molecules and Clusters*, vol. 4, no. 3, pp. 227–241, 1987.

[44] K. Heilig and A. Steudel, "Changes in mean-square nuclear charge radii from optical isotope shifts," *Atomic Data and Nuclear Data Tables*, vol. 14, no. 5, pp. 613–638, 1974. Nuclear Charge and Moment Distributions.

[45] G. Breit and L. A. Wills, "Hyperfine Structure in Intermediate Coupling," *Physical Review*, vol. 44, no. 6, pp. 470–490, 1933.

[46] J. R. Guest, N. D. Scielzo, I. Ahmad, K. Bailey, J. P. Greene, R. J. Holt, Z.-T. Lu, T. P. OConnor, and D. H. Potterveld, "Laser Trapping of Ra225 and Ra226 with Repumping by Room-Temperature Blackbody Radiation," *Physical Review Letters*, vol. 98, no. 9, p. 093001, 2007.

[47] J. Biero, "Multiconfiguration dirachartreefock calculations of the hyperfine structures of radium," *Journal of Physics B: Atomic, Molecular and Optical Physics*, vol. 38, p. 2221, jun 2005.

[48] M. V. Romalis and E. N. Fortson, "Zeeman frequency shifts in an optical dipole trap used to search for an electric-dipole moment," *Phys. Rev. A*, vol. 59, pp. 4547–4558, Jun 1999.

[49] A. Kramida, Yu. Ralchenko, J. Reader, and and NIST ASD Team. NIST Atomic Spectra Database (ver. 5.12), [Online]. Available: `https://physics.nist.gov/asd` [2024, October 18]. National Institute of Standards and Technology, Gaithersburg, MD., October 2024.

[50] G. Schettler, H. Oberhnsli, and K. Hahne, "Ra-226 and rn-222 in saline water compartments of the aral sea region," *Applied Geochemistry*, vol. 58, 04 2015.

[51] M. Alfred, A. Christos, K. Clemens, S. Mike, K. Leszek, and B. Frank, "An overview of targeted alpha therapy with ^{225}actinium and ^{213}bismuth," *Current Radiopharmaceuticals*, vol. 11, no. 3, pp. 200–208, 2018.

[52] R. Ready, H. Li, S. Kofford, R. Kwapisz, H. Dan, A. Sawhney, M. Fan, C. Holliman, X. Shi, L. Sever-Walter, A. N. Gaiser, J. R. Griswold, and A. M. Jayich, "Laser cooling of radium-225 ions," 2024.

[53] E. P. Abel, K. Domnanich, H. K. Clause, C. Kalman, W. Walker, J. A. Shusterman, J. Greene, M. Gott, and G. W. Severin, "Production, collection, and purification of 47ca for the generation of 47sc through isotope harvesting at the national superconducting cyclotron laboratory," *ACS Omega*, vol. 5, no. 43, pp. 27864–27872, 2020. PMID: 33163769.

[54] E. P. Abel, K. Domnanich, H. K. Clause, C. Kalman, W. Walker, J. A. Shusterman, J. Greene, M. Gott, and G. W. Severin, "Production, collection, and purification of 47ca for the generation of 47sc through isotope harvesting at the national superconducting cyclotron laboratory," *ACS Omega*, vol. 5, no. 43, pp. 27864–27872, 2020. PMID: 33163769.

[55] E. J. Salumbides, V. Maslinskas, I. M. Dildar, A. L. Wolf, E.-J. van Duijn, K. S. E. Eikema, and W. Ubachs, "High-precision frequency measurement of the 423-nm ca i line," *Phys. Rev. A*, vol. 83, p. 012502, Jan 2011.

[56] W. Nrtershuser, N. Trautmann, K. Wendt, and B. Bushaw, "Isotope shifts and hyperfine structure in the 4s2 1s0 4s4p1p1 4s4d 1d2 transitions of stable calcium isotopes and calcium-41," *Spectrochimica Acta Part B: Atomic Spectroscopy*, vol. 53, no. 5, pp. 709–721, 1998.

[57] J. R. D. Paul T. Boggs, "Orthogonal distance regression," *NISTIR 89-4197*, December 1989.

[58] D. R. Olander and V. Kruger, "Molecular beam sources fabricated from multichannel arrays. iii. the exit density problem," *Journal of Applied Physics*, vol. 41, pp. 2769–2776, 06 1970.

[59] V. P. I. C. B. Alcock and M. K. Horrigan, "Vapour pressure equations for the metallic elements: 2982500k," *Canadian Metallurgical Quarterly*, vol. 23, no. 3, pp. 309–313, 1984.

[60] M. Mantina, A. C. Chamberlin, R. Valero, C. J. Cramer, and D. G. Truhlar, "Consistent van der waals radii for the whole main group," *The Journal of Physical Chemistry A*, vol. 113, no. 19, pp. 5806–5812, 2009. PMID: 19382751.

[61] J. C. Slater, "Atomic radii in crystals," *The Journal of Chemical Physics*, vol. 41, pp. 3199–3204, 11 1964.

APPENDIX A. DOCUMENTATION OF THE BLUREI LASER LOCK PROGRAM

Introduction

This document outlines the purpose and workings of the program named "Wavemeter_Solstis_LockingV2.vi" contained in the folder "I:\projects\spinlab\vis_Labview\ABFLabviewProgramsGAK\WavemeterData".

The purpose of this program is to allow the SOLSTIS laser to receive wavelength data from a Bristol 871 wavemeter. The SOLSTIS comes with a program that allows it to connect and communicate with a HighFinesse brand wavemeter, but not a Bristol one. This connection is done by creating a TCP server for the HighFinesse wavemeter, that the SOLSTIS connects to. Our program works by creating a custom TCP server that the SOLSTIS connects to, thinking it's the HighFinesse Server. We then receive commands from the Solstis, and reply back with commands that either give the SOLSTIS what it wants to keep running, or, when it asks for the wavelength, giving it the response with the wavelength measured from the Bristol wavemeter.

To begin, we will give an outline of the thinking behind the development of this program. Then, we will show how to do various smaller tasks, all necessary components of the completed program. Then, we will give a list of commands given from the SOLSTIS to the TCP Wavemeter. Then, we will show how the program itself works

Outline

We began thinking about the wavemeter locking program by breaking it down into smaller tasks, that we would then stitch together as a whole in for the final program:

-Figure out how to measure the wavelength from the Bristol 871 wavemeter with its own NuView software

-Figure out how to measure the wavelength from the Bristol 871 wavemeter using labview

-Figure out how to make a TCP connection in labview

-Figure out how to make a TCP server that the SOLSTIS can connect to

-Figure out how to make a TCP Listener that can connect to the TCP_Wavemeter software that the SOLSTIS normally connects to

-Figure out what the commands and responses sent between the SOLSTIS and the TCP_Wavemeter software are

-Figure out how to insert a wavelength measured from the Bristol wavemeter into the response to the SOLSTIS whenever it asks for the wavelength

Tasks

Connecting and using Bristol 871 wavemeter with nuview

There was difficulty in initially connecting the Bristol 871 wavemeter. To start off with, the old 1350LAS2 computer did not have .NET Framework 3.5 Since the computer was getting replaced soon anyway, we waited for a different computer. Gordon also needed to get admin permissions on the computer. Once we got the new computer, we installed the software, but

Figure A.1: Page 88 of the Bristol manual.

Windows 10

When a RNDIS enabled device is connected to a Windows 10 PC for the first time, the PC occasionally recognizes the instrument as a COM port device instead of an Ethernet Gadget/RNDIS. To fix this, update the driver associated with the instrument. Updating the driver causes the PC to reassign the COM port device as an Ethernet Gadget/RNDIS. After connecting the 871 system to the PC via USB interface and powering up the 871 system, a successful connection will show up in the **Device Manager** (**Control Panel>Device Manager**) under **Network Adapters** as **USB RNDIS/Ethernet Gadget**.

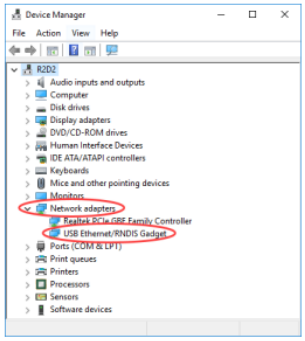

An unsuccessful USB connection with a RNDIS device will appear under **Ports (COM & LPT)** as a COM device.

it was unable to connect to the wavemeter. The solution to this problem was found in the Bristol troubleshooting section, pages 88-90. The Bristol is connected to 1350LAS2 through a USB cable. Apparently, 1350LAS2 was recognizing it as a COM port device, and not an RNDIS device. The fix was to update the driver software. Since 1350LAS2 can't connect to the internet, we used software Bristol supplied us with on a CD.

The Screenshots of the relevant pages of the manual are here:

It should also be noted that, when the new 1350LAS2 computer arrived, it initially would also not connect to the SOLSTIS laser itself. If we typed the IP address into firefox, it simply timed out. The solution to this was provided by the IT department here in the lab in an email:

Figure A.2: Page 89 of the Bristol manual.

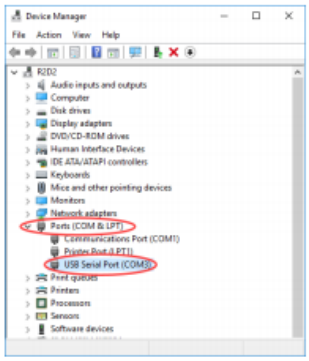

NOTE: This is incorrect for a USB connection only. The RS-422 to USB cable provided by Bristol Instruments appears as a COM device when correctly connected.

Use the following instructions to update the RNDIS driver:

1. Right click on **USB Serial Port** and select **Update Driver Software** as shown below.

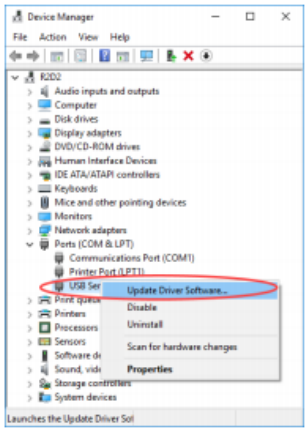

2. If an internet connection is available, select **Search automatically for updated driver software** to retrieve the latest driver from the internet.

Figure A.3: page 90 of the Bristol manual.

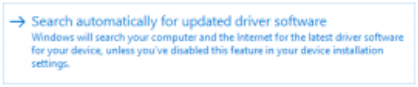

3. If no internet connection is available, or searching automatically does not resolve the issue, select **Browse my computer for driver software** and locate the **RNDIS Driver** zip file on the customer CD supplied with the instrument. Unzip the files, and choose the 32-bit or 64-bit file according to the Windows operating system of the PC.

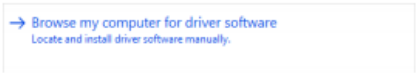

NOTE: If you need to connect to a RNDIS device from a virtual machine, it is usually easier to set up the RNDIS driver on your "real" machine and then share it with the virtual machine as you do with other network connections.

Figure A.4: IP address repair email.

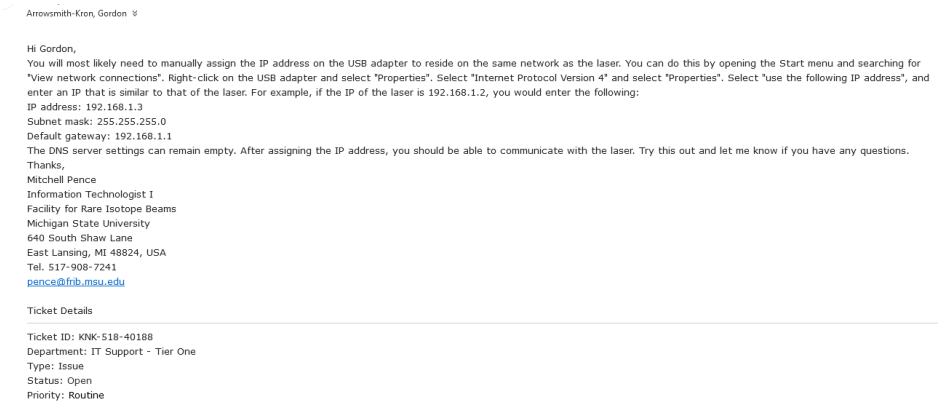

Arrowsmith-Kron, Gordon

Hi Gordon,
You will most likely need to manually assign the IP address on the USB adapter to reside on the same network as the laser. You can do this by opening the Start menu and searching for "View network connections". Right-click on the USB adapter and select "Properties". Select "Internet Protocol Version 4" and select "Properties". Select "use the following IP address", and enter an IP that is similar to that of the laser. For example, if the IP of the laser is 192.168.1.2, you would enter the following:
IP address: 192.168.1.3
Subnet mask: 255.255.255.0
Default gateway: 192.168.1.1
The DNS server settings can remain empty. After assigning the IP address, you should be able to communicate with the laser. Try this out and let me know if you have any questions.
Thanks,
Mitchell Pence
Information Technologist I
Facility for Rare Isotope Beams
Michigan State University
640 South Shaw Lane
East Lansing, MI 48824, USA
Tel. 517-908-7241
pence@frib.msu.edu

Ticket Details

Ticket ID: KNK-518-40188
Department: IT Support - Tier One
Type: Issue
Status: Open
Priority: Routine

Measuring Wavelength in Labview with Bristol 871

Before we started trying to get labview to work with the Bristol, we first figured out how to communicate with the wavemeter using Telnet. The instructions are in pages 55-56 of the Bristol manual, and are here:

The manual lists various commands that can be used, including one to measure the wavelength.

NOTE: When using this software, and typing in commands, the commands have to be typed in perfectly, the FIRST time. Using the delete key will appear to work, and will seem to let you correct any typos you make, but this is a lie. If you make a mistake, just hit "enter" and it'll say your command is not recognized, and then you can try again on the next line. This was highly confusing at first, as with the delete key appearing to work, it was possible to type in what appeared to be the same command twice, and have one work and the other not be recognized. Also, the colon was not strictly necessary to type in the command.

After this, labview code was found on the flashdrive sent by Bristol that allows a contin-

Figure A.5: Pages 55 and 56 of the bristol manual.

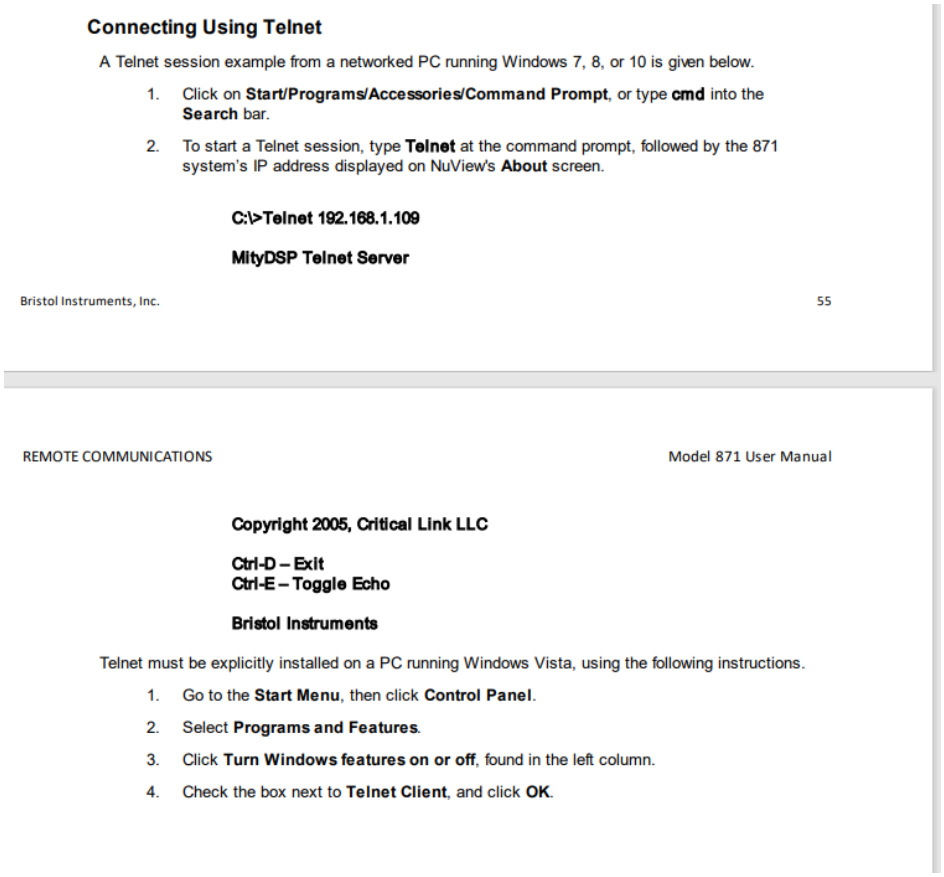

Connecting Using Telnet

A Telnet session example from a networked PC running Windows 7, 8, or 10 is given below.

1. Click on **Start/Programs/Accessories/Command Prompt**, or type **cmd** into the **Search** bar.
2. To start a Telnet session, type **Telnet** at the command prompt, followed by the 871 system's IP address displayed on NuView's **About** screen.

C:\>Telnet 192.168.1.109

MityDSP Telnet Server

Copyright 2005, Critical Link LLC

Ctrl-D – Exit
Ctrl-E – Toggle Echo

Bristol Instruments

Telnet must be explicitly installed on a PC running Windows Vista, using the following instructions.

1. Go to the **Start Menu**, then click **Control Panel**.
2. Select **Programs and Features**.
3. Click **Turn Windows features on or off**, found in the left column.
4. Check the box next to **Telnet Client**, and click **OK**.

Figure A.6: Front face of the SCPI$_Telnetprogram$.

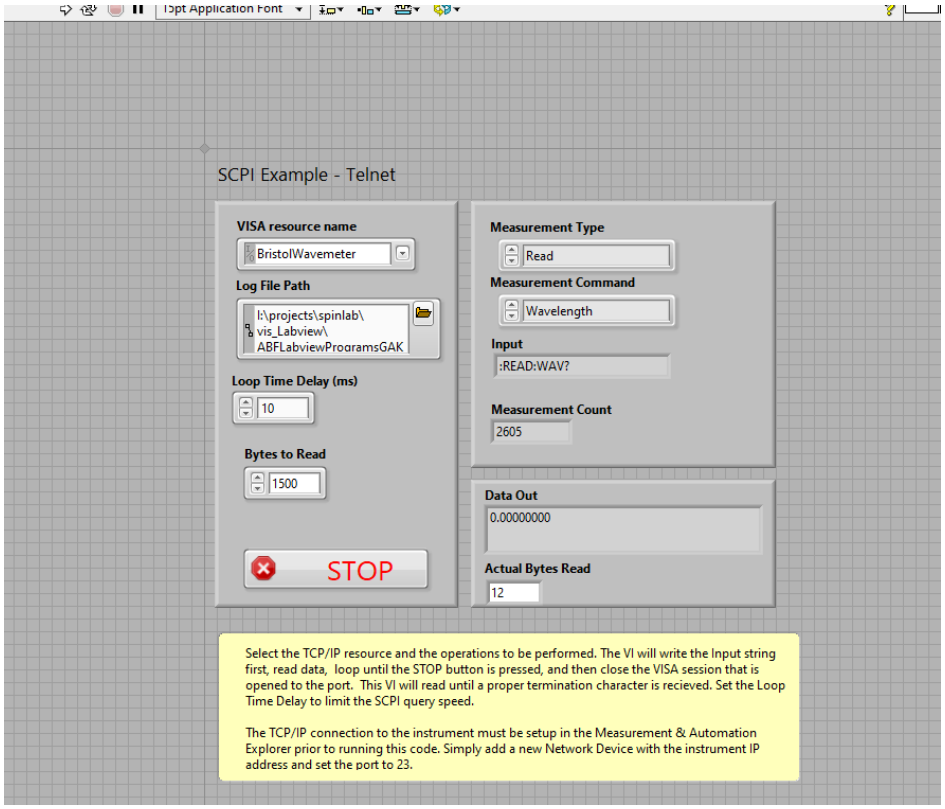

uous measurement of the wavelength it reads. Here's the front end of the program:

And here's the block diagram for it:

Looking at the program, it first initializes the values needed - Measurement Type, Measurement Command, and VISA resource string. Note that there are 3 subvis included that the program is dependent on, and that the locking program is dependent upon as well. Basically, it writes the command to measure the wavelength, and then receives the data that is returned. It does this over and over again until told to stop, or an error occurs. This program contained all the functionality for measuring the wavelength that our locking program needed.

Figure A.7: Block diagram of the SCPI$_Telnetprogram$.

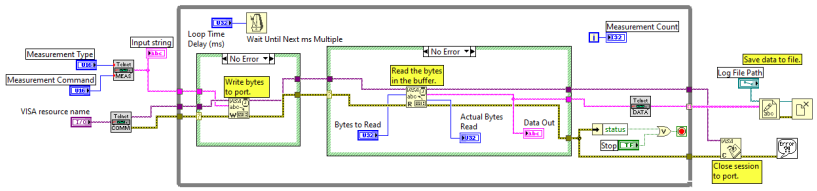

Figure A.8: Network connections for the SOLSTIS.

External devices

Device	IP address	Port number	Link
Wavelength meter	192.168.1.224	48824	Enable / Disable

Making a TCP server for SOLSTIS to connect to

SOLSTIS Settings

In order to make a TCP server that can connect to the SOLSTIS, it's first important to look at the "Network Settings" supervisor option, in the configure menu. In this tab, there is a list of external hardware, with an IP address and port number for the wavemeter:

To create a server that connects to the SOLSTIS, and can recieve and write commands, the following program was made:

Note disconnected pink lines; these lead to an array of strings containing commands to write to the SOLSTIS, a detailed description of these commands will come later.

Figure A.9: Block diagram of test server to connect to SOLSTIS.

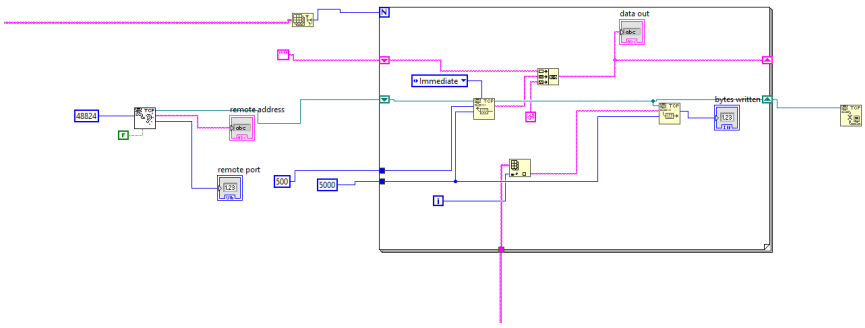

TCPListen

The program works first by using the TCPListen block to create a server. The input to this block requires the port number in order to connect to the SOLSTIS. This should be the same as the port number for "Wavelength meter" in "Network Settings". There is also a false constant connected to it - this determines whether or not to resolve the IP address output in "remote address". I chose this to be false.

Coming out of the TCPListen VI block is an indicator for the remote address, an indicator for the remote port, and the task output. The task output then enters a for loop.

TCPRead

The for loop does two things: It reads from the SOLSTIS, and then it writes to the SOLSTIS. The first command always seems to be the SOLSTIS to the server, and not vice versa. The Read function has 4 inputs: The first, the TCP task, is created by the TCPListen block. It also takes in the number of bytes to read, in this case set to 500. It also takes in a timeout parameter. This tells how long the program should wait for there to be data to read, in

ms. In this case it's set to 5000 ms. Finally, there's a mode setting, in this case set to immediate. This parameter is VERY important to set to immediate. By default, the mode is set to "standard". In the standard setting, the read function waits until the total number of bytes specified in "bytes to read" are all read, or until the timeout happens. If the timeout happens, it will throw an error, and stop the program. It will also more often than not wait the full timeout cycle each time. By setting this to "Immediate", it immediately returns any bytes received, as soon as it receives them. It will only throw an error if it times out without receiving any bytes. This means it doesn't have to receive the full number of bytes, and it will return the bytes it receives as soon as it gets them.

The outputs from the read block are the string that is received, and the output task. The string recieved is displayed on the front page of the software, while the task is then taken to write.

TCPWrite

To write to the SOLSTIS, two inputs are needed: The first is the timeout parameter, which we keep to be 5000 ms. The second is the string that we want to write. In this case, we have an array of strings not shown, which are written once per loop. In this way, the program reads the SOLSTIS, then writes a specific command, then reads again from the SOLSTIS, then writes the next command, and so on. This program then outputs the task again, though that ouput is not used in this particular program, as well as a number that returns the number of bytes that it wrote.

Making a TCP connection to the TCP_Wavemeter server

A simple program to be able to connect is here:

Figure A.10: Simple program to connect to the TCP wavemeter server.

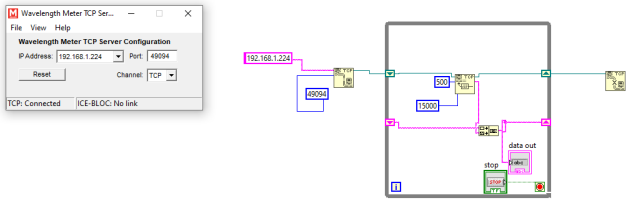

This labview program uses the TCP Open Connection block to open a connection to the TCP_Wavemeter server. Two inputs are required: the IP address and port both have to match. Note the port assigned here is different than the port used by the SOLSTIS. From there, the program enters an infinite read loop until told to stop. I ran this program, to demonstrate that upon running it, the TCP_Wavemeter server says it's connected. After the loop is exited, the connection is closed.

To give and receive commands to the TCP_wavemeter server, the following program was constructed:

The framework of this program is essentially the same as the program connected to the SOLSTIS. The only difference is that it writes first from an off-screen array, and then reads. As can be seen, this program can also be used to find the strings used.

Figure A.11: Data received from TCP server.

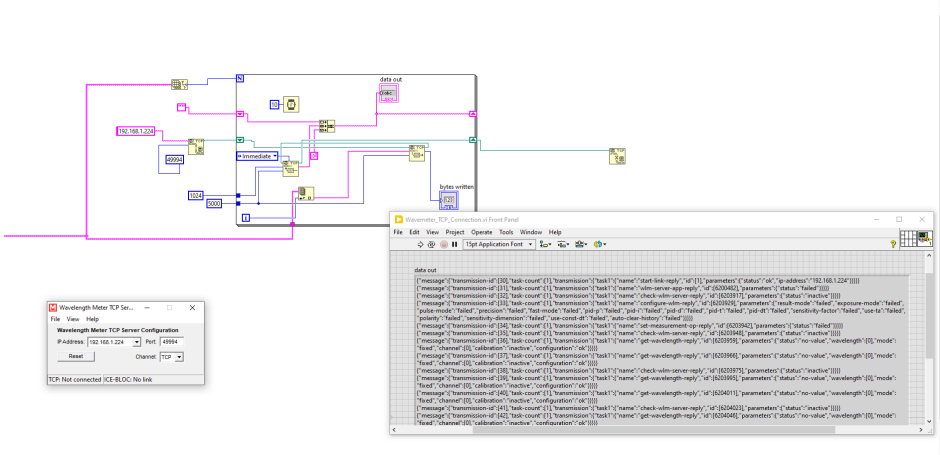

Commands

The commands seem to come in pairs. The Solstis seems to write first, and then recieve a response from the TCP_Wavemeter program. The exact ordering and conditions of these commands is sometimes different, and is not quite clear to us. After finding these commands, and the responses that the SOLSTIS wants, it became possible to send the SOLSTIS the wavelength whenever it sent a command asking for it, and to simply send back whatever it wants to hear for every other command, to keep it happy. At first, we hoped to categorize the order of these commands, but we later realized it would be easier just to use a case structure for our locking program, dependent upon input command from the SOLSTIS. Our initial documentation of these commands is in the file "TCP Pingpong.txt".

NOTE: There are a variety of IDs in the following commands and responses. It seems that the "transmission-id" from the SOLSTIS is always the same as the "id" that comes later in its command. I believe that, when the Wavelength_TCP server writes back, the "id" contained in the task is supposed to be the same as the "transmission-id"/"id" of

the SOLSTIS command it's responding to. I don't think the "transmission-id" of the server response matters. When we were studying what the commands were, we at first ignored this. We cut and pasted strings between each other, and this would result in the server responses sometimes not having matching IDs to the SOLSTIS commands that were sent. This didn't cause any problems, and everything seemed to work fine. If you look at the commands and the responses below, you'll see that sometimes the IDs match, and sometimes they don't; this is why. On the actual locking program itself, however, we paid attention to this, and took care to add in a feature that read what the "transmission-id" was from the SOLSTIS command, and then inserted it into the "id" of the server response. How we did that will be discussed later.

"Start-Link"

SOLSTIS writes:

{"messag":{"transmission-id":[1],"task-count":[1],"transmission":

{"task1":{"name":"start-link","id":[1],"parameters":

{"ip-address":"192.168.1.222"}}}}}

Server writes back:

{"message":{"transmission-id":[15577],"task-count": [1],"transmission":

{"task1":{"name":"start-link-reply","id":[1],"parameters":

{"status":"ok","ip- address":"192.168.1.224"}}}}}

Seems to initialize the link

"wlm-server-app"

Solstis Writes:

{"message":{"transmission-id":[6200482],"task-count": [1],"transmission":{"task1":

{"name": "wlm-server-app","id":[6200482],"parameters":{"action":"start"}}}}}

If wavemeter software is closed:

Sever Writes:

{"message":{"transmission-id":[15580],"task-count": [1],"transmission":{"task1":

{"name": "wlm-server-app-reply","id":[6200482],"parameters": {"status":"failed"}}}}}

If wavemeter software is open:

Server writes

{"message":{"transmission-id":[15580],"task-count": [1],"transmission":{"task1":

{"name": "wlm-server-app-reply","id":[6200482],"parameters": {"status":"ok"}}}}}

Seems to check whether wavemeter software is open

"check-wlm-server"

SOLSTIS writes:

{"message":{"transmission-id":[6203912],"task-count": [1],"transmission":{"task1":

{"name": "check-wlm-server","id":[6203917]}}}}

Server writes:

{"message":{"transmission-id":[7],"task-count":[1],"transmission": {"task1":

{"name": "check-wlm-server-reply","id":[6203917],"parameters": {"status":"active"}}}}}

Not sure what this does

”configure-wlm”

SOLSTIS writes:

{“message”:{“transmission-id”:[6203929],“task-count”: [1],“transmission”: {“task1”: {“name”:“configure-wlm”,“id”:[6203929],“parameters”: {“result-mode”: “reset”, “exposure-mode”:“auto”,“pulse- mode”:“continuous”,“precision”:“fine”,“fast-mode”: “false”,“pid-p”: [0],“pid-i”:[0],“pid-d”:[0],“pid-t”:[0],“pid-dt”:[0],“sensitivity- factor”: [0],“use-ta”:“false”,“polarity”:“negative”,“sensitivity-dimension”: [0],“use-const-dt”:“false”,“auto-clear-history”:“false”}}}}}

Server writes:

{“message”:{“transmission-id”:[40],“task-count”:[1],“transmission”: {“task1”:{“name”: “configure-wlm-reply”,“id”:[6203929],“parameters”:{“result- mode”:“ok”,“exposure-mode”: “ok”,“pulse-mode”:“ok”,“precision”:“ok”,“fast-mode”:“ok”,“pid-p”: “failed”,‘pid-i”: “failed”,‘pid-d”:“failed”,“pid-t”:“failed”,“pid- dt”:“failed”,“sensitivity-factor”: “failed”,“use-ta”:“failed”,“polarity”:‘failed”,“sensitivity- dimension”: “failed”,“use-const-dt”:“failed”,“auto-clear-history”:“failed”}}}}}

Seems to configure the wavelength measurement

”set-measurement-op”

SOLSTIS writes:

{“message”:{“transmission-id”:[6203942],“task-count”: [1],“transmission”:{“task1”: {“name”: “set-measurement-op”,“id”:[6203942],“parameters”: {“operation”:“measurement”}}}}}

Server writes:

{“message”:{“transmission-id”:[50],“task-count”:[1],“transmission”: {“task1”:

{“name”: “set-measurement-op-reply”,“id”:[6203942],“parameters”: {“status”:“ok”}}}}}

Not sure what this does

get-wavelength

Finally, the command that sends the measured wavelength to the SOLSTIS

SOLSTIS writes:

{“message”:{“transmission-id”:[50],“task-count”:[1],“transmission”: {“task1”:

{“name”: “set-measurement-op-reply”,“id”:[6203942],“parameters”: {“status”:“ok”}}}}}

If the wavemeter is underexposed, Server writes:

{“message”:{“transmission-id”:[63],“task-count”:[1],“transmission”: {“task1”:

{“name”: “get-wavelength-reply”,“id”:[6203959],“parameters”:{“status”:

“low- signal”,“wavelength”: [0],“mode”:“fixed”,“channel”:

[0],“calibration”:“inactive”,“configuration”:“ok”}}}}}

if the wavemeter is overexposed, Server writes:

{“message”:{“transmission-id”:[77],“task-count”:[1],“transmission”: {“task1”:{“name”:

“get-wavelength-reply”,“id”:[6203959],“parameters”:{“status”:“high- signal”,

“wavelength”: [0],“mode”:“fixed”,“channel”:

[0],“calibration”:“inactive”,“configuration”:“ok”}}}}}

If there is no measurement available, Server writes:

{“message”:{“transmission-id”:[85],“task-count”:[1],“transmission”: {“task1”:

{“name” “get-wavelength-reply”,“id”:[6203966],“parameters”:{“status”:

‘no- value”,“wavelength”: [0],“mode”:“fixed”,“channel”: [0],“calibration”:

“inactive”,“configuration”:“ok”}}}}}

If there is a measurement ready, Server writes:

{“message”:{“transmission-id”:[136],“task-count”:[1],“transmission”: {“task1”:{“name”: “get-wavelength-reply”,“id”:[6203995],“parameters”: {“status”:

“ok”,“wavelength”: [779.985261],“mode”:“fixed”,“channel”: [0],“calibration”:

“inactive”,“configuration”:“ok”}}}}}

The “779.985261” is the measurement of the wavelength in nanometers. It has a higher precision that that shown on the high finesse output.

In our program, we only send two types of returns: either the measurement ready reply, with the wavelength measured from the Bristol inserted, or the underexposed ”low-signal” setting. The Bristol wavemeter returns ”0.00000000” when either underexposed or overexposed, so we just chose the underexposed reply, since that should happen more.

Wavemeter_Solstis_LockingV2.vi

Here, I will give an overview of how our V2 Software works:

Initial Parameters

here are the input parameters for our program:

-The ”port” is the port number used to create the TCP server, for the SOLSTIS to connect, in the same way as shown before for creating a TCP server for the SOLSTIS to connect to

- ”Bytes to Read” specifies how many bytes the read program should read

- ”Timeout (ms)” specifies the timeout in milliseconds of how long the read and write functions should wait to give or recieve data

Figure A.12: Input parameters for locking program.

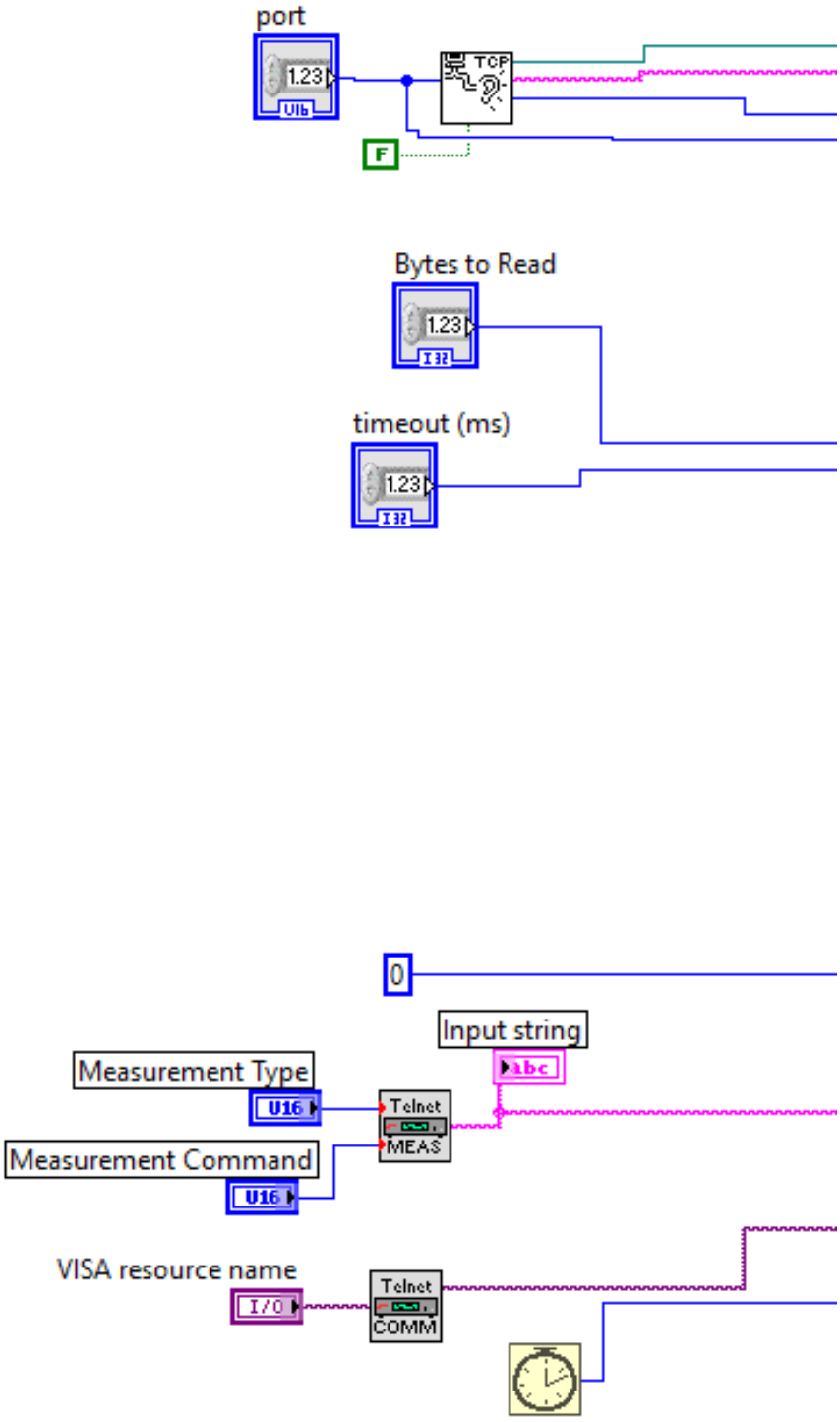

Figure A.13: The file creation in the locking program.

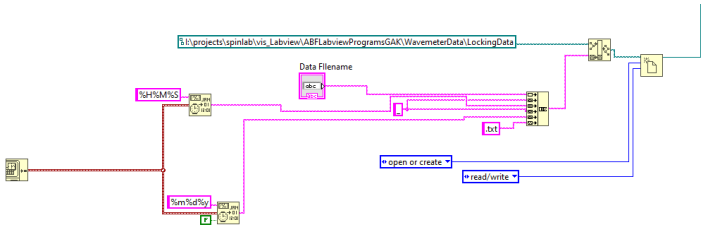

The "Measurement Type", "Measurement Command", "VISA resource name", and the TELNET MEAS and TELNET COMM blocks were copied from the Bristol sample code, and are for communicating with the wavemeter.

Filename Creation

In order to save the data, We made the following group of blocks:

This creates a text file in the folder specified in the green path constant. If another folder is desired, this constant should be changed. The filename is created by first taking a user input filename in "Data Filename". From there, a 6 digit string is appended which tells the time it was created, with two digits for hour in military time, then two digits for the minute, then two digits for the second, followed by another 6 digit string with 2 digits for the month, 2 digits for the day, then 2 digits for the year. The Data Filename, time, and date are all separated by an underscore. Then, by appending ".txt", the file is configured as a text file. In this way, every data file created and saved by this program automatically records the date and the time it was run, and extremely useful feature from our experience.

Figure A.14: Section of locking program that reads in commands.

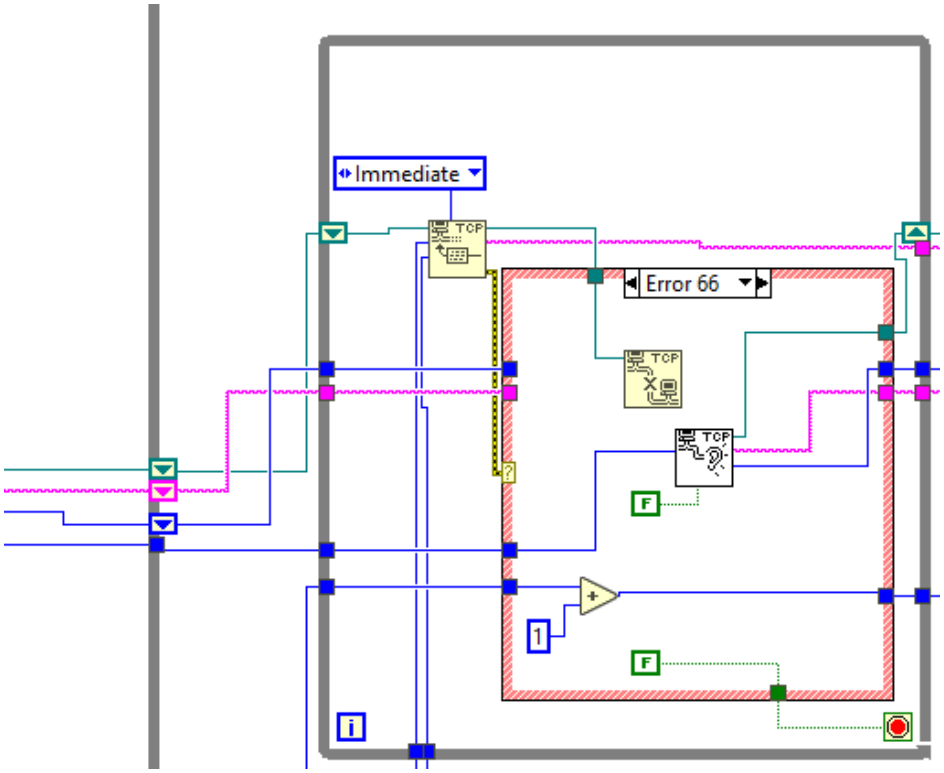

Reading SOLSTIS

Inside the main loop of the program, the first thing thing the program does is read from the SOLSTIS. The code is here:

The reading happens in a nested loop. The reason for this is that, if the connection is interrupted, the program automatically creates a new listener for the SOLSTIS to connect to.

Inside this nested loop, the READ block is first utilized, with the Bytes to Read and Timeout specified by the initialization, and its mode set to immediate. It also takes the input task from the TCP connection. It outputs the output task, an error signal and the data it read.

The second part of the loop looks at the error signal. This is done to make sure that the connection is still running. If it isn't, the relevant error seems to be "Error 66", in which case the connection will have to be restarted. As can be seen, if Error 66 is thrown, the task output from the READ cube is closed, and a new TCP server is created, using the same port number as specified in the initialization. The outputs from this block, the remote address and the remote port, are updated, and the output task is changed. The loop also makes an increment in the number of disconnections to have occured, and also throws a "false" boolean to the loop, telling the loop to read again, this time with the new connection. If that connection also fails, it will loop again, and again, unitl a succesfull read is made.

When there is no error, none of the input parameters to the case structure are changed, and a "true" boolean is thrown to the stop condition of the loop, and the loop is exited.

NOTE: The task input for the TCP connection, you will notice, uses a shift register. The reason for this is, if the connection is at some point interrupted and needs to reconnect, then the task from that new connection needs to be read from and written to, and not the task from the first connection made at the beginning of the program.

The command read from the SOLSTIS is output from this loop. From here, two things need to be done: Determine what the command is, and what the transmission ID was.

Determine Command

As a reminder, the commands written look something like:

{"message":{"transmission-id":[1],"task-count":[1],"transmission": {"task1":

{"name": "start-link","id":[1],"parameters":{"ip- address":"192.168.1.222"}}}}}

The command that is written to the server comes directly after the string "name", so the following block diagram was made:

Figure A.15: Command text processing.

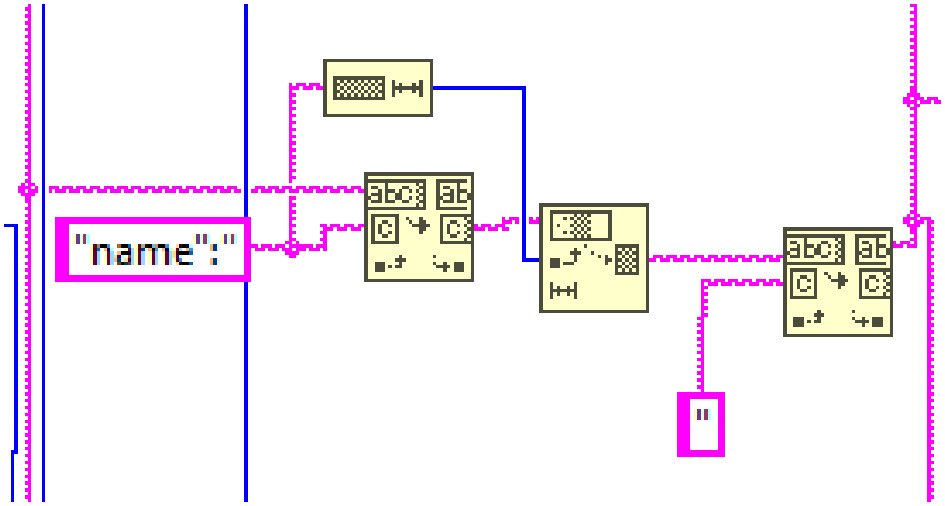

This series of blocks takes in the command, and does three operations:

-It removes everything before the string ”name”:”

-It then removes the string ”name”:” from that, the first character in the string is now the first character of the command

-It then removes the first ” it sees, along with anything after, leaving only the string of the command itself

Determine ID

The transmission ID seems to be the same as the ID of the task number, and to be careful, we want the task number of the response from our server to be the same. So, we need to get either the transmission ID or the task ID. We take advantage of the fact that the first open square brackets is right before the transmission ID. The following diagram was made:

The program does four things:

-It removes the first closing square bracket it sees, and everything after it

-It then removes everything before the first open square bracket. What is left now is an

Figure A.16: Processing the ID.

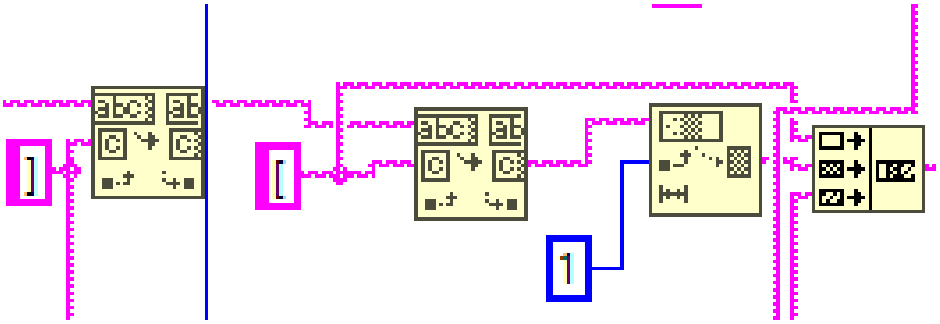

open square bracket followed by the transmission ID

-It then removes the first character, which is the open square bracket. What is left is the transmission ID

-It then places the transmission ID in between a pair of square brackets again; this is so it can be easily inserted into the server response later. Note that the closing square brackets constant leads to the botttom input of the concatenation box.

Writing to SOLSTIS

To begin, here's what the loop looks like, with inputs labeled, for giving the wavelength to the SOLSTIS:

Much like the read block, the write block is in a loop as well. The loop is there for the same reason. If a disconnection happens, the program can reconnect, and try to write again. Let's now go over how the server gives the wavelength to the SOLSTIS.

What the server responds with depends completely on what command was sent to the SOLSTIS. That's why a case structure is utilized. The case structure's conditional depends on the command string, as different commands sent by the SOLSTIS require different responses. If the SOLSTIS is asking for the wavelength, the command string will be "get-

Figure A.17: Writing software for the SOLSTIS.

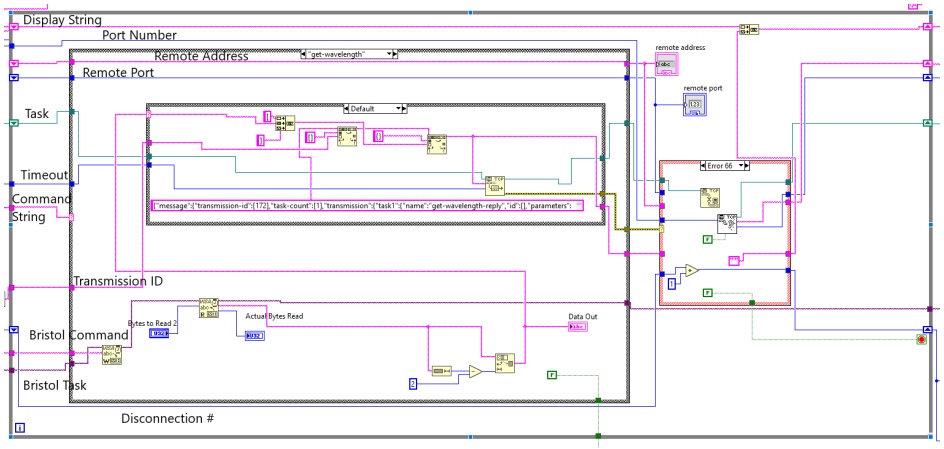

wavelength", and the case shown above will take effect.

Passing Wavelength to SOLSTIS

If the SOLSTIS asks for the wavelength, then a measurement must be taken from the wavemeter. This is done in the matter shown in the sample code provided by Bristol. Note that two characters are deleted from the end of the data string measured from the Bristol; this is because there are two extra characters, we believe a line end and carriage return, that are also there. The data from there is then passed into another case structure.

Bristol measures 0.00000000

If the Bristol returns 0.00000000, it is most likely underexposed. We then have to tell the SOLSTIS it is. The case structure for this is here:

Inside the second case structure, there is the string constant:

{"message":{"transmission-id":[63],"task-count":[1],"transmission": {"task1": {"name": "get-wavelength-reply","id":[],"parameters":{"status":"low- signal","wavelength": [0],"mode":"fixed","channel": [0],"calibration":"inactive","configuration":"ok"}}}}}

Figure A.18: Case structure of wavemeter reading of 0.

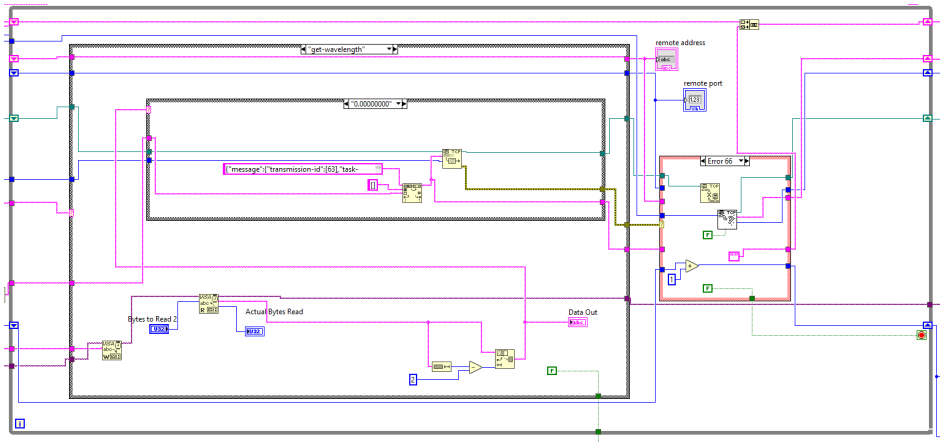

This is the command returned by the server when it's underexposed, with one key difference: The task ID, instead of being a number in between two square brackets, is just an open and then closed square bracket. This substring "[]" only appears once in the command, in a unique place. From there, this string has the substring "[]" replaced with a substring of the form "[*taskID*]", and the resulting string is thus the underexposed command with the task ID from the SOLSTIS command inserted in the right place. This command is then written to the SOLSTIS. From there, a similar error check to the read command is done, where if the write cannot be done due to a disconnection, the program automatically reconnects. This whole structure is in a loop, so that if the write command doesn't go through due to disconnection, it automatically tries again after reconnecting.

Bristol measures wavelength

If the Bristol measures a proper wavelength, the case structure from above is executed, shown here again:

Note that this case occurs as the default, except when "0.00000000" is passed. A similar process happens as with the underexposed case, except this time two different values need

Figure A.19: Case structure of normal wavelength reading.

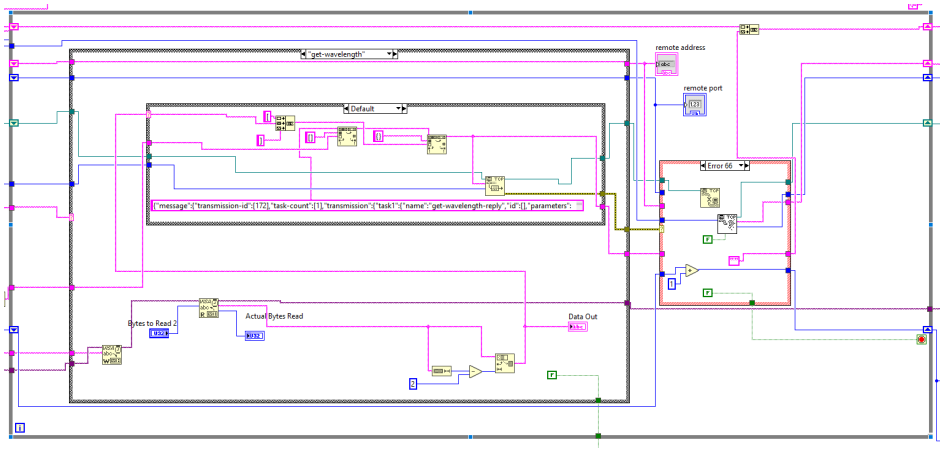

to be passed: The task ID, AND the wavelength. To do this, the starting string is:

{“message”:{“transmission-id”:[136],“task-count”:[1],“transmission”: {“task1”:

{“name”: “get-wavelength-reply”,“id”:[],“parameters”: {“status”:“ok”,“wavelength”:

{},“mode”:“fixed”,“channel”:

[0],“calibration”:“inactive”,“configuration”:“ok”}}}}}

Which is the correct form for the return string for the wavelength, except the Task ID is followed by ”[]” and ”wavelength”: is followed by ”{}”. Both of these substrings only occur once in the command, so they can be replaced by their respective values. The wavelength string is put in between a pair of square brackets, and then replaces ”{}”. Similarly, the Task ID, already in between a pair of square brackets, replaces ”[]”. The resulting string is precisely the form that we want to pass to the SOLSTIS. This command is then written, and any error is once again checked. In the case where there is no error, the loop looks like this:

Note that when there is no error, the exit condition for the loop is set as ”true”.

Figure A.20: Case structure with no wavelength reading.

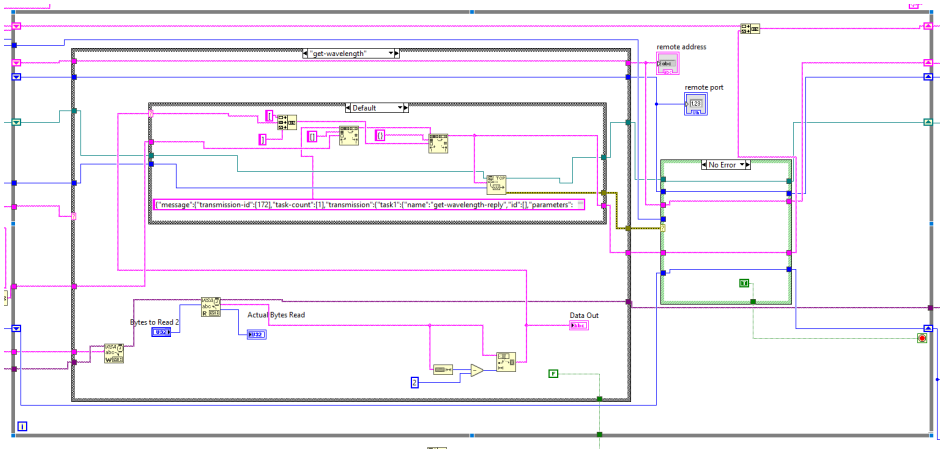

Figure A.21: Case strucutre with non-wavelength command.

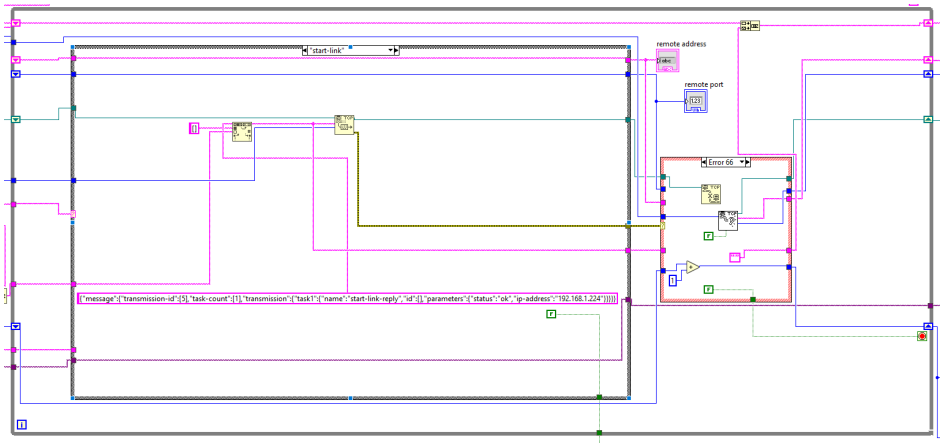

Bristol recieves non-wavelength command

In the case when the SOLSTS sends a command that doesn't ask for the wavelength, the outer case structure looks like this:

This particular case uses the case when the command is "start-link", but all other non-wavelength commands are similar. There is a string constant that is the same as the command that the SOLSTIS wants to see, except the task ID is followed by "[]". This string then has this "[]" replaced by the task ID taken from the SOLSTIS, and is then written.

Figure A.22: Case structure with unrecognized command.

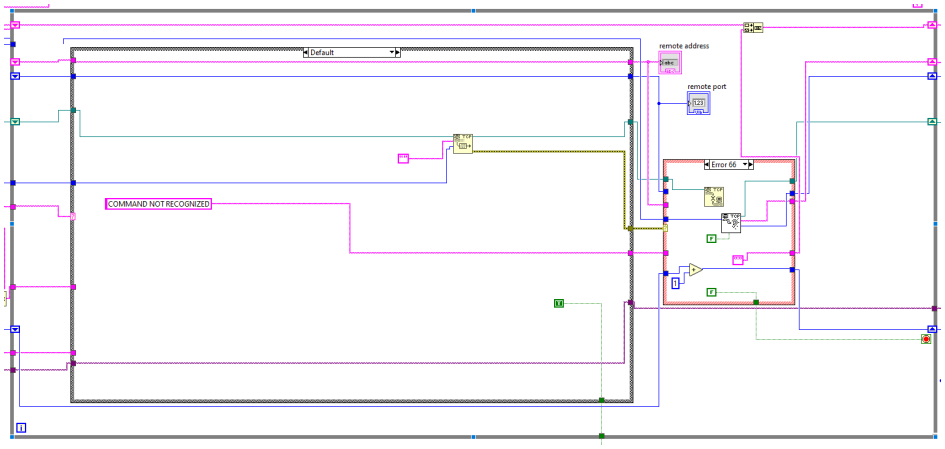

From there, the error is checked, to see if it has to reconnect.

Bristol receives unrecognized command

In the case where the case structure receives a command string it does not recognize, the following case occurs:

Nothing is written to the SOLSTIS, and the string "UNRECOGNIZED COMMAND" is written to the output. There is also a true boolean constant that is false in every other case; This constant is in an OR gate with a manual stop button for the outer loop. This means that, if the server doesn't recognize the command, the outer loop of the program is exited, and the program stops automatically

APPENDIX B. DOCUMENTATION OF THE HIGH VOLTAGE DIVIDER ASSEMBLY

Introduction

In order to improve voltage measurement precision for the RaEDM experiment, a new high voltage divider had to be constructed. This HV divider design is traceable to PTB in Germany, and instructions were sent over of how to build it. This technote aims to give further detail as to the assembly process.

Parts List

The individual parts needed to assemble the HV divider can be seen in Table B.1

Notes about Parts and Additional Machining

MDN1475 Caddock Resistors

The MDN-1475 resistors came in 12 sets of 5 each. These resistors are specially selected resistors from the Caddock USFS-370 10.0 MΩ, 9.99 MΩ, and 9.90 MΩ series. They are selected so that, when each group of 5 resistors is used in series, the total resistance is equivalent to five 9.95 MΩ resistors in series, with a temperature coefficient of $< \pm 1$ ppm/°C. As such, it is extremely important that each set of 5 stay together, and they have been numbered to ensure this. Each of the MDN-1475 resistors is rated to 1 kV DC, which means that there has to be one resistor per maximum voltage applied, to ensure that the potential

Table B.1: Parts list for the improved HV divider.

Part	Part #	Vendor	Quantity	Additional Machining?
HV Resistors	MDN1475	Caddock	60	No
Resistor Mounting	Custom	Custom	3	3D Printed
1/2" thick, 4" Diameter Copper Disk	9103K5	Mcmaster-Carr	1	yes
1" thick, 4.5" Diameter Aluminum Disk	1610T39	Mcmaster-Carr	1	yes
1" Thick, 1.25" Diameter Aluminum Disk	1610T12	Mcmaster-Carr	1	yes
Acrylic tube, 5" OD, 4.5" ID, 3 feet long	8486K581	Mcmaster-Carr	1	yes
2" diameter Copper Ball Float	2892K12	Mcmaster-Carr	1	no
1/4"-20 threaded nylon rods, 2 feet long	98831A369	Mcmaster-Carr	4	yes
1/4"-20 threaded nylon nuts	94812A700	Mcmaster-Carr	4	no
100 kΩ Resistor	Y0007100K000T9L	Newark	1	no
NPN Darlington Transistor	MJH11022G	Digikey	1	no
12 V, 50 x 50 x 10 mm Fan	CFM-5010V-143-260-20	digikey	1	no
12 V AC/DC Power Supply	pmt-12v150w1aa	Newark	1	no
Temperature Controller	ESCN-HV2M-500	Newark	1	no
700 Ω Resistor	CW02B700R0JE70	Newark	1	no
0.2 Ω Resistor	MP850-.20-1%	Newark	1	Burns out, a different resistor is needed
Diodes	1N4007-T	Newark	3	no
Box for electronics	1458D3B	Newark	1	yes
Corona Ring Halves with Holes	330035	Ross Engineering	2	yes

difference across each resistor is at maximum 1 kV. The MDN-1475 resistors were originally requested by the first HV divider assembled by PTB. It was fortunate that Caddock still had some spare sets of 5 left over, as it means that these resistors were selected in the exact same method as the previous HV dividers. Further information on these resistors can be found in entry 1196 of the Spinlab RaEDM electronic logbook.

Resistor Mounting

The caddock resistors are held in place in a spiral pattern by a 3d-printed central column. The 3D STL file is located in I:\projects\spinlab\Designs\HV Divider. The central column consists of 3 of these pieces stacked on top of one another.

Copper Disk

The copper disk which serves as the base for the central resistor column, as well as a heat conductor for the temperature control, required extensive further machining. First, a hole directly in the center was drilled and tapped with a 6-32 threading. This was for screwing

in the Darlington transistor, to secure it. Then, two more holes were drilled on each side of the center hole, 5/16" away from it. These were drilled with a #26 drill bit, and were left untapped. These were holes for the screws that secure the copper disk to the aluminum post below it. Then, holes were drilled and tapped to 8-32 to allow for the fan to be installed right above the transistor. Then, holes were drilled and tapped with 1/4"-20 threading to allow for the nylon rods to secure the resistor mounting on top. A diagram of the holes drilled at this point can be seen in Figure B.1

Figure B.1: Precisely drilled holes on copper disk, with threadings specified.

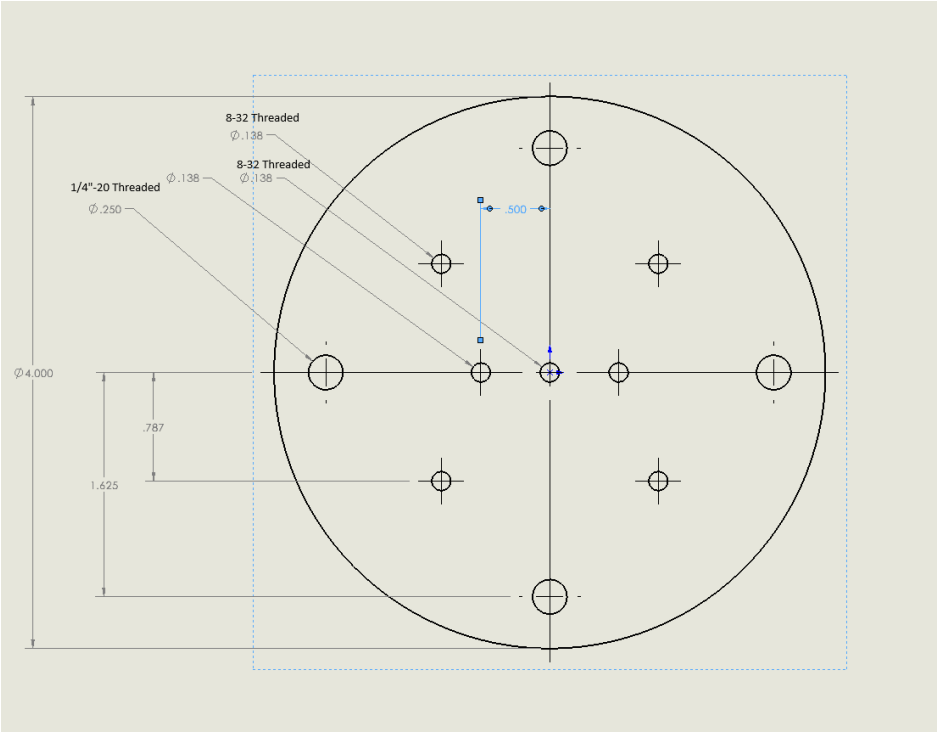

Once these holes were drilled, 16 untapped holes were drilled around the circle made by the fan threadings to allow for air circulation. These did not have to be very precise, as they weren't attaching to other components. Finally, a hole was drilled off to the side to allow for wiring to be fed through the copper disk. This also did not have to be very precise.

1" thick, 4.5" Diameter Aluminum disk

This element was meant to be used as the base of the HV divider, mounted on top of the electronic wiring box. It was around this element that the acrylic tube would fit. As such, it needed to be able to screw into the top of the electronics box, and to the bottom of the aluminum post. It also required a hole to be drilled to allow for wires to be fed through. The bottom of the resulting disk can be seen in Figure B.2, and the top in Figure B.3

Notice that the two center screws, used to screw the disk into the aluminum post, have larger holes drilled halfway into the disk on the bottom. This is to make sure the heads of the 6-32 screws used to screw in the post are able to enter into the aluminum disk, so that the bottom of the disk can be flush with the top of the electronics box. Also note that the two holes on the bottom, used to screw the disk to the electronics box, are 10-32 threaded. Finally, a hole had to be drilled and threaded into the side of the disk, to allow it to be fixed to the acrylic tube slipped over it.

1 Thick, 1.25 Diameter Aluminum Disk

This is the post that lifts the 4" copper disk off of the 4.5" aluminum disk. On both its top and bottom, two 6-32 holes are drilled and tapped. The bottom is shown in Figure B.5 and the top is shown in Figure B.4.

Note that there are additional holes and indents drilled, where the initial holes were misaligned, or where drill taps broke.

Figure B.2: Bottom of the 4.5” aluminum disk.

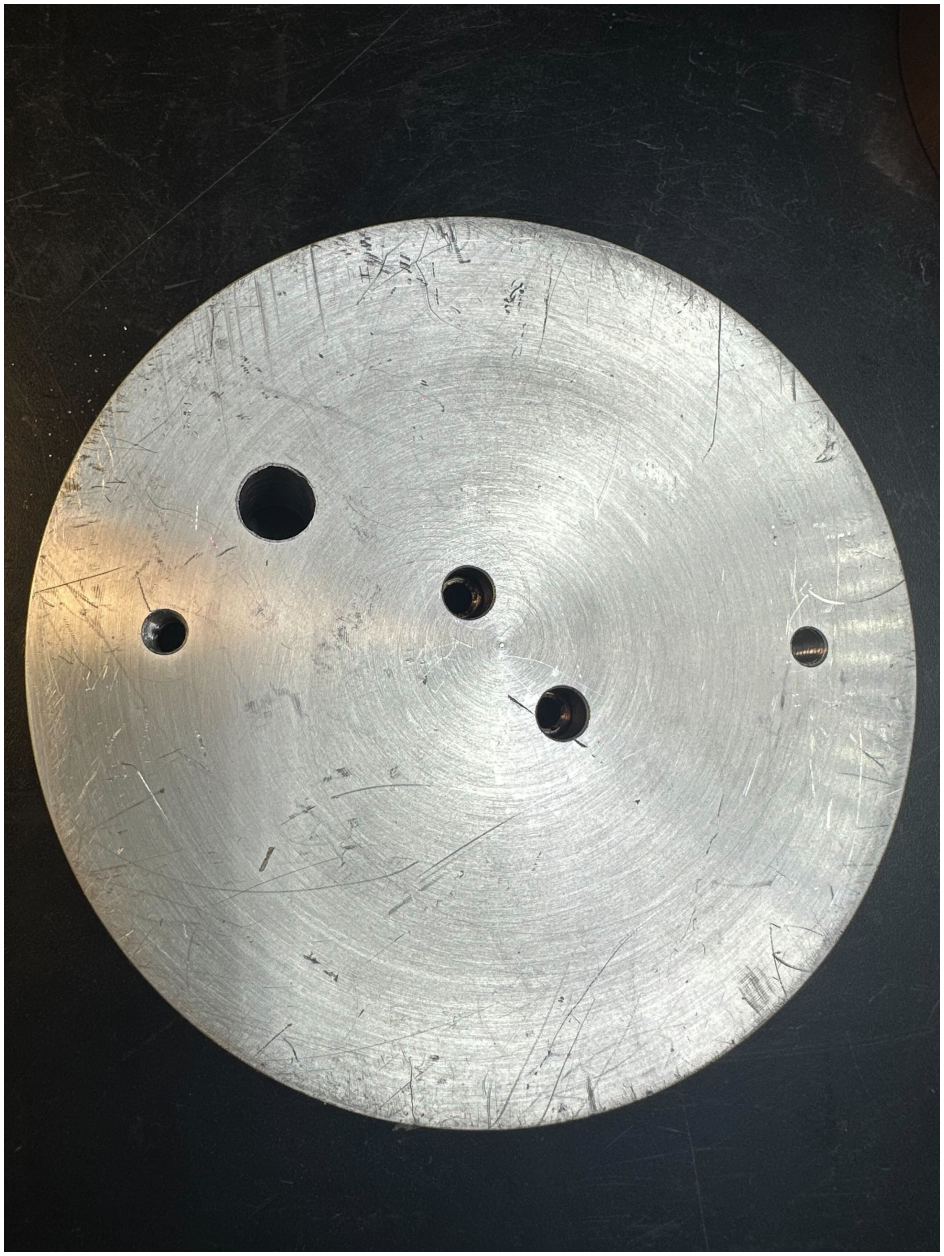

Acrylic tube, 5” OD, 4.5” ID, 3 feet long

This tube required machining in the machine shop. First, the tube had to be cut into two 1.5 foot pieces. Only one of these pieces was needed, but both proved to be necessary, since the first piece cracked from trying to force it onto the 4.5” aluminum disk. In order to get

Figure B.3: Top of the 4.5” aluminum disk.

the second piece to fit, the 4.5” aluminum disk had to be brought to the machine shop again, and very slightly reduced in thickness. This allowed the acrylic tube to slip over it. A notch also had to be drilled and cut from its side, to allow a screw to affix it to the disk.

Figure B.4: Top of the 1.25” aluminum post.

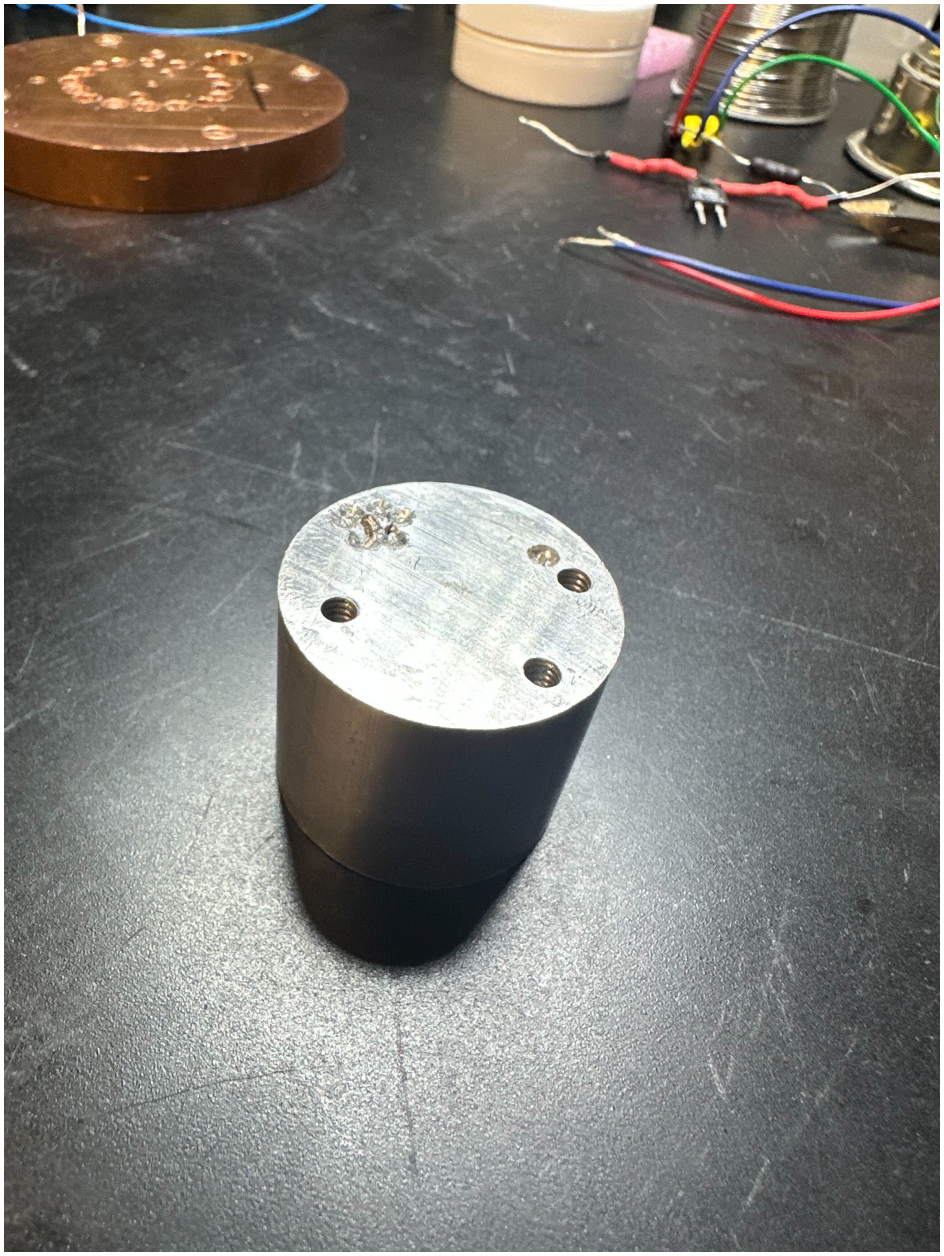

1/4”-20 threaded nylon rods, 2 feet long

These rods need to be cut down to a reasonable length once final assembly is done.

Figure B.5: Bottom of the 1.25” aluminum post.

Box for electronics

The box used is 8” x 8” x 3”. It consists of 4 metal parts, and requires machining to makes sure the right components can fit. The first task was to drill holes to allow the 24 V power supply to be affixed to the side of the box. Two pictures of the power supply screwed to the

side of the wall can be seen in Figures B.6 and B.7.

Figure B.6: Outward side of the wall with the power supply screwed in.

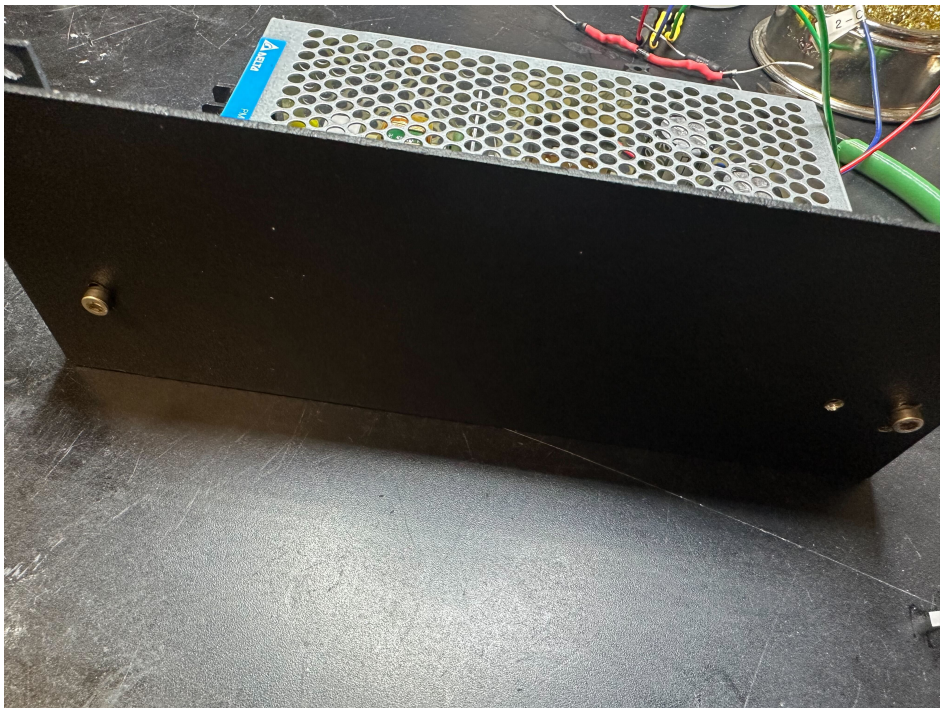

In order to make this fit, a small section of the wall had to be cut away. This cut did not interfere with the assembly of the box itself. Pictures of this cut can be seen in Figures B.8 and B.9

In addition to these holes and cuts, additional cuts had to be made for the temperature controller and feedthrough for the power cord. For the C13 plug, a square hole was cut into the top of one of the walls, and holes drilled so it could be screwed into the side. Two pictures can be seen in Figures B.10 and B.11.

Figure B.11 also contains the first of the two square cuts needed to install the temperature controller. The other can be seen in Figure B.12.

An image of how the temperature controller sits installed in the box can be seen in Figure B.13

Figure B.7: Inward side of the wall with the power supply screwed in.

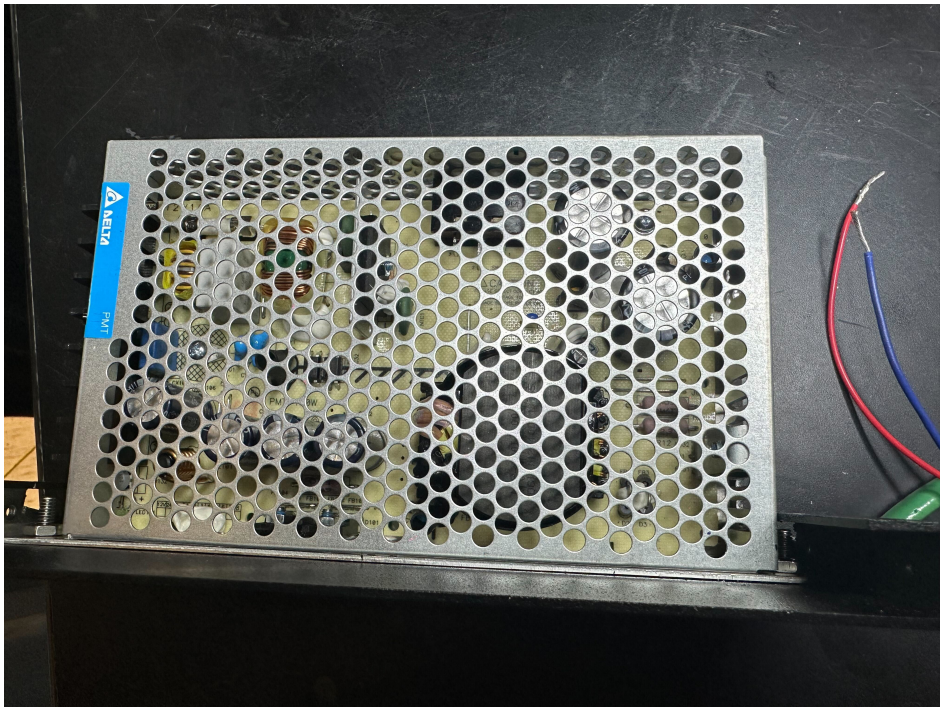

Figure B.8: Front cut made to allow for power supply to fit. Note that the cut made is below the hole required for assembling the box together.

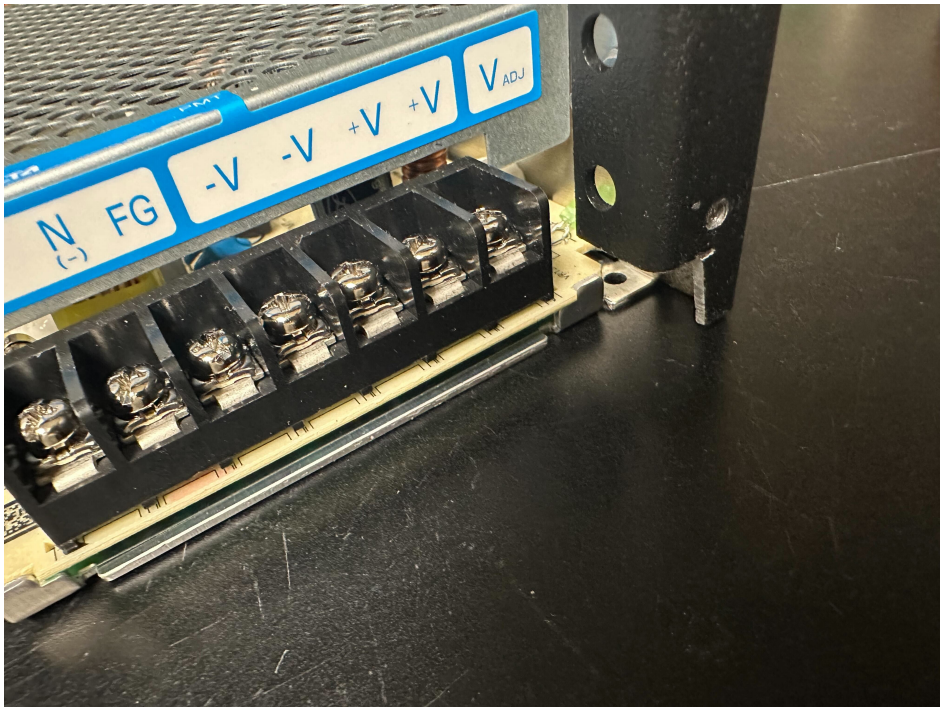

Figure B.9: Back cut made to allow for power supply to fit. Note that the cut made is below the hole required for assembling the box together.

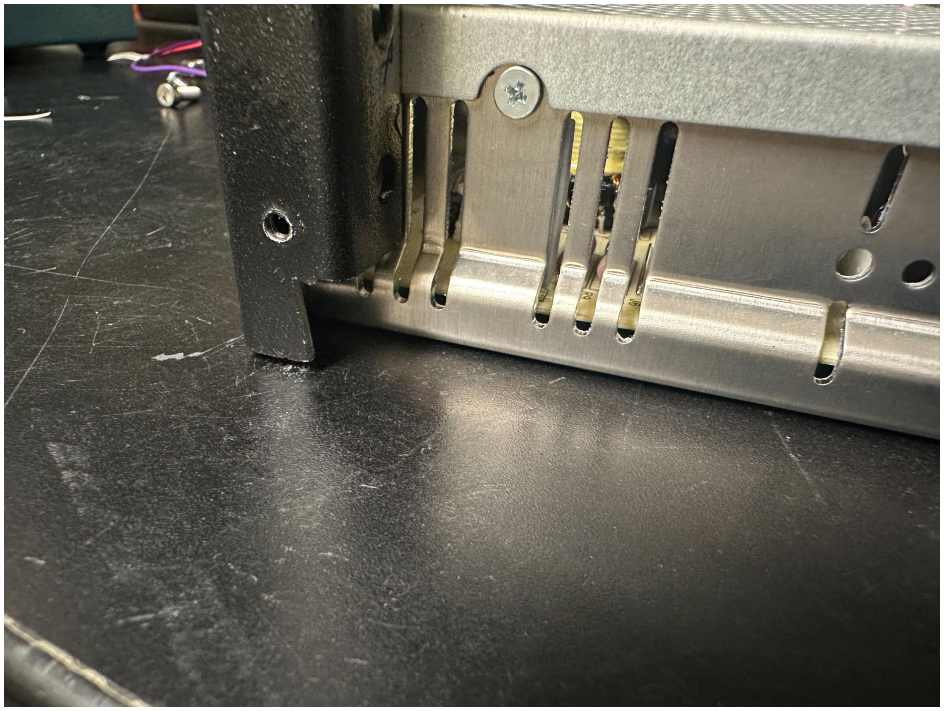

Corona Ring Halves with Holes

In order to fasten the corona ring onto the top of the HV divider, 4 holes had to be drilled to allow for the nylon rods to be fed through.

Circuitry

The circuit diagram for the temperature controlling element can be seen in Figure B.14. The power for this comes from a wall socket, and an additional modification made for this HV divider was to provide a power plug feedthrough on the side of the box.

The thermocouple was affixed to the side of the 3d-printed columnt by drilling holes and using zip ties, as can be seen in Figure B.15.

Figure B.10: Square cut made to allow C13 plug to fit. Note that holes were also drilled, to allow the plug to be fastened to the side of the wall.

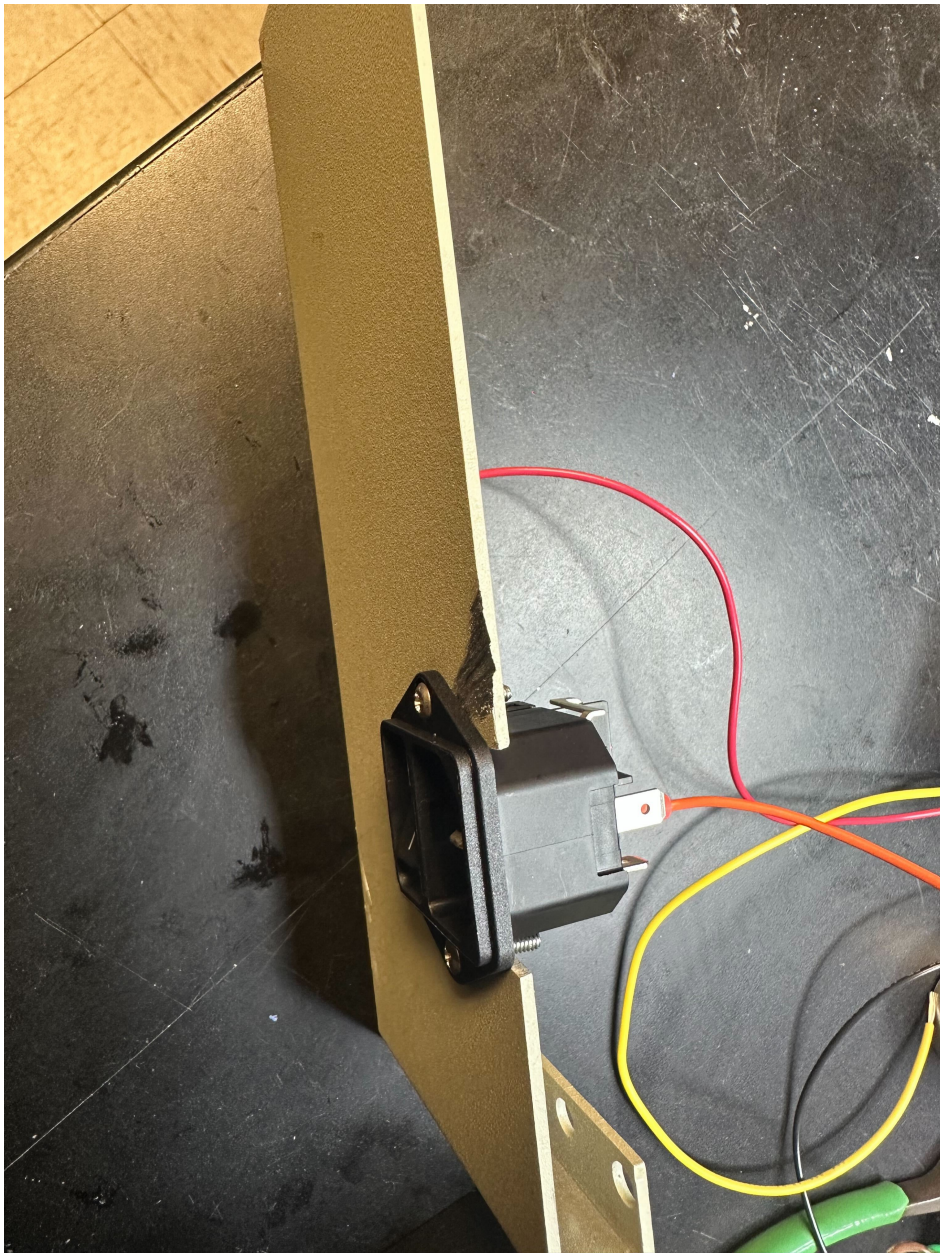

With these parts machined, the HV divider can be fully assembled

Figure B.11: Another view of the square cut made to allow C13 plug to fit. Note the power supply affixed to the left wall, and the square cut at the bottom of the front, to allow the temperature controller to be installed.

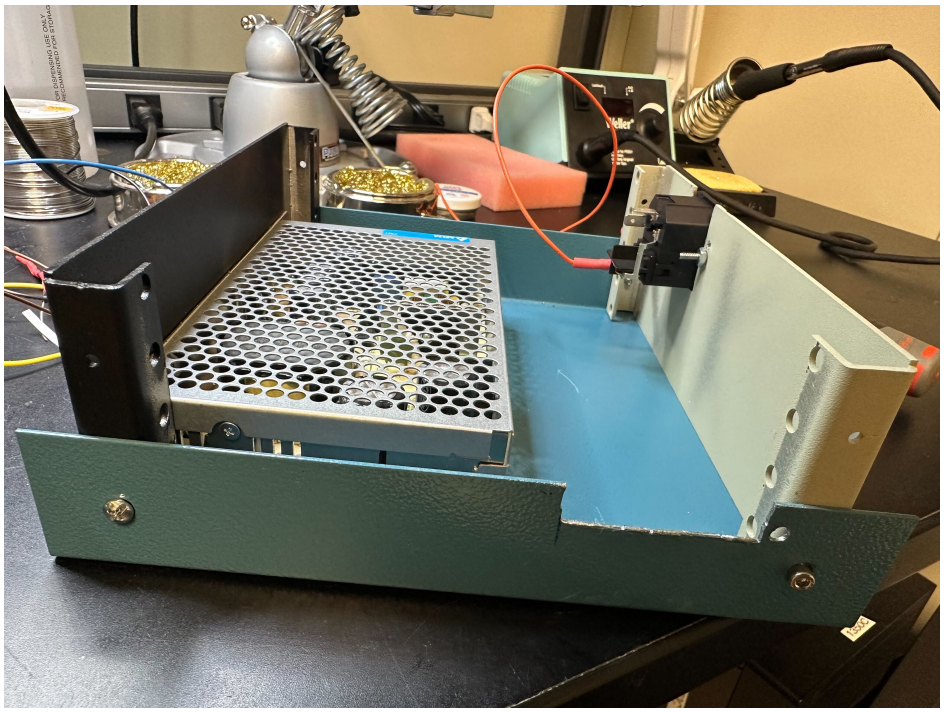

Assembly

First, the three disks that make up the stand have to be assembled together, as seen in Figure B.16.

Then, the transistor was affixed, using thermal paste, as seen in Figure B.17

The, the fan was installed on top of this, using 3d-printed spacers to lift it above the transistor, as seen in Figure B.18

Meanwhile, the 3d-printed columns were glued together, and had the HV resistors soldered together in a spiral column. The thermocouple was also installed on the inside of the column. This can be seen in Figure B.19

After this, the column was affixed to the copper disk using the nylon rods, as can be seen

Figure B.12: View of the partially assembled HV divider. On the bottom, notice the square cut made to the top piece of the box. This is made to allow the temperature controller to fit.

in Figure B.20.

Once this was done, the circuitry between the temperature controlling box and the elements on the copper disk were wired together, as can be seen in Figure B.21.

Figure B.13: View of the temperature controller installed inside the box. Holes were drilled to allow a screw to be used to fasten the controller to the bottom portion of the box. Another hole is used for the top part of the box.

After this, the temperature controlling box and column stand could be attached together, and the acrylic tube slid on, as in Figure B.22.

The wiring for the tube at the bottom of the stand had to be made, which attached to

Figure B.14: Circuitry diagram for the temperature controller of the HV divider.

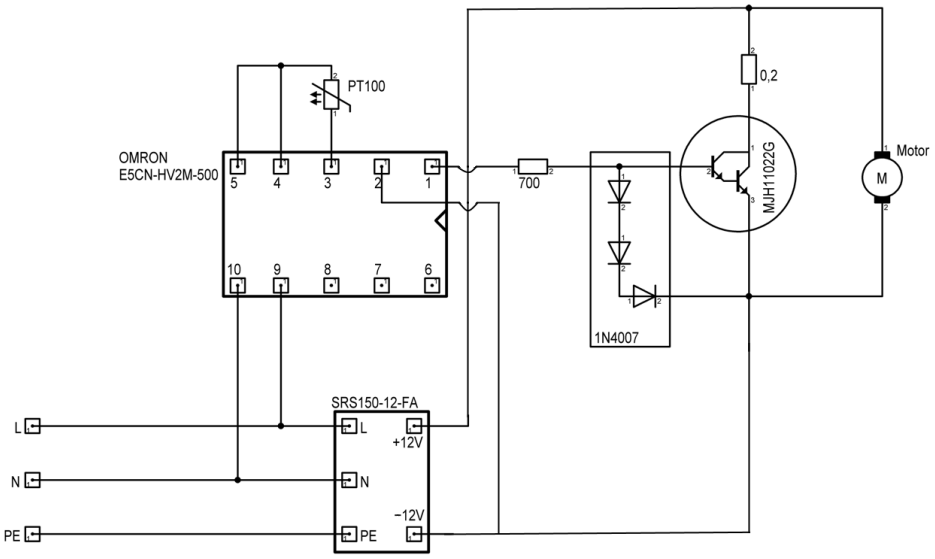

both sides of the 700 Ω resistor soldered to the last of the HV resistors. By measuring the voltage across this resistor, the divider ratio could be used to find the voltage at the top. The wire used to connect this to a volt meter is shielded, with the shield being grounded. An image of this can be seen in Figure B.23

Future Work

The HV divider is still not completed. There are a variety of tasks left to perform:

1. Install the top of the HV divider. These parts have already been machined to do this, all that has to be done is put the two corona rings on top of the nylong rods, and screw the copper corona ball to the top. Then, attach the bottom of the corona ball to the top of the HV dividing resistors.

2. The original 0.2 Ω resistors seems to burn out when the temperature controlling circuit

Figure B.15: Zipties used to affix thermocouple to the inside of the 3d-printed column.

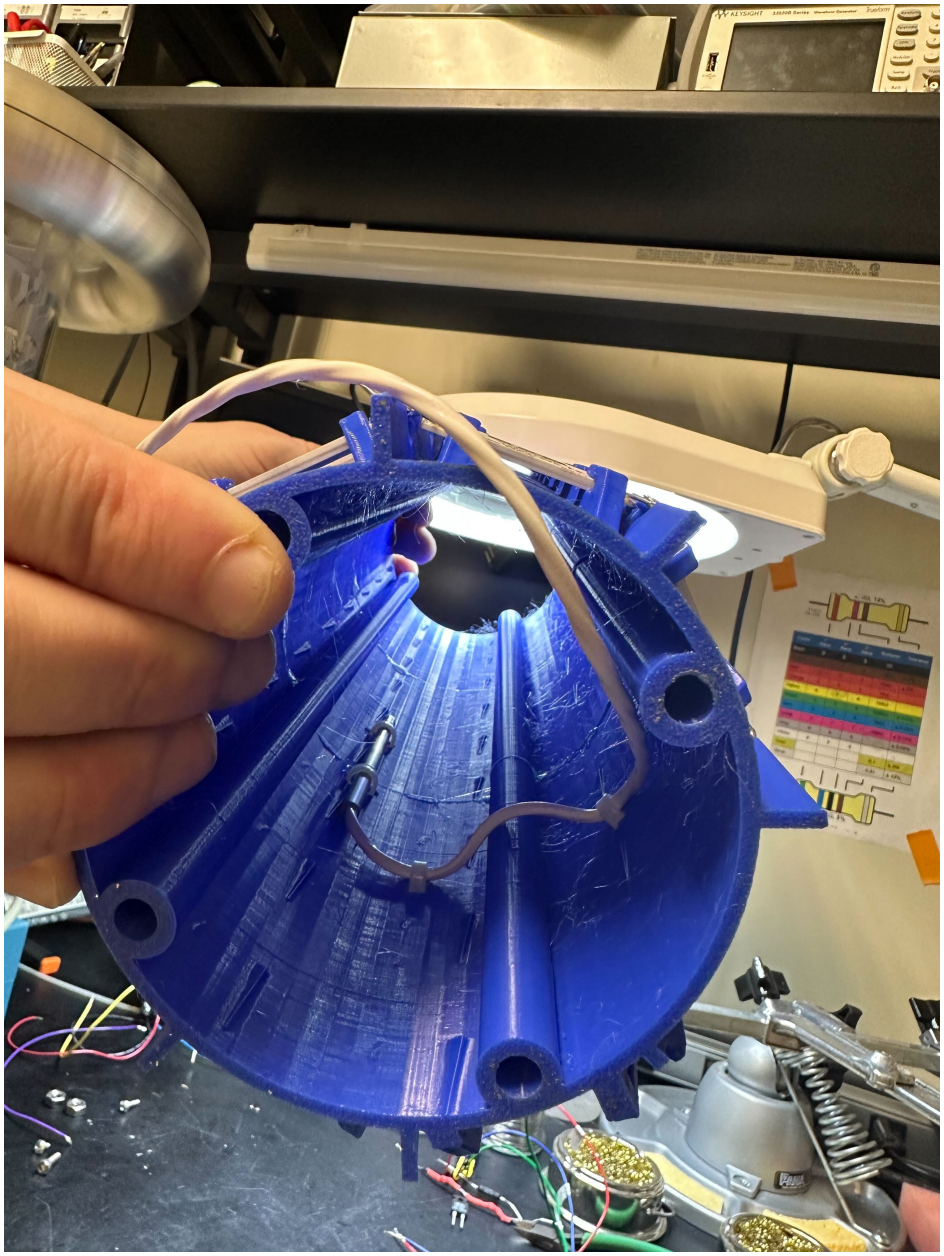

is tested. A high-power 1.5 Ω resistor has been aquired. Once it is installed on the circuit, and potentially affixed to the bottom of the copper disk with thermal paste, it should work.

3. The whole HV divider needs to be tested agains the other that we currently have, to

Figure B.16: All three of the metal disks fastened together.

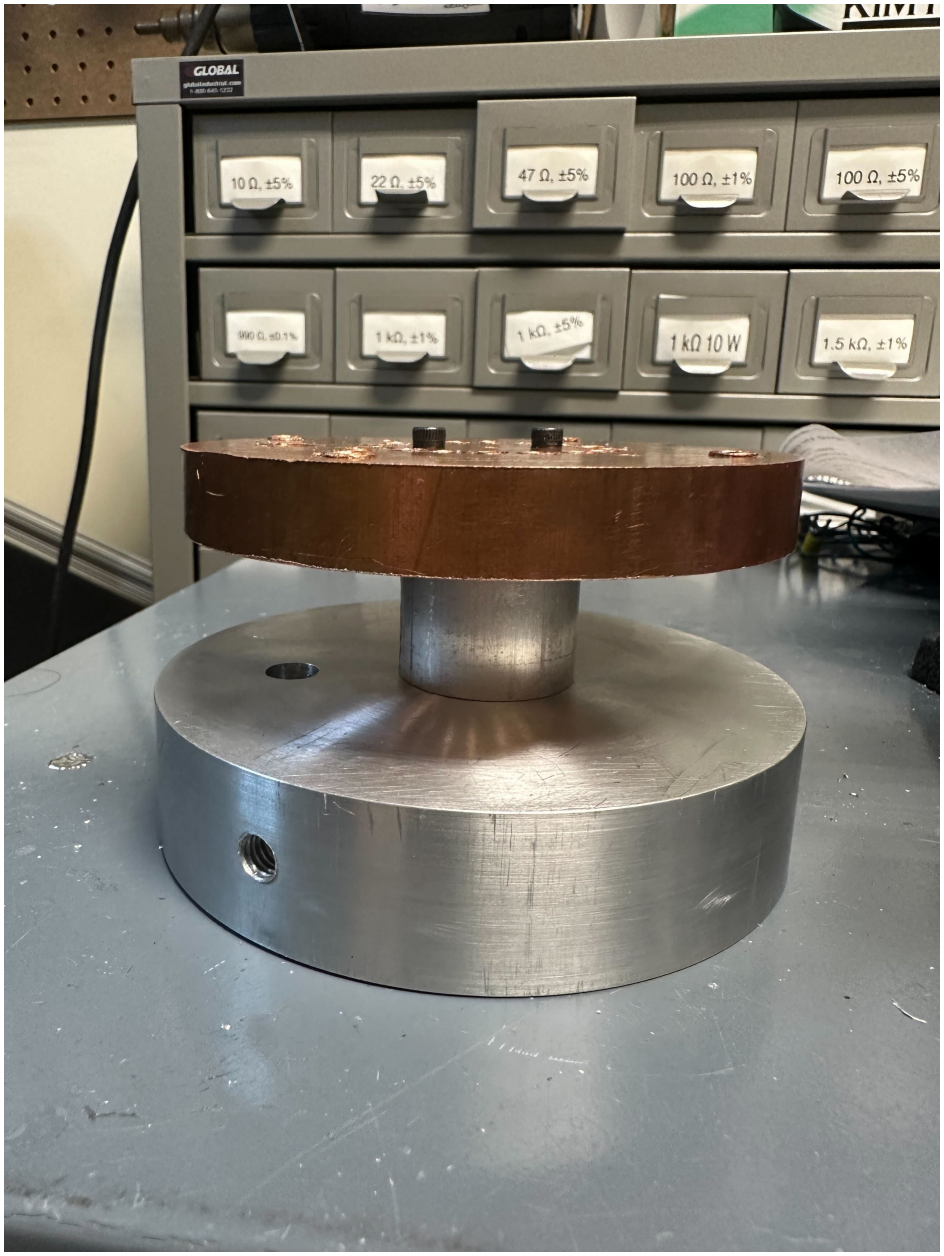

make sure its very reproducible.

Figure B.17: Darlington transistor affixed to the top copper electrode with thermal paste.

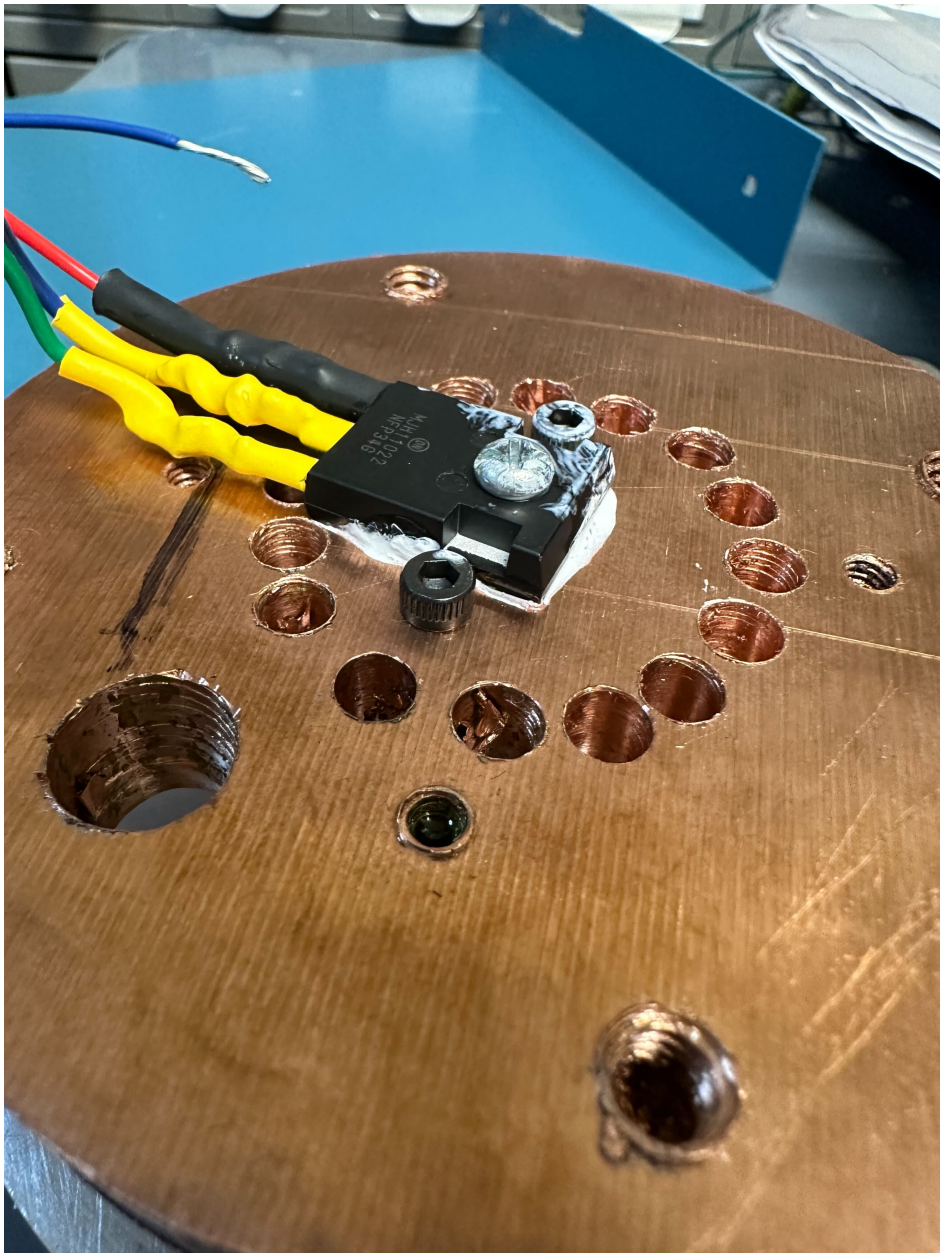

Figure B.18: Fan element screwed into the top of the copper disk.

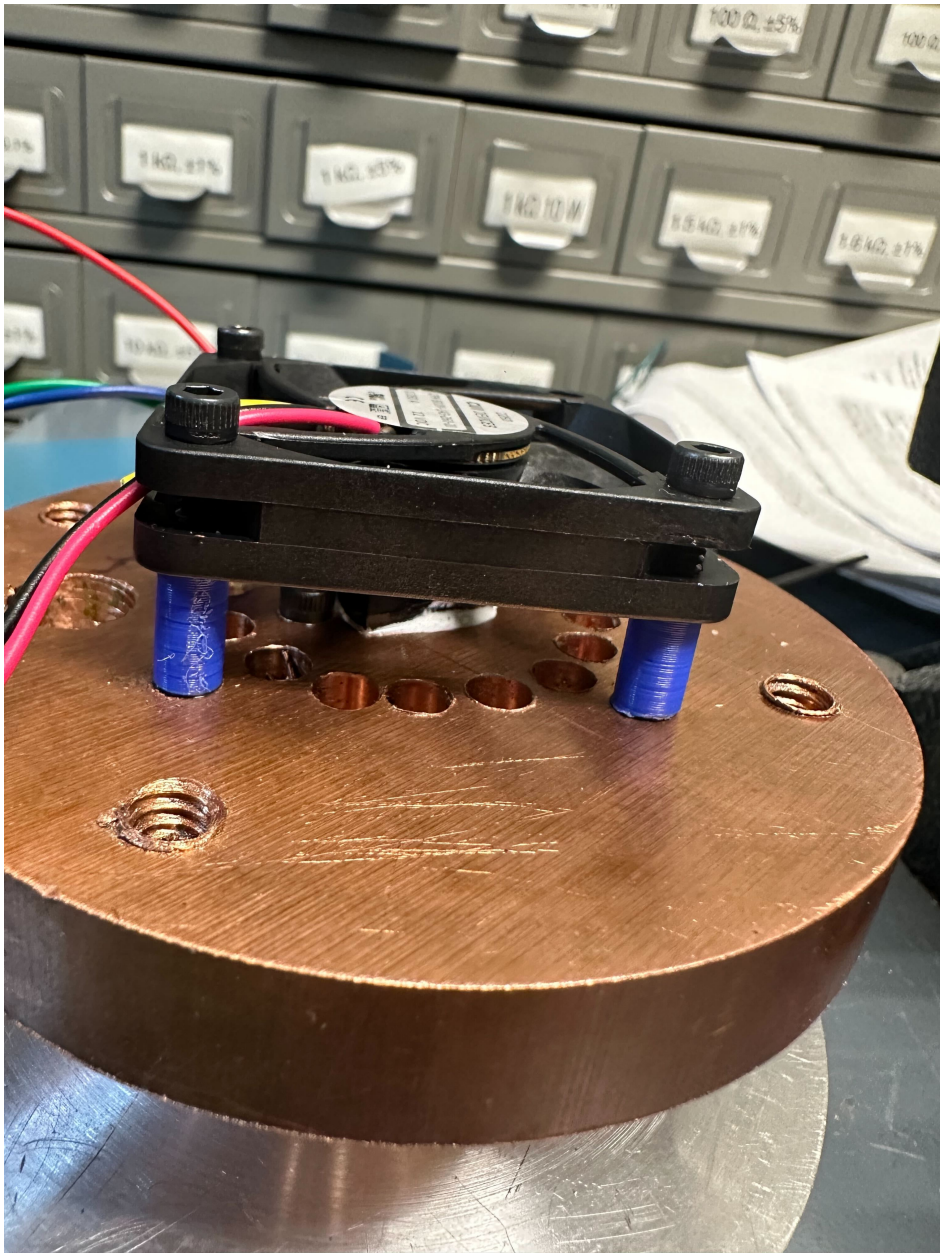

Figure B.19: HV resistors installed in a spiral pattern around the 3d-printed column. Note the zipties, which are used to hold the thermocouple in place. Also note that the 3d-printed columns are glued together.

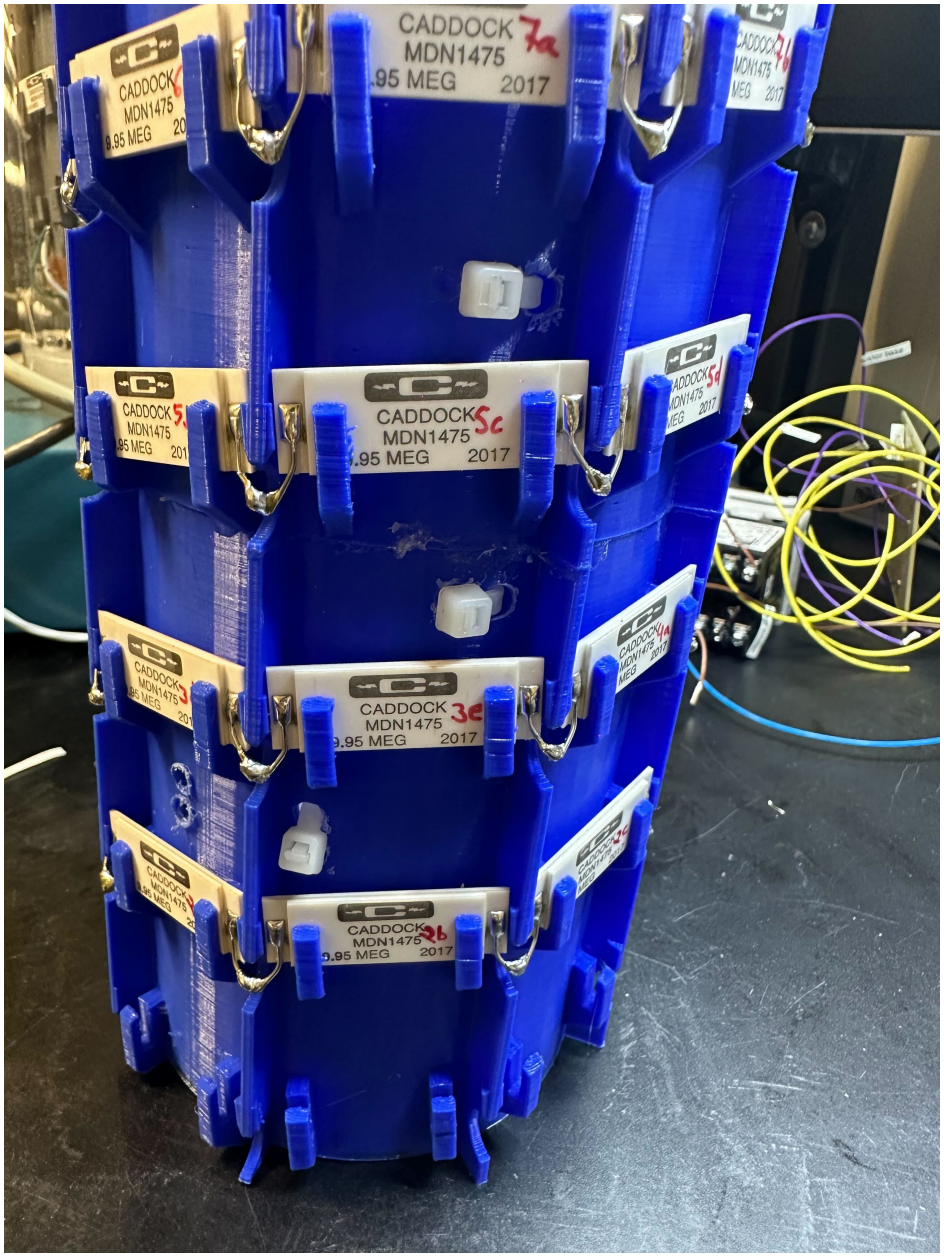

Figure B.20: The 3d-printed column installed on the copper disk. Note the nylon rods used for holding the column in place.

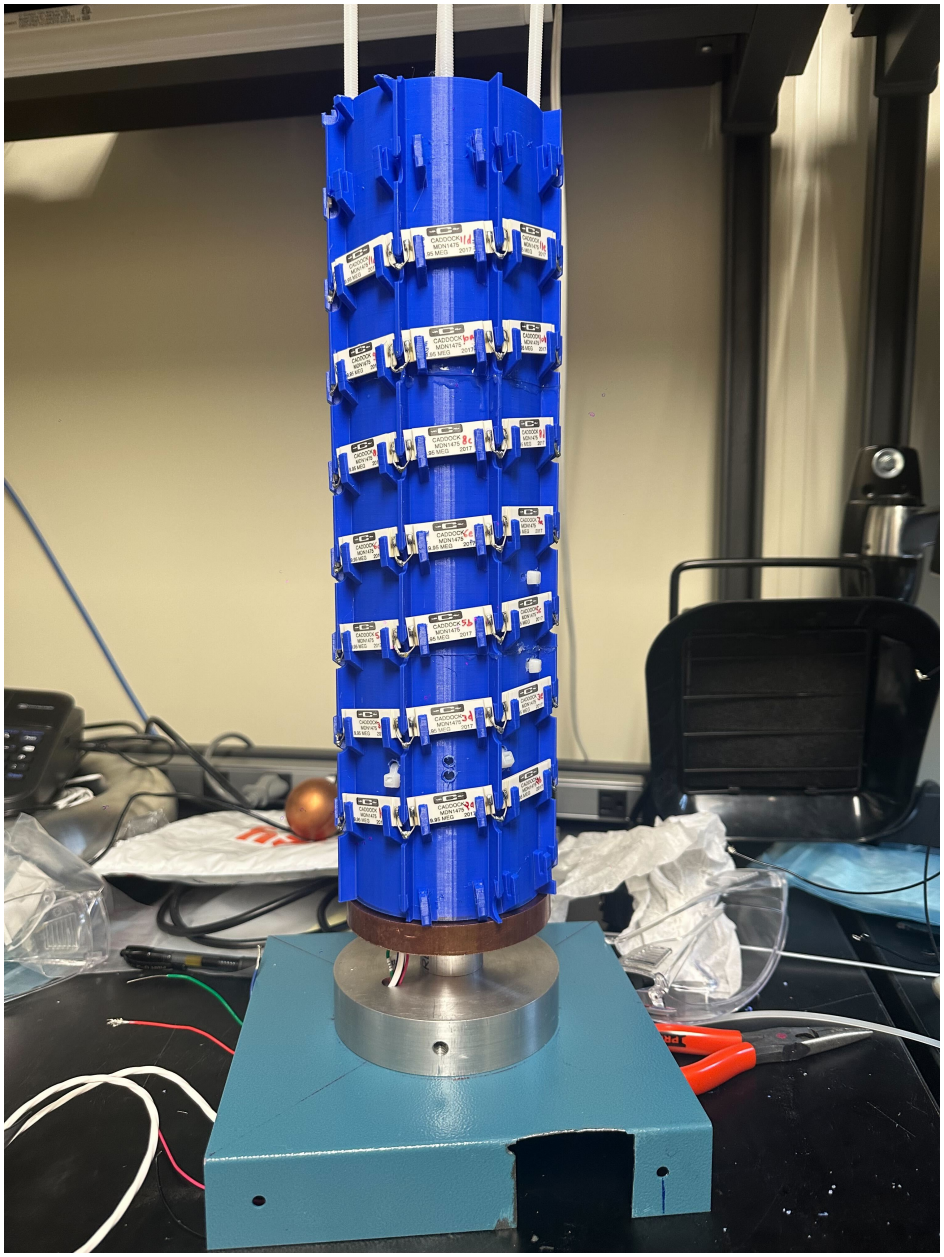

Figure B.21: Circuitry for the temperature controller wired together.

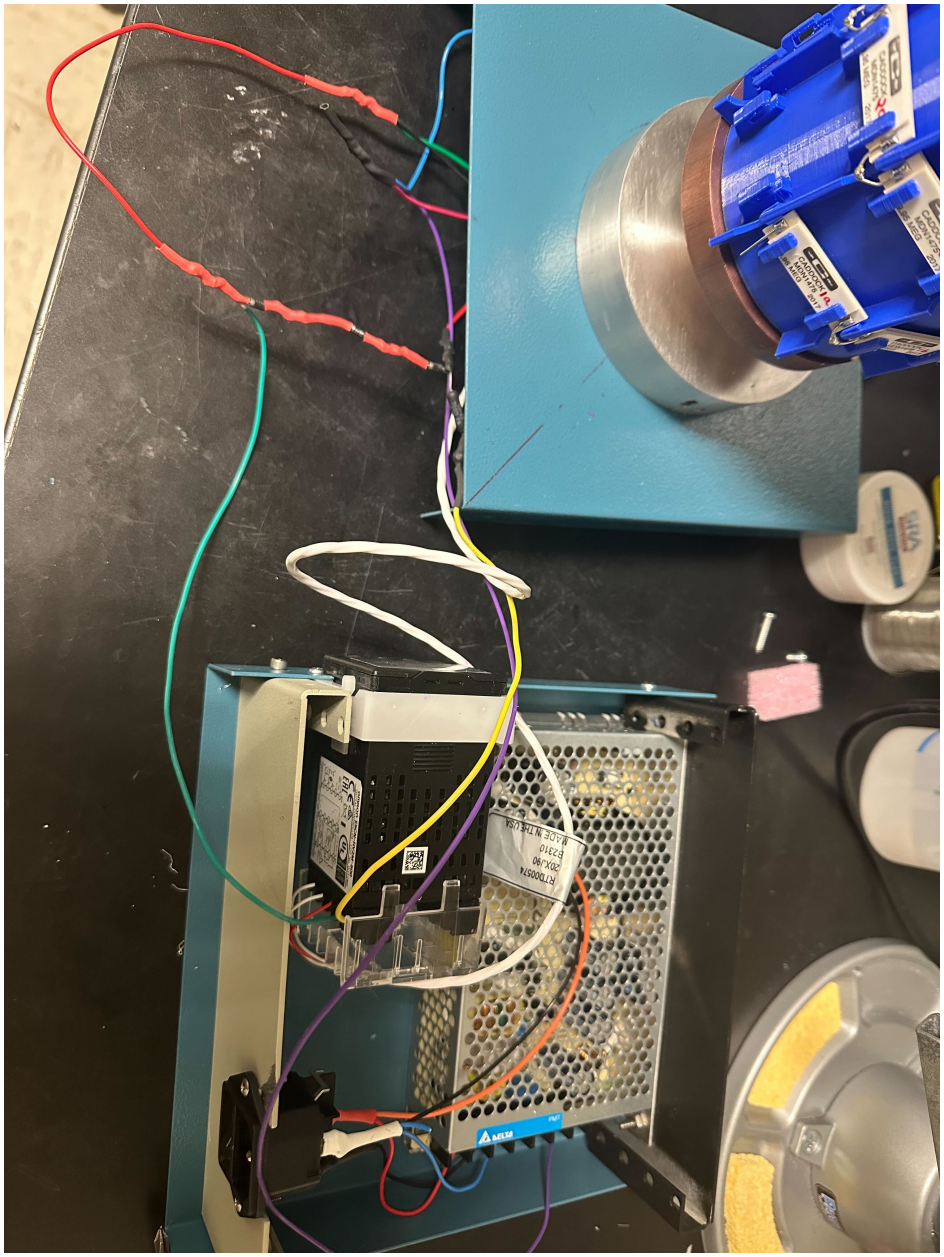

Figure B.22: HV resistor stand installed on top of the temperature controlling box, with the acrylic tube for protection.

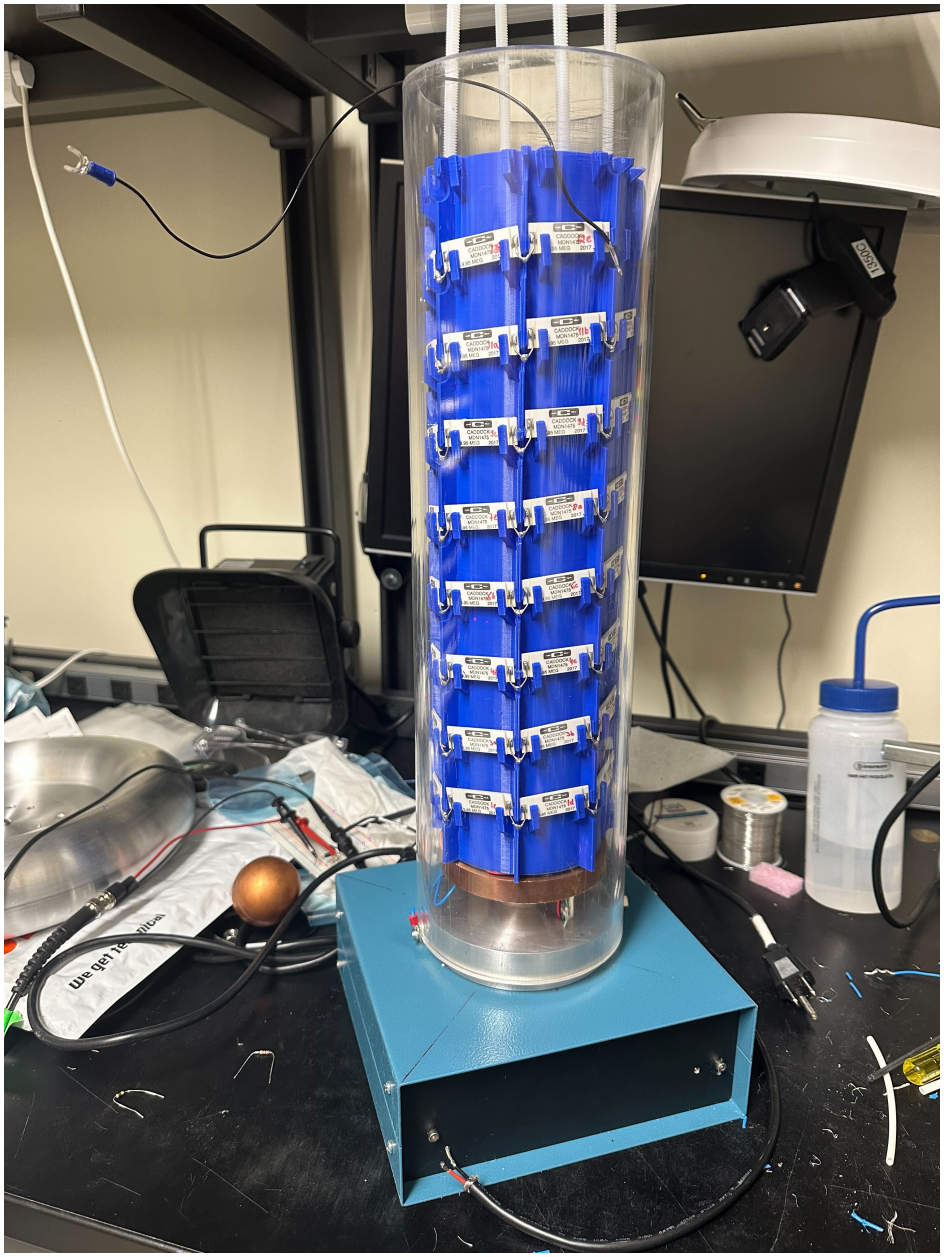

Figure B.23: Shielded double-wire, attached to either side of the 700 Ω resistor, with the shield being grounded. Measuring the voltage across this resistor can be used to find the total voltage across the full HV divider.